

WISSENSCHAFTLICH-TECHNISCHE BERICHTE

FZR-322

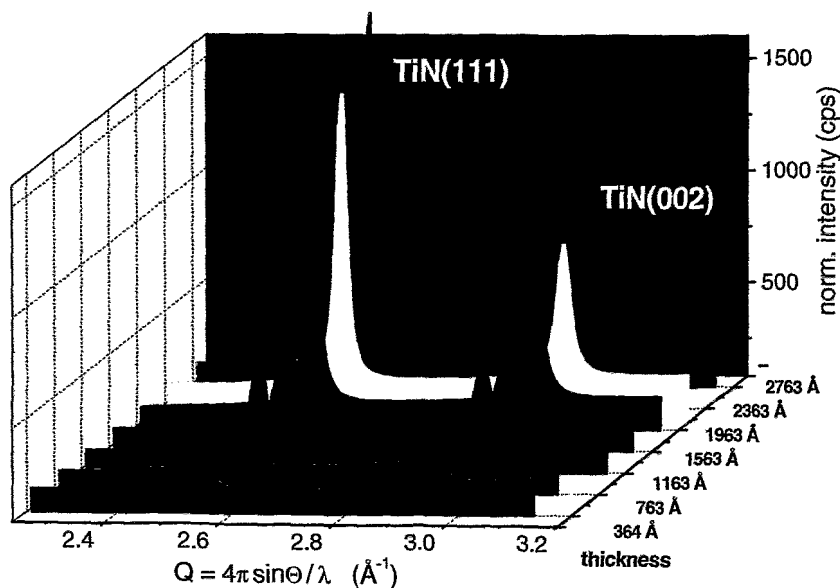
Juni 2001

ISSN 1437-322X



Archiv-Ex. 11

Project-Group ESRF-Beamline (ROBL-CRG)



Bi-Annual Report 1999/2000

Cover picture:

Representation of a series of vertical Bragg-Brentano scans as a function of film thickness collected during *in situ* observation of TiN film desposition at ROBL-MRH. The sequence demonstates the change of texture of TiN with increasing film thickness. At the beginning of the deposition process (002) planes if the cubic lattice are parallel to the surface. For larger thicknesses the preferred orientation becomes (111), indicated by the much faster intensity increase of this reflection (see contribution on p. 5).

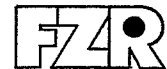
Forschungszentrum Rossendorf e. V.

Postfach 51 01 19
D-01314 Dresden
Bundesrepublik Deutschland

Telefon +49 (3 51) 2 60 31 22
Telefax +49 (3 51) 2 60 34 62
E-Mail W.Matz@fz-rossendorf.de
Internet <http://www.fz-rossendorf.de/FWE>

FORSCHUNGSZENTRUM ROSSENDORF

Mitglied der Wissenschaftsgemeinschaft Gottfried Wilhelm Leibniz



WISSENSCHAFTLICH-TECHNISCHE BERICHTE

FZR-322

Juni 2001

Bi-Annual Report 1999/2000

**Project - Group ESRF-Beamline
(ROBL-CRG)**

Editor: W. Matz

Preface

The second report from the Project-Group ESRF-Beamline of the Forschungszentrum Rossendorf covers the period from July 1999 until December 2000. The ROssendorf BeamLine (ROBL) at the European Synchrotron Radiation Facility (ESRF) in Grenoble, France performed quite well during this time. In the beamtime used by the FZR and collaborating institutes 44 scheduled experiments were performed, while in the ESRF scheduled beamtime 12 experiments. Additionally, a distinct amount of beamtime was devoted to in-house research of the FZR and methodical experiments.


The main effort from the technical point of view during the reporting period was made in the improvement of equipment. At the radiochemistry end-station a closed cycle He cryostat was commissioned and a newly developed control software XATROS for control and data acquisition in the EXAFS/XANES experiments was installed. At the materials research end-station an analyser system in front of the detector and the two-dimensional CCD-detector were commissioned during the period. Additionally, a small chamber for *in situ* structural studies of thin films during sputter deposition was designed and commissioned. Two of the following contributions demonstrate as examples the new scientific possibilities with this equipment.

Since February 2000 ROBL is part of the European Commission's programme "Access to Research Infrastructure" which supports user groups from member and associated states of the EU during experiments at ROBL. In the year 2000 ROBL hosted 6 groups for experiments.

The "2nd Euroconference and NEA Workshop on Speciation, Techniques, and Facilities for Radioactive Materials at Synchrotron Light Sources" took place in Grenoble 10-12 September 2000. The FZR was main organiser of this workshop which was attended by over 70 scientist from 10 countries.

The ROBL-CRG would like to thank all partners, research groups and organisations who supported its progress during the last 18 months. Special thanks are due to the FZR management, the CRG office and the Safety group of the ESRF.

The report is organised in three main parts. The first part contains extended contributions on results obtained at ROBL. The second part gives an overview about the scheduled experiments, publications, guests having visited ROBL with support of the EC, and some other information. Finally, the third part collects the experimental reports of the user groups received.



Dr. Wolfgang Matz

Contents

	Page
Contributions	
A miniature sputter deposition chamber for <i>in situ</i> film growth studies by synchrotron radiation scattering	5
<i>In situ</i> study of phase transformation at elevated temperature and correlated mechanical degradation of nitrogen implanted Ti-6Al-4V alloys	12
X-ray waveguides at ROBL: New developments and applications	18
EXAFS measurements of radioactive samples at low temperature	22
XANES and EXAFS measurements of plutonium hydrates	27
Local structure of Th complexes on montmorillonite clay mineral determined by extended X-ray absorption fine structure (EXAFS) spectroscopy	33
Statistics	
Overview about the beamtime distribution at ROBL	39
Support of user groups by the European Commission	40
List of EC supported users of ROBL	41
Scheduled experiments at the radiochemistry end-station	42
Scheduled experiments at the materials research end-station	45
List of publications	47
Personnel of the Project-Group ESRF-Beamline	50
Experimental reports	
Experimental reports from the radiochemistry end-station (No. 20_01_xxx)	51
Experimental reports from the materials research end-station (No. 20_02_xxx)	74
Experimental reports from experiments scheduled by the ESRF	98

A miniature sputter deposition chamber for *in situ* film growth studies by synchrotron radiation scattering

N. Schell¹, W. Matz^{1,2}, W. Neumann³

¹ Project Group ESRF-Beamline; ² Institute of Ion Beam Physics and Materials Research;

³ Central Department Experimental Facilities and Information Technology
Forschungszentrum Rossendorf, P.O. Box 51 01 19, 01314 Dresden, Germany

J. Bøttiger, J. Chevallier, P. Kringhøj

Institute of Physics and Astronomy, University of Aarhus, 8000 Aarhus C, Denmark

1. Introduction

The technological importance of thin films has stimulated an increasing interest in the detailed characterisation of the structure and morphology of thin films and their interfaces as well as the underlying growth mechanisms. It is a challenge to understand, both experimentally and theoretically, the growth mode and the micro-structural development during deposition of thin films. This development depends crucially on the deposition parameters, and such knowledge is required to tailor the film microstructure for specific applications.

One widespread technique for layer deposition is sputtering. It is applied for pure elements as well as for compounds. As its vacuum requirements are only moderate, electron diffraction as *in situ* characterisation method is not applicable. However, x-rays are in that case a powerful probe. In the literature some deposition chambers for *in situ* x-ray diffraction and reflectivity during sputtering are described [1-4]. They are, however, mostly adapted to a special dedicated instrument and use instrumental functions not commonly available. Our approach was to develop a low cost chamber which allows to follow *in situ* the film growth and post deposition annealing by different modes of synchrotron radiation scattering. The chamber should fit into the standard HUBER six-circle goniometer which is used as a multi-purpose instrument for many other experiments at the materials end-station of the Rossendorf Beamline ROBL in Grenoble [5].

2. Chamber design

In order to get as much information as possible on the growth process, the sputter deposition chamber allows for the following types of experiments:

- symmetric x-ray diffraction (Bragg-Brentano geometry) for measuring out-of-plane lattice constants and texture
- vertical grazing incidence diffraction for enhancing the signal of very thin films and suppressing substrate scattering
- reflectometry for determining the film thickness and interface roughness
- in-plane grazing incidence/exit diffraction (GIXS) for the determination of lattice constants, stress and preferred orientation in the surface plane
- crystal truncation rod scattering to determine the growth mode (*step flow*, *layer-by-layer* or *island formation*).

To allow the preparation of either multi-component films or multi-layer structures, the chamber is equipped with two magnetrons and inlets for two sputter gases. To start with clean i.e. defined conditions, the vacuum reaches a base pressure of less than 10^{-6} mbar before starting the sputtering process. Furthermore, substrate heating and bias are installed.

Costs aside, the main limitations in the design were geometrical ones. It was necessary to respect the maximum load (15 kg) and space restrictions of the existing standard HUBER goniometer in order to guarantee the high precision of the settings (0.001°) [6]. Taking those

limitations into account one can use all existing installations/equipment at the goniometer like detectors, slits, collimators, filter units without any further modifications. The goniometer itself allows horizontal as well as vertical scattering geometries, and thereby all scattering techniques described above.

Fig. 1 shows the sputter deposition chamber inserted for experiments and Fig. 2 an interior cross-section. A detailed description can be found in Ref. [7]. The chamber consists of three separable parts: A central one connected to the ϕ -circle of the goniometer and equipped with different flanges on the circumference (for pumps, connected via throttle valves, vacuum gauges and a liquid nitrogen trap) and one bigger flange in the bottom which goes through the opening of the ϕ -circle and connects the demountable substrate carrier to the chamber. The hemispherical top is equipped with four radiation windows (made from 125 μm thick Kapton and sealed with Viton rings), flanges for the two unbalanced magnetrons (commercially available from AJA International [8]) – each placed at a distance of 100 mm from the substrate and tilted 30 degrees away from the substrate normal.

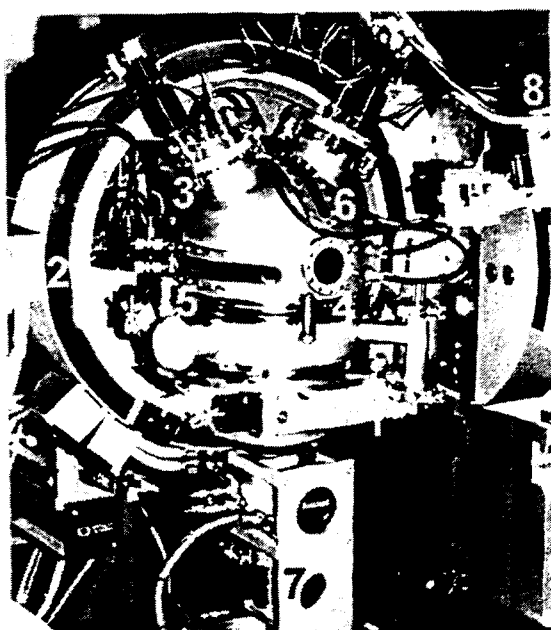


Fig. 1: Photo of the deposition chamber mounted into the standard Huber six-circle goniometer in the materials end-station of ROBL. 1: ϕ -circle, 2: χ -circle of Eulerian cradle, 3: magnetrons, 4: beam exit x-ray window, 5, 6: semi-circular large x-ray windows for the diffracted beam in horizontal and vertical planes, respectively, 7: drive for height adjustment of sample, 8: detector unit with slits. The power supply and the gas inlets for both magnetrons come from the top. (The turbo pumps are, however, not yet connected.)

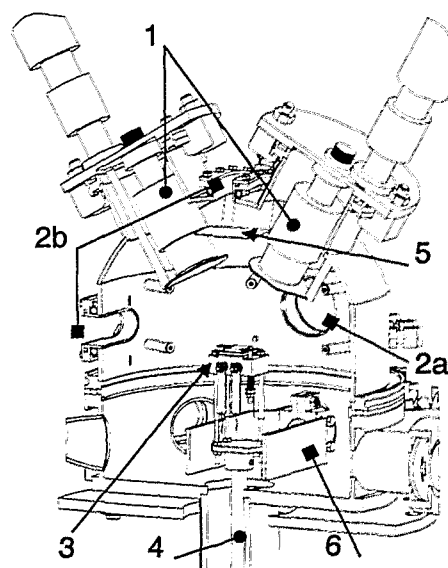


Fig. 2: Cross section with interior view of the sputter deposition chamber in a central plane. 1: magnetrons with shutters, 2a: entrance window for the incoming beam, 2b: exit windows for the diffracted beams, 3: substrate carrier with heating wires and bias voltage, 4: tube to the z-drive, 5: window protection foils to be fastened at inside protruding bolts, 6: copper disc as liquid nitrogen trap.

All the radiation window flanges are water cooled through outside copper tubes. Additionally, 1 μm thin aluminium foils are mounted on the inner side of the windows in order to protect the Kapton from thermal radiation and contamination by sputtered material. To avoid cross contamination of the two targets, each with a diameter of 1 inch, cylindrical chimneys separate them. Air-pressure-controlled shutters are placed in front of the

chimneys. For each magnetron a sputtering gas inlet is located separately on its corresponding flange.

The substrate (typical size 10x10 mm²) can be changed by disconnecting only the substrate carrier unit at the bottom flange of the chamber and flooding the chamber with dry nitrogen to minimise contamination of the chamber's inner walls from moisture or oxygen. The BN ceramics substrate holder is mounted on an inside tube connected via a flexible bellow to a precision slide. Driven by an outside stepper motor this allows the sample height to be adjusted by ± 7 mm. The electrical feedthroughs for sample heating (resistivity heater up to 650°C), bias voltage and thermocouple are also connected to the substrate carrier unit. The substrate is spring loaded to the BN block by three clamps, one of which is acting as the bias contact. The sample height adjustment and the magnetrons (sputter gas flow, shutter movements) are remote controlled.

The windows limit the angular range for the synchrotron radiation beam. The entrance and exit windows are circular shaped (diameter 40 mm) and asymmetrically arranged (-2° up to $+16^\circ$). They are used for reflectometry (total scattering angle usually $< 5^\circ$) and symmetric wide angle diffraction (total scattering angle $< 32^\circ$). A second, symmetric, long window in the same vertical plane gives an angular range from 33° to 100° (for wide angle diffraction under grazing incidence). A horizontal window (arranged from -4 mm to +17 mm in respect to the sample horizon) with an opening of 32° to 100° allows in-plane grazing incidence/exit diffraction under maximum grazing angles of 6° .

Despite the angular limitations one can study a large number of substances with widely varying crystal lattice spacings. The tunability of the monochromatic synchrotron radiation wavelength allows for an optimal adaptation to the substance under study.

3. First experiments: texture development in TiN films

After successful trial tests concerning handling and intensity considerations for future typical samples, a question of considerable interest was tackled: the texture development with thickness of TiN films, its manipulation by change of deposition parameters and the identification of the mechanism(s) controlling the crystallographic orientation. In many applications this texture is of paramount importance. The wear resistance of TiN deposited on tools, e.g., depends on the preferred orientation, and with the (111) orientation one gets the largest wear resistance [9]. Frequently, a crossover phenomenon is observed: at small thickness (002) oriented grains (the (002) plane is parallel to the film surface) dominate, while at larger thickness (111) oriented grains take over. In most previous studies [10] the preferred orientation of thin films was explained in terms of surface energy and kinetic factors. In the case of TiN films, it was suggested, that close to equilibrium the (111) grains dominate, while, away from equilibrium, (002) grains dominate.

Pelleg *et al.* [11] have suggested that the thermodynamic driving force for change in orientation of the grains from (002) to (111) in TiN is the difference of the sums of the surface energy and the strain energy of the two types of grains. The strain energy is proportional to the film thickness. The (111) grains have a larger surface energy than the (002) grains and the smaller strain energy. Based on this, they predicted that TiN films will grow with (002) grains at small thickness, where the surface term dominates, while (111) grains appear at larger thickness, because in this state the strain energy dominates. The model did not include details of the mechanism(s) controlling the orientation change of the growing grains. Later, Oh and Je [12] observed experimentally this prediction. But the mechanism for changing the orientation of the growing grains was not described in detail.

By real time synchrotron x-ray scattering, Je *et al.* [13] have studied the preferred orientation of TiN films, deposited by magnetron sputtering and TiN targets (not the usual reactive magnetron sputtering from Ti targets). They observed a crossover thickness, where the dominating growth direction switched from the $\langle 002 \rangle$ direction to the $\langle 111 \rangle$ and based

their interpretation on the model of Pelleg *et al.* [11]. After change of the growth direction, (002) planes still form the growing surface. However, they were tilted away from the film surface normal, so the (111) planes of the growing grains were parallel with the film surface, and the surface became faceted with a large surface roughness.

In a theoretical paper, Dong and Srolovitz [15] demonstrated that texture may develop by recrystallisation. With computer simulations, they showed that in the case of two neighbouring grains, with different larger defect density (strain energy), the grain boundary migrates. The grain with smaller defect density grew into the other grain. To our knowledge, recrystallisation has not been observed in TiN films.

Experimental studies of the development of the microstructure of TiN films deposited by reactive magnetron sputtering, especially the formation of texture during growth, were performed with the chamber described. The characterisation was done by *in situ* x-ray diffraction and reflectivity in order to determine the dependence on film thickness. Making use of mutual perpendicular scattering geometries allows to determine the orientation of the growing grains. Variable deposition parameters investigated were the deposition temperature (250°C to 450°C) and the bias voltage of the substrate (-30 V or -60 V). Previous RBS measurements have shown that within those parameters stoichiometric TiN films can be grown. The annealing behaviour of the growing films was followed by diffraction.

4. Experimental and performance of the sputter chamber

In order to optimise the deposition parameters different TiN films were grown in the chamber. These films were examined with RBS, TEM, and *ex situ* x-ray scattering at a laboratory source. Before deposition the base pressure in the chamber was about 2×10^{-5} Pa. The reactive sputter gas was a mixture of Ar (99.9996%) and N₂ (99.99990%) with the ratio 4:1 and a total gas pressure of 0.3 Pa. Only one magnetron was used and run at a dc power of 80 W. The substrates were Si(100) wafers with a 1000 Å amorphous oxide layer on top. For the deposition parameters chosen (bias voltages of -30 V and -60 V and substrate temperatures of 250°C, 350°C and 450°C) the deposition rate was about 1.4 Å/s. The incident x-rays were monochromatised to 12.651 keV ($\lambda = 0.980$ Å).

Fig. 3 shows two typical x-ray reflectivity curves recorded *in situ*. Fig. 4 gives the correlation of film thickness with sputtering time for all samples determined from reflectivity, demonstrating the linearity of the sputter deposition with time and the subtle dependence on the corresponding deposition parameters.

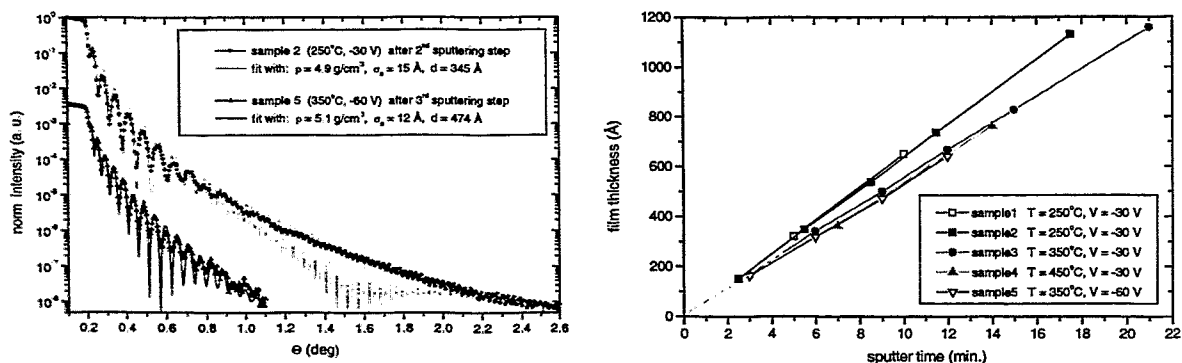


Fig. 3 (left): Typical specular reflectivity data. The upper curve is obtained after the 2nd sputtering step on a film that was deposited at 250°C with a bias voltage of -30 V, and the lower curve is obtained after the 3rd sputtering step on a film that is grown at (350°C; -60 V). The dotted and solid lines are model simulations with the fit values for density, surface roughness and film thickness indicated in the inset.

Fig. 4 (right): Comparison of film thickness against sputtering time for various deposition conditions indicated in the inset.

5. Development of the microstructure and recrystallisation of TiN films

For all chosen parameters the experimental procedure was the same: cleaning by pre-sputtering, sputter deposition for a certain time, interruption of the growth process to characterise the sample by reflectivity (giving density, thickness and roughness of surface and interface), vertical Bragg-Brentano scattering and in-plane (horizontal) GIXS (incidence/exit angles = $0.2^\circ/0.4^\circ$, i.e. the x-rays penetrated only approximately 100 Å). The whole process was repeated manyfold. Sometimes several identical scans had been taken to elucidate the temporal (annealing) behaviour (at the elevated deposition temperatures). Sometimes, after film completion, high temperature annealing had been performed. In addition the films had been characterised by TEM. For more details see [16].

Generally, it is found that for all deposition parameters the film growth is characterised by a crossover of the crystallographic orientation of the surface (Figs. 5 and 7) as also seen by other workers [12, 14]. At small film thickness, the (002) grains dominated the vertical diffraction scans while (111) grains took over at larger thickness. Cross sectional TEM micrograph of the TiN films show a columnar structure where the individual columns are composed of grains with low-angle grain boundaries. There is no indication of “competitive growth” in micrographs.

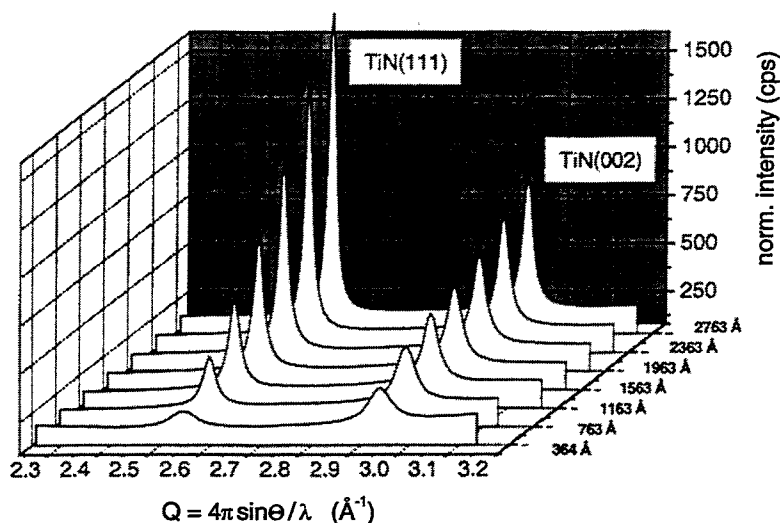


Fig. 5: Three-dimensional representation of a series of vertical Bragg-Brentano diffractograms as a function of film thickness for a film grown at 450°C with a bias of -30 V. A crossover is clearly seen, with grains having (002) planes parallel with the film surface dominating in the beginning while (111) grains take over at a larger film thickness.

For the first time, however, the underlying mechanism for this texture change could be observed by repeated GIXS scans as demonstrated in Fig. 6. It directly reveals recrystallisation of the topmost layer immediately after deposition. Another proof is the comparison of integrated peak intensities in vertical Bragg-Brentano geometry with those taken by horizontal GIXS scans as demonstrated in Fig. 7: the volume of the (111) grains (their (111) planes are parallel to the film surface) steadily increases with thickness, while the volume of the (002) grains levels off and stays then nearly constant with thickness. This saturation of the volume of the (002) grains stands in contrast to the summed (002) intensity that steadily increases with film thickness, i.e. with each new deposition step. Without recrystallisation (change of crystallographic orientation) of the (002) grains after deposition, the (002) Bragg-Brentano signal should be proportional to the summed (002) horizontal signal, since both signals reflect the volume of (002) grains. The saturation of the (002) signal, therefore, indicates recrystallisation of the (002) grains. Other mechanisms that also influence the texture development – the crossover – cannot be completely excluded. However, mechanisms like the “tilted-(002) surface” [13] and “competitive growth” [14] cannot play a significant role with the present deposition conditions. They should especially

lead to a levelling-off or even decreasing intensity for horizontal-scan (002) diffraction which, however, is in contrast to the actual observations (comp. Fig. 7).

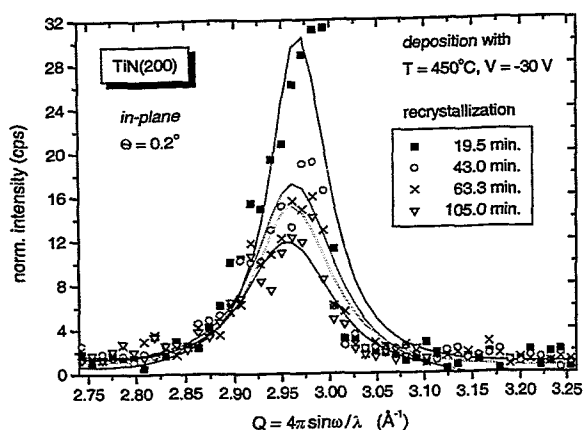


Fig. 6: TiN(200) horizontal-scan diffraction peaks obtained from a 1963 Å thick film (grown at 450°C with bias -30 V), measured 19.5 min., 43.0 min., 63.3 min. and 105 min., respectively, after the deposition was stopped. The substrate temperature was held constant at 450°C.

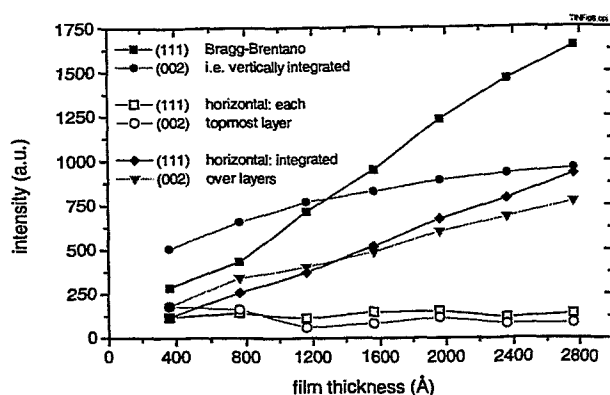


Fig. 7: Intensity data of the same film as in Fig. 5 (450°C, bias -30 V) shown as a function of thickness. Upper two curves: intensities of the (111) (filled squares) and the (002) (filled circles) Bragg-Brentano diffraction peaks. Lower two curves: intensities of the (111) (open squares) and the (200) (open circles) horizontal-scan diffraction peaks taken under grazing incidence/exit. The two curves in the middle represent the added GIXS intensities – summed up to the corresponding total thickness in question: (111) as filled diamonds and (200) as filled triangles.

The experimental data are consistent with the driving force proposed by Pelleg *et al.* [11]. Assuming this driving force, the crossover thickness increases with decreasing defect density, i.e. lower strain energy. As the defect density decreases with increasing deposition temperature due to defect annealing, the crossover thickness increases with temperature which is indeed observed. During growth, enhancement in the grain size is observed (by TEM micrographs and by a diminishing FWHM of the Bragg peaks with film thickness) which cannot be explained as normal grain growth. Otherwise grain growth/defect annihilation should be observable also during post-annealing. Rather than being thermodynamically driven, the increasing grain size with film thickness is probably controlled by kinetics. As the in-plane lattice constant is smaller than the out-of-plane lattice constant, it is concluded that the films are stressed in compression, with the stress-free lattice parameter lying somewhere between the in-plane and the out-of-plane lattice parameters.

6. Summary

A new, compact sputter deposition chamber which allows for *in situ* study of the growth process by synchrotron x-ray scattering was developed. During growth, the micro-structural development of TiN films – especially the change in texture with film thickness – was studied using *in situ* x-ray reflection and diffraction. Grains with (002) orientation, observed in vertical

diffraction scans, dominate at small film thickness, while (111) grains take over at larger thickness leading to a crossover depending on the deposition parameters. Recrystallisation is identified as a mechanism that controls the development of the texture. The topmost deposited layer has always a significant part of [002] orientation not changing in the deposition process while the lower film parts have already dominating [111] orientation. The recrystallisation of the topmost layer of the film proceeds immediately after the deposition. Post annealing does not change the texture state of the film. The data are consistent with the driving force for the change of orientation of the grains that was suggested by Pelleg *et al.* [11], i.e. the sum of the surface energy and the strain energy of the individual grains was minimised. During growth, the grain size increases with film thickness. This increase is not due to normal grain growth but is probably controlled by the kinetics. As concluded from the measured lattice constants, the films experience compressive stresses.

Acknowledgement

The authors wish to thank I. Heyne, W. Boede, U. Strauch, J. Claußner and A. Bauer for their technical support and assistance during the design and commissioning phase and during the measurements in Grenoble.

References

- [1] Hsin-Yi Lee, K.S. Liang, Chih-Hao Lee, and Tai-Bos Wu, *J. Mater. Res.* **15** (2000) 2606
- [2] J.H. Je, D.Y. Noh, H.K. Kim, and K.S. Liang, *J. Appl. Phys.* **81** (1997) 6126
- [3] S. Williams, J.Q. Zheng, M.C. Shih, X.K. Wang, S.J. Lee, E.D. Rippert, S. Maglic, H. Kajiyama, D. Segel, P. Dutta, R.P.H. Chang, J.B. Ketterson, T. Roberts, Y. Lin, R.T. Kampwirth, and K. Gray, *J. Appl. Phys.* **72** (1992) 4798
- [4] J.Q. Zheng, M.C. Shih, X.K. Wang, S. Williams, P. Dutta, R.P. Chang, and J.B. Ketterson, *J. Vac. Sci. Technol.* **A9** (1991) 128
- [5] W. Matz, N. Schell, G. Bernhard, F. Prokert, T. Reich, J. Claußner, W. Oehme, R. Schlenk, S. Dienel, H. Funke, F. Eichhorn, M. Betzl, D. Pröhl, U. Strauch, G. Hüttig, H. Krug, W. Neumann, V. Brendler, P. Reichel, M.A. Denecke, and H. Nitsche, *J. Synchr. Rad.* **6** (1999) 1076
- [6] HUBER X-ray Diffraction Equipment, 83253 Rimsting, Germany
- [7] W. Matz, N. Schell, W. Neumann, J. Böttiger, and J. Chevallier, *Rev. Sci. Instrum.* (2001) in press
- [8] AJA International, P.O. Box 246, 809 Country Way, North Scituate, MA 02060, USA
- [9] S. Veprek, *Thin Solid Films* **130** (1985) 135
- [10] M. Kobayashi and Y. Doi, *Thin Solid Films* **111**, 259 (1984); J.E. Sundgren, *Thin solid Films* **128**, 21 (1985); J.I. Jeong, J.H. Hong, J.S. Kang, H.J. Shin, and Y.P. Lee, *J. Vac. Sci. Technol. A* **9**, 261 (1991); D.S. Rickerby, A.M. Jones, and B.A. Bellamy, *Surf. Coat. Technol.* **37** (1989) 4375
- [11] J. Pelleg, L.Z. Zevin, S. Lungo, and N. Croitoru, *Thin Solid Films* **197** (1991) 117
- [12] U.C. Oh and J.H. Je, *J. Appl. Phys.* **74** (1993) 1692
- [13] J.H. Je, D.Y. Noh, H.K. Kim, and K.S. Liang, *J. Appl. Phys.* **81** (1997) 6126
- [14] F. Adibi, I. Petrov, J.E. Greene, L. Hultman, and J.-E. Sundgren, *J. Appl. Phys.* **73** (1993) 8580
- [15] L.Dong and D.J. Srolovitz, *Appl. Phys. Lett.* **75** (1999) 584
- [16] N. Schell, W. Matz, J. Böttiger, J. Chevallier, and P. Kringhøj, *submitted to J. Appl. Phys.* (2001)

***In situ* study of phase transformation at elevated temperature and correlated mechanical degradation of nitrogen implanted Ti-6Al-4V alloys**

F. Berberich¹, W. Matz^{1,2}, E. Richter¹, N. Schell²

¹Institute of Ion Beam Physics and Materials Research, ² Project-Group ESRF-Beamline
Forschungszentrum Rossendorf, P.O. Box 51 01 19, 01314 Dresden, Germany

1. Introduction

Ti-6Al-4V (wt.%) is one of the mostly used titanium alloys. Compared to pure titanium it has a similar low density but favourable physical and mechanical properties. The higher tensile strength, hardness and proof stress, the lower elongation or the good corrosion resistance make it interesting for technical applications ranging from construction materials (aeronautics, submarines) [1] to medical implant materials [2, 3]. However, the untreated alloy surface often has nonsufficient tribological properties [4, 5]. A poor wear behaviour is not acceptable for a rotating part (e.g. in a turbine) or for a medical implant material (not only because of the potential toxicity).

It was shown that a nitrogen implantation treatment can improve the surface hardness and/or tribological properties [6, 7, 8]. This ion treatment works well for medical applications like knee and hip-joint prostheses. However, for the application in aerospace industry, which accounts for more than 80% of Ti-6Al-4V usage [9], a good performance at higher temperature is also desired. Therefore, it is important to understand the mechanisms of hardening and the stability of the improved surface quality at higher temperatures.

Samples treated with ion beam implantation (IBI) and plasma immersion ion implantation (PIII) were compared. IBI allows to deposit nitrogen in wide range of depth depending on the implantation energy. However, this method works only for plane surfaces and takes a long implantation time, whereas the PIII method seems more suitable for industrial applications because of lower costs, the shorter implantation times and its easier handling. For work pieces with irregular surface no sample manipulation is necessary [10].

To understand the structural changes in the nitrogen implanted layer near the surface of the Ti-6Al-4V alloy at higher temperatures, x-ray diffraction by grazing incidence technique (GIXRD) was performed at ROBL [11]. The use of a high-temperature chamber and synchrotron radiation allows *in situ* experiments in times comparable to technical annealing procedures.

2. Experimental

Samples from commercial polycrystalline Ti-6Al-4V alloys (wt.%) were cut from a rod to disc specimens of 25 mm diameter and 2 mm thickness. These specimens were grinded and finally polished with a colloidal silica polishing suspension.

A slight fibre texture of the material was determined from XRD pole figures. Therefore, the sample orientation was selected in a direction of practical no textural change. For all the X-ray experiments the same sample orientation was used in order to exclude texture influences.

The implantations were done at the Forschungszentrum Rossendorf. IBI was performed with a DANFYSIK 1090 Ion Implanter with fluences of 1, 3 and 6×10^{17} N⁺/cm² at an energy of 20, 80 and 180 keV. Such implantation leads to a Gaussian nitrogen profile at a depth of 150 nm for 80 keV or 300nm for 180 keV. The temperature at the sample surface measured by a thermocouple was below 200°C.

For the PII implantation the plasma was produced by an electron cyclotron resonance source (ECR) in a UHV chamber. The nitrogen gas (N_2^+) had a pressure of 0.2 Pa, the voltage was 40 kV, the power 350 W, the frequency 400 Hz and the pulse duration 5 μ s. Under these conditions the sample temperature was also maintained below 200°C in order to avoid direct nitrogen diffusion into the alloy. The implantation time respectively the number of pulses was adopted to have a fluence of 1.7×10^{17} N/cm².

After the implantation the microhardness depth profiles were recorded using an ultramicrohardness tester from Shimadzu. The hardness was recorded with a Vickers indenter at a maximum load of 5 mN, 10 mN and 50 mN, respectively, for the as received, implanted and annealed samples.

The *in situ* x-ray diffraction experiments were performed at ROBL at the wavelength of 0.154 nm. Grazing incidence technique was applied. By varying the angle of incidence from 0.5° to 4° depth dependent structural information from 0.1 to 1 μ m below the surface can be obtained assuming an average density of 4.43 g/cm³ for Ti-6Al-4V.

3. Implantation and its effect on hardness

Fig. 1 shows the relative hardness-depth functions for a maximum load of 5 mN, normalised to the unimplanted sample for the PIII and the IBI at different annealing temperatures. Two different types of behaviour are observed.

For PII, the as implanted sample and those with low annealing temperatures have typical profiles of a near surface hardening effect, where the relative hardness value tends to 1 with increasing penetration depth. The maximum of the hardness increase (factor 1.4) is

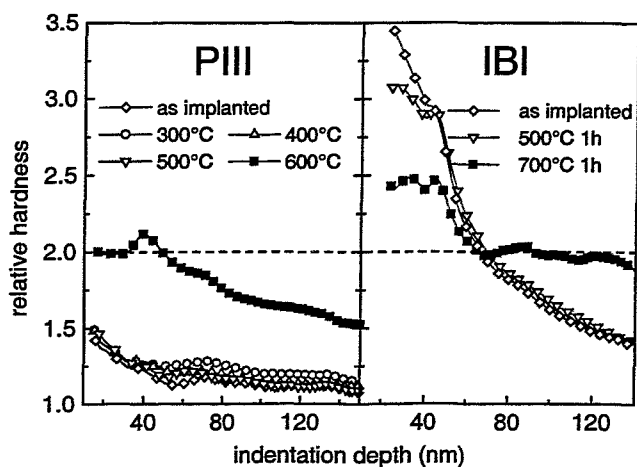


Fig. 1: Relative hardness as function of indentation depth for PII and IBI implanted Ti-6Al-4V at different annealing temperatures.

found immediately below the surface. In contrast, the hardness-depth function for the sample annealed at 600°C shows first an increase until a relative hardness of about 2.1. Then in the deeper regions the hardness rests on a high level of approximately 1.5 times the value of the virgin material.

In comparison IBI samples for an implantation energy of 80 keV and a fluence of 6×10^{17} N⁺/cm² show a completely different hardness behaviour with annealing temperature. Here, the N implantation increases the surface hardness up to 350% and the hardness depth function shows an exponential decay nearly to the original value (120%). After annealing at 500°C the surface hardness decreases only slightly to 86% and in the deeper regions no difference compared to the as-implanted sample is observed. However, after annealing at 700°C the surface hardness decreases to 70% of the as-implanted value, whereas it increases in deeper regions compared to all other treatments of the alloy. At depth of between 70 and 140 nm the relative hardness reaches about 200% of the virgin material.

4. Structural characterisation with synchrotron light

4.1 Phase transformation with increasing temperature

In order to characterise the structural changes in the N implanted samples at elevated temperature, which should be the reason of the changed hardness reported above, *in situ* XRD experiments were performed. PII and IB implanted Ti-6Al-4V samples were used. For both implantation methods the same structural characteristics are observed. The scanning time for each diffraction pattern was 30 min. So the duration of the *in situ* experiment corresponds to the typical annealing time used for such alloys. When comparing the diffraction pattern measured at incidence angles of 1° and 4°, respectively, the formation of the TiN phase is seen much more clearly at the measurement sensitive to the surface layer. Fig. 2 depicts the spectra at the angle of incidence of 1°.

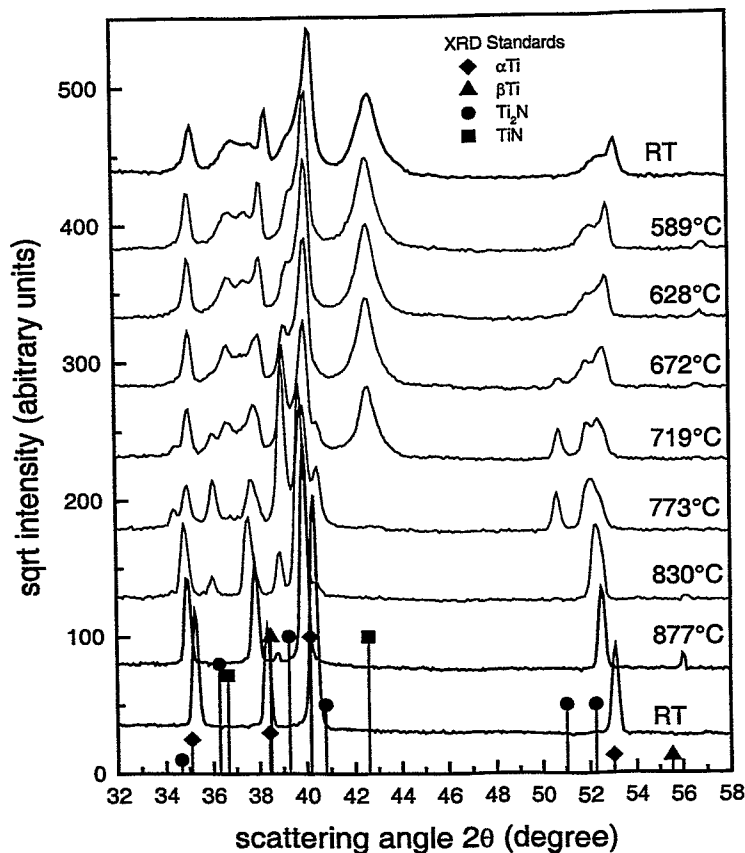


Fig. 2: Synchrotron radiation XRD pattern recorded at the angle of incidence of 1° and a wavelength of 0.154 nm during *in situ* annealing. The Ti-6Al-4V alloy was nitrogen implanted using IBI method at 80 keV with a fluence of $6 \times 10^{17} \text{ N}^+/\text{cm}^2$. The Bragg peak positions of the phases as taken from the data base are indicated.

The pattern of the as-implanted alloy (corresponding to the upper RT curve in Fig. 2) consists of the Bragg peaks from both Ti phases ($\alpha + \beta$) and cubic TiN formed by implantation. The hexagonal α -Ti phase is the dominating one in this alloy. The lattice constant of TiN was measured to be $a = 0.4207 \text{ nm}$ which is -0.8% different from the value for the stoichiometric phase [12]. It may be the indication for a nitrogen deficit or compressive stress in the grains, which can not be decided from the available data. The TiN peaks are very broad, indicating a small crystallite size of only about 6-8 nm as calculated with the Scherrer formula.

Up to 500°C the pattern remains unchanged and with further increasing temperature the intensity of the TiN peaks decreases. This can be most clearly observed for the (200)TiN reflection at a scattering angle of 42.6° in Fig 2. The onset of Ti_2N formation is observed at temperatures between 628° and 672°C. At the temperature of 773°C the Ti_2N peaks are

developed very clearly. These peaks have a similar width as the former TiN peaks, indicating Ti₂N crystallites with average sizes of about 10 nm.

From the development of the integrated intensities for TiN and Ti₂N as function of temperature it can be seen that this phase transformation is a continuous process. Additional *in situ* experiments have shown that at a fixed temperature of 680°C the same result is obtained, but the process takes more time, the lower the temperature is.

With further increasing temperature the Ti₂N phase dissolves also. At 773°C the corresponding Bragg reflection are very clearly developed but at the next temperature step no Ti₂N phase is seen in the diffraction pattern. At 877°C the cubic high temperature phase β-Ti is detected but is not quenched during the slow cooling process after the experiment.

Another structural effect is the change in the lattice parameters in both the α-Ti and β-Ti phases, which is not conform with thermal expansion [13]. Especially, the lattice expansion of the β-Ti phase of 2% over a temperature range of 200 K is remarkable. It is known, that V in Ti reduces the cubic lattice parameter significantly [14]. From the behaviour one may conclude that the annealing is connected with a reduction of the V-content in the β-Ti.

The PIII treated material shows essentially the same behaviour [15]. At 500°C the pattern consists of the Bragg peaks from both Ti phases (α + β) and TiN formed by implantation. The lattice constant of TiN was estimated to be $a = 0.4217$ nm which is -0.7% different from the value for the stoichiometric phase [12]. The TiN peaks are again very broad, and the calculated crystallite size is with 10 nm a little bit higher than for the IBI case. With increasing temperature the intensity of the TiN peaks decreases. At 750°C however, a new peak comes up at a slightly lower Bragg angle than the TiN peak observed so far. It remains in the pattern after the annealing process when cooling the sample to room temperature. In isothermal time dependent experiments it was found, that this peak does not arise from a peak shift, but is growing only after the original TiN peak disappeared. The two other peaks belonging to the pattern of a cubic phase are also observed but with low intensity. The room temperature lattice parameter of the new phase TiN* arising after annealing at 750°C is slightly different and amounts to $a = 0.428$ nm.

The onset of Ti₂N formation is observed at temperatures between 600 and 650°C. At the final temperature of 750°C, as well as at the room temperature measurement after the annealing process, the Ti₂N peaks are much sharper than the former TiN peaks, indicating well developed crystallites of Ti₂N with mean sizes of 35-40 nm.

4.2 Depth resolved measurements

With variation of α_i , the incidence angle, the average penetration depth of the x-ray and hence the near surface region where phases are detected can be changed. Fig. 3 depicts two depth profiles recorded from a PIII implanted Ti-6Al-4V sample. The profile of the as implanted sample shows all Bragg peaks in the range from 37 to 44 degrees.

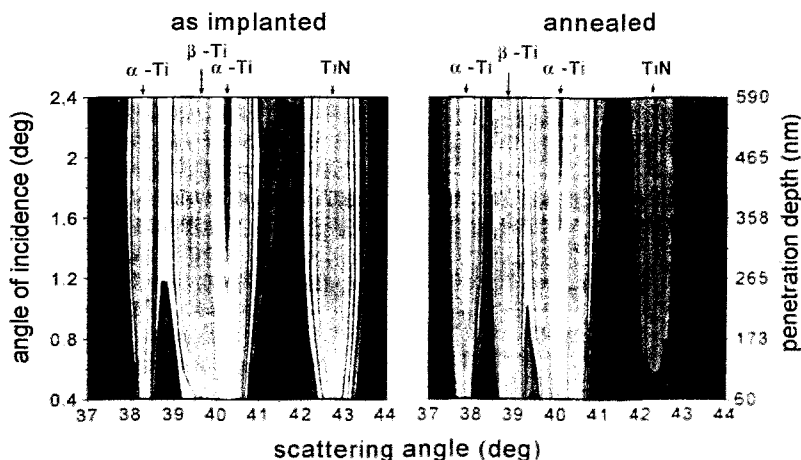


Fig. 3: Depth profile of a PIII treated (40 keV / 1.7×10^{17} N⁺/cm²) Ti-6Al-4V alloy in the as implanted state and after annealing at 680°C for 1h

The maximum of the TiN peak lies at an incidence angle of about 1.2 degree with corresponding average penetration depth of 270 nm. As this sample was PII implanted it is clear that the formation of TiN took place in the very surface region. At higher incidence angles only the reflections from the bulk increase in intensity. The high depth limit of the phase formation is difficult to determine because of accumulative nature of the scattering, so a scattering signal from the surface will be present at all higher α_i . Nevertheless some changes can be observed. The annealed sample shows a decreased intensity of the TiN peak and the maximum shifted towards higher depth. This is an obvious hint to a starting TiN dissolution and diffusion process. This result corresponds well with the changes in the hardness depth profiles after annealing. Another obvious change could be seen at the β -Ti Bragg reflection. In the annealed state it can be easily separated from the much more intense α -Ti reflection. This shows the expansion of the β -Ti phase mentioned above.

4.3 Activation energies

The annealing experiments with nitrogen implanted Ti-6Al-4V showed phase transformation from TiN to Ti_2N . In order to describe the temperature stability of TiN more quantitatively the activation energies for the dissolution of the TiN crystallites were determined. The kinetics of the dissolution process of the TiN phase was studied by recording the (200) Bragg peak during isothermal experiments at three different temperatures. The appropriate temperatures were estimated from the previously performed temperature scans. Some experiments were done at different incidence angles to compare the process in different depth but no significant changes were observed.

All measured peaks were fitted with Gaussian curves. Neglecting texture, the integrated intensity of the Bragg peak is proportional to the amount of crystallites of the phase of interest. With the data taken at three different temperatures it is possible to calculate the actual reaction velocities. From reaction velocities at different temperatures the activation energy is deduced by an Arrhenius plot.

Tab.1 gives an overview of the measured activation energies for the dissolution of TiN. For TiN an activation energy of (198 ± 14) kJ/mol is found for the temperature range $600^\circ\text{C} - 800^\circ\text{C}$. The literature value [16] is given with 210 kJ/mol for a temperature range of $1300^\circ\text{C} - 1670^\circ\text{C}$. For a comparison with the literature data one has to take into consideration that the activation energy is a temperature dependent value. So it seems that the values determined by XRD are realistic. The differences between the implantation modes obviously result from the different damage profile associated with implantation. The low energy implantations (IBI 20 keV; PIII 40 keV) produce TiN very near to the surface where also the main damage is located. Also implantation at 180 keV induces more damage and the TiN dissolution may be masked partially by damage recovery. The value for 80 keV IBI, which corresponds well with thermodynamic data, indicates that the Ti-6Al-4V matrix obviously has no significant influence on the stability of TiN.

Implantation method	Energy (keV)	Fluence ($10^{17} \text{ N}^+/\text{cm}^2$)	Activation energy (kJ/mol)	
			measured	Ref. [16]
IBI	80	6.0	198 ± 14	210 @ 1300°C
IBI	20	1.5	291 ± 55	
IBI	180	6.0	277 ± 17	
PII	40/20	1.7	328 ± 68	

Tab. 1:

Activation energies for TiN calculated from the dissolution of TiN in Ti-6Al-4V. Two different ion implantation methods, beamline (IBI) and plasma ion immersion (PIII), are represented. Values for the IBI at different implantation energies and fluences.

5. Summary

Ti-6Al-4V alloy was implanted with nitrogen in order to enhance surface hardness. Two different implantation techniques (beamline and plasma immersion) were applied. The effects and mechanisms seem to be independent on the implantation method. Only the absolute values of changes differ. The hardness increase is correlated with the formation of TiN crystallites (size 6 to 10 nm) just below the surface. The nitrogen concentration is not sufficient to form a layer. Annealing partially destroys the additional surface hardening achieved by ion implantation at 600 to 700°C.

The structural changes in N implanted Ti-6Al-4V alloys were investigated with *in situ* XRD experiments. It was shown, that the phase transformation TiN to Ti₂N is the main process. It is a continuous process and connected with nitrogen diffusion at higher temperatures. The formation of TiN is located around the projected implantation range while the formation of Ti₂N as the higher temperature phase occurs also in deeper region as consequence of nitrogen diffusion. The existence of Ti₂N in the alloy is responsible for the remaining hardness after annealing. From crystallite size, total nitrogen concentration and the similar effect of TiN and Ti₂N it was concluded that dispersion hardening is the relevant mechanism.

The determination of the activation energies of the dissolution of the formed TiN crystallites gives a hint at the stability of TiN in Ti-6Al-4V and allow to estimate a temperature limit where the phase remains stable. In addition to the structural investigation also elastic recoil detection analysis was applied which supports the onset of a diffusion process after a threshold temperature.

References

- [1] M. Peters, J. Kumpfert, C. Leyens in: Titan und Titanlegierungen, ed. M. Peters, J. Kumpfert, C. Leyens; DGM Informationsgesellschaft Verlag, Oberursel, 1996, p. 187-203
- [2] R. van Noort, J. Mater. Sci., **22** (1987) 3801-3811.
- [3] P. Sioshansi, Nuclear Instr. and Methods, **B 18-20** (1987) 204-208.
- [4] S.M. Johns, T. Bell, M. Samandi and G.A. Collins, Surf. Coatings Technol., **85** (1996), 7-14.
- [5] I.C. Clarke, H.A. McKellop, P. McGuire, R. Okuda and A. Sarmiento, in: Titanium in Surgical Implants, ASTM STP 766, 1983, pp. 136-147.
- [6] K.-T. Rie, T. Stucky, R.A. Silva, E. Leitão, K. Bordji, J.-Y. Jouzeau and D. Mainard, Surf. Coatings Technol., **74-75** (1995) 973-980.
- [7] T.M. Muraleedharan, E.I. Meletis, Thin Solid Films, **221** (1992) 104-113.
- [8] A. Loinanz, M. Rinner, F. Alonso, J.I. Oñate and W. Ensinger, Surf. Coatings Technol., **103-104** (1998), 262-267.
- [9] R. Boyer, G. Welsch and E. Collings, Materials Properties Handbook: Titanium Alloys, ASM Ohio 1994, 483 ff.
- [10] W. Matz, N. Schell, G. Bernhard, F. Prokert, T. Reich, J. Claußner et al., J. Synchrotron Rad., **6** (1999) 1076-1085.
- [11] W. Möller, E. Richter, Galvanotechnik, **89** (1998) 858.
- [12] Powder diffraction file PDF-2, No. 38-1420; ICDD, Newton Square, PA 19073-3273, USA
- [13] F. Berberich, W. Matz, E. Richter, N. Schell, U. Kreißig, W. Möller, Surf. Coatings Technol., **128-129** (2000), 418-422.
- [14] U. Zwicker, Titan und Titanlegierungen, Springer-Verlag, Berlin, 1974, p. 68.
- [15] F. Berberich, W. Matz, U. Kreißig, E. Richter, N. Schell, W. Möller, Appl. Surf. Sci. (2001) in press
- [16] F.W. Wood, O.G. Paasche, Thin Solid Films, **40** (1977) 133-137.

X-ray waveguides at ROBL: New developments and applications

F. Pfeiffer¹, T. Salditt¹, N. Schell²

¹Experimentalphysik, Universität des Saarlandes, Im Stadtwald 38, 66041 Saarbruecken

²Forschungszentrum Rossendorf, ROBL-CRG (ESRF), P.O.B. 510019, 01314 Dresden, Germany

A great number of optical devices and experimental techniques has taken a tremendous benefit in recent years from the development of optical fibers and related structures. In particular, the field of optical near-field microscopy combined with fiber optics and spot sizes of under 1000 nm has led to a variety of new and important results concerning the structure and physical properties of various materials in the nm-range. Unfortunately, the resolution is still limited for light in the visible range and an extension to smaller wavelengths is therefore an interesting and important venture. One could envision hard x-rays with wavelengths of ~ 0.1 nm and specially designed optical components. X-rays can be focussed either coherently by Fresnel zone plates and Bragg Fresnel lenses, or incoherently by bent crystal optics and coated fiber optics (generally speaking by highly reflective materials, e.g. supermirrors etc.). Typical beam spots in the micrometer range can be achieved for x-rays by these approaches. However, a beam with a still significantly smaller cross section could open up a whole new range of applications in scattering, microscopy and spectroscopy with real space resolution on the sub nm scale, e.g. elemental analysis of nanoparticles by x-ray fluorescence analysis or high resolution tomography, currently referred to as x-ray microscopy.

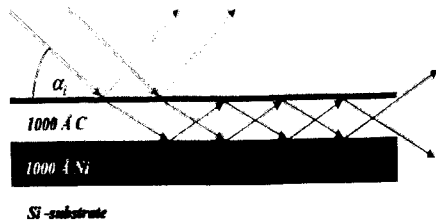


Fig. 1:

Sketch of a hard x-ray waveguide consisting of a low density guiding layer (e.g. Carbon) sandwiched in between layers of higher density (e.g. Ni).

As a new approach, multilayered systems can be used for one-dimensional beam concentration, where a precise control of layer thickness, index of refraction (density), and interface roughness by modern deposition techniques (spin-coating, MBE, rf sputtering) allows for the construction of efficient waveguide structures, which operate under grazing incidence and guide the beam by a resonant beam coupling mechanism within a layer of a few nm thickness until it exits at the side of the layered structure (see Fig 1).

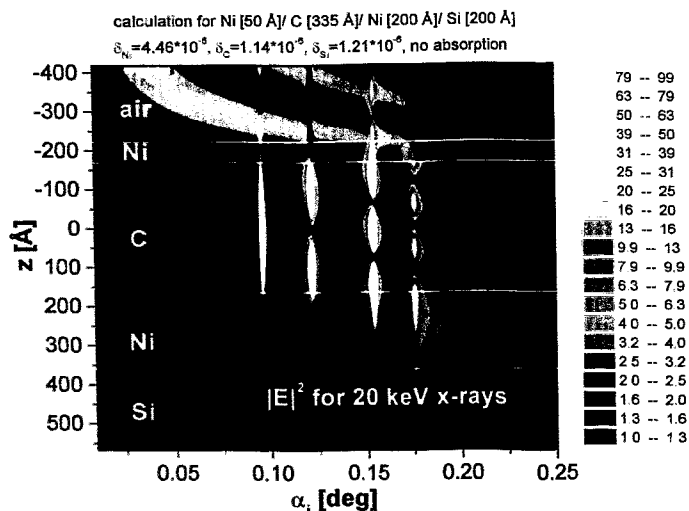


Fig. 2:

Logarithmic contourplot of the calculated transverse electric field intensity inside a x-ray waveguide structure, demonstrating the field-enhancement for excited modes.

The theoretical model was obtained by applying basic optical principles and results from waveguides for visible light to the general optical treatment of hard x-rays, where the index of refraction is less than 1 and typical wavelengths are 0.1 nm. Following this approach, we have discussed the guiding mechanism in planar waveguides and resonant beam couplers. By calculating the internal electric field (Fig. 2) and the corresponding farfield - distribution of exiting modes as a function of various parameters we showed that these structures can be considered as waveguides themselves with defined properties of the angular acceptance, coupling length and efficiency.

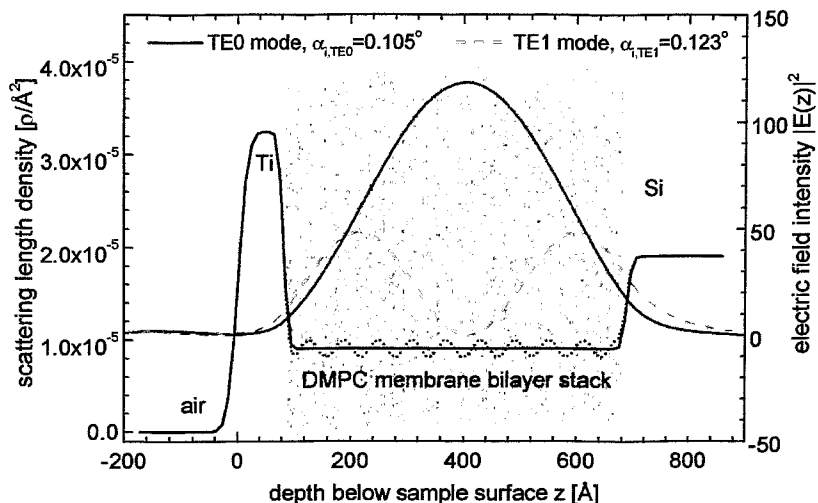
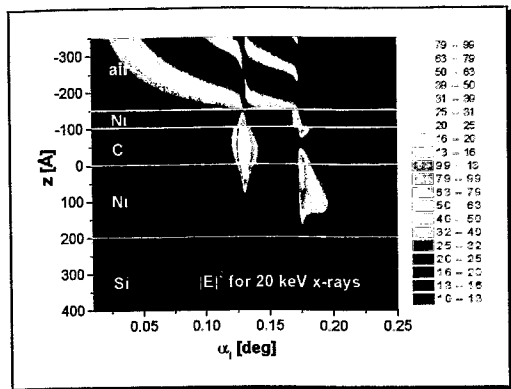
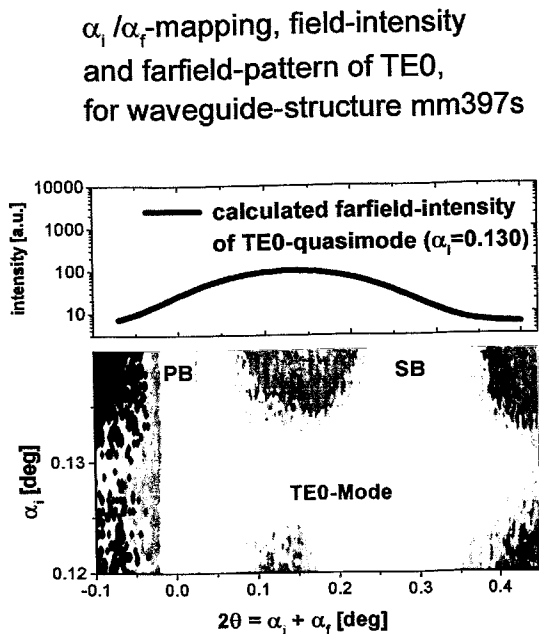


Fig. 3: Sketch of a x-ray resonant beam coupling device consisting of ten DMPC bilayers sandwiched in between a thin metal-layer and the Si-substrate. Overimposed, the normalized electric field intensity is plotted as a function of z , calculated for two different angles of incidence.

We have applied the principle of resonant beam coupling to structural studies of organic or biomolecular thin film samples. In this approach the samples are directly incorporated in the waveguide (Fig. 3). The resonantly enhanced diffraction signal can then be measured by tuning the incidence angle to a resonant mode of the waveguide. We have applied this scheme to a highly oriented stack of ten 1,2-dimyristoyl-sn-glycero-3-phosphatidylcholine (DMPC) bilayers, which was shown to be structural isomorphous to a control sample without metal cap layer. In the future, the novel kind of organic/ inorganic hybrid structure may offer several new experimental options. For example, the metal cap layer may serve as a solid state electrode, which would allow interesting experiments on biomolecular films in well controlled AC or DC electrical fields. To this end, details of the sample preparation will be published elsewhere.

The scattering signal measured by grazing incidence diffraction could significantly be enhanced by making use of the resonantly enhanced field-distributions corresponding to the TE_0 -/ TE_1 -modes. The measured diffraction peaks would otherwise be unobservable under the given experimental conditions. As a corollary, even smaller signals (of more disordered systems) become observable at highly brilliant third generation undulator beamlines using the technique presented here. Simulations indicate that signal-to-noise ratios can be improved by up to two orders of magnitude. In the future, high spacial resolution can be gained by the combined analysis of measurements carried out under the excitation of different modes, leading to a depth profile of the scattering signal, stemming e.g. from molecular ordering, lattice constants, or phase state.



$\lambda=0.62$ (20keV-xrays),
 $\delta_{Ni}=4.46 \cdot 10^{-6}$, $\delta_C=1.14 \cdot 10^{-6}$,
 $\delta_{Si}=1.21 \cdot 10^{-6}$, no absorption

Fig. 4:
 Calculation of the electric field intensity (right) and measurement of the farfield pattern (left) from a single mode x-ray waveguide with a 100 Å guiding layer.

Waveguide-enhanced scattering from various macromolecular and supramolecular structures, ranging from synthetic polymers to two-dimensional protein crystals, can thus be envisioned. In addition to sample structure, dynamics may be probed by photon correlation spectroscopy, with the RBC acting as a coherence filter for the incoming radiation. In an other experiment, the waveguiding effect could be observed in a single moded waveguide structure with a 100 nm thin guiding layer resulting in an exiting divergent beam with a FWHM beam size smaller than 10 nm (Fig. 4).

Furthermore we have successfully demonstrated the principle of multiple guiding layer x-ray waveguide structures (Fig. 5) and have shown that they can be understood by a straightforward generalization of the single waveguide case. The results can most simply be understood as a diffraction pattern of a grating structure for hard x-rays with a tailored periodicity in the range $100 \text{ \AA} < d < 2000 \text{ \AA}$, controlled by the design and growth of the

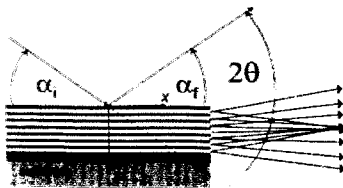


Fig. 5:
 Sketch of a waveguide containing multiple guiding layers.

structure (Fig. 6). Importantly the device differs from a hypothetical transmission grating in that the field intensity impinging on the grating is enhanced up to two orders of magnitude by the waveguide resonance. Furthermore, one should be able to tailor specific shapes of the exiting coherent x-ray beam after careful parameter studies in the simulation of the electric

field and the corresponding farfield, possibly leading to new focussing devices. Such optical components could be of particular interest for thermal and cold neutrons, where one could use structures with more than a hundred resonance layers without significant limits by absorption. Guiding layer structures for hard x-rays e.g. with two guiding layers could lead to novel applications in x-ray interferometry, as the far field distribution is crucially sensitive to phase changes in one of the interference beams. In this way information on the local, nanoscale electronic density can be projected onto macroscopic area detectors. Furthermore dynamic properties could also be probed in a two-beam or multi-beam interference setup, as the exiting beam is fully coherent and therefore amenable to photon correlation spectroscopy.

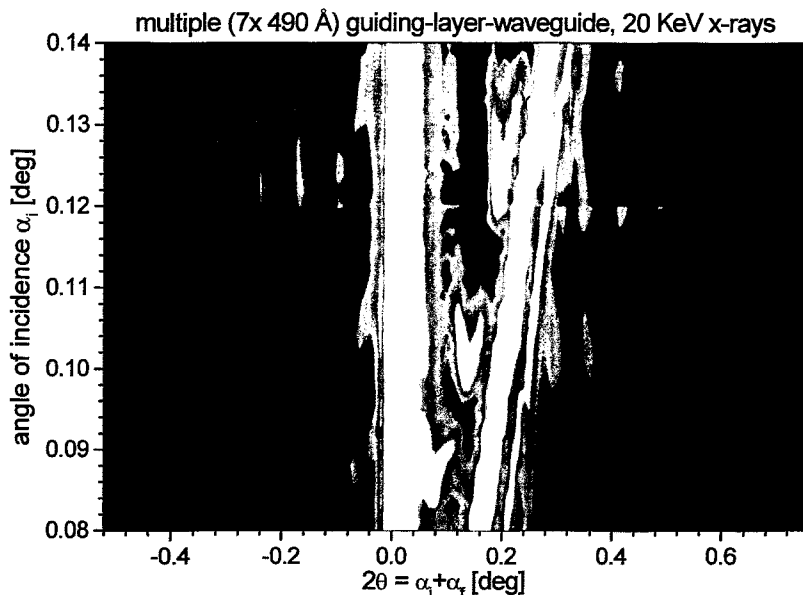


Fig. 6: Measured farfield interference pattern of a waveguide containing multiple guiding layers.

References:

- [1] A. Malik, A.R. Sandy, L.B. Lurio, et al., Phys.Rev.Lett. **81** (1998) 5832.
- [2] S. Mochrie, A. Mayes, A. Sandy, et al., Phys.Rev.Lett. **78** (1997) 1275.
- [3] M.J. Zwanenburg, F. Peters, J.H. Boengerts, et al., Phys.Rev.Lett. **82** (1999) 1696.
- [4] C.Raven, A. Snigirev, I. Snigireva, et al., Appl.Phys.Lett. **23** (1996) 1826.
- [5] S. Kuznetsov, I. Snigireva, A. Snigireva, et al., Appl.Phys.Lett. **65** (1994) 827.
- [6] Y.P. Feng, S.K. Sinha, et al., Phys. Rev. Lett. **71** (1993) 537.
- [7] S. Lagomarsino, A. Cedola, P. Cloetens, et al., Appl. Phys. Lett. **71** (1997) No. 18.
- [8] F. Pfeiffer, T.Salditt, P. Hoghoj, I. Anderson, *to be published*
- [9] F. Pfeiffer, Diploma thesis: *X-ray waveguides*, Ludwig-Maximilians-Universitaet Muenchen, Sektion Physik (1999)
- [10] S.I. Zheludeva et al., Crystallography reports, **40** (1995) 132.
- [11] Shenon M.R., Thyagarajan K., and Gatah A.K., J. Lightwave Tech., LT-6 (1988) 1285.
- [12] L.G. Parratt, Phys. Rev. **95** (1954) 359. (
- [13] P.K. Tien and R. Ulrich, J. Opt. Soc. Am. **60** (1970) 1325
- [14] Y.P. Feng, H.W. Deckmann and S.K. Sinha, Appl. Phys. Lett. **64** (1993). 1.

EXAFS measurements of radioactive samples at low temperature

C. Hennig¹, T. Reich¹, H. Funke¹, A. Roßberg¹, S. Dienel², W. Oehme², U. Strauch³, G. Bernhard¹

Forschungszentrum Rossendorf e.V., ¹Institute of Radiochemistry, ²Central Department of Experimental Facilities and Information Technology, ³Project-Group ESRF-Beamline

1. Introduction

Thermal oscillations of atoms lead to damping effects in the EXAFS amplitude. In the EXAFS equation, the amplitude reduction factor (Debye-Waller factor) is included in the form of $\exp(-2\sigma^2k^2)$. It summarises the contribution of thermal as well as structural disorder $\sigma^2 = \sigma_{\text{therm}}^2 + \sigma_{\text{stat}}^2$. Low temperature reduces this EXAFS amplitude damping which allows the extension of measurements to a higher k range. Consequently, the Fourier transform reveals more backscattering shells. In spite of the fact that the chemical bondings are preserved for most of the phase transitions at low temperature, EXAFS spectroscopy has proven to be a reliable tool for determining local bond lengths. This contribution demonstrates the gain in short-range structural information from EXAFS measurements at low temperature using the cryostat installed recently at ROBL.

2. Apparatus design

The safety regulations for the radiochemistry hutch at ROBL prohibit a water circulation with the surroundings outside of the experimental station. Therefore, an air-cooled helium compressor (CTI-Cryogenics) was combined with a specially designed closed-cycle helium cryostat (OXFORD Instruments) to an unconventional arrangement (Fig. 1). In order to allow sample change inside the glove box, the sample holder is horizontally arranged. Based on an intelligent temperature controller module (OXFORD Instruments), a temperature control software was written and extensively tested. The device is designed to perform XAFS measurements in transmission and in fluorescence. The cooldown time from ambient to base temperature of 15 K is 120 minutes. At this temperature, the cooling power is 1.5 W and the temperature stability is ± 0.1 K. Inner and outer windows are made from clear mylar foils. The maximal sample dimension is limited by the window diameter of 10 mm.

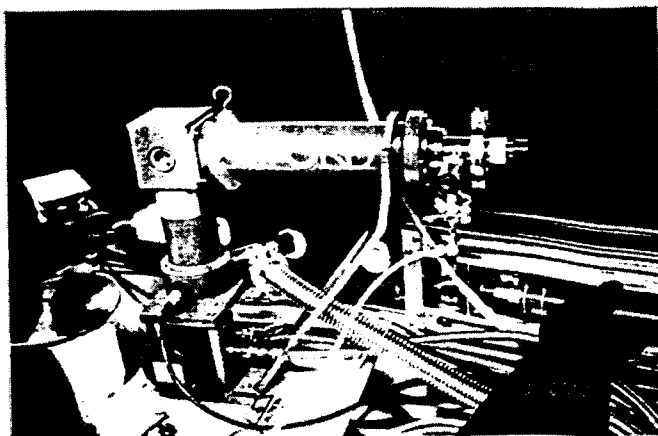


Fig. 1:
View into the ROBL glove box:
special designed helium cryostat
(OXFORD Instruments) with
horizontally arranged sample
holder.

3. Experimental results

3.1. Analysis of atomic distances in inaccurately determined heavy-atom crystal structures: $\text{Cu}[\text{UO}_2\text{AsO}_4]_2 \cdot 8\text{H}_2\text{O}$ and $\text{H}[\text{UO}_2\text{AsO}_4] \cdot 4\text{H}_2\text{O}$

X-ray diffraction analysis in the presence of heavy atoms can be complicated because the structure factor is mainly influenced by the heavy scatterers. The error in the determination of atomic coordinates increases for light atoms. Additional, if the heavy atoms are located at special positions, the space group can remain uncertain. EXAFS spectroscopy allows a direct determination of bond lengths in heavy-atom structures and avoids, therefore, problems caused by the coexistence of heavy and light scatterers.

EXAFS was used to determine bond lengths around heavy scatterers in meta-zeunerite, $\text{Cu}[\text{UO}_2\text{AsO}_4]_2 \cdot 8\text{H}_2\text{O}$, and trögerite, $\text{H}[\text{UO}_2\text{AsO}_4] \cdot 4\text{H}_2\text{O}$. These compounds belong to the structure family with the chemical formula $\text{A}^{n+}[\text{UO}_2\text{XO}_4]_n \cdot m\text{H}_2\text{O}$, where $[\text{XO}_4]^{3-}$ appears as phosphate or arsenate and A^{n+} is a hydrated monovalent or divalent cation. Tetrahedra of $[\text{XO}_4]^{3-}$ and tetragonal dipyramidal coordinated uranyl ions $[\text{UO}_2]^{2+}$ built up two-dimensional layers. Charge neutrality of the uranyl arsenate layers is given by different interlayer cations like $[\text{Cu}(\text{H}_2\text{O})_4]^{2+}$ in meta-zeunerite and $[\text{H}_3\text{O}]^+$ in trögerite. Uranium and the axial oxygen atoms are located at the fourfold symmetry axes. The positions of the surrounding O_{eq} and As atoms are symmetry-equivalent.

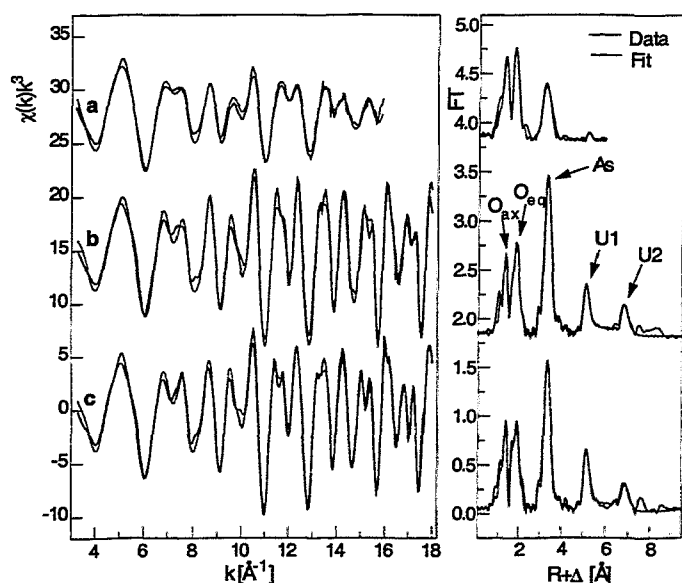


Fig. 2:
U L_{III} -edge k^3 -weighted transmission EXAFS spectra (left) and the corresponding Fourier transforms (right) for

(a) $\text{Cu}[\text{UO}_2\text{AsO}_4]_2 \cdot 8\text{H}_2\text{O}$
at $T = 298 \text{ K}$,

(b) $\text{Cu}[\text{UO}_2\text{AsO}_4]_2 \cdot 8\text{H}_2\text{O}$
at $T = 15 \text{ K}$,

(c) $\text{H}[\text{UO}_2\text{AsO}_4] \cdot 4\text{H}_2\text{O}$
at $T = 15 \text{ K}$.

Room temperature U L_{III} -edge EXAFS measurements of both $\text{Cu}[\text{UO}_2\text{AsO}_4]_2 \cdot 8\text{H}_2\text{O}$ (Fig. 2a) and $\text{H}[\text{UO}_2\text{AsO}_4] \cdot 4\text{H}_2\text{O}$ (not depicted) show a distance between uranium and the axial oxygen atoms, O_{ax} , of 1.77-1.78 Å. The second shell corresponds to the bond distance of four symmetry-equivalent equatorial atoms (O_{eq}) with a bond length of 2.29-2.30 Å. The arsenic scattering contribution gives a significant third Fourier transform peak with a calculated distance of 3.69-3.70 Å. At $T = 298 \text{ K}$ the U-U scattering contribution generates only a very weak peak. To analyse higher shells, low temperature measurements were performed. A measurement of $\text{Cu}[\text{UO}_2\text{AsO}_4]_2 \cdot 8\text{H}_2\text{O}$ at a temperature of 15 K shows that the scattering contributions of uranium appear at an U-U1 distance of 5.39 Å and an U-U2 distance of 7.15 Å. EXAFS measurements on $\text{H}[\text{UO}_2\text{AsO}_4] \cdot 4\text{H}_2\text{O}$ (Fig. 2c) show within the error limits comparable distances. The atomic distance U-U2 corresponds to the lattice constant a .

In Tab. 1 atomic distances determined by EXAFS measurements are compared to X-ray diffraction data from literature. The EXAFS data on the $\text{H}[\text{UO}_2\text{AsO}_4] \cdot 4\text{H}_2\text{O}$ sample show a good agreement with the diffraction data of the literature. The measurements on $\text{D}[\text{UO}_2\text{AsO}_4] \cdot 4\text{D}_2\text{O}$, were taken with neutron diffraction on a powder sample at room temperature [1] and at 4 K [2].

In $\text{Cu}[\text{UO}_2\text{AsO}_4]_2 \cdot 8\text{H}_2\text{O}$ the atomic distances between heavy and light scatterers observed by EXAFS deviate approximately 0.1-0.2 Å in comparison with single crystal X-ray diffraction measurements from the literature [3]. However, the atomic distances between the heavy scatterers agree well with the EXAFS data. As sometimes observed in heavy atom structures, the position of the heavy scatterers are correctly determined, but the positions of the light atoms are incorrect. However, EXAFS measurements are restricted to atomic distance determinations in form of radial distribution functions.

Shell	$\text{Cu}[\text{UO}_2\text{AsO}_4]_2 \cdot 8\text{H}_2\text{O}$		$\text{X}[\text{UO}_2\text{AsO}_4] \cdot 4\text{X}_2\text{O}$	
	EXAFS	XRD [3]	EXAFS	ND [1, 2]
U-O _{ax}	1.78	1.94, 1.78	1.78	1.78, 1.80
U-O _{eq}	2.30	2.17	2.30	2.30
U-As	3.69	3.68	3.70	3.70
U-U1	5.39*	5.38	5.40*	5.39
U-U2	7.15*	7.10	7.21*	7.16
As-O _{eq}	1.68	1.77	1.69**	1.68
As-As	5.02*	5.02	5.06**	5.06
As-U2	8.01*	8.00	8.04**	8.04

Tab. 1: Comparison of the atomic distances from EXAFS measurements with diffraction data from literature. Distances are given in Å.

XRD = X-ray diffraction, ND = Neutron diffraction

X=H for the EXAFS measurements, X=D in the literature [1, 2] *T = 15K, **T = 43K

This is connected with a loss of the bonding angle information. For this reason and taking into account that Hanic [3] could use only intensities from Weissenberg photographs for his structure analysis, the crystal structure of meta-zeunerite was completely redetermined using single crystal diffraction measurements [4]. These measurements confirmed the structural parameters given by the EXAFS measurements.

3.2. Investigation of compounds with symmetry-dependent structure modifications: $\text{Cu}[\text{UO}_2\text{AsO}_4]_2 \cdot 12\text{H}_2\text{O}$ and $\text{Cu}[\text{UO}_2\text{AsO}_4]_2 \cdot 8\text{H}_2\text{O}$

$\text{Cu}[\text{UO}_2\text{AsO}_4]_2 \cdot 12\text{H}_2\text{O}$ and $\text{Cu}[\text{UO}_2\text{AsO}_4]_2 \cdot 8\text{H}_2\text{O}$ show differences only in the crystal-water content, connected with a swap in the space group symmetry. Only one backscattering shell is visible in the Cu K-shell EXAFS Fourier transform measured at 289K (Fig. 3c). In comparison, strong differences are visible at the low temperature measurements.

The structure of $\text{Cu}[\text{UO}_2\text{AsO}_4]_2 \cdot 12\text{H}_2\text{O}$ contains two non symmetry-equivalent Cu positions. In the EXAFS analysis only one Cu atom position is considered, because the second one has only an occupation factor of 0.075. The structure of $\text{Cu}[\text{UO}_2\text{AsO}_4]_2 \cdot 8\text{H}_2\text{O}$ contains one symmetry-independent Cu atom position. In addition, this powder of this sample contained 14% $\text{Cu}[\text{UO}_2\text{AsO}_4]_2 \cdot 12\text{H}_2\text{O}$. However, the EXAFS is dominated by the scattering contribution of $\text{Cu}[\text{UO}_2\text{AsO}_4]_2 \cdot 8\text{H}_2\text{O}$. Due to the damping of thermal oscillations, a lot of backscattering shells occur in the Fourier transform (FT). For simplifying the data analysis, the FT between $R+\Delta=5.5-10$ Å was Fourier filtered, back transformed and subtracted from raw Cu K-shell EXAFS data of each spectrum. The $[\text{Cu}(\text{H}_2\text{O})_4]^{2+}$ group causes dominant FT peaks with Cu-O distances of 1.94 Å for both samples. The sample of $\text{Cu}[\text{UO}_2\text{AsO}_4]_2 \cdot 12\text{H}_2\text{O}$ shows one Cu-U peak at a distance of 4.22 Å. A strong Cu-U-O_{ax}-Cu multiple scattering contribution appears because the involved atoms are arranged linearly. This observation points to a highly symmetric arrangement of the $[\text{UO}_2\text{AsO}_4]_n$ layers concerning Cu. In contrast, the

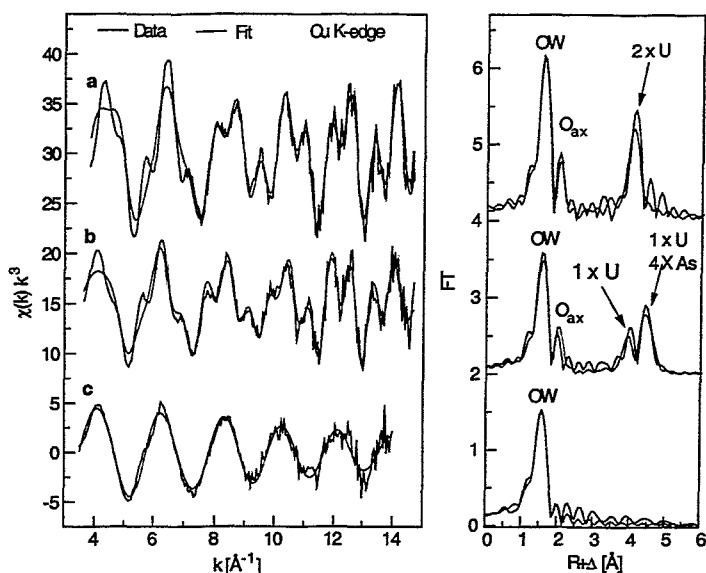


Fig. 3: Cu K-edge k^3 -weighted fluorescence EXAFS spectra (left) and corresponding Fourier transform (right) for

- (a) $\text{Cu}[\text{UO}_2\text{AsO}_4]_2 \cdot 12\text{H}_2\text{O}$ at $T = 15 \text{ K}$,
- (b) $\text{Cu}[\text{UO}_2\text{AsO}_4]_2 \cdot 8\text{H}_2\text{O}$ at $T = 15 \text{ K}$,
- (c) $\text{Cu}[\text{UO}_2\text{AsO}_4]_2 \cdot 8\text{H}_2\text{O}$ at $T = 298 \text{ K}$.

spectrum of $\text{Cu}[\text{UO}_2\text{AsO}_4]_2 \cdot 8\text{H}_2\text{O}$ shows two FT peaks in the region $R+\Delta = 3.5\text{-}5.0 \text{ \AA}$. The first peak originates from one uranium atom in a distance of 4.04 \AA . The second peak consists of arsenic atoms at a distance of 4.84 \AA and one uranium atom at a distance of 4.52 \AA . These observations indicate that in $\text{Cu}[\text{UO}_2\text{AsO}_4]_2 \cdot 8\text{H}_2\text{O}$ one $[\text{UO}_2\text{AsO}_4]_n$ layer is arranged closer to the Cu atom.

3.3. Analysis of a structure sequence: $\text{UO}_2[\text{H}_2\text{AsO}_4]_2 \cdot \text{H}_2\text{O}$

It is no problem to determine the atomic coordinates of uranium using X-ray powder diffraction because the scattering contribution of heavy atoms dominates. Indeed it is difficult to locate the light atoms. On the other hand, a method like EXAFS, sensitive to short range order, gives reliable atomic distances in the surroundings of heavy atoms and allows to characterise the coordination polyhedra. This method allows to elucidate the main structure sequence. Including the information from EXAFS as restraints in the structure solving procedure, the probability increases to obtain the complete structure. As an example, the EXAFS interpretation of a structure sequence is demonstrated using $\text{UO}_2[\text{H}_2\text{AsO}_4]_2 \cdot \text{H}_2\text{O}$.

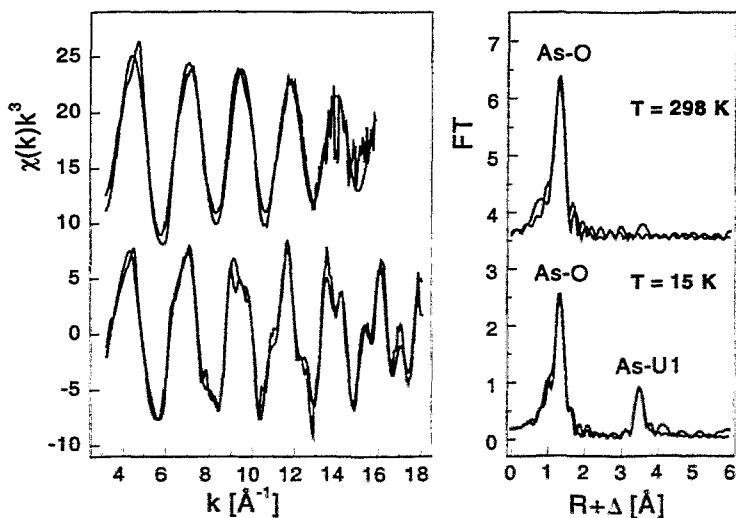


Fig. 4: As K-edge k^3 -weighted transmission EXAFS spectra of $\text{UO}_2[\text{H}_2\text{AsO}_4]_2 \cdot \text{H}_2\text{O}$ (left) and their Fourier transform (right).

Fig. 4 depicts the As K-edge k^3 -weighted EXAFS spectra of $\text{UO}_2[\text{H}_2\text{AsO}_4]_2 \cdot \text{H}_2\text{O}$. The measurement at room temperature (298 K) shows that As is surrounded by four oxygen atoms an average distance of 1.68 Å indicating a $[\text{AsO}_4]$ tetrahedron. In order to reduce the thermal atomic movement, the same sample was measured at 15 K. This measurement shows that each $[\text{AsO}_4]$ tetrahedron is surrounded by two uranium atoms at a distance of 3.71 Å. This bond length points to a monodentate connection between arsenate and uranyl polyhedra.

EXAFS measurements of $\text{UO}_2[\text{H}_2\text{AsO}_4]_2 \cdot \text{H}_2\text{O}$ at the U L_{III} -edge are shown in Fig. 5. There are two axial oxygen atoms at a distance of 1.77 Å and five equatorial oxygen atoms are detected at an average distance of 2.38 Å. That they are not symmetry-equivalent is indicated by the high Debye-Waller factor of 0.0069 Å². The U-As distance is determined to 3.70 Å. The uranium atom is coordinated by four As atoms via oxygen atoms. Therefore, the fifth equatorial oxygen atom belongs to the H_2O molecule given in the chemical formula.

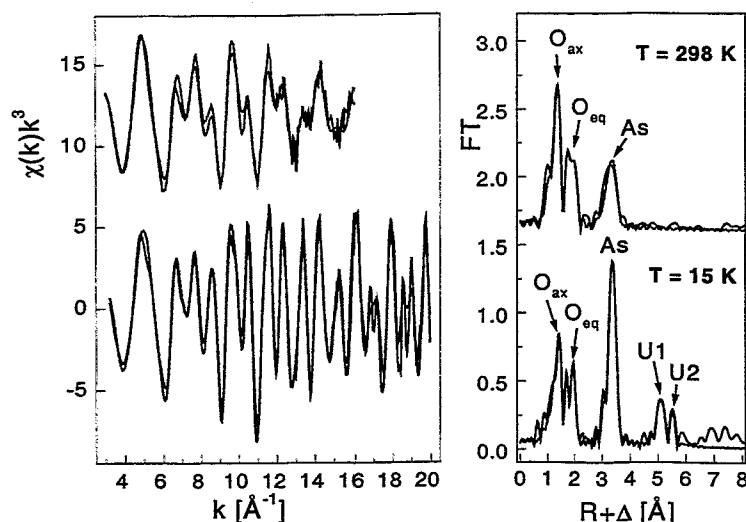


Fig. 5: U L_{III} -edge k^3 -weighted transmission EXAFS spectra of $\text{UO}_2[\text{H}_2\text{AsO}_4]_2 \cdot \text{H}_2\text{O}$ (left) and their Fourier transform (right).

In conclusion, our specially designed closed-cycle He cryostat allows to measure low-temperature (15 K) EXAFS spectra of radioactive samples both in transmission and fluorescence in excellent quality. The U L_{III} -edge and As and Cu K-edge EXAFS spectra of several uranyl arsenates showed that distant heavy backscattering atoms, i.e., U and As, that are "silent" at room temperature, become "visible" at low temperature. This greatly enhances the amount of structural information available from EXAFS measurements.

References

- [1] Fitch, A.N., Bernard, L., Howe, A.T. Wright, A.F., Fender, B.E.F.: The room-temperature structure of $\text{DUO}_2\text{AsO}_4 \cdot 4\text{D}_2\text{O}$, *Acta Cryst. C* **39** (1983) 159-162
- [2] Fitch, A.N., Bernard, L., Howe, A.T. Wright, A.F., Fender, B.E.F.: The structure of $\text{UO}_2\text{DAsO}_4 \cdot 4\text{D}_2\text{O}$ at 4 K by powder neutron diffraction, *Acta Cryst. B* **39** (1982) 2546-2554
- [3] Hanic, F.: The crystal structure of meta-zeunerite $\text{Cu}(\text{UO}_2)_2(\text{AsO}_4)_2 \cdot 8\text{H}_2\text{O}$, *Czech. J. Phys. B* **10** (1960) 169-181
- [4] Hennig, C., Reck, G., Reich, T., Rossberg, A., Kraus, W., Sieler, J.: in preparation

XANES and EXAFS measurements of plutonium hydrates

T. Reich, G. Geipel, H. Funke, C. Hennig, A. Roßberg, G. Bernhard

Institute of Radiochemistry, Forschungszentrum Rossendorf, P.O.B. 510119, 01314 Dresden, Germany

1. Introduction

This report describes the first X-ray Absorption Fine-Structure (XAFS) measurement of plutonium samples at ROBL. Two liquid samples containing Pu(III) and Pu(VI) hydrates were chosen for this experiment. The goal of this study was twofold. Firstly, we wanted to demonstrate that all requirements were met for the preparation and transportation of plutonium solutions from the home institution in Germany to the ESRF and for the XAFS measurements at ROBL. This should encourage others to do similar experiments on transuranium samples. Secondly, the hydrate is the simplest chemical form of plutonium in solution. The knowledge of the structural parameters of the hydration sphere is important for the interpretation of Extended X-ray Absorption Fine-Structure (EXAFS) results on complicated aqueous plutonium complexes or sorbates on mineral surfaces where the water molecules are partly or fully replaced by other ligands. In general, the number of water molecules in the hydration sphere depends on such factors as ionic radius and charge and ionic strength. The aquo ions of trivalent actinides have the general formula $An(H_2O)_n^{3+}$. In the literature the number of water molecules in the hydration sphere is discussed controversially and values range from eight to eleven [1]. It has been established that hexavalent actinides form trans-dioxo cations, $AnO_2(H_2O)_n^{2+}$, with five water molecules in the hydration sphere.

2. Experimental

High-purity PuO_2 (Pu-242) purchased from AEA Technology, QSA GmbH served as starting material for the sample preparation. It was dissolved by catalytic oxidation to Pu(VI) according to the following reaction: $2Ag^{2+} + PuO_2 = PuO_2^{2+} + 2Ag^+$. The silver ions were removed from the reaction solution by electrochemical reduction to Ag^0 . Part of the Pu(VI) solution was electrochemically reduced to Pu(III). The Pu(III) and Pu(VI) hydrates were in perchloric and nitric media (1 M acidic solution), respectively. The final Pu concentration was 50 mM. The Pu oxidation states were confirmed by UV/Vis measurements [2]. For the XAFS measurements, 4.7 mL solution was filled and sealed in polyethylene cuvettes of 10 mm path length. The samples were measured at ROBL within 48 hours after their preparation in Rossendorf.

Three scans of the Pu L_{III} -edge (18057 eV) and L_I -edge (23104 eV) XAFS spectra were collected in transmission mode at room temperature using the Si(111) double-crystal monochromator in fixed-exit mode [3]. For energy calibration purpose, the transmission spectra of metallic reference foils were measured simultaneously with the sample. The Pu L_{III} -edge XAFS spectrum was calibrated using the first inflection point of the K-edge absorption spectrum of a Zr foil (17997 eV). The K-edge absorption spectrum of a Pd foil (24354 eV) was measured to calibrate the Pu L_I -edge XAFS spectrum. The energy shifts relative to these references was less than 0.5 eV during the entire measurement.

The EXAFSPAK software package [4] was used for the EXAFS analysis. Theoretical scattering phases and amplitudes for the Pu L_{III} -edge EXAFS analysis were calculated for

hypothetical clusters of PuO_8 and PuO_2O_5 using FEFF6 [5]. For the cubic PuO_8 cluster, the assumed Pu-O bond distance was 2.39 Å. The Pu-O bond distances in the pentagonal bipyramid PuO_2O_5 were 1.76 and 2.41 Å, respectively. In addition to the Pu-O single-scattering paths, the multiple-scattering (MS) path $\text{Pu} \rightarrow \text{O}_1 \rightarrow \text{Pu} \rightarrow \text{O}_2 \rightarrow \text{Pu}$ within the linear O-Pu-O chain was calculated. This MS path was included in the EXAFS fit of the Pu(VI) hydrate in a similar way as described for uranyl compounds [6]. The amplitude reduction factor, S_0^2 , equalled 0.9. The shift in threshold energy, ΔE_0 , was varied as one global fit parameter for all scattering paths.

3. Results and Discussion

3.1 Pu XANES Spectra

The Pu L_{III} -edge X-ray Absorption Near-Edge Structure (XANES) of Pu(III) and Pu(VI) hydrates are shown in Fig. 1. Both spectra were normalised to equal intensity at 18200 eV.

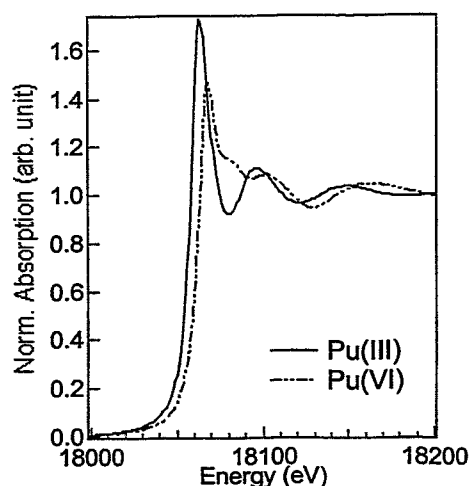


Fig. 1: Experimental L_{III} -edge XANES spectra of Pu hydrates.

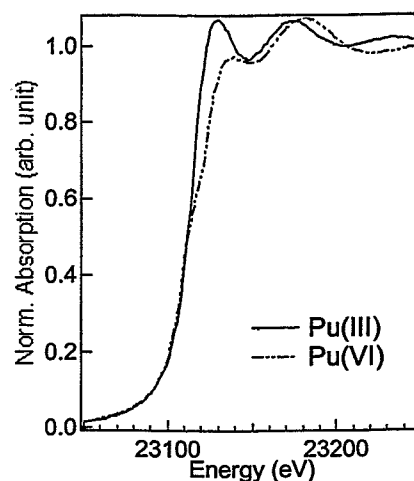


Fig. 2: Experimental L_I -edge XANES spectra of Pu hydrates.

The inflection point of the rising edge of the XANES spectra has been determined and is used throughout this paper as the energy position of the absorption edge. The L_{III} -edge energy of the Pu(III) and Pu(VI) hydrates is 18058.1 and 18062.3 eV, respectively (Tab. 1). The 4 eV shift of the L_{III} absorption edge of Pu(VI) toward higher energy as compared to Pu(III) can also be seen in Fig. 1. The distinct differences in the XANES features of Pu hydrates have been reproduced by *ab initio* calculations with the code FEFF7 [7]. However, there are quantitative discrepancies in the theoretical edge positions for the different Pu oxidation states. The experimental values of the Pu L_{III} -edge energies for tri-, tetra-, penta-, and hexavalent Pu aquo ions are 18060.1, 18063.2, 18062.6, and 18064.8 eV, respectively [8]. These values for trivalent and hexavalent Pu agree with our result after taking into account a 2 eV difference in the energy of Zr K-edge, which was used for energy calibration. When using the simple method of defining the edge energy as the first inflection point, it is difficult or impossible to derive the Pu oxidation state from it, in particular for mixtures of the oxidation states (IV)/(V), (IV)/(VI), and (V)/(VI).

The XANES at the Pu L_I -edge (Fig. 2) differs significantly from the L_{III} -edge spectra due to the dipole selection rule and the density of unoccupied states. The optical transition at the L_I and L_{III} edges, respectively, mainly map the unoccupied 7p and 6d states in the presence of

Table 1: Experimental Pu L_{III}- and L_I-edge energies of Pu(III) and Pu(VI) hydrates derived from the inflection point of the XANES spectrum.

Edge	Edge energy (eV)		ΔE (eV)
	Pu(III)	Pu(VI)	
Pu L _{III}	18058.1	18062.3	4.2
Pu L _I	23115.4	23109.0	-6.4
		23123.5	8.1

The energy axis was calibrated using the K-edges at 17997 and 24354 eV from Zr and Pd foils, respectively.

the core hole. For the Pu(III) hydrate, the L_I absorption edge has one inflection point at 23115.4 eV (Tab. 1). In contrast, two inflection points at 23109.0 and 23123.5 eV are observed for the L_I absorption edge of Pu(VI) hydrate. It should be noted that this splitting of 14 eV could not be reproduced by *ab initio* calculations using FEFF7. Only a single inflection point is seen in the XANES calculation of Pu hydrates [7]. It may be necessary in this case to use *ab initio* molecular orbital methods to obtain a better agreement between theoretical and experimental L_I-edge XANES features of Pu(VI) hydrate. It appears that the L_I-edge XANES is more sensitive to changes in the electronic and molecular structure of Pu species and, therefore, more suited for oxidation state determination using XANES than the L_{III} edge.

3.2 Pu EXAFS Spectra

The different molecular structures of Pu(III) and Pu(VI) hydrates are also reflected in the EXAFS spectra shown in Fig. 3. The Pu L_{III}-edge k³-weighted EXAFS spectrum of Pu(III) hydrate shows a single-frequency oscillation and the corresponding Fourier transform (FT)

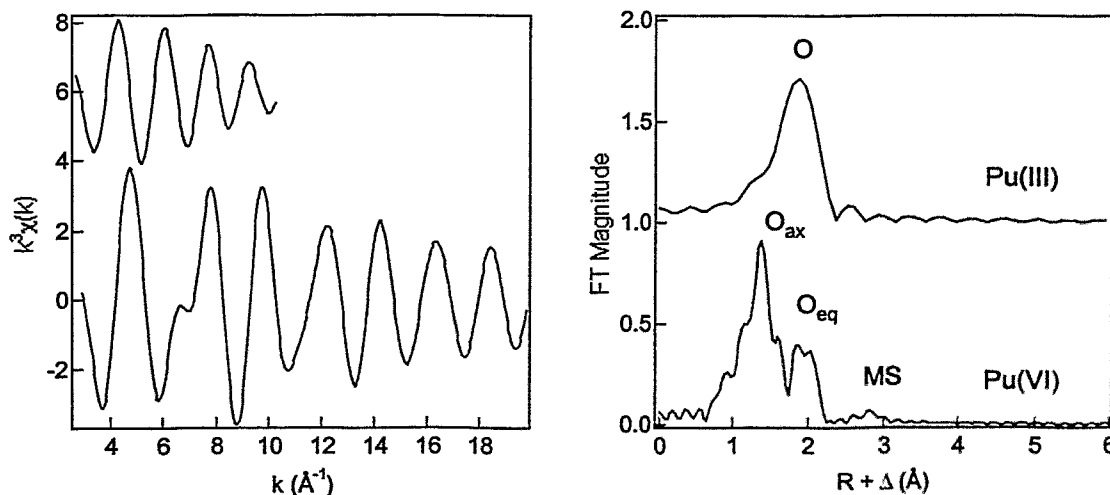


Fig. 3: Raw Pu L_{III}-edge k³-weighted EXAFS data (left) and corresponding Fourier transforms (right) for Pu hydrates: experimental data - dotted line; theoretical fit - solid line.

only one peak. Therefore, the experimental EXAFS spectrum was modelled with one Pu-O coordination shell. The obtained structural parameters are summarised in Tab. 2. The hydration sphere of Pu(III) consists of approximately eight water molecules with an average Pu-O distance of 2.48 Å. These results can be compared to those of an EXAFS study of a 20 mM Pu(III) solution in 10 mM LiCl [9] (see Tab. 2). The Pu L_{III}-edge k³-weighted EXAFS

spectrum was analysed using the same software, i.e., EXAFSPAK and FEFF6. According to this study, the Pu(III) aquo ion coordinates approximately ten water molecules at a Pu-O distances of 2.51 Å. In a later publication by the same group [10], their previous Pu L_{III}-edge EXAFS spectrum was fit with S_0^2 set equal to 1.0 instead of 0.9. As a result, the Pu-O coordination number decreased from 10.2. to 9.2 (Tab. 2). The Pu-O bond distance remained unchanged. It should be noted that partly due to the uncertainties of the correct choice of the parameter S_0^2 , the accuracy in the determination of coordination numbers from EXAFS is ± 1 [11]. Differences between these results and our result may indicate an influence of the media (10 mM LiCl vs. 1 M HClO₄) on the hydration sphere of Pu(III). This effect should be studied in more detail to verify its nature. EXAFS structural parameters of Pu(III) aquo ions are also given in refs. [12, 13]. The coordination numbers are between eight and ten. The Pu-O bond distances range from 2.49 to 2.51 Å (Tab. 2). Unfortunately, these authors gave non or very little experimental details on their EXAFS experiments.

The Pu L_{III}-edge k^3 -weighted EXAFS spectrum of Pu(VI) hydrate shows two oscillations (Fig. 3). Therefore, the corresponding FT shows two peaks due to the axial, O_{ax} , and equatorial, O_{eq} , oxygen atoms, respectively. The weak feature in the FT at $R+\Delta \approx 2.8$ Å is the MS contribution of the plutonyl moiety. The theoretical model to fit the experimental data

Table 2: EXAFS structural parameters for Pu(III) hydrates.

[Pu] mM	Medium	R(Å)	N	$\sigma^2(\text{Å}^2)$	Ref.
50	1 M HClO ₄	2.48	7.6(2) ^a	0.010	Present
20	0.01 M LiCl	2.51	10.2(2) ^a	0.010	[9]
20	0.01 M LiCl	2.51	9.2(3) ^a	0.010	[10]
-	-	2.49	8-9		[12]
-	1 M HCl, Zn amalgam	2.51(1) ^a	9.9(9) ^a	0.010(2) ^a	[13]

^a The 95% confidence limit is given in parentheses. The errors in R and σ^2 are estimated as ± 0.01 Å and ± 0.001 Å², respectively.

included two single-scattering paths O_{ax} and O_{eq} and the MS path. The Pu- O_{ax} distance in the plutonyl group is 1.74 Å (Tab. 3). In the equatorial plane, the Pu is coordinated by four to five water molecules with a Pu- O_{eq} distance of 2.42 Å. As to our knowledge, this result can be compared only with the result of ref. [12] (Tab. 3). Within the experimental uncertainties the results are in good agreement except for the O_{eq} coordination number (Tab. 3). Given the lack of experimental information, one cannot discuss the difference in the O_{eq} coordination number, i.e., 4.4 vs. 6.

Table 3: EXAFS structural parameters for Pu(VI) hydrates.

[Pu] mM	Medium	Shell	R(Å)	N	$\sigma^2(\text{Å}^2)$	Ref.
50	1 M HNO ₃	O_{ax}	1.74	1.9(1) ^a	0.001	Present
		O_{eq}	2.42	4.4(2) ^a	0.005	
-	-	O_{ax}	1.74	2		[12]
		O_{eq}	2.40	6		

^a The 95% confidence limit is given in parentheses. The errors in R and σ^2 are estimated as ± 0.01 Å and ± 0.001 Å², respectively.

Table 4 compares the EXAFS structural parameters of hexavalent U, Np [14], and Pu hydrates measured at ROBL. As one can see, the structural parameters both for the axial and the equatorial oxygen coordination shell are almost identical. However, two weak dependencies are seen. Firstly, the An- O_{ax} bond distance decreases from 1.76 to 1.74 Å by

going from U to Pu. This is in agreement with the well-known actinide contraction [15]. Secondly, the O_{eq} coordination number determined by EXAFS decreases systematically from 4.9 to 4.4 from U to Pu. The average An- O_{eq} bond length remains unchanged. Again, due to the relatively large error in the determination of coordination numbers, it is difficult to draw conclusions from this small decrease without further systematic EXAFS studies, in combination with other spectroscopic techniques, over a range of different sample conditions.

Table 4:

EXAFS structural parameters for An(VI) hydrates. The An concentration was 50 mM.

An	Medium	Shell	R(Å)	N ^a	$\sigma^2(\text{Å}^2)$	Ref.
U	1 M HClO ₄	O _{ax}	1.76	1.9(1)	0.001	Present
		O _{eq}	2.41	4.9(2)	0.006	
Np	0.1 M HNO ₃	O _{ax}	1.75	2.0(1)	0.002	[14]
		O _{eq}	2.41	4.6(2)	0.006	
Pu	1 M HNO ₃	O _{ax}	1.74	1.9(1)	0.001	Present
		O _{eq}	2.42	4.4(2)	0.005	

^a The 95% confidence limit is given in parentheses. The errors in R and σ^2 are estimated as ± 0.01 Å and ± 0.001 Å², respectively.

4. Conclusion

In summary, the first XAFS measurements of aqueous solutions of Pu-242 were an important milestone for the Rossendorf Beamline ROBL. The Pu L_{III}- and L_I-edge XANES spectra of Pu(III) and Pu(VI) are sensitive to changes in the electronic and molecular structures of the Pu species and can be used for the identification of these Pu oxidation states. In case of environmental samples, which may contain several Pu oxidation states simultaneously, it is recommended to utilise the Pu L_I-edge XANES for the determination of Pu oxidation states.

The Pu(III) aquo ion can be written as Pu(H₂O)₈³⁺ with an average Pu-O bond distance of 2.48 Å. The Pu(VI) forms a plutonyl ion PuO₂(H₂O)₄₋₅²⁺. The axial and equatorial Pu-O bond distances are 1.74 and 2.42 Å. Future studies on these species should determine the influence of Pu concentration and the conditions of the media (ionic strength, electrolyte) on the hydration sphere. These studies will also include the *in situ* preparation of Pu oxidation states, which are not stable during transportation from the home institute to ROBL. Recently, all oxidation states from Np(III) to Np(VII) have been prepared in a spectroelectrochemical cell [16], which was positioned in the synchrotron beam at the Advanced Photon Source to simultaneously record the Np L_{III}-edge XANES [17] and EXAFS spectra [18]. The knowledge of the EXAFS structural parameters of the Pu hydrates are important for the interpretation of EXAFS results on complicated systems. In so far, such measurements contribute toward a better understanding of the behaviour of actinide elements in the environment.

Acknowledgement

We thank G. Grambole for her help during the sample preparation.

References

- [1] Madic, C., Den Auwer, C. and Guillaumont, R., Application of X-ray absorption spectroscopy (XAS) to actinide solution chemistry, Euroconference and NEA Workshop on Speciation,

- Techniques, and Facilities for Radioactive Materials at Synchrotron Light Sources (NEA/OECD (Paris), Grenoble, France, 1999), pp. 69-79.
- [2] Weigel, F., Kratz, J.J. and Seaborg, G.T., in: *The chemistry of the actinide elements*, Eds. J. J. Kratz, G.T. Seaborg, L.R. Morss (Chapman & Hall, London New York, 1986), vol. 1, pp. 582-587.
- [3] Matz, W., Schell, N., Bernhard, G., Prokert, F., Reich, T., Claußner, J., Oehme, W., Schlenk, R., Dienel, S., Funke, H., Eichhorn, F., Betzl, M., Pröhl, D., Strauch, U., Hüttig, G., Krug, H., Neumann, W., Brendler, V., Reichel, P., Denecke, M.A. and Nitsche, H., ROBL - a CRG beamline for radiochemistry and materials research at the ESRF, *J. Synchrotron Rad.* **6** (1999) 1076-1085.
- [4] George, G.N. and Pickering, I.J., Stanford Synchrotron Radiation Laboratory, EXAFSPAK: A Suite of Computer Programs for Analysis of X-Ray Absorption Spectra (1995).
- [5] Zabinsky, S.I., Rehr, J.J., Ankudinov, A., Albers, R.C. and Eller, M.J., Multiple-scattering calculations of x-ray-absorption spectra, *Phys. Rev. B* **52** (1995) 2995-3009.
- [6] Hudson, E.A., Allen, P.G., Terminello, L.J., Denecke, M.A. and Reich, T., Polarized x-ray-absorption spectroscopy of the uranyl ion: Comparison of experiment and theory, *Phys. Rev. B* **54** (1996) 156-165.
- [7] Ankudinov, A.L., Conradson, S.D., Mustre de Leon, J. and Rehr, J.J., Relativistic XANES calculations of Pu hydrates, *Phys. Rev. B* **57** (1998) 7518-7525.
- [8] Conradson, S.D., Al Mahamid, I., Clark, D.L., Hess, N.J., Hudson, E.A., Neu, M.P., Palmer, P.D., Runde, W.H. and Tait, C.D., Oxidation state determination of plutonium aquo ions using x-ray absorption spectroscopy, *Polyhedron* **17** (1998) 599-602.
- [9] Allen, P.G., Bucher, J.J., Shuh, D.K., Edelstein, N.M. and Reich, T., Investigation of aquo and chloro complexes of UO_2^{2+} , NpO_2^+ , Np^{4+} , and Pu^{3+} by X-ray absorption fine structure spectroscopy, *Inorg. Chem.* **36** (1997) 4676-4683.
- [10] Allen, P.G., Bucher, J.J., Shuh, D.K., Edelstein, N.M. and Craig, I., Coordination chemistry of trivalent lanthanide and actinide ions in dilute and concentrated chloride solutions, *Inorg. Chem.* **39** (2000) 595-601.
- [11] Rehr, J.J. and Ankudinov, A.L., New developments in the theory of X-ray absorption and core photoemission, *J. Electron Spectrosc. Related Phenom.* **114-116** (2001) 1115-1121.
- [12] Conradson, S.D., Application of X-ray absorption fine structure spectroscopy to materials and environmental science, *Appl. Spectrosc.* **52** (1998) 252A-279A.
- [13] David, F., Fourest, B., Hubert, S., Le Du, J.F., Revel, R., Den Auwer, C., Madic, C., Morss, L.R., Ionova, G., Mikhalko, V., Vokhmin, V., Nikonov, M., Berthlet, J.C. and Ephritikhine, M., Aquo ions of some trivalent actinides: EXAFS data and thermodynamic consequences, Euroconference and NEA Workshop on Speciation, Techniques, and Facilities for Radioactive Materials at Synchrotron Light Sources (NEA/OECD (Paris), Grenoble, France, 1999), pp. 95-100.
- [14] Reich, T., Bernhard, G., Geipel, G., Funke, H., Hennig, C., Rossberg, A., Matz, W., Schell, N. and Nitsche, H., The Rossendorf Beam Line ROBL - a dedicated experimental station for XAFS measurements of actinides and other radionuclides, *Radiochim. Acta* **88** (2000) 633-637.
- [15] Kratz, J.J., Morss, L.R. and Seaborg, G.T., in: *The chemistry of the actinide elements*, Eds. J. J. Kratz, G. T. Seaborg, L. R. Morss (Chapman and Hall, London New York, 1986), vol. 2, pp. 1164-1165.
- [16] Antonio, M.R., Soderholm, L. and Song, I., Design of spectroelectrochemical cell for in situ X-ray absorption fine structure measurements of bulk solution species, *J. Appl. Electrochem.* **27** (1997) 784-792.
- [17] Soderholm, L., Antonio, M.R., Williams, C. and Wasserman, S.R., XANES spectroelectrochemistry: A new method for determining formal potentials, *Anal. Chem.* **71** (1999) 4622-4628.
- [18] Antonio, R., Soderholm, L., Williams, C.W., Blaudeau, J.P. and Bursten, B.E., Neptunium redox speciation, *Radiochim. Acta* **89** (2001) 17-26.

Local structure of Th complexes on montmorillonite clay mineral determined by extended X-ray absorption fine structure (EXAFS) spectroscopy*

R. Dähn¹, A. M. Scheidegger¹, A. Manceau², B. Baeyens¹ and M. H. Bradbury¹

¹Waste Management Laboratory, Paul Scherrer Institute, CH-5232 Villigen, Switzerland

²Environmental Geochemistry Group, LGIT - IRIGM, University of Grenoble, BP53, F - 38041 Grenoble Cedex 9, France

Abstract

The research at the Waste Management Laboratory, PSI, concentrates on the understanding of safety relevant mechanisms and processes that govern the release of radionuclides from waste matrices, and their transport through engineered barrier systems and the surrounding geosphere. For this reason, detailed sorption studies of radionuclides in clay and cement systems are conducted. The studies are combined with extended X-ray absorption fine structure (EXAFS) spectroscopy measurements in order to understand the sorption mechanisms on an atomic level.

In this manuscript, a case study of Th(IV) uptake on montmorillonite is presented. EXAFS samples were prepared by incubating a montmorillonite suspension with Th for 7 days at pH = 5 ($Th_{initial}$: 4.3×10^{-5} - 4×10^{-4} M). The resulting Th loadings on the clay varied between 14 and 166 $\mu\text{mol/g}$. L_{III}-Th EXAFS spectra of Th treated montmorillonite were measured at the Rossendorf Beamline at the European Synchrotron Radiation Facility. Data analysis revealed the presence of two O shells at 2.27 Å and 2.45 Å in all samples. The spectra at low Th uptake suggest the presence of Si/Al and Th backscattering atoms at distances of 3.85 Å and 3.77 Å respectively. The presence of a Th-Si/Al backscattering pair suggests that Th is bound to Si tetrahedra by a double corner-sharing manner. At higher Th uptake, however, the spectrum shows a strong similarity with the spectrum of amorphous Th(OH)₄ and suggests that Th is predominately present as a newly formed Th(OH)₄-like phase.

1. Introduction

Sorption on mineral surfaces strongly affects the fate and mobility of contaminants in the geosphere. Therefore, an atomic level understanding of sorption mechanisms of contaminants on mineral surface is of fundamental importance for maintaining environmental quality and assessing the long-term stability of waste repositories. On clay minerals several uptake mechanisms of divalent metal ions such as Ni(II), Co(II), and Zn(II) have been proposed: Sorption on edge sites, sorption on interlayer sites (Figure 1), and the formation of lamellar nucleation phases such as neoformed layer silicates and mixed layered double hydroxides (Scheidegger *et al.* 1997; Schlegel *et al.* 1999a; Schlegel *et al.* 1999b; Scheinost *et al.* 2000).

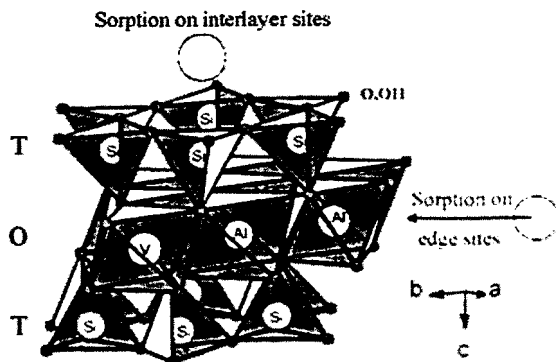


Fig. 1:

Sorption modes on dioctahedral aluminous clays (V=vacancy) (Structure from Tsipursky *et al.* 1984).

In this study EXAFS was used to investigate the uptake process of Th(IV) on montmorillonite. Th has long been recognized as an important tracer element in natural waters, soils and sediments because of its accurately known source terms, long half-life and single redox state (Santschi *et al.* 1989). Thorium is, therefore, a suitable analogue for other tetravalent actinides. Furthermore, Th is of major concern in nuclear waste management and an important contaminant in fly ashes from lignite power plants (Savanonda *et al.* 1985). Th has been added to synthetic silicate glasses in order to study the structural environment of Th as a function of melt composition and polymerisation (Farges 1991). Long-term spontaneous radiation will make crystalline compounds (e.g. ZrSiO_4) to become aperiodic and also oxide glasses to nucleate (Lumpkin *et al.* 1986; Ewing *et al.* 1987). Dioctahedral aluminous clays are used as a backfill material in the Swiss concept for a high level radioactive waste repository and, therefore, metal sorption on montmorillonite has been investigated in our laboratory in great details (Baeyens *et al.* 1997).

2. Materials and methods

The montmorillonite STx-1 used in this study ($\text{Si}_4\text{Al}_{1.67}(\text{Fe}^{2+}, \text{Mg})_{0.33}\text{O}_{10}(\text{OH})_2(\text{Me}_{0.33}, \text{H}_2\text{O})$, where Me refers to a metal cation in the interlayer space between sheets) was purchased from the Source Clay Minerals Repository Project of the Clay Minerals Society.

The EXAFS samples were prepared by adding 11-100 ml of a Th stock solution ($1 \cdot 10^{-3}$ M ($\text{Th}(\text{NO}_3)_4 \cdot 5\text{H}_2\text{O}$), pH 3.0, 0.001 M HNO_3) to 50 ml of a conditioned and purified montmorillonite suspension (ionic strength of 0.1 M (NaClO_4) to block cation exchange processes). The suspension was then filled up with a 0.1 M NaClO_4 solution to 250 ml resulting in a solid to liquid ratio of 2.4 g/L and an initial Th concentration of $4.3 \cdot 10^{-5} - 4.0 \cdot 10^{-4}$ M. The pH was adjusted and kept constant (pH = 5) and the samples were shaken end-over-end. The preparations were performed in a glove box under N_2 atmosphere (CO_2 and $\text{O}_2 < 5$ ppm). The reaction conditions were within the solubility limit of $\text{Th}(\text{OH})_4$ (Ryan *et al.* 1987; Östhols *et al.* 1994; Neck *et al.* 2000). After 7 days of reaction time the suspensions were centrifuged and the wet pastes were filled into Plexiglas holders. The supernatant solutions were analysed by ICP-MS in order to determine the Th uptake on the Th/montmorillonite sorption system. Th L_{III} -edge EXAFS spectra were recorded at the Rossendorf Beamline (ROBL) at the ESRF (Matz *et al.* 1999) using a Si (111) crystal monochromator and Pt coated mirrors. All sorption samples were measured at RT in fluorescence mode using a 4-element Ge solid-state detector.

Data reduction was carried out by using the WinXAS 97 1.3 software package (Ressler 1998). Radial structure functions (RSFs) were obtained by Fourier transforming k^3 -weighted $\chi(k)$ functions between 2.9 to 10 \AA^{-1} using a Bessel window function with a smoothing parameter of 4. Amplitude and phase shift functions were calculated with FEFF 8.0 (Rehr *et al.* 1991) using the structure of thorite ($\alpha\text{-ThSiO}_4$) (Taylor *et al.* 1978) as reference. Since the inner potential corrections (ΔE_0) in the Th sorption samples varied between 5.5-6.5 eV, the parameter was fixed to 6 eV in order to reduce the number of free fit parameters. Furthermore, the amplitude reduction factor (S_0^2) was set to 1.0.

The theoretical Th-O, Th-Si and Th-Th phase and amplitude functions calculated with FEFF 8.0 were tested by fitting the EXAFS spectrum of a synthetic thorite compound provided by Farges (1991). The results gave an average coordination number and bond distance of 8.5 ± 1.7 O atoms at 2.39 \AA ($\sigma^2 = 0.005 \text{ \AA}^2$), of 5.3 ± 1.1 Th atoms at 3.9 \AA ($\sigma^2 = 0.005 \text{ \AA}^2$) and of 3.9 ± 0.8 Si atoms at 3.92 \AA ($\sigma^2 = 0.005 \text{ \AA}^2$). The structural parameters for thorite as determined by X-ray diffraction (XRD) are four equatorial O at 2.36 \AA , four axial O at 2.47 \AA , four Si at 3.9 \AA and four Th at 3.9 \AA (Taylor *et al.* 1978). The differences between EXAFS and XRD structural data are within the uncertainty of EXAFS parameters, that is $\sim 20\%$ for coordination numbers and $\sim 0.02 \text{ \AA}$ for interatomic distances.

3. Results

Fig. 2 shows the background subtracted, normalized, and k^3 -weighted EXAFS spectra of montmorillonite treated with Th (sorbed Th concentrations of 14, 40 and 166 $\mu\text{mol/g}$). The corresponding RSFs are shown in Fig. 3. For the lowest Th concentration the first peak is split into two and the amplitude is reduced, and the second peak is shifted to higher distance with higher Th concentration.

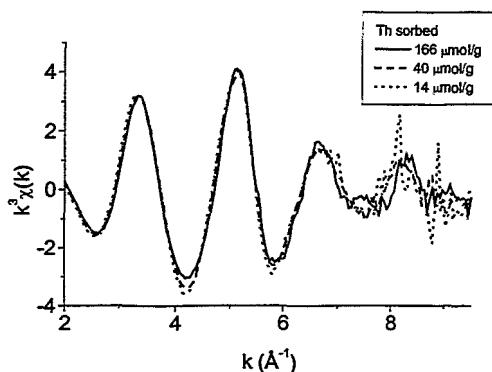


Fig. 2: k^3 -weighted Th L_{III} -edge EXAFS spectra for Th sorbed on montmorillonite (pH=5).

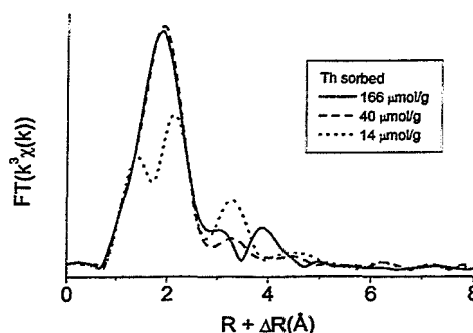


Fig. 3: RSFs of k^3 -weighted Th L_{III} -edge EXAFS spectra for Th sorbed on montmorillonite (pH=5).

The simulation of the Fourier filtered χ_0 functions obtained by back transforming first RSF peaks ($\Delta R = 1\text{-}2.5 \text{ \AA}$) indicated that two nearest O distances are present in all Th sorption samples. To constrain fit parameters, the Debye-Waller (DW) factor of the second oxygen shell was fixed to $\sigma^2 = 0.005 \text{ \AA}^2$, as in the thorite reference. Furthermore, the DW of the first oxygen shell was set to $\sigma^2 = 0.002 \text{ \AA}^2$ in order to obtain a total coordination number of 10 for the two O shells. For crystallographic and steric reasons the total number of oxygen atoms in the first and second shell should not exceed 10. EXAFS structural parameters for the two nearest O shells are listed in

Table 1. The shorter shell consists of 2.6-3.0 O atoms at 2.27 – 2.28 \AA and the longer of 6.6-7.1 O atoms at 2.45 – 2.46 \AA .

Table 1: Structural Information derived from EXAFS Analysis.

Sample	Th-O			Th-O			ΔE_0^f [eV]	%Res
	N	R [\AA]	σ^{2f} [\AA^2]	N	R [\AA]	σ^{2f} [\AA^2]		
166 $\mu\text{mol/g}$	2.6	2.27	0.002	6.6	2.45	0.005	6	15.7
40 $\mu\text{mol/g}$	2.6	2.27	0.002	6.9	2.45	0.005	6	16.5
14 $\mu\text{mol/g}$	3.0	2.28	0.002	7.1	2.46	0.005	6	6.6

N, R, σ^2 , ΔE_0 are the coordination numbers, interatomic distances, Debye-Waller factors and inner potential corrections; f: Fixed during the fit procedure

The deviation between the fitted and the experimental spectra is given by the relative residual in percent, %Res.

The k^3 -weighted Fourier back-transformed spectra of second RSF peaks ($\Delta R = 2.9\text{-}4.2 \text{ \AA}$ for the highest concentrated sample and $\Delta R = 2.9\text{-}3.7 \text{ \AA}$ for the two other) are shown in Figure 4. The structural results obtained by data analysis using Th and Si as backscatter atoms are shown in Table 2.

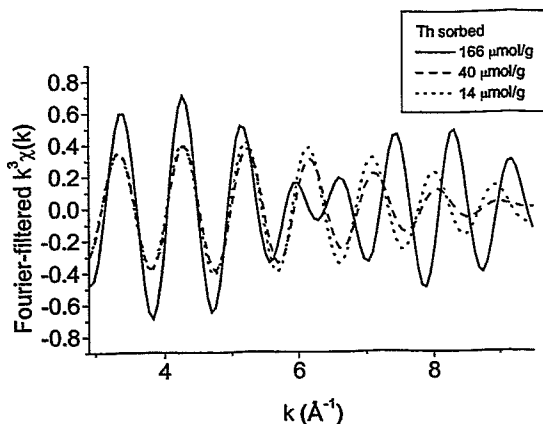


Fig. 4: k^3 -weighted EXAFS functions obtained by Fourier back-transforming second RSF peaks in Fig. 3 ($\Delta R = 2.9$ - 4.2 Å for $166 \mu\text{mol/g}$ and $\Delta R = 2.9$ - 3.7 Å for $14, 40 \mu\text{mol/g}$).

Table 2: Structural Information derived from EXAFS Analysis.

Sample	Th-Si			Th-Th			ΔE_0^f [eV]	%Res
	N	R [Å]	σ^{2f} [Å ²]	N	R [Å]	σ^{2f} [Å ²]		
166 $\mu\text{mol/g}$	A reasonable fit could not be achieved							
40 $\mu\text{mol/g}$	1.5	3.84	0.005	0.7	3.76	0.005	6	29.7
14 $\mu\text{mol/g}$	1.7	3.85	0.005	0.7	3.77	0.005	6	25.0

f: Fixed during the fit procedure

Accordingly, the second peak consists of 1.5-1.7 Si at ~ 3.85 Å and ~ 0.7 Th at 3.77 Å (14 and 40 $\mu\text{mol/g}$). The σ^2 terms were set to 0.005 Å² as in the thorite reference. The spectrum of the most concentrated Th sample (166 $\mu\text{mol/g}$) clearly differs from the spectra of the two less concentrated samples (14 and 40 $\mu\text{mol/g}$), indicating differences in the Th coordination environment. For example, there is a beat pattern near 6.5 Å⁻¹ in the most concentrated Th sample which indicates the presence of at least two cationic subshells containing heavy atoms such as Th.

At high Th concentration (166 $\mu\text{mol/g}$) neither a Th-Th and Th-Si, nor a Th-Th₁ and Th-Th₂ two-shell model provided a good fit to the experimental spectrum. Nevertheless, it is possible to propose an uptake mechanism for Th in this sample. In Fig 5 the EXAFS spectra of thorite (Farges 1991) and amorphous Th(OH)₄ are compared to the 166 $\mu\text{mol/g}$ Th sample. The likeness of the sorption sample and the Th amorphous precipitate is striking, and suggests the formation of a similar precipitate at high Th concentration. Again it was not possible to fit Th(OH)₄ data with just one or two Th-Th backscattering pairs. The reason lies probably in the fact, that the second peak of the Th(OH)₄ compound is too disordered to be fitted with a two-Th shell harmonic model (Östhois *et al.* 1997).

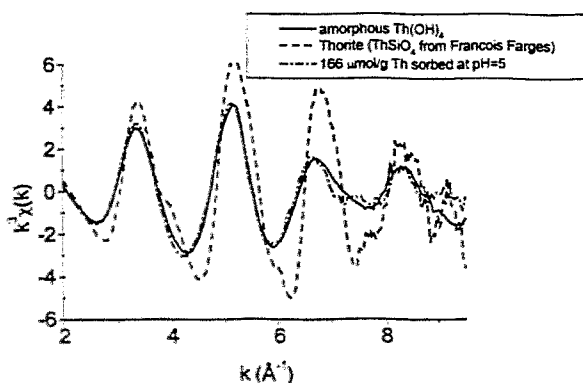


Fig 5: Comparison of k^3 -weighted XAFS functions of reference compounds and the highest concentrated Th sample.

4. Discussion

The results obtained in this study for the two most diluted samples compare well with those reported by Östhols et al (1997) for the sorption of Th on amorphous silica: 1.7-2.7 O at 2.27-2.34 Å vs. 2.6-3.0 O at 2.27-2.28 Å (this study), 4.4-5.4 O at 2.53-2.56 Å vs. 6.9-7.1 O at 2.45-2.46 Å (this study), and 1.3-2.7 Si at 3.79-3.89 Å vs. 1.5-1.7 Si at 3.84-3.85 Å (this study). While the coordination numbers and interatomic distances for the first O and the Si shell match well, the second Th-O distance in the Th/montmorillonite system is significantly shorter. The distance of the second shell is characteristic for Th-H₂O bonds (2.44-2.45 Å) (Moll *et al.* 1999) and therefore does not modify the structural interpretation. EXAFS structural parameters for Th-sorbed silica were interpreted by Östhols et al. (1997) as the formation of a double corner-sharing Th surface complex. Based on the similarity of structural parameters in the two systems, Th can be hypothesized to be bound to Si tetrahedra in a similar manner.

In conclusion, this study reveals the presence of two Th-O coordination spheres for the uptake of Th on montmorillonite at pH = 5. At low Th concentration (14 and 40 µmol/g), Th is bound to about two Si tetrahedra by a double-corner sharing mechanism as in Th sorbed silica. At high Th concentrations (166 µmol/g), Th precipitated as a Th(OH)₄-like amorphous thorium hydroxide.

Based on the data obtained in this study two structural mechanisms can be inferred for the samples with low Th concentration: The formation of a Th surface complex at the montmorillonite surface or the precipitation/neof ormation of a Th-silicate. The neof ormation of mixed (i.e. sorbate + sorbent metals) precipitates has been recently demonstrated in the case of Ni uptake on clay minerals (Scheidegger *et al.* 1997; Dähn *et al.* 2000; Scheinost *et al.* 2000) and Co on quartz (Manceau *et al.* 1999).

Acknowledgements

The authors thank the staff of the Rossendorfer Beamline at the ESRF for their support during the XAFS measurements, and the European Synchrotron Radiation Facility (ESRF) at Grenoble, France, for the provision of beamtime. Francois Farges is thanked for providing the thorite spectrum. Partial financial support was provided by the National Co-operative for the Disposal of Radioactive Waste (Nagra), Wettingen (Switzerland).

References

- Baeyens, B. & Bradbury, M. H. (1997). *J. Contam. Hydrol* **27**: 199-222.
- Dähn, R., Scheidegger, A., Manceau, A., Schlegel, M., Baeyens, B. & Bradbury, M. H. (2000). *Journal of Synchrotron Radiation in review*.
- Ewing, R. C., Chakoumakos, B. C., Lumpkin, G. R. & Murakami, T. (1987). *Nuclear Instruments and Methods in Physics Research* **32**(1-4): 487-497.
- Farges, F. (1991). *Geochim. Cosmochim. Acta* **55**: 3303-3319.
- Lumpkin, G. R., Ewing, R. C., Chakoumakos, B. C., Gregor, R. B., Lytle, F. W., Foltyn, E. M., Clinard, F. W. J., Boatner, L. A. & Abraham, M. M. (1986). *Journal of Materials Research* **1**(4): 564-576.
- Manceau, A., Schlegel, M., Nagy, K. L. & Charlet, L. (1999). *J. Colloid Interface Sci.* **220**: 181-197.
- Matz, W., Schell, N., Bernhard, G., Prokert, F., Reich, T., Claussner, J., Oehme, W., Schlenk, R., Diemel, S., Funke, H., Eichhorn, F., Betzl, M., Prohl, D., Strauch, U., Huttig, G., Krug, H., Neumann, W., Brendler, V., Reichel, P., Denecke, M. & Nitsche, H. (1999). *Journal of Synchrotron Radiation* **6**: 1076-1085.
- Moll, H., Denecke, M. A., Jalilvand, J., Sandström, M. & Grenthe, I. (1999). *Inorganic Chemistry* **38**(8): 1795-1799.
- Neck, V. & Kim, J. I. (2000). *Radiochim. acta in review*.
- Östhols, E., Bruno, J. & Grenthe, I. (1994). *Geochim. Cosmochim. Acta* **58**(2): 613-623.
- Östhols, E., Manceau, A., Farges, F. & Charlet, L. (1997). *J. Colloid Interface Sci.* **194**: 10-21.

- Rehr, J. J., Mustre de Leon, J., Zabinsky, S. & Albers, R. C. (1991). *Journal of the American Chemical Society* **113**(14): 5135-5140.
- Ressler, T. (1998). *Journal of Synchrotron Radiation* **5**(2): 118-122.
- Ryan, J. L. & Rai, D. (1987). *Inorg. Chem.* **26**: 4140-4142.
- Santschi, P. H. & Honeymann, B. D. (1989). *Radiat. Phys. Chem.* **34**(2): 213-240.
- Savanonda, N., Prongpunyasakul, E. & Ratanakorn, S. (1985). New York, Gordon and Breach.
- Scheidegger, A. M., Lambie, G. M. & Sparks, D. L. (1997). *J. Colloid Interface Sci.* **186**: 118-128.
- Scheinost, A. C. & Sparks, D. L. (2000). *J. Colloid Interface Sci.* **223**: 1-12.
- Schlegel, M., Manceau, A., Chateigner, D. & Charlet, L. (1999a). *J. Colloid Interface Sci.* **215**: 140-158.
- Schlegel, M. L., Manceau, A. & Charlet, L. (1999b). *J. Colloid Interface Sci.* **220**: 392-405.
- Taylor, M. & Ewing, R. C. (1978). *Acta Cryst. B* **34**: 1074-1079.
- Tsipursky, S. I. & Drits, V. A. (1984). *Clay Minerals* **19**(2): 177-193.

** These results have been presented at and are accepted for publication in the proceedings of the "2nd Euroconference and NEA Workshop on Speciation, Techniques, and Facilities for Radioactive Materials at Synchrotron Light Sources", Grenoble, France, September 10-12, 2000.*

Overview about the beamtime distribution at ROBL

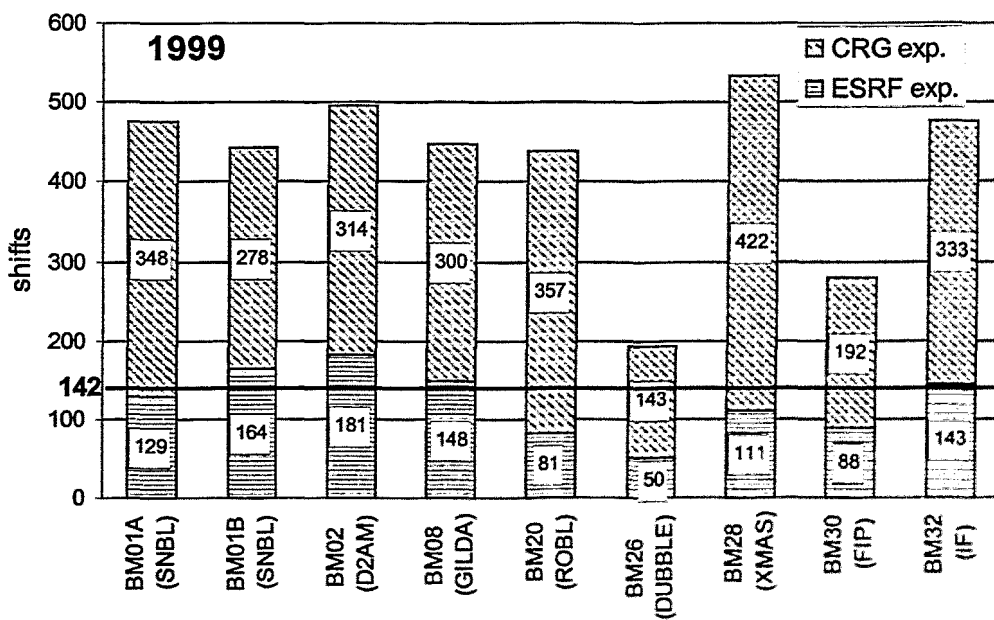
During the actual report period 50 scheduled experiments were performed at ROBL. The overall number of shifts (à 8 hours) delivered for these experiments is given in the table. The shifts are divided into experiments allocated in the CRG beamtime and such allocated in the ESRF time (maximum 1/3 of user beamtime). Additionally, about 100 shifts are used for in-house and methodical experiments during the report period.

The table also contains the number of user groups (excluding FZR groups), where the figures in brackets indicate how many groups came more than once the year. The total number of users visiting ROBL for the experiment, including FZR users permanently working at Rossendorf, is given in the last column. This figure demonstrates that the ROBL team in Grenoble has to make a significant organisational effort for running the experiments.

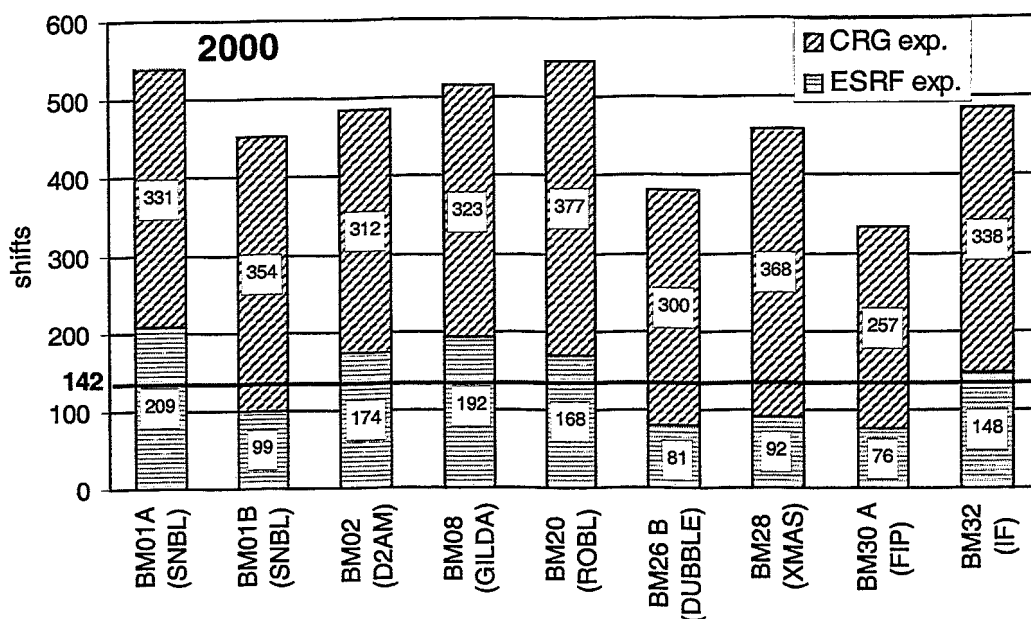
period	Shifts CRG experiments	Shifts ESRF experiments	User groups	Users (persons)
Aug-Dec 1999	135	25	8 (1)	77
Jan-Dec 2000	374	144	20 (5)	223

ROBL has to deliver 142 user shifts for ESRF users in every scheduling period. The two viewgraphs below[#] show the total number of scheduled shifts and the ESRF part for all CRG beamlines. Note, that the statistical period of the ESRF of each year extends to January/February of the next year (first run). Therefore, the figures in the table above and the second viewgraph are slightly different.

Both viewgraphs show that ROBL is stable working. The experimental possibilities as well as the users request for beamtime is comparable to the most other CRG beamlines.



[#] supplied by the CRG-office of the ESRF



The following tables list up in detail the experiments performed. There are some experiments with a high number of shifts (>18) which are part of long term research programmes of the FZR or connected with the work of Ph.D. students.

From the tables one can also extract the collaborating institutions using the experimental possibilities of ROBL.

The experimental reports were provided by the applicants of the research. The responsibility for the communicated results is at the users, ROBL made only minor changes concerning exclusively the layout. All reports received until May 2001 are reproduced here.

Support of user groups by the European Commission

In the frame of the general programme "Improving Human Research Potential" of the European Commission (EC) ROBL is supported under the programme activity "Access to Research Infrastructure" since February 2000 for 3 years. Under the contract HPRI-CT-1999-00077 research groups from Member and Associated States of the EU can obtain a grant for experiments at ROBL.

ROBL publishes calls for proposals where the deadline for submission is given (March, September 2000, April 2001). A user selection panel established with approval of the EC decides which experiments will be performed at ROBL. At maximum 15 % of the beamtime is available for the EC supported user groups.

More information about this access way one can obtain by contacting our Web-site: <http://www/fz-rossendorf.de/FWE/> (see under: EC supported access)

The performed experiments are included in the table and indicated by a second number beginning with EU-xxx.

List of EC supported users of ROBL

J. Bøttiger

University of Aarhus, Institute of Physics and Astronomy, Aarhus, Denmark, 20-02-38 (EU-M02)

G. Deves

CNRS, Laboratoire Chimie Nucleaire et Analytique, Gradignan, France, 20-01-23 (EU-R06)

J. Gaca

Institute of Electronic Materials Technology, Warsaw, Poland, 20-02-37 (EU-M01)

I. Grenthe

Royal Institute of Technology (KTH), Department of Chemistry, Stockholm, Sweden,
20-01-26 (EU-R04)

K. Guerman

CNRS, Laboratoire Chimie Nucleaire et Analytique, Gradignan, France, 20-01-23 (EU-R06)

F. Livens

University of Manchester, Department of Chemistry, Manchester, Great Britain,
20-01-28 (EU-R01)

K. Mazur

Institute of Electronic Materials Technology, Warsaw, Poland, 20-02-37 (EU-M01)

L. Moyes

University of Manchester, Department of Chemistry, Manchester, Great Britain,
20-01-28 (EU-R01)

K. Rasmussen

University of Aarhus, Institute of Physics and Astronomy, Aarhus, Denmark,
20-02-38 (EU-M02)

W. Reed

University of Manchester, Department of Chemistry, Manchester, Great Britain,
20-01-28 (EU-R01)

J. Sass

Institute of Electronic Materials Technology, Warsaw, Poland, 20-02-37 (EU-M01)

Z. Szabo

Royal Institute of Technology (KTH), Department of Chemistry, Stockholm, Sweden,
20-01-26 (EU-R04)

M. H. Vesvres

CNRS, Laboratoire Chimie Nucleaire et Analytique, Gradignan, France, 20-01-23 (EU-R06)

M. Wójcik

Institute of Electronic Materials Technology, Warsaw, Poland, 20-02-37 (EU-M01)

Scheduled Experiments at ROBL-RCH

number	title	proposers	institution	experimentators	shifts
20_01_009	Lutetium L _{III} and Europium L _{II} -edge EXAFS measurements of Eu(III) and Lu(III)-sorbed iron compounds	K. Dardenne, M. Denecke	FZ Karlsruhe-INE	Dardenne, Rothe, Hennig	6
20_01_010	XANES and EXAFS measurements on V and Ag inorganic compounds	T. Reich, H. Funke, C. Chartroux, A. Roßberg	FZ Rossendorf TU-Dresden	Reich, Chartroux, Hennig, Roßberg	7
20_01_011	Application of EXAFS to technetium speciation in pyrometallurgy reprocessing of spent nuclear fuel and in sulfur-rich environmental samples	M. Simonoff, K. Guerman, T. Reich	CR-CNRS Gradignan, FZ Rossendorf	Sergeant, Ortega, Deves, Reich, Künstler, Hennig, Roßberg, Funke	4
20_01_012	Tc K-edge EXAFS on dilute solutions	T. Reich, C. Hennig, H. Funke, A. Roßberg	FZ Rossendorf	Hennig, Reich, Roßberg, Geipel	3
20_01_013	EXAFS measurements of Pu Hydrates	T. Reich, G. Geipel, G. Bernhard	FZ Rossendorf	Hennig, Reich, Roßberg, Geipel	4
20_01_014	Interaction between bacteria and materials using EXAFS	S. Selenska-Pobell, H. Funke, M. Merroun, J. Raff, T. Reich, C. Hennig, A. Roßberg	FZ Rossendorf	Funke, Hennig, Merroun, Reich, Roßberg, Moll	9
20_01_015	X-ray Absorption Spectroscopy investigations on environmental colloids (Fe matrix)- Interaction with heavy and hazardous elements (As, Pb)	H. Moll, T. Reich, C. Hennig, H. Funke, A. Roßberg	FZ Rossendorf	Moll, Funke, Hennig, Reich, Roßberg, Merroun	24
20_01_016	EXAFS investigation of U(VI) sorption on silica gel at low temperature	T. Reich, C. Hennig, H. Moll	FZ Rossendorf	Reich, Hennig, Roßberg, Funke, Rutsch, Amayri	9
20_01_017	Structural investigations of uranium(VI) at different fluoride concentrations using EXAFS. A comparison between experiment and theory.	H. Moll, I. Grenthe, T. Reich, C. Hennig, H. Funke, A. Roßberg	FZ Rossendorf KTH-Stockholm	Amayri, Funke, Hennig, Reich, Roßberg, Rutsch	3
20_01_018	EXAFS investigation of U(VI) complexation with acetic acid	T. Reich, A. Roßberg, V. Brendler	FZ Rossendorf	Funke, Hennig, Roßberg, Rutsch, Amayri	18
20_01_019	EXAFS measurements at low temperature	C. Hennig, T. Reich, A. Roßberg, S. Amayri, M. Rutsch, H. Funke	FZ Rossendorf	Funke, Hennig, Roßberg, Rutsch, Amayri, Reich, Tsuschima	17
20_01_020	Investigations to test a „splice“ program unifying two EXAFS-scans with an overlapping region	H. Funke, T. Reich, C. Hennig, A. Roßberg	FZ Rossendorf	Funke, Hennig, Roßberg, Rutsch, Amayri	6

20_01_021	Interaction between bacteria and metals using EXAFS	S. Selenska-Pobell, H.Funke, T. Reich, J. Raff, C. Hennig, A. Roßberg	FZ Rossendorf	Funke, Hennig, Reich, Roßberg, Tsuschima	6
20_01_022	Structural investigation of complexes between actinides (Np(IV/V), U(IV/VI), Th(IV) and humic substances, BioRex70 and ATP	K. Schmeide, S. Pompe, T. Reich, C. Hennig, A. Roßberg, H. Funke	FZ Rossendorf	Schmeide, Funke, Hennig, Pompe, Reich, Roßberg	18
20_01_023 <i>EU-R06</i>	Application of EXAFS to technetium speciation in pyrometallurgy reprocessing of spent nuclear fuel and in sulfur-rich environmental samples. Part 1. Technetium in chloride system.	M. Simonoff, K. Guerman, T. Reich, R. Ortega, C. Sergeant, G. Deves	CE-CNRS Gradignan	Guerman, Reich, Vesvres, Simonoff, Deves, Hennig, Roßberg	9
20_01_024	Polarized EXAFS measurements at uranyl sorbed montmorillonite	C. Hennig, T. Reich, A. Rossberg, H. Funke	FZ Rossendorf	Funke, Reich, Hennig, Moll, Rossberg	18
20_01_025 <i>EU-R03</i>	Speciation of monomer and polymer forms of technetium (IV) in aqueous sulphate solutions	M. Fattahi, B. Grambow, V. Vichot	Subatech, Ecole des Mines de Nantes	Fattahi, Vichot, Hennig	6
20_01_026 <i>EU-R04</i>	Water co-ordination in uranium(VI) fluoride and oxalate complexes as studied by EXAFS and ab initio calculations	I. Grenthe	KTH Stockholm	Szabo, Grenthe, Hennig	6
20_01_027	Structural investigation of Pu(III) complexes with humic substances, BioRex70	K. Schmeide, S. Pompe, H. Funke, T. Reich, C. Hennig, A. Rossberg	FZ Rossendorf	Schmeide, Pompe, Reich, Hennig, Rossberg	6
20_01_028 <i>EU-R01</i>	Catecholate complexes of NpO_2^+ and NpO_2^{2+} in aqueous solution and reactions of NpO_2^+ with the surface of mackinawite (tetragonal FeS)	F. Livens, D. Vaughan, R. Patrick	University of Manchester	Moyes, Livens, Charnock, Mosselmans, Reed, Jones, Hennig	9
20_01_029	EXAFS study of Np(VII) solutions	T. Fanghänel, H. Moll, G. Geipel, H. Funke, T. Reich, C. Hennig, A. Rossberg	FZ Rossendorf	Fanghänel, Schmeide, Hennig, Rossberg, Reich, Zayarnaya	3
20_01_030	EXAFS investigation on uranium uptake by plants	A. Günther, G. Bernhard, G. Geipel, H. Moll, S. Amayri, H. Funke, T. Reich, C. Hennig, A. Rossberg, M. Walter	FZ Rossendorf	Moll, Amayri, Funke, Reich, Hennig, Rossberg, Walter	5

20_01_031	X-ray absorption spectroscopy investigation on uranyl complexes with alpha-substituted carboxylic acid	H. Moll, T. Reich,	FZ Rossendorf	Moll, Reich, Funke, Rossberg, Amayri, Walter	3
20_01_032	Uranium (VI) sorption onto ferrihydrite	T. Reich, T. Arnold	FZ Rossendorf	Reich, Amayri, Moll, Funke, Hennig, Rossberg	3
20_01_IH2	Annealing temperature dependence of atomic structure in submicrocrystalline Cu	T. Reich, Yu. Babanov, H. Funke	FZ Rossendorf IMP RAS Ekatarienburg	Reich, Funke, Babanov	5

ESRF Allocated Time for ROBL-RCH

number	title	proposers	institution	experimentators	shifts
LS-1395	EXAFS studies of [⁹⁹ Tc] technetium carbonyl complexes	S. Seifert, B. Johannsen, J.U. Künstler, T. Reich, H. Funke, C. Hennig, A. Roßberg	FZ Rossendorf	Seifert, Künstler, Funke, Reich, Hennig, Roßberg	27
ME-44	Uranium sorption onto ZrSiO ₄ and Zr(PO ₃) ₄ surfaces: EXAFS studies	R. Drot, E. Simoni, C. Lomenech, E.Ordenez Regil	IPN-Orsay	Drot, Lomenech, Ordonez, Simoni, Hennig, Reich	15
ME-49	Determination of Th sorption mechanisms onto montmorillonite	A. Scheidegger, R. Dähn, P. Spieler, A. Manceau	PSI Villigen, LGIT-IRIGM Grenoble	Dähn, Spieler, Scheidegger, Struis, Hennig	18
ME-50	Elucidation of structural environment of Th(IV) in mixed-metal ligand systems using XAFS	A. Scheidegger, M. Glaus, R. Dähn, K. Vercammen, K. Hegetschweiler	PSI Villigen Uni Saarland	Dähn, Spieler, Wieland, Scheidegger, Hennig	12
ME-129	The use of EXAFS to study sorption on illite	A. Scheidegger, R. Dähn, P. Spieler, I. Bonhoure	PSI Villigen Waste Management Lab.	Dähn, Spieler, Bonhoure, Reich	18
ME-131	Application of EXAFS to technetium speciation in pyrometallurgy reprocessing of spent nuclear fuel and sulphur-rich environmental samples	M. Simonoff, K. Guerman, T. Reich, R. Ortega, C. Sergeant, G. Deves,	CNRS, Université de Bordeaux	Guerman, Vesvres, Kawai, Deves, Sergeant, Ortega, Hennig, Pravikoff	24
MI-346	Photoacoustic Detection of the XAS Signal	G. Geipel, G. Bernhard, T. Reich	FZ Rossendorf	Geipel, Funke, Reich, Hennig, Roßberg	6

Scheduled Experiments at ROBL-MRH

number	title	proposers	institution	experimentators	shifts
20_02_023	Analysis of correlation in the distribution of disorientations in deformed copper and aluminium single crystals	M. Habermann, M. Motylenko	University of Freiberg (IPM)	Habermann, Motylenko, Schell, Matz	6
20_02_024	High-precision determination of atomic positions in 6H- and 4H-SiC crystals and investigation of germanium nano-structures on silicon carbide	A. Bauer, K. Götz, J. Kräußlich, G. Heß	FSU Jena	Bauer, Kräußlich, Schell, Matz	12
20_02_025	Structure of thin Ta-based films	N. Mattern	IFW Dresden	Mattern, Hecker, Schell	6
20_02_026	Influence of O ₂ -integration in a NiFe/Cu-multilayer sequence on the structural properties of the layers and interfaces	M. Hecker, N. Mattern, C. M. Schneider	IFW Dresden	Hecker, Mattern, Schell	6
20_02_027	Scanning XRD investigations of the gradient of the martensite content in a fatigued hour glass sample of steel X6CrNiTi18.10	M. Grosse, M. Niffenegger	PSI Villigen	Grosse, Niffenegger, Schell	6
20_02_028	Diffraction of synchrotron radiation at Bi-2223/Ag superconductors at high temperature	T. Fahr, W. Häßler, G. Koebernik	IFW Dresden	Fahr, Häßler, Koebernik, Schell, Berberich	18
20_02_029	Study of structural properties of sputterdeposited and selfassembled multilayer waveguides	T. Salditt, F. Pfeiffer	LMU Munich (CeNS)	Pfeiffer, Salditt, Schell, Spaar, Menicke, Berberich	16
20_02_030 long term	Investigation of the lateral ordering in InGaAsP/InP multilayers on InP substrate	J. Sass, J. Gaca, K. Mazur, M. Wójcik, F. Eichhorn	ITME Warsaw, FZ Rossendorf (FWIS)	Sass, Mazur, Eichhorn, Schell	12
20_02_031 long term	Structural changes in N ⁺ -ion implanted Ti-6Al-4V alloys during annealing by in-situ x-ray diffraction	F. Berberich, W. Matz, N. Schell	FZ Rossendorf (FWIS)	Berberich, Schell, Klimenkov, Prokert, Matz	46
20_02_032	Analysis of the defect structure in severely deformed micro-, submicro- and nanocrystalline nickel after thermal treatment	E. Thiele, C. Holste, R. Klemm	TU Dresden (IPMK)	Thiele, Klemm, Schell	11
20_02_033	X-ray investigation of silicon / germanium nanostructures on silicon carbide	G. Heß, K. Goetz, J. Kräußlich, A. Bauer	FSU Jena	Heß, Kräußlich, Bauer, Schell	12
20_02_034	Studies of silicidation processes during thermal treatment in the system Si-Co-Ti	J. Rinderknecht	AMD Saxony Manufacturing Dresden	Rinderknecht, Berberich	6
20_02_035	Study of preferential orientation of SiC particles formed by carbon implantation into silicon	F. Eichhorn, N. Schell, W. Matz, R. Kögler	FZ Rossendorf (FWIS, FWIM)	Eichhorn, Schell, Reichel, Berberich	21
20_02_036	Microstructure of ultra thin diffusion barriers	N. Mattern, M. Hecker, C. Wenzel, D. Fischer	IFW Dresden, TU Dresden	Mattern, Hecker, Schell, Berberich, Fischer	18

20_02_037 EU-M01	Investigation of the lateral ordering and chemical composition in lattice matched A_3B_5 quarternary and ternary superlattices	J. Sass, J. Gaca, M. Wójcik, K. Mazur, F. Eichhorn	ITME Warsaw, FZ Rossendorf (FWIS)	Mazur, Gaca, Wójcik, Eichhorn, Schell, Reichel Sass, Bauer	12
20_02_038 EU-M02	Thin film growth studies by <i>in-situ</i> x-ray diffraction	J. Bøttiger, P. Kringhøj, J. Chevallier	University of Aarhus	Bøttiger, Rasmussen, Schell, Matz, Bauer	15
20_02_039	Investigation of grain structure and lattice defects in fatigued and annealed submicro- and nanocrystalline nickel	E. Thiele, C. Holste, R. Klemm	TU Dresden (IPMK)	Thiele, Klemm, Schell	9
20_02_040	Time resolved pursuit of martensitic phase transformation in Ti	N. Darowski, G. Vogl	HMI Berlin	Darowski, Vogl, Grenzer, Sladeczek, Berberich, Schell	11
20_02_IH2	Crystalline phases in tungsten carbide materials after the implan-tation of light B ions	F. Eichhorn	FZ Rossendorf (FWIS)	Eichhorn, Schell	6
20_02_IH3	Crystallisation of TaSi thin layers	W. Matz E. Wieser	FZ Rossendorf (FWIS., FWII)	Matz, Peikert, Berberich	7
20_02_IH4	Reflectometry on multilayers	F. Prokert	FZ Rossendorf (FWIS)	Prokert, Schell	12

ESRF Allocated Time for ROBL-MRH

number	title	proposers	institution	experimentators	shifts
HS-1183	Structural investigation on molten eutectic Cu-Ge using anomalous x-ray scattering	Th. Halm, J. Nomssi, W. Hoyer	TU Chemnitz	Halm, Nomssi, Giegengack, Schell	17
HS-1184	Structure investigation of the liquid Ag-Bi alloy using anomalous x-ray scattering in reflection geometry	J. Nomssi, Th. Halm, W. Hoyer	TU Chemnitz	Nomssi, Halm, Giegengack, Schell	17
ME-130	Influence of dopant atoms in cubic boron nitride (c-BN) thin films on lattice parameters and intrinsic stress investigated by x-ray diffraction	F. Richter, H. Giegengack, Th. Pfeifer	TU Chemnitz	Halm, Linss, Schell	15

List of publications which contain results from experiments at ROBL

1999

Eichhorn, F., Schell, N., Matz, W., and Kögler, R.
Strain and SiC particle formation in silicon implanted with carbon ions of medium fluence studied by synchrotron X-ray diffraction.
Journal of Applied Physics, **86** (1999) 4184-4187.

Funke, H., Reich, T., Bernhard, G., Brendler, V., Claussner, J., Hüttig, G., Matz, W., Neumann, W., Oehme, W.
The radiochemistry experimental station at the Rossendorf beamline
Speciation, Techniques and Facilities for Radioactive Materials at Synchrotron Light Sources: Workshop Proceedings, Grenoble, France, October 4-6, 1998, OECD/NEA Paris, France (1999), pp. 181-187,

Hennig, C., Nolze, G.
Characterization of the preferred orientation in EXAFS-samples using Bragg-Brentano x-ray diffraction
Speciation, Techniques and Facilities for Radioactive Materials at Synchrotron Light Sources: Workshop Proceedings, Grenoble; France, 4-6 October 1998, OECD/NEA Paris, France (1999), pp. 235-243

Matz, W.
Introduction to x-ray diffraction at synchrotron light sources
Speciation, Techniques and Facilities for Radioactive Materials at Synchrotron Light Source: Workshop Proceedings, Grenoble, France, October 4-6, 1998, OECD/NEA Paris, France (1999), pp. 39-48.

Matz, W., Schell, N., Bernhard, G., Prokert, F., Reich, T., Claußner, J., Oehme, W., Schlenk, R., Dienel, S., Funke, H., Eichhorn, F., Betzl, M., Pröhl, D., Strauch, U., Hüttig, G., Krug, H., Neumann, W., Brendler, V., Reichel, P., Denecke, M.A. and Nitsche, H.
ROBL – a CRG Beamline for Radiochemistry and Materials Research at the ESRF.
Journal of Synchrotron Radiation, **6** (1999) 1076-1085.

Nitsche, H., Reich, T., Hennig, C., Roßberg, A., Geipel, G., Denecke, M.A., Baraniak, L., Panak, P., Abraham, A., Mack, B., Selenska-Pobell, S., Bernhard, G.
Application of synchrotron radiation techniques to radionuclide studies
Speciation, Techniques and Facilities for Radioactive Materials at Synchrotron Light Sources: Workshop Proceedings, Grenoble; France, 4-6 October 1998, OECD/NEA Paris, France (1999) pp. 15-27

Reich, T., Moll, H., Arnold, T., Denecke, M.A., Hennig, C., Geipel, G., Bernhard, G., Nitsche, H., Allen, P.G., Bucher, J.J., Edelstein, N.M., Shuh, D.K.
EXAFS studies of uranium(VI) sorption on mineral surfaces
Speciation, Techniques and Facilities for Radioactive Materials at Synchrotron Light Sources: Workshop Proceedings, Grenoble; France, 4-6 October 1998, OECD/NEA Paris, France (1999) pp. 83-92

Reich, T., Brendler, V., Denecke, M.A., Bubner, M., Pompe, S., Nitsche, H.
Structural analysis of the interaction of uranium(VI) with humic acid and simple carboxylic acids using EXAFS
Speciation, Techniques and Facilities for Radioactive Materials at Synchrotron Light Sources: Workshop Proceedings, Grenoble; France, 4-6 Oct. 1998, OECD/NEA Paris, France (1999). pp. 277-283

Thiele, E., Hecker, M., and Schell, N.
Change of internal strains in ultrafine-grained nickel due to cyclic plastic deformation.
Materials Science Forum, **321-324** (1999) 598-603

2000

Berberich, F., Matz, W., Richter, E., Schell, N., Kreißig, U. and Möller, W.
Structural mechanisms of the mechanical degradation of Ti-Al-V alloys: in-situ study during annealing
Surf. Coat. Techn. **128-129** (2000) 450-454

Hecker, M., Tietjen, D., Prokert, F., Schell, N., Schneider, C. M.
Investigation of Co/Cu/NiFe-multilayers by x-ray reflectometry and diffraction
Mikrochim. Acta **133** (2000) 239-241

Heß, G., Bauer, A., Kräußlich, J., Fissel, A., Schröter, B., Richter, W., Schell, N., Matz, W.,
Goetz, K.
Si/Ge- nanocrystals on silicon carbide
Thin Solid Films **380** (2000) 86-88

Mattern, N., Hecker, M., Fischer, D., Wenzel, C., Schell, N., Matz, W., Engelmann, H.,
Zschech, E.
Structure characterization of Ta-N barrier layers,
Microelectronics Reliability **40** (2000) 1765-1770.

Moll, H., Reich, T., Hennig, C., Rossberg, A., Szabó, Z., Grenthe, I.
Solution coordination chemistry of uranium in the binary UO_2^{2+} - SO_4^{2-} and the ternary UO_2^{2+} - SO_4^{2-} - OH^- system
Radiochim. Acta **88** (2000) 559-566

Moll, H., Reich, T., Szabó, Z.
The hydrolysis of dioxouranium(VI) investigated using EXAFS and ^{17}O -NMR
Radiochim. Acta **88** (2000) 411-415

Noetzel, J., Rössler, U. K., Tselev, A., Prokert, F., Eckert, D., Müller, K.-H., Wieser, E.,
Möller, W.
Preparation of granular Co/Cu by ion-beam mixing of laser-deposited multilayer
Appl. Phys. **A71** (2000) 105-107

Pfeiffer, F., Salditt, T., Høghøj, P., Anderson, I., Schell, N.
X-ray waveguides with multiple guiding layers
Phys. Rev. **B 62** (2000) 16939-16943

Reich, T., Bernhard, G., Geipel, G., Funke, H., Hennig, C., Rossberg, A., Matz, W., Schell, N., and
Nitsche, H.
*The Rossendorf Beam Line ROBL – a dedicated experimental station for XAFS measurements of
actinides and other radionuclides.*
Radiochim. Acta **88** (2000) 633-637

Reich, T., Geipel, G., Funke, H., Hennig, C., Rossberg, A., Bernhard, G.
Plutonium. XAFS measurements of plutonium hydrates
ESRF Highlights 1999, (2000) 32-33

Roßberg, A., Baraniak, L., Reich, T., Hennig, C., Bernhard, G., Nitsche, H.
EXAFS structural analysis of aqueous uranium(VI) complexes with lignin degradation products
Radiochim. Acta **88** (2000) 593-597

Seifert, S., Künstler, J.-U., Gupta, A., Funke, H., Reich, T., Hennig, C., Roßberg, A.,
Pietzsch, H.-J., Alberto, R., Johannsen, B.
EXAFS analyses of technetium(I) carbonyl complexes - stability studies in solutions
Radiochim. Acta **88** (2000) 239-245

Thiele, E., Bretschneider, B., Hollang, L., Schell, N., and Holste, C.
Influence of thermal treatment and cyclic plastic deformation on the defect structure in ultrafine-grained nickel.
In: T.C. Lowe and R.Z. Valiev (eds.) Investigations and Applications of Severe Plastic Deformation, Proceedings of NATO Advanced Research Workshop, Moscow, 2-6 August 1999; Kluwer Academic Publishers, 2000, pp. 173-178.

Oehme, W., Dienel, S., Proehl, D., Matz, W., Reich, T., Schell, N., Bernhard, G., Krug, H.,
Reichel, P., Strauch, U., Prokert, F., Claussner, J., Funke, H., Neumann, W., Brendler, V.,
Hennig, C., Berberich, F.
Beamline- Instrumentierung und Experimentautomatisierung für ROBL an der ESRF / Grenoble (F)
FZR-291, Rossendorf, März 2000

Personnel of the Project Group ESRF-Beamline

The personnel of the project group comes from different institutes and departments of the FZR.

Head of the Project Group / Spokesman of the CRG:	Dr. W. Matz
Local contact at ESRF and responsible for MRH:	Dr. N. Schell
Responsible for RCH at ESRF and for radiation protection:	Dr. T. Reich

Staff at ESRF in Grenoble

Dr. Ch. Hennig (2005)	A. Bauer (2849) since 09/00	U. Strauch (2372)
Dr. T. Reich (2339)	F. Berberich (2847)	
Dr. N. Schell (2367)	A. Roßberg (2848)	

Postal address:

ROBL-CRG
ESRF / sector 21
BP 220
F-38043 Grenoble Cedex, France

Phone: +33 4 76 88 xx xx
Fax: +33 4 76 88 25 05
e-mail: *surname@esrf.fr*

FZR - personnel working at ROBL

Institute for Ion Beam Physics and Materials Research

Dr. F. Eichhorn	W. Boede	Dr. M. Klimenkov
Dr. W. Matz	J. Kreher	M. Peikert
Dr. F. Prokert	P. Reichel	A. Höfgen

Institute of Radiochemistry


Prof. G. Bernhard	Dr. H. Moll	S. Amayri
Dr. H. Funke	Dr. S. Pompe	M. Merroun
Dr. G. Geipel	Dr. K. Schmeide	M. Rutsch
Dr. K.-H. Heise	Dr. S. Tsushima	M. Walter

Institute of Bioanorganic and Radiopharmaceutical Chemistry

Dr. S. Seifert	J.-U. Künstler
----------------	----------------

Central Department Experimental Facilities and Information Technology

J. Claußner	Dr. W. Oehme	T. Riedel
S. Dienel	Dr. D. Pröhl	S. Winkelmann
Dr. H. Krug	R. Schlenk	Y. Zimmermann
W. Neumann		

 ROBL-CRG	Experiment title: Lutetium L3 and europium L2-edge EXAFS measurements of Lu(III)/Eu(III)-sorbed iron compounds	Experiment number: 20-01-009
	Beamline: BM 20	Date of experiment: from: 24 Aug 99 to: 26 Aug 99
Shifts: 6	Local contact(s): Dr. C. Hennig	Received at ROBL: 12 Feb 2000
Names and affiliations of applicants (* indicates experimentalists): Dr. K. Dardenne*, Dr. M.A. Denecke, Dr. J. Rothe* Institut für Nukleare Entsorgungstechnik, Forschungszentrum Karlsruhe GmbH, Postfach 3640, D-76021 Karlsruhe, Germany		

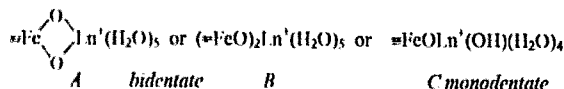
Report:

EXAFS and TRILFS study of lanthanides(III) sorbed onto Hydrous Ferric Oxide (HFO)

The purpose of this study is to characterize trivalent lanthanide (Ln(III)) species sorbed onto hydrous ferric oxide (HFO) by combining wet-chemical sorption data with spectroscopic investigations. Both extended x-ray absorption spectroscopy (EXAFS) and time resolved-fluorescence spectroscopy (TRILFS) experiments were performed. Eu(III) fluorescence in the visible range ${}^1D_0 \rightarrow {}^3F_4$ was used for the determination of the number of coordinated water molecules from the fluorescent lifetime. TRILFS is not possible for Lu(III), due to its full 4f shell. EXAFS transmission experiments on HFO:Lu(III) sorbed samples were performed at ROBL and at beamline A1, HASY1 AB. Lutetium was used to avoid the spectral interference with the Fe K edge, which is a problem for investigations of HFO:Eu samples at the Eu L3 edge. Using the Eu L2 edge avoids this interference. However, the L2 transition has only one-half the intensity and a high residual Fe absorption, thereby limiting the measurable Eu(III) sample loadings. The transferability of TRILFS results from HFO:Eu(III) to HFO:Lu(III) and EXAFS results on HFO:Lu(III) to HFO:Eu(III) is justified because wet-chemical sorption behavior of both these Ln(III) onto HFO is the same.

A Eu(III)-lifetime of 205 μ s was obtained from TRILFS on a HFO:Eu solid sample, prepared at pH 5.7. This increase in lifetime over that for the Eu(III) aquo species indicates that five water molecules (and/or hydroxyl groups) are in the first Eu(III) coordination sphere [1].

Sorption studies indicate a change in the sorbed species with increasing pH. At low pH, formation of a monodentate species according to the reaction $\equiv\text{Fe}-\text{OH} + \text{Lu}^{3+}(\text{H}_2\text{O})_9 \rightarrow \equiv\text{Fe}-\text{O}-\text{Lu}^{3+}(\text{H}_2\text{O})_5$ is proposed, where $\equiv\text{Fe}$ represents an iron atom on the HFO surface. At pH values above ~ 5.5 , a change in the surface species formed is observed. The following three structures for the sorbed species are possible.



EXAFS structural parameters for the Lu coordination in HFO:Lu(III) samples prepared at varying pH allow characterization of the monodentate species formed at low pH and differentiation between species at higher pH, the monodentate deprotonated species (C) and the two possible bidentate binding, A, with Lu(III) bonding via iron oxide polyhedral edges, and B, with geminal corner-sharing bonding.

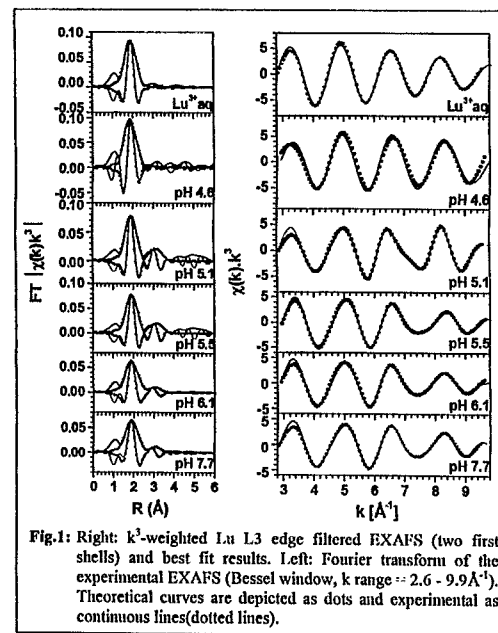


Fig.1: Right: k^3 -weighted Lu L3 edge filtered EXAFS (two first shells) and best fit results. Left: Fourier transform of the experimental EXAFS (Bessel window, k range = 2.6 - 9.9 \AA^{-1}). Theoretical curves are depicted as dots and experimental as continuous lines (dotted lines).

EXAFS spectra exhibit a single first shell of 7 ± 1 oxygen atoms around Lu atoms at a distance of $2.30 (\pm 0.01)$ \AA . The coordination number of Lu sorbed onto HFO is lower than that of the aquo species (9 ± 1), but the Lu-O bond lengths are comparable, without evidence of any splitting of the first coordination shell into more than one distance.

The presence of a second peak above pH 5 at ~ 3.1 \AA (not corrected from phase shift) is attributed to a Lu-Fe distance observed for sorption samples at $\text{pH} \geq 5.5$, at $3.38 (\pm 0.01)$ \AA . This distance is associated with the formation of a bidentate complex with bonding via edge sharing (species A) to FeO_6 -octahedra. The samples prepared at $\text{pH} < 5.1$ show no Fe shell, as expected for monodentate coordination. No evidence for surface precipitation and no noticeable difference between wet paste and dried powder samples is found.

Table 1: Average structural parameters N, R and their statistical error obtained from fits in k and R scale for different extraction procedures. S_0^2 was held constant at 1.

Sample	pH	Lu - O				Lu - Fe			
		N	R [\AA]	σ^2 10^{-3} [\AA^2]	ΔE_0 [eV]	N	R [\AA]	σ^2 10^{-3} [\AA^2]	ΔE_0 [eV]
Lu(III):HFO	4.6	6.2 ± 0.8	2.28	2.5 ± 0.5	3.9	-	-	-	-
Lu(III):HFO	5.1	6.5 ± 0.5	2.31	6.1 ± 0.5	5.6	1.7 ± 0.3	3.48	6.3 ± 1.7	4.6
Lu(III):HFO	5.5	7.7 ± 1.0	2.30	10.3 ± 1.3	7.0	2.7 ± 0.8	3.38	15 ± 3	3.9
Lu(III):HFO	6.1	7.6 ± 0.6	2.30	10.5 ± 1.0	6.5	3.2 ± 0.8	3.38	21.5 ± 3	3.4
Lu(III):HFO	6.1	7.3 ± 0.4	2.30	7.7 ± 0.6	6.5^b	2.7 ± 0.4	3.38	17 ± 2	3.4^*
Lu(III):HFO	7.7	7.0 ± 0.5	2.30	9.2 ± 0.7	6.1	3.3 ± 0.3	3.38	20.5 ± 0.4	3.2
Lu(III) aquo		9.1 ± 0.3	2.31	7.8 ± 0.5	4.9				

* wet paste sample - * fixed to the value of the dried sample

^b held constant at the value obtained for the dried sample, pH 6.1.


[1] W. De W. Horrocks and D.R. Sudnick, J. Am. Chem. Soc. 101, 334 (1979)

[2] A.L. Ankudinov, B. Ravel, J.J. Rehr and S.D. Conradson, Phys. Rev. B, 7565 (1998)

[3] K. Dardenne, T. Schäfer, M.A. Denecke, J. Rothe, and J.I. Kim, Radiochim. Acta (2001, accepted)

The k^3 -weighted Lu L3 edge EXAFS spectra for air-dried Lu(III):HFO sorption samples and their corresponding FT's are shown Fig. 1. From visual comparison of the spectra, it is evident that the sample prepared at pH 4.6 shows a larger oscillatory amplitude than the other samples. Furthermore, this sample shows no evidence for further distant coordination shells, whereas the other four samples all exhibit a FT peak at ~ 3.1 \AA . Although the intensity of this peak is small, its presence corresponds to the perturbation of the main oscillation frequency in the EXAFS spectra at around 7\AA^{-1} . Metrical parameters obtained from fits to these spectra using a model of one Lu-O coordination shell are summarized in Table 1. Also included are results for the Lu(III) aquo species, $\text{Lu}^{3+}(\text{H}_2\text{O})_9$, used as a reference. Phase and amplitude functions generated by FEFF8 [2] for a single scattering Lu-O and Lu-Fe paths were used in the fits.

EXAFS results for Lu(III):HFO sorption samples prepared in the pH range 4.6 to 7.7 [3] show that their

 ROBL-CRG	Experiment title: Application of EXAFS to technetium speciation in pyrometallurgy reprocessing of spent nuclear fuel and in sulfur-rich environmental samples.	Experiment number: 20_01_11
	Beamline: BM 20	Date of experiment: from: 05/09/1999 to: 6/09/1999
Shifts: 4	Local contact(s): T. Reich	Received at ROBL: 30/03/2001
Names and affiliations of applicants (* indicates experimentalists): Simonoff M., CNRS-UMR 5084, Le Haut Vigneau, B.P. 120, F33175 Gradignan Cedex, France Guerman K., CNRS-UMR 5084, Le Haut Vigneau, B.P. 120, F33175 Gradignan Cedex, France Reich T.*, FZR, Institute for Radiochemistry, Dresden, Germany Hennig C.*, FZR, Institute for Radiochemistry, Dresden, Germany Sergeant C., CNRS-UMR 5084, Le Haut Vigneau, B.P. 120, F33175 Gradignan Cedex, France Ortega R., CNRS-UMR 5084, Le Haut Vigneau, B.P. 120, F33175 Gradignan Cedex, France Deves G., CNRS-UMR 5084, Le Haut Vigneau, B.P. 120, F33175 Gradignan Cedex, France		

Report:

EXAFS is one of most promising methods to enable us with speciation of radioactive nuclides. It is important to use it for Te speciation in pyrometallurgy which is now considered the alternative approach to reprocessing of nuclear fuel. The associated study of long-lived fission products forms the basis for its non-hazardous treatment in radioactive wastes. During pyrometallurgical reprocessing, technetium can remain in the molten salt or enter either the sedimented phase contaminating Pu enriched phase, either electrodeposited U phase. Our preliminary results show that under some conditions Te can also form several oxydes, oxychlorides and chlorides of different but rather high volatility, turning on an important polluting risk for gas-off treatment. As the data on EXAF spectra of technetium is now very fragmentary and do not present the whole of the species possible in the pyrometallurgy conditions, it is of high importance to carry synthetic work to supply a large set of technetium compounds in the closed containers which will meet the ESRF/ROBL security and quality demands, radioactivity level, special requirements on sample size, thickness, sample homogeneity. The chemical part of the work is planned to be carried out in Laboratory of radioanalytical and bioenvironmental chemistry, UMR5084, Gradignan. It includes the construction of pyrometallurgical reactors for the treatment of radioactive technetium samples in molten salts permitting to separate the truly dissolved, as well as sediments and sublimate.

The first part of the program deals with the pyrochemical behavior of technetium under reducing conditions. It comprises a set of reference technetium compounds (1 chloride,


1 bromide, 1 pertechnetate) and some samples of simulated pyrometallurgically reprocessed nuclear fuel including technetium hexachlorides in fused salts, and Te precipitated fraction from sulfur-rich environmental fresh water lake sediments with the only Te as a radionuclide.

These samples were studied by means of EXAFS spectroscopy at the Radiochemistry Hutch of ROBL providing with beamsizes of 3 x 20 mm², integrated flux at sample 6 x 10¹¹ /s, 200mA, 20 keV, spectral range 5-35 keV, 2/3 filling mode, beam line control carried out with VME, SUN workstation. SPEC The radioactive samples were positioned in the glove box.

During this first series of shifts, we analysed 3 reference technetium compounds: [(CH₃)₄N]₂TcBr₆, K₃[Tc₂Cl₈]*2H₂O, NH₄TcO₄.

Preliminary results have been presented by posters:

- K. GUERMAN, T. REICH, C. SERGEANT, R. ORTEGA, V. TASAROV, M. SIMONOFF
Technetium metal and pyrometallurgically formed sediments study and speciation by Tc-NMR and EXAFS/XANES
OECD/NEA Workshop on pyrochemical separations, march 14-15, 2000, Villeneuve les Avignon, France
- M. SIMONOFF, K.E. GUERMAN, T. REICH, C. HENNIG, R. ORTEGA, C. SERGEANT, G. DEVES, M.H. VESVRES
Technetium speciation in radioactive wastes generated in pyrochemical reprocessing
2nd Euroconference and NEA workshop on speciation, techniques, and facilities for radioactive materials at Synchrotron light sources, september 10-12, 2000, Grenoble, France
- K.E. GUERMAN, T. REICH, C. SERGEANT, R. ORTEGA, V.P. TARASOV, M. SIMONOFF, G. SIMONOFF
Etude et speciation par RMN et EXAFS du Technétium métallique et de sels formés par voie pyrométallurgique
7^e Rencontres Nationales de Radiochimie, september 27-29, 2000, Saint Rémy les Chevreuse, France

	Experiment title:	Experiment number:
	EXAFS Measurement of Pu Hydrates	20-01-13
Beamline:	Date of experiment:	Date of report:
BM 20	from: 03.12.1999 to: 04.12.1999	11.03.2000
Shifts:	Local contact(s):	<i>Received at ROBL:</i>
4	T. Reich	11.03.2000
Names and affiliations of applicants (* indicates experimentalists):		
T. Reich*, G. Gelpel, H. Funke*, C. Hennig*, A. Roßberg*, G. Bernhard		
Forschungszentrum Rossendorf, Institute of Radiochemistry, P.O. Box 51019, D-01314 Dresden, Germany		

Report:

Experimental

Plutonium(VI) hydrate was prepared by dissolution of PuO₂ (Pu-242, AEA Technology, QSA GmbH) and electrochemical oxidation. Part of this solution was reduced to Pu(III) in an electrochemical cell. The Pu(III) and Pu(VI) hydrates were in perchloric and nitric media (1 M acidic solution), respectively. The final Pu concentration was 50 mol/L. The Pu oxidation states were confirmed by UV/vis spectroscopy. For the measurements 4.7 mL of solution (7.5 MBq) was filled and sealed in polyethylene cuvettes. The samples were measured at the Rossendorf Beamline ROBL at the European Synchrotron Radiation Facility (ESRF), Grenoble, France within 48 hours after their preparation.

Multiple scans of the Pu L_{III}-edge EXAFS were collected in transmission mode at room temperature using the Si(111) double-crystal monochromator in fixed-exit mode /1/. The energy scale was calibrated using the first inflection point of the absorption spectrum of a Zr foil (17998 eV). The scattering phases and amplitudes were calculated for hypothetical clusters of PuO_n and PuO₂O₅ using FEFF6.

Results

As one can see from the XANES spectra given in Fig. 1, the L_{III} absorption edge of Pu(VI) is shifted by 4 eV toward higher energy as compared to that of Pu(III). The energy shift and the distinct XANES features of these two Pu hydrates can be used for the determination of the Pu oxidation states /2/. The different electronic and molecular structures of Pu(III) and Pu(VI) hydrates are also reflected in the EXAFS shown in Fig. 2. The coordination sphere of Pu(III) hydrate can be written as Pu(H₂O)₈³⁺ with an average Pu-O bond distance of 2.48 Å. The Fourier transform corresponding to the EXAFS of Pu(VI) hydrate shows two coordination shells. The Pu(VI) forms a plutonyl ion PuO₂(H₂O)₄²⁺. The axial and equatorial Pu-O bond distances are 1.74 and 2.42 Å, respectively. The structural parameters of Pu(VI) hydrate are nearly identical to those of U(VI) and Np(VI) hydrates (see Tab. 1), which were measured recently at ROBL /3/.

Reference

- 1/ W. Matz et al., J. Synchrotron Rad., 6, 1076 (1999)
- 2/ S.D. Conradson et al., Polyhedron, 17, 599 (1998)
- 3/ T. Reich et al., Radiochim. Acta (accepted for publication).

Tab. 1: EXAFS structural parameters for 50 mMol/L Pu hydrates and comparison with 50 mMol/L Np(VI) and U(VI) hydrates.

Sample	Shell	R(Å)	N	σ^2 ^{a)}
Pu(III)	Pu-O	2.48	7.6(2)	1.02
Pu(VI)	Pu-O _{ax}	1.74	1.9	0.12
	Pu-O _{eq}	2.42	4.4(2)	0.50
Np(VI)	Np-O _{ax}	1.75	2.0	0.15
	Np-O _{eq}	2.42	4.6(2)	0.56
U(VI)	U-O _{ax}	1.76	1.9	0.12
	U-O _{eq}	2.41	4.9(2)	0.61

a) σ^2 in units of 10^{-2} Å²

Fig. 1: Pu L_{III}-edge XANES spectra Pu(III) and Pu(VI) hydrates.

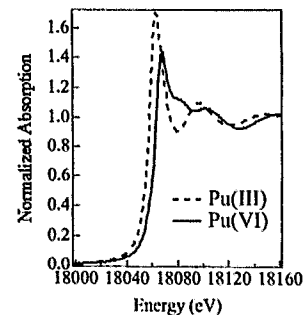
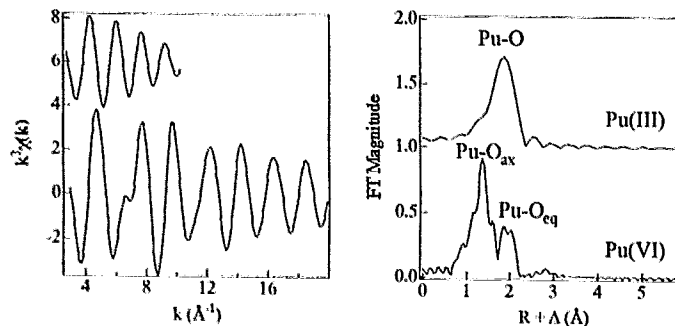
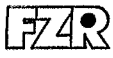


Fig. 2: Raw Pu L_{III}-edge k³-weighted EXAFS spectra (left) and corresponding Fourier transforms (right) of 50 mMol/L Pu hydrates. Solid line – theoretical fit; dots – experiment.



 ROBL-CRG	Experiment title: Interaction between bacteria and metals using EXAFS	Experiment number: 20_01_014
	Beamline: BM 20	Date of experiment: from: 19-02-2000 to: 21-02-2000
Shifts: 9	Local contact(s): Dr. Tobias Reich	Received at ROBL: 09-04-2001
Names and affiliations of applicants (* indicates experimentalists): M. Merroun*, S. Selenska-Pobell, H. Funke*, H. Moll*, C. Hennig*, T. Reich*, A. Rossberg* Institute of Radiochemistry FZR Dresden Germany		

Report:

The structural parameters of the uranium complexes formed at the surfaces of three *A. ferrooxidans* eco-types were studied, using extended X-ray absorption fine structure (EXAFS) spectroscopy. The EXAFS spectra demonstrated that the phosphorus or sulphur-containing residues of *A. ferrooxidans* cells are involved in interaction with uranium.

Sequence analysis of the 16S rRNA genes of several reference strains and uranium-mining waste-pile isolates of *A. ferrooxidans* revealed specific signatures which distinguish three types within the species /1/. These types differ in their capability to accumulate and tolerate uranium /2/.

In this study applying EXAFS spectroscopy, we analysed the nature of the uranium complexes formed at the cell surfaces of the three *A. ferrooxidans* types.

The samples were measured at the Rossendorf Beamline (ROBL) at the European Synchrotron Facility (ESRF), Grenoble, France. The samples studied were: Dry biomass samples of *A. ferrooxidans* W1, 33020 and D2, (a), (c) and (e), and wet paste samples of *A. ferrooxidans* W1, 33020 and D2, (b), (d) and (f), respectively. In all samples uranium is coordinated by two axial oxygen atoms (Oax) at a distance of 1.77-1.78 Å. The average distance between uranium and the equatorial oxygen atoms (Oeq) is 2.35 Å. The coordination number of Oeq is 5-6.

Using U-C and U-P phase and amplitude functions, the third and fourth peaks in the FT of *A. ferrooxidans* indicate a distance of 2.91 and 3.58 ± 0.02 Å, respectively. The latter is the same U-P bond distance as for the organic uranyl phosphate (U(VI)-ATP complex). But we do not exclude the possibility of implication of sulphur because these 2 elements (P and S) are close to each other in the periodic system of elements and EXAFS cannot distinguish between them. In addition, P (or S) is bonded in a monodentate mode to the uranyl ion. Bidentate bonding would result in

an atomic distance of approximately 3.2 Å. No structural differences were observed between the uranium complexes formed by the 3 types of *A. ferrooxidans*. However, the EXAFS spectra indicate a formation of uranium complexes different from those formed by Bacilli.

References

- /1/ Selenska-Pobell, S., et al., Antonie van Leeuwen-huek (in press).
 /2/ Merroun, M. and Selenska-Pobell, S. Biometals (in press).

SAMPLE	SHELL	N	R [Å]	σ^2 [Å ²]
a	U-O _{ax}	2 ^a	1.78	0.0014
	U-O _{eq}	4.7(5)	2.35	0.0071
	U-C	1.6(4)	2.92	0.0037 ^a
	U-P	0.9(3)	3.58	0.0070
b	U-O _{ax}	2 ^a	1.77	0.00126
	U-O _{eq}	5.4(5)	2.35	0.0089
	U-C	1.6(3)	2.92	0.002 ^a
	U-P	1.3(3)	3.56	0.007 ^a
c	U-O _{ax}	2 ^a	1.77	0.0015
	U-O _{eq}	4.5(4)	2.35	0.0076
	U-C	1.0(3)	2.92	0.004 ^a
	U-P	0.8(3)	3.59	0.008 ^a
d	U-O _{ax}	2 ^a	1.78	0.00127
	U-O _{eq}	5.1(5)	2.35	0.0082
	U-C	1.6(4)	2.90	0.0033 ^a
	U-P	0.9(4)	3.58	0.008 ^a
e	U-O _{ax}	2 ^a	1.77	0.00155
	U-O _{eq}	5.7(5)	2.35	0.0093
	U-C	1.2(4)	2.90	0.004 ^a
	U-P	1.4(3)	3.59	0.007 ^a
f	U-O _{ax}	2 ^a	1.77	0.00146
	U-O _{eq}	5.2(3)	2.35	0.0087
	U-C	1.4(2)	2.91	0.003 ^a
	U-P	1.0(1)	3.59	0.004 ^a

Tab. 1:
Structural parameters of the *A. ferrooxidans* uranium complexes

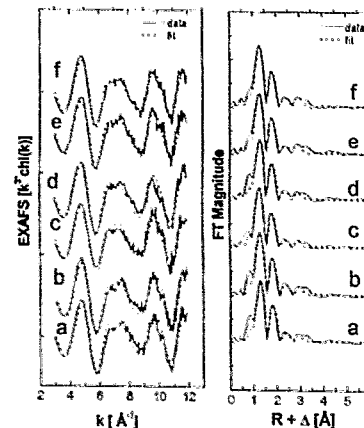



Fig.1:
Uranium L_{III}-edge k³-weighted EXAFS spectra (left) and corresponding FT (right) of the *A. ferrooxidans* uranium complexes

 ROBL-CRG	Experiment title: X-ray Absorption Spectroscopy investigations on environmental colloids (Fe matrix)- Interaction with heavy and hazardous elements (As, Pb)	Experiment number: 20_01_015
	Beamline: BM 20	Date of experiment: from: 23/02/2000 to: 28/02/2000 01/09/2000 03/09/2000
Shifts: 24	Local contact(s): Dr. Reich, Tobias	<i>Received at ROBL:</i> 27/03/2001
Names and affiliations of applicants (* indicates experimentalists): Henry Moll*, Tobias Reich*, Christoph Hennig*, Harald Funke*, Mohamed Merroun*, Andre, Roßberg* and Harald Zänker Institute of Radiochemistry, Forschungszentrum Rossendorf e.V., P.O. Box 510119, D-01314 Dresden, Germany		

Report:

Highly mineralised, red-coloured solutions are formed by weathering of ore particles which causes acid rock drainage (ARD). Major cationic components (>1 g/l) of the ARD solution under study were Zn, Fe, Mg, Al, and Mn. Important minor components were toxic heavy metals, e.g. As, Cu, Pb, and Cd. This XAS investigation deals with the in-situ characterisation of the near-order surrounding of As in ARD solutions containing colloidal particles as well as with the determination of the particle mineralogy.

Experimental. XAFS data were recorded at the Rossendorf Beamline (ROBL) at the ESRF in Grenoble. The data were treated using the EXAFSPAK software. Theoretical back-scattering phase and amplitude functions used in data analysis were calculated using FEFF6.

Table 1: Chemical analysis of the ARD samples.

Sample	Fe [M]	As [M]	[As]/[Fe]
Raw sample	0.080	5.2×10^{-3}	0.065
5 µm filtrate	0.070	4.8×10^{-3}	0.068
1 kD retentate	0.368	0.080	0.217
1 kD filtrate	0.054	1.4×10^{-3}	0.026
	Fe [mg/g]	As [mg/g]	
Precipitate	324	68	0.210

Results and Discussion. The Fe EXAFS data (not shown here) of the freshly formed colloids suggest that an amorphous Fe phase dominates the colloidal matrix. On the other hand, the EXAFS oscillation of the precipitate shows the presence of a more crystalline Fe phase. The data of the 5 µm filtrate indicate an intermediate between these two stages. The Fe-Fe distance of ~3.60 Å suggests a relatively close relationship between the ARD samples and the jarosite. Considering the REM/EDX analysis of particle agglomerates on a Nucleopore filter [1] and the EXAFS results, we assume that the colloidal particles represent an intermediate in the precipitate formation process having a mineralogy similar to that of the precipitate, i.e., consisting of H-jarosite and amorphous Fe phases. The As K-edge XANES data, the intensive white line and the As K-edge energies of 11875 eV indicate the +5 oxidation

state of As in all ARD samples. Fig. 1 depicts the EXAFS spectra measured at the As K-edge.

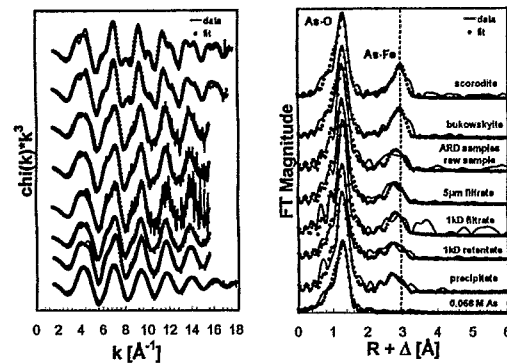


Fig. 1. Experimental EXAFS oscillations and corresponding Fourier Transforms of the model compounds and the ARD fractions at the As K-edge.


Table 2: Summary of the EXAFS structural parameters. In parenthesis XRD values [2].

Sample	Shell	N	R [Å]	σ^2 [Å ²]
Scorodite (mineral) FeAsO ₄ ·2H ₂ O	As-O	5.0 (4)	1.68 (1.68)	0.0027
	As-Fe	3.7 (4)	3.34 (3.33)	0.0048
Bukowskyite (mineral) Fe ₂ AsO ₄ SO ₄ OH ₃ 7H ₂ O	As-O	5.2	1.68	0.0025
	As-Fe	3.2	3.33	0.0042
ARD solution raw sample	As-O	4.3	1.69	0.0013
	As-Fe	2.2	3.28	0.0047
ARD solution (5 µm filtrate)	As-O	4.5	1.69	0.0017
	As-Fe	2.2	3.27	0.0046
ARD solution (1 kD filtrate)	As-O	4.4	1.68	0.0011
	As-Fe	1.9	3.26	0.0032
ARD solution (1 kD retentate)	As-O	4.7	1.69	0.0021
	As-Fe	2.5	3.29	0.0067
ARD solution, precipitate	As-O	5.0	1.68	0.0022
	As-Fe	4.5	3.28	0.0110
0.066 M As solution	As-O	5.2	1.68	0.0025

Taking the EXAFS results alone (Fig. 1, Tab. 2), one might draw the conclusion that arsenate interacts with the solid iron hydroxy sulfates in a similar way in all fractions. The pronounced As-Fe contribution at 3.28 Å (see Fig. 1) measured in the ARD raw sample and the different filtrates shows that arsenate is bound to the colloids (iron hydroxy sulfate) in a similar way to that of arsenate onto ferrihydrite, i.e., by inner-sphere surface complexation [3]. The picture is different for the precipitate. The relatively large arsenic content and the small particle surface of the precipitate make surface complexation unlikely. A better explanation is an epitaxial growth of a scorodite phase within/on the iron hydroxy sulfate. Relaxation processes of the As-Fe bond occurring in such small scorodite zones could explain the atypical As-Fe distance of 3.28 Å.

References

- [1] Zänker, H., et al., submitted to Appl. Geochem.(2001).
- [2] Hawthorne, F.C., Acta Cryst. B 32, 2891 (1976).
- [3] Waychunas, G.A., et al., Geochim. Cosmochim. Acta 57, 2251 (1993).

 ROBL-CRG	Experiment title: Structural investigations of uranium(VI) at different fluoride concentrations using EXAFS. A comparison between experiment and theory.	Experiment number: 20 01 017
	Beamline: BM 20	Date of experiment: on: 25/03/2000
Shifts: 3	Local contact(s): Dr. Reich, Tobias	<i>Received at ROBL:</i> 27/03/2001
Names and affiliations of applicants (* indicates experimentalists): Henry Moll ^a , Zoltán Szabó ^b , Tobias Reich ^a , Christoph Hennig ^a , Harald Funke ^a , Margret Rutsch ^a , Andre Roßberg ^a , Samer Amayri ^{a*} and Ingmar Grenthe ^b		
^a Institute of Radiochemistry, Forschungszentrum Rossendorf e.V., P.O. Box 510119, D-01314 Dresden, Germany ^b Inorganic Chemistry, Department of Chemistry, Royal Institute of Technology (KTH), S-100 44 Stockholm, Sweden		

Report:

Experimental. Appropriate aliquots of the U(VI) stock solutions were taken to obtain the 0.05 M test solutions B, C and D. Their fluoride concentrations, 0.21, 0.45 and 3.00 M, respectively, were adjusted by adding NaF (solutions B and C) or tetramethyl-ammonium fluoride (solution D). The $-\log[H^+]$ of the test solutions was adjusted using NaOH and/or HClO₄. EXAFS data were recorded at the Rossendorf Beamline (ROBL) at the ESRF in Grenoble. For energy calibration of the sample spectra, the spectrum from a Zr foil was recorded simultaneously. The ionization energy of the U L_{III} electron, E₀, was arbitrarily defined as 17 185 eV. The data were treated using the EXAFSPAK software developed by George and Pickering (1995) at SSRL. Theoretical backscattering phase and amplitude functions used in data analysis were calculated for the model complex UO₂F₄(H₂O)²⁻ and UO₂F₅³⁻ using the FEFF7 program. The MS path O-U-O (4 legged path) of the linear UO₂²⁺ unit was included in the model fitting.

Results and discussion. The EXAFS oscillations of U(VI) at different fluoride concentrations are similar (see Fig. 1). The uranyl sample in the acidic pH region shows a different pattern of the EXAFS oscillation [1]. The differences are more transparent in the FTs. There are two trends observable in the EXAFS data shown in Fig. 1. The first one is a pronounced lengthening of the uranium -"yl" oxygen distance and the second is a shortening of the U-(O_{eq},F) distance in fluoride containing test solutions, compared to the U(VI) aqua cation. Similar trends were found in alkaline uranyl systems [1-3] as well as in U(VI) oxide precipitates prepared at pH values above 7 [4]. The first co-ordination sphere, presumably fluoride, is stronger bonded to the uranyl center as the water ligands in the aqua ion shown by the distance of 2.26 Å.

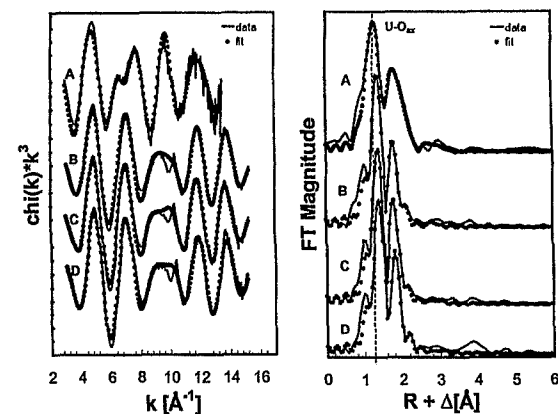



Fig. 1: U L_{III} -edge k^3 -weighted EXAFS data and corresponding FT's measured for (A) 0.05 M UO₂²⁺ in 0.1 M HClO₄, (B) 0.052 M UO₂²⁺ + 0.21 M F⁻ (pH=5.0), (C) 0.052 M UO₂²⁺ + 0.45 M F⁻ (pH=5.3), and (D) containing UO₂F₅³⁻. The solid line is the experimental data, and the dashed line represents the best theoretical fit of the data.

A main result of the EXAFS data evaluation was the improvement of the fit by including a third shell, in contrast to the tetrahydroxo uranyl complex at high pH [3]. It is very likely that the third shell represents coordinated water at a distance of 2.50 Å. The two equatorial shells interfere another and the fact that oxygen is a light backscatterer makes it difficult to estimate a precise value of the number of coordinated water. On the other hand the calculations showed that the number of ligands in the second shell can be determined within an error range of ± 0.5 . We used chemical information for the final refinement of the data. The speciation within the system is perfectly known from the literature [5]. And we used this chemical information and fixed the coordination numbers to the theoretical values. A further argument for fluoride as the second shell might be that similar U-F bond distances are reported for the solid-state structure of Na₄[(UO₂)₂(OCH₂COO)₂F₄] \times 6H₂O [6]. With increasing fluoride within the second coordination sphere of uranium, an increasing coordination number for fluoride was determined. The FT magnitude of sample D shows a peak at around 4.1 Å. This feature could result from MS pathways like U-O-F. But fit calculations including such contributions failed. Another explanation would be an U-U interaction. This is on the other hand not very likely because bridging fluoride is only known in solid state structures, not in solution. Furthermore, one would also expect that the bond distance U-F in the bridge to be substantially longer than in the non-bridged bonded fluorides. No such evidence is seen. The changes in distance of the second shell are within the error limit of this method.

References

- [1] Wahlgren, U., et al., J. Phys. Chem. A 103, 8257-8264 (1999).
- [2] Clark, D.L., et al., Inorg. Chem. 38, 1456-1466 (1999).
- [3] Moll, H., et al., Radiochim. Acta 88, 411 (2000).
- [4] Allen, P.G., et al., Radiochim. Acta 75, (1996) 47-53.
- [5] Grenthe, I., et al., in: Wanner, H. and Forrest, I. (eds.): *Chemical Thermodynamics of Uranium*, NEA OECD, Issy-les-Moulineaux, France (1992).
- [6] Farkas, I., et al., Acta Chim. Scand. 53, 1009-1012 (1999).

	Experiment title: The application of iterative transformation factor analysis for the decomposition of multicomponent EXAFS spectra of uranium(VI) complexes with acetic acid	Experiment number: 20_01_018
	Beamline: BM 20	Date of experiment: from: 26/03/00 to: 27/03/00
Shifts: 6	Local contact(s): C. Hennig, T. Reich, A. Rossberg	Received at ROBL: 05/04/2001
Names and affiliations of applicants (* indicates experimentalists): A. Rossberg* ¹ , T. Reich* ¹ , C. Hennig* ¹ , H. Funke* ² , G. Bernhard ² ¹ ROBL - CRG, ESRF, Avenue des Martyrs, B.P. 220, 38043 Grenoble Cedex, France ² Forschungszentrum Rossendorf e.V., Institut für Radiochemie, P.O. Box 510119, 01314 Dresden, Germany		

Report:

Experimental

Eight solutions were prepared with 0.05 mol/l U(VI) and 1.0 mol/l acetic acid under norm conditions. The pH was varied in the interval from pH 0.10 to pH 4.48. The ionic strength was 1.2 mol/l. Figure 1 shows the pH-speciation of the complexes according to stability constants from the literature [1]. The U L_{III}-edge EXAFS spectra were measured in transmission mode at ROBL.

Results and Discussion

The Eigenanalysis of the EXAFS spectra yields that only two pure spectroscopic components (factors) are necessary to describe the variance in the spectra. By employing the iterative transformation factor analysis (ITT), the relative concentrations (matrix C) and the EXAFS spectra (matrix R) of the two factors result. The measured spectra (matrix D) can be reproduced with two factors (Fig. 2, left). Therefore all complex species must consist of the fractions of the two isolated factors. Factor 1 consists of five equatorial oxygen atoms (O_{eq,1}) at a short distance (2.41 Å). Factor 2 consists of six equatorial oxygen atoms (O_{eq,2}) at a longer distance (2.46 Å) to the uranyl unit. The structural parameters from factor 1 are in agreement with those of the uranyl hydrate. For factor 2 the structural parameters indicate that the carboxylic groups of three acetate ligands are bidentate coordinated to the uranyl unit. The EXAFS spectra of the 1:1 and 1:2 uranyl acetates cannot be isolated since these complexes coordinate water and acetate simultaneously.

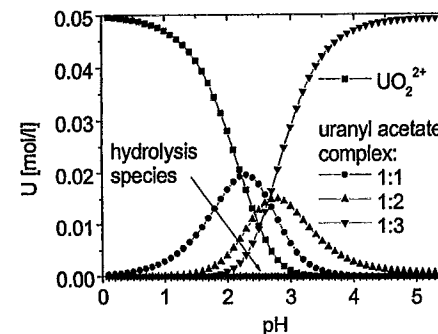


Fig. 1: Calculated pH-speciation (conditions: see experimental).

By multiplying the relative concentration of factors 1 and 2 by 5 and 6, respectively, one can plot the coordination numbers for O_{eq,1} and O_{eq,2} as a function of pH (Fig. 2, right). If one assume that 4 and 2 water molecules are coordinated in the 1:1 and 1:2 uranyl complexes then, the average O_{eq,1} and O_{eq,2} coordination numbers can be calculated from the speciation diagram (Fig. 1) for all pH values. The calculated values are in agreement with the experimental results (Fig. 2, right).

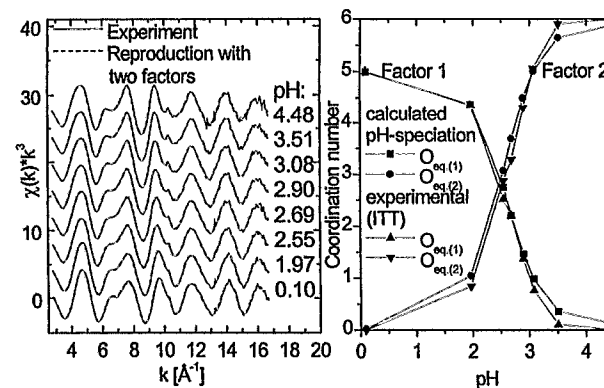



Fig. 2: The raw k^3 -weighted U L_{III}-edge EXAFS spectra and their reproductions with $D = RC$ (left). The result of the ITT and the calculated pH-speciation (right).

References

[1] Ahrlund, S., Acta Chemica Scandinavica 5, 199 (1951)

 ROBL-CRG	Experiment title: EXAFS measurements at low temperature	Experiment number: 20_01_019
	Beamline: BM 20	Date of experiment: from: 29/03/00 to: 01/04/00 on: 10/05/00
Shifts: 14	Local contact(s): C. Hennig	<i>Received at ROBL:</i> 26/03/2001
Names and affiliations of applicants (* indicates experimentalists): C. Hennig*, M. Rutsch*, T. Reich*, H. Funke*, A. Roßberg*, S. Amyri*, S. Tsushima*, ^{a)} Forschungszentrum Rossendorf e.V., Institute of Radiochemistry, D-01314 Dresden a) University of Tokyo, Dept. Quantum Engineering System Sci., Tokyo, Japan		

Report:

The aim of these low temperature measurements is to obtain structural information on solid uranium compounds using EXAFS. The analysis of structural differences between $\text{Cu}[\text{UO}_2\text{AsO}_4]_2 \cdot 12\text{H}_2\text{O}$ and $\text{Cu}[\text{UO}_2\text{AsO}_4]_2 \cdot 8\text{H}_2\text{O}$ serves as an example. Sample **1** is obtained by synthesis and consists of pure $\text{Cu}[\text{UO}_2\text{AsO}_4]_2 \cdot 12\text{H}_2\text{O}$. The structure contains two symmetry-inequivalent Cu positions. In the EXAFS analysis, only one Cu atom position is considered, because the second one has only an occupation factor of 0.075 [1]. Sample **2** is a natural meta-zeunerite mineral. This structure contains one symmetry-independent Cu atom position [1]. The powdered sample contains 14% $\text{Cu}[\text{UO}_2\text{AsO}_4]_2 \cdot 12\text{H}_2\text{O}$. However, the EXAFS is dominated by the scattering contribution of $\text{Cu}[\text{UO}_2\text{AsO}_4]_2 \cdot 8\text{H}_2\text{O}$. Due to the damping of thermal oscillations at 15K, a lot of backscattering shells occur in the Fourier transform (FT). To simplify the data analysis, the FT between $R+\Delta=5.5\text{-}10\text{\AA}$ was Fourier filtered, back transformed and subtracted from raw EXAFS data of each spectrum. The $[\text{Cu}(\text{H}_2\text{O})_4]^{2+}$ group causes dominant FT peaks with Cu-O distances of 1.94Å for sample **1** and **2**. Sample **1** shows one Cu-U peak at a distance of 4.22Å. A strong Cu-U-O_{ax}-Cu MS contribution appears because the involved atoms are arranged linearly. This observation points to a highly symmetric arrangement of the $[\text{UO}_2\text{AsO}_4]_\infty$ layers concerning Cu.

	Shell	R [Å] ^a	N ^b	σ^2 [Å ²]	ΔE_0 [eV]
1	Cu-OW	1.94	3.1(2)	0.0016	-4.4
	Cu-O _{ax}	2.46	1.1(2)	0.0016**	
	Cu-U	4.22	1.3(5)	0.0013	
	Cu-U _{MS}	4.22**	2.7**	0.0026**	
2	Cu-OW	1.94	2.4(1)	0.0018	-13.9
	Cu-O _{ax}	2.46	1.2(1)**	0.0018**	
	Cu-U1	4.04	0.8(1)	0.002*	
	Cu-U2	4.52	0.7(1)*	0.002*	
	Cu-As	4.84	1.6(2)	0.002*	

Tab. 1: EXAFS structural parameters

^aErrors in distances R are ± 0.02 Å, ^berrors in coordination numbers N are ± 25 % with standard deviations in parentheses, *value fixed during the fit, **dependent from the previous variable

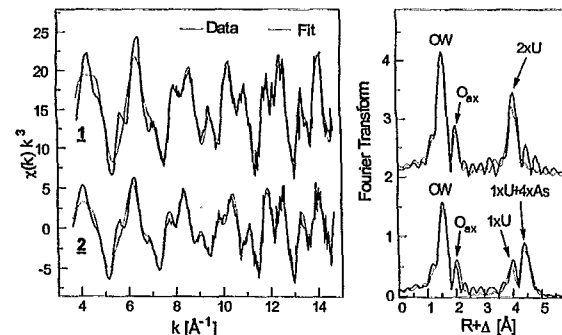



Fig. 1: Cu K-edge k^3 -weighted EXAFS spectra (left) and corresponding Fourier transform (right) for sample **(1)** and **(2)** at $T = 15$ K.

In contrast, the spectrum of sample **2** shows two FT peaks in that region. The first peak is originated by one uranium atom in a distance of 4.04Å. The second peak consists of arsenic atoms in a distance of 4.84Å and one uranium atom in a distance of 4.52Å. These observations indicate that in meta-zeunerite one $[\text{UO}_2\text{AsO}_4]_\infty$ layer is arranged closer to the Cu atom.

References

[1] Hennig et al., unpublished

 ROBL-CRG	Experiment title: Experiments to test the SPLICE program using real EXAFS spectra	Experiment number: 20_01_20
	Beamline: BM 20	Date of experiment: from: 02. 04. 2000 to: 03. 04. 2000
Shifts: 6	Local contact(s): T. Reich	<i>Received at ROBL:</i> 10.04.2001
Names and affiliations of applicants (* indicates experimentalists): Harald Funke ^{1*} , Horst Böttger ² , Tobias Reich ^{1*} , Christoph Hennig ^{1*} , André Rossberg ^{1*} Forschungszentrum Rossendorf e.V., 01314 Dresden, Postfach 510119, Germany ¹ Institute of Radiochemistry ² Department Communication and Data Processing		

Report:

During the first commissioning experiments with the cryostat in autumn 1999, sometimes the technical problem arose that it was impossible to get one continuous EXAFS scan over a wide k range. In spite of the fact that this situation was overcome, the idea of connecting two different parts of an EXAFS scan in a unique way was developed. So, the computer program SPLICE was written to merge two different EXAFS spectra of the same sample in an overlapping energy region. The word "splice" was chosen because of the analogy to the old sailing trade "splicing". The SPLICE program may be a useful tool to overcome difficulties due to insufficient time during an EXAFS experiment. Different situations may cause such time problems, e.g.:

- Any interruption or perturbation of the synchrotron beam,
- The refill times are too frequent for the experiment,
- Only the noisy part (in general the rear part of the spectrum) needs some repetitions for an amendment of the statistics of the EXAFS scan.

Two raw EXAFS scans of the same sample, F_1 and F_2 , are given. Both sets are recorded at different energy regions with an overlapping region of about 50 data points. The intention of the program is to find an optimal translation for F_2 (concerning x and y) and a re-calibration factor λ for "splicing" both scans together to handle them like **one continuous scan**. Experiments were performed to test the SPLICE program using real EXAFS spectra up to a k of 22 \AA^{-1} at the L_{III} edge of a uranyl arsenate sample $(H_2[UO_2AsO_4])_2 \cdot 8H_2O$.

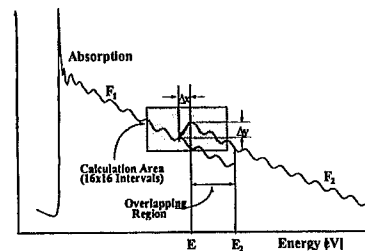


Figure 1. Schematic illustration of the task of the program SPLICE

The final range of the parameters found is usually:

$$|\Delta x| < 1 \text{ eV},$$

$$|\Delta y| < 0.005,$$

$$|\lambda - 1| < 0.001$$

To reduce thermal vibrations, the sample was cooled to 15 K using a closed-cycle He cryostat.

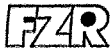
Three different EXAFS spectra, their Fourier transforms and fit-results were compared. The first two spectra consist of two different scans connected by the program SPLICE, and the third spectrum consists of one uninterrupted continuous scan.

- Splice A: Two absorption spectra, both scanned with an equal step in k -space of $\Delta k = 0.05 \text{ \AA}^{-1}$ are spliced at $k = 15 \text{ \AA}^{-1}$ to give an EXAFS-spectrum with a length of $k = 22 \text{ \AA}^{-1}$.
- Splice B: Two absorption spectra, the first scanned with an equal step in k -space of $\Delta k = 0.05 \text{ \AA}^{-1}$ and the second with an equal step of $\Delta k = 0.02 \text{ \AA}^{-1}$ are spliced at $k = 15 \text{ \AA}^{-1}$ to give an EXAFS spectrum with a length of $k = 22 \text{ \AA}^{-1}$ as demonstration of the ability of the SPLICE program to connect two scans recorded with different steps in k -space.
- Without splicing C: For comparison with the spliced spectra, one entire spectrum was recorded over the whole range of $k = 22 \text{ \AA}^{-1}$ with an equal step of $\Delta k = 0.05 \text{ \AA}^{-1}$.

Table 1. As example: fitted co-ordination numbers and distances of the three test spectra (see text) for the five relevant co-ordination shells.

Coord. shell	N			R [Å]		
	A	B	C	A	B	C
Oax	1.94(0.11)	2.05(0.10)	1.82(0.10)	1.789(0.003)	1.791(0.002)	1.790(0.002)
Oeq	4.65(0.26)	4.31(0.22)	4.76(0.25)	2.296(0.003)	2.306(0.002)	2.302(0.003)
As	3.99(0.17)	4.15(0.15)	3.90(0.15)	3.702(0.001)	3.700(0.001)	3.702(0.001)
U1	5.88(0.67)	5.16(0.49)	5.32(0.57)	5.402(0.003)	5.400(0.002)	5.400(0.003)
U2	4.61(1.16)	5.88(1.17)	5.92(1.32)	7.191(0.006)	7.181(0.004)	7.180(0.005)

Significant differences are not visible between the graphs of the three spectra. For comparison, table 1 shows the numerical values of the fitted data including the standard deviations. The differences between the fit results have the same order as the usual experimental uncertainties of EXAFS measurements. Therefore, the possibility to connect two different absorption spectra of the same sample with an overlapping energy region using the program SPLICE is demonstrated by examples.

 ROBL-CRG	Experiment title: Interaction between bacteria and metals using EXAFS	Experiment number: 20_01_21
	Beamline: BM 20	Date of experiment: from: 13.05.2000 to: 14.05.2000
Shifts: 6	Local contact(s): Dr. T. Reich	Received at ROBL: 09.04.2001
Names and affiliations of applicants (* indicates experimentalists): S. Scelenska-Pobell, J. Raff, T. Reich*, C. Hennig*, H. Funke*, A. Roßberg* Forschungszentrum Rossendorf e.V., Institute of Radiochemistry, D-01314 Dresden		

Report:**Introduction**

Surface layers (S-layer) are highly ordered protein layers on the surface of many bacteria and possess a high potential to bind metals. In this work interactions between Pt- and Pd-nanoclusters and the S-layer protein of the uranium waste pile isolate *Bacillus sphaericus* JG-A12 and the reference strain *B. sphaericus* NCTC 9602 were studied to identify the chemical groups of the protein which were responsible for the binding of the metal nanoclusters. Additionally the nanocluster formation during reduction of the metals should be confirmed. The latter was demonstrated with HR-TEM examinations.

Experimental procedure for EXAFS sample preparation

The S-layer samples (with a protein content of 3.9-9.3mg/ml in 50mM $\text{KH}_2\text{PO}_4/\text{Na}_2\text{HPO}_4$, 3mM NaN_3 , 1mM MgCl_2 pH 7.5) were prepared by adding a 24h


old 30mM K_2PtCl_4 and K_2PdCl_4 solution and incubation for 24h in darkness. Using dialysis and centrifugation the protein with bound metal nanoclusters was separated from surplus K_2PtCl_4 - or K_2PdCl_4 -solution, resuspended in water, dried in a vacuum incubator and grounded. Assuming that 50% of K_2PtCl_4 or K_2PdCl_4 was reduced to Pt or Pd clusters, 2 to 8 mg platinum or palladium should be bound to the S-layer. Reference samples were prepared with 50mM $\text{KH}_2\text{PO}_4/\text{Na}_2\text{HPO}_4$, 3mM NaN_3 , 1mM MgCl_2 pH 7.5 buffer instead of a protein buffer solution

EXAFS measurement

The EXAFS measurements were carried out at the Rossendorf Beamline (ROBL). Platinum L_{III}-edge and Palladium K-edge X-ray absorption spectra of the dry samples were collected in transmission and fluorescence mode.

Results

In all Pd samples the Fourier transformation (FT) of the first dominating peak shows a amplitude function, which is typical for oxygen or nitrogen. Using Pd-O phase and amplitude functions, the FT gives a distance of $1.99\text{-}2.02 \pm 0.02 \text{ \AA}$ for the Pd-S-layer samples. This bond length is in good agreement with the distance between palladium and oxygen in PdO (2.018 \AA). The reference sample of pure Pd-clusters shows an additional peak at a distance of $3.06 \pm 0.02 \text{ \AA}$ originated by Pd-Pd interaction. The equivalent but less distinctive peak the Pd-S-layer samples give distances of $3.03\text{-}3.04 \pm 0.02 \text{ \AA}$. This distance differs significantly from the distance expected for the Pd metal ($R=2.758 \text{ \AA}$), but is in good agreement with the Pd-Pd distance in PdO ($R=3.03 \text{ \AA}$). For this reason the dominating species in all samples seems to be oxidized. The latter makes it difficult to get information about the chemical groups, which are responsible for binding of the metal clusters. For the Pt samples similar results are obtained with the exception, that there is no clear Pt-Pt interaction.

	Experiment title: Neptunium(IV) Humate Complexation Studied by XAFS Spectroscopy	Experiment number: 20_01_022 (a)
	Beamline: BM 20	Date of experiment: on: 30/09/00
Shifts: 3	Local contact(s): Tobias Reich	<i>Received at ROBL:</i> 22.03.2001
Names and affiliations of applicants (* indicates experimentalists): K. Schmeide*, S. Pompe*, T. Reich*, C. Hennig*, H. Funke*, A. Roßberg*, T. Ye. Zayarnaya ^{a)} , G. Geipel, V. Brendler, K.H. Heise, G. Bernhard Forschungszentrum Rossendorf e.V., Institute of Radiochemistry, P.O.Box 510 119, D-01314 Dresden, Germany a) Institute of Metal Physics, Russ. Acad. Sci., Ekaterinburg, Russia		

Report:

For the first time, structural parameters of the near-neighbor surrounding of Np(IV) sorbed onto natural and synthetic humic and fulvic acids (HA, FA) were determined at pH 1 by XAFS spectroscopy. Bio-Rex70 was used as reference substance for humic substances.

Experimental: The Np loading of the wet pastes prepared at pH 1 from Aldrich HA (AHA), Kranichsee FA (KFA), synthetic HA type M42, and Bio-Rex70 (from Bio-Rad) was between 4 and 41 mg Np per g sorbent /1/. The samples were measured in transmission mode at the Rossendorf Beamline at the ESRF in Grenoble.

Results: The tetravalent oxidation state of Np and its stability in the humate and Bio-Rex70 complexes within the time of our experiment is verified by XANES spectroscopy. In Fig. 1, the XANES spectrum of Np(IV)-AHA is shown in comparison to that of the corresponding Np(V) sample. The spectrum of Np(IV) humate shows the characteristic near-edge features of Np(IV) compounds: A more intense 'white line' peak, but no additional shoulder on the high energy side of the peak as generally observed for Np(V) samples.

The Np L_{III}-edge k³-weighted EXAFS spectra of the Np(IV) samples and the corresponding Fourier transforms (FTs) are shown in Fig. 2 (solid lines: experiment, dashed lines: fit). Both the EXAFS oscillations and the FTs of all Np(IV) complexes are similar. The structural parameters are given in Tab. 1.

In the Np(IV) humate complexes, the Np ion is surrounded by about 11 oxygen atoms at a distance of 2.36 Å. Similar parameters are determined for the Np(IV) complex with Bio-Rex70, which has solely carboxylic groups as metal binding functional groups. This verifies that in the humate complexes predominantly the carboxylic groups are responsible for binding Np ions at pH 1. This was expected.

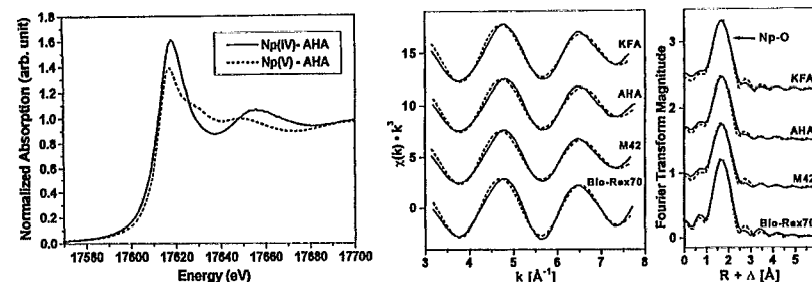


Fig. 1: Normalized Np L_{III}-edge XANES spectra.

Fig. 2: Raw Np L_{III}-edge k³-weighted EXAFS spectra and corresponding FTs of Np(IV) samples.

Tab. 1: Structural parameters of Np(IV) samples

Sample	Shell	N	R [Å]	σ ² [Å ²]
Np(IV)-KFA	Np-O	11.3±1.7	2.36	0.0162
Np(IV)-AHA	Np-O	10.1±1.7	2.36	0.0159
Np(IV)-M42	Np-O	11.0±1.7	2.36	0.0166
Np(IV)-Bio-Rex70	Np-O	10.2±1.3	2.37	0.0127
Np(IV) in 1 M HCl /2/	Np-O	11.2±1.1	2.40	0.0075
Np(IV) in 2 M H ₂ SO ₄ /3/	Np-O	11±1	2.39	0.0118
	Np-S	2.2±0.9	3.07	0.0070


ΔE₀ = -11.1 eV; R ± 0.01 Å; The 95 % confidence limits are given for N and R as estimated by EXAFSPAK.

Compared to the hydrated Np(IV) ion in hydrochloric or sulfuric medium /2,3/, the coordination number of the humates is similar, only the Np-O bond length is shortened by about 0.04 Å due to humate complexation. Since no carbon atoms of the binding humic acid carboxylate groups could be detected, it is not possible to determine separate coordination numbers for carboxylate groups and water molecules coordinated to Np by EXAFS analysis. To identify the binding mode of the carboxylate groups, the bond distances of the Np(IV) humates are compared to those of Np(IV) model compounds which contain carboxylic groups. The results show that the bond distance of the Np(IV) humates is smaller than found for bridging and chelate forming carboxylate groups in Np(IV) oxalate (R=2.39 Å, 2.51 Å) /4/ or for bidentate binding carboxylate groups in Np(IV) formate (R=2.50 Å) /5/. We conclude that humic acid carboxylate groups are predominantly monodentately bound to Np(IV) ions. This has to be verified by future studies with further Np(IV) model compounds.

Acknowledgment: This work was supported by the BMWi (no. 02 E 9299).

References:

- Schmeide, K., et al., Proceedings of Internat. Conf. Actinide-XAS-2000, Grenoble, France, in press;
- Allen, P.G., et al., Inorg. Chem. 36, 476 (1997);
- Reich, T., et al., Radiochim. Acta 88, 633 (2000);
- Grigor'ev, M.S., et al., Radiokhim. 39, 419 (1997);
- Hauck, J., Inorg. Nucl. Chem. Lett. 12, 617 (1976).

	Experiment title: EXAFS Study of the Np(V) Complexation by Humic Acids In Neutral Solution	Experiment number: 20_01_022 (b)
	Beamline: BM 20	Date of experiment: from: 24/06/00 to: 26/06/00
Shifts: 9	Local contact(s): Tobias Reich	<i>Received at ROBL:</i> 26.03.01
Names and affiliations of applicants (* indicates experimentalists): S. Pompe*, K. Schmeide*, T. Reich*, C. Hennig*, H. Funke*, A. Roßberg*, G. Geipel, V. Brendler, K.H. Heise, G. Bernhard Forschungszentrum Rossendorf e.V., Institute of Radiochemistry, P.O. Box 510 119, D-01314 Dresden, Germany		

Report:

Structural parameters for Np(V) humic acid (HA) complexes were determined by EXAFS. For the first time, the influence of phenolic OH groups on the Np(V) complexation by HA was studied with a chemically modified HA and Bio-Rex70, a cation exchange resin having only carboxyl groups as proton exchanging sites.

Experimental: Np(V) complexes were prepared from natural HA Aldrich (AHA), modified Aldrich HA with blocked phenolic OH groups (AHA-PB) /1/, synthetic HA type M42, and Bio-Rex70 from Bio-Rad. The phenolic OH group content of AHA and AHA-PB amounts to 3.1 and 1.1 meq/g. Np(V) humate solutions were prepared under N₂ at pH 7 with Np and HA concentrations of 0.88-0.90 mmol/L and of 8.1-10.8 g/L, respectively (0.1 M NaClO₄). The formation of Np(V) humate complexes was verified by NIR absorption spectroscopy. In addition, Np(V) was sorbed onto Bio-Rex70 at pH 7 (0.1 M NaClO₄). The sorbate had a loading of 121.3 mg Np/g Bio-Rex70. The Np(V) humates were studied in form of solutions, the Bio-Rex70 sorbate in form of a wet paste. Np L_{III}-edge EXAFS spectra were recorded at ROBL at room temperature in fluorescence mode (Np(V) humates) and in transmission mode (Np(V)-Bio-Rex70).

Tab. 1: EXAFS structural parameters of Np(V) samples.
(95 % confidence limits are given for N and R).

Sample	Np-O _{ax}			Np-O _{eq}			ΔE ₀ (eV)
	N	R(Å)	σ ²	N	R(Å)	σ ²	
Np(V)-AHA	2	1.84 ± 0.01	0.0035	2.9 ± 0.7	2.48 ± 0.01	0.0047	-7.8
Np(V)-AHA-PB	2	1.85 ± 0.01	0.0034	2.8 ± 0.8	2.49 ± 0.01	0.0054	-8.0
Np(V)-M42	2	1.84 ± 0.01	0.0048	3.3 ± 0.9	2.48 ± 0.01	0.0078	-8.8
Np(V)-Bio-	2	1.85 ± 0.01	0.0034	2.9 ± 0.5	2.50 ± 0.01	0.0046	-8.2
NpO ₂ (H ₂ O) _x ⁺ /2/	1.9 ± 0.2	1.822 ± 0.003	0.0023	3.6 ± 0.6	2.488 ± 0.009	0.006	

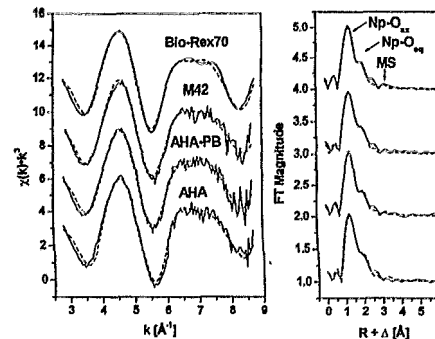


Fig. 1: Np L_{III}-edge k³-weighted EXAFS spectra and corresponding FT of Np(V) samples. Solid lines: experiment, dashed lines: fit, MS: multiple scattering along the NpO₂⁺ unit.


Results and discussion: The Np L_{III}-edge k³-weighted EXAFS oscillations and their Fourier transforms (FT) are shown in Fig. 1. The EXAFS oscillations were fitted to the EXAFS equation using a model with two Np coordination shells containing oxygen as backscatterer and including multiple scattering along the NpO₂⁺ unit. The axial coordination number was held constant at 2 during the fit. The data are shown in Tab. 1.

Independent of the HA origin and their functionality, the axial (ax) and equatorial (eq) coordination numbers (N) and Np-O bond lengths (R) for all Np(V) humates are comparable with each other as well as with the data of Np(V)-Bio-Rex70. Due to the fact that the Np(V) humates of AHA-PB and AHA show comparable structural parameters it can be concluded that the blocking of humic acid phenolic OH groups has no influence on the local structure around Np in the Np(V) humates. Since Bio-Rex70 solely has carboxyl groups as proton exchanging sites, similar coordination numbers and bond lengths of Np(V) humates and Np(V)-Bio-Rex70 indicate that carboxylate groups dominate the interaction between Np(V) and HA at pH 7. However, a contribution of phenolic OH groups to the interaction between HA and Np(V) cannot completely be excluded, because the EXAFS results are average values over all interactions between HA and Np(V). There is the possibility that phenolic OH groups interacting with Np(V) show equatorial bond lengths similar to those of carboxylate groups. The equatorial Np-O bond lengths (R_{Np-Oeq}) of the humates are comparable with R_{Np-Oeq} of monodentate coordinated carboxylate groups in a Np(V) malonate complex /3/. Due to the fact that R_{Np-Oeq} of the humates are also comparable with R_{Np-Oeq} of NpO₂(H₂O)_x⁺ (Tab. 1) /2/, a differentiation between monodentate coordinated carboxylate groups and water molecules is not possible. A predominant bidentate coordination of humic acid carboxylate groups to Np(V) can be excluded. R_{Np-Oeq} of 2.60 ± 0.04 Å was found for bidentate coordinated carboxylate groups in a Np(V) formate complex /4/.

Acknowledgment: This work was supported by BMWi under contract no. 02E9299.

References:

- 1/ Pompe, S. et al., Radiochim. Acta 88, 553 (2000).
- 2/ Reich, T. et al., Radiochim. Acta 88, 633 (2000).
- 3/ Grigoriev, M.S. et al., Radiokhim. 4, 24 (1993).
- 4/ Grigoriev, M.S. et al., J. Neorgan. Chim. 39, 1328 (1994).

	Experiment title: Th(IV) Complexation by Humic Acids Studied by EXAFS	Experiment number: 20_01_022 (c)
	Beamline: BM 20	Date of experiment: from: 30/08/00 to: 31/08/00
Shifts: 6	Local contact(s): Tobias Reich	<i>Received at ROBL:</i> 26.03.01
Names and affiliations of applicants (* indicates experimentalists): S. Pompe, K. Schmeide, T. Reich*, C. Hennig*, H. Funke*, A. Roßberg*, H. Moll*, K.H. Heise, G. Bernhard Forschungszentrum Rossendorf e.V., Institute of Radiochemistry, P.O. Box 510 119, D-01314 Dresden, Germany		

Report:

Structural parameters of a Th(IV) complex with natural humic acid (HA) from Aldrich were determined by EXAFS. The results were compared to those obtained for Th(IV) sorbed onto Bio-Rex70, a cation exchange resin having only carboxyl groups as proton exchanging sites. In addition, we compared our results with EXAFS data for the HA and Bio-Rex70 interaction with Th(IV) /1/ and Np(IV) /2/, respectively, as well as with data of Th(IV) hydrate /3/ and carboxylates /4/.

Experimental: Aldrich HA (AHA) and pre-equilibrated Bio-Rex70 from Bio-Rad were suspended in 0.1 M HClO₄. After addition of a 0.052 M Th(IV) stock solution the pH was adjusted to pH 1 and the suspensions were stirred for 48 h. The separated Th(IV) sorbates were studied in form of wet pastes. The resulting loadings were 41 mg Th/g AHA and 2 mg Th/g Bio-Rex70. Th L_{III}-edge EXAFS spectra were recorded at room temperature in fluorescence mode at ROBL.

Results and discussion: Fig. 1 shows the Th L_{III}-edge k³-weighted EXAFS oscillations and their corresponding Fourier transforms (FT). The EXAFS oscillations and FT are comparable for both samples. The FT are dominated by a peak which represents oxygen atoms coordinated to Th(IV). The EXAFS oscillations were fitted to the EXAFS equation involving one coordination shell of Th with oxygen as backscatterer. The obtained structural data are summarized in Tab. 1. Th(IV)-AHA and Th(IV)-Bio-Rex70 show comparable coordination numbers (N) and Th-O bond lengths (R). In both samples Th(IV) is surrounded by 11 oxygen atoms at a distance of 2.44 Å. Since Bio-Rex70 solely shows carboxyl groups as proton exchanging sites we conclude that under the applied experimental conditions the interaction between AHA and Th(IV) is dominated by humic acid carboxyl groups, as expected for pH 1. However, the higher EXAFS-Debye-Waller factor, σ², for the oxygen coordination shell of Th(IV)-AHA compared to Th(IV)-Bio-Rex70 and Th⁴⁺(aq) indicates a greater bond lengths distribution in Th(IV)-AHA.

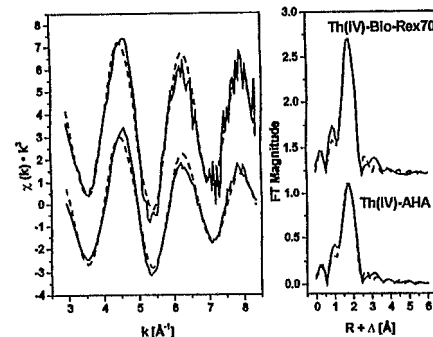


Fig. 1: Th L_{III}-edge k³-weighted EXAFS spectra and their corresponding FT. Solid lines: experiment, dashed lines: fit.

Tab. 1: EXAFS structural parameters in comparison to literature data. (95 % confidence limits for N and R).


Sample	Th-O			ΔE ₀	Ref.
	N	R (Å)	σ ²		
Th(IV)-AHA	10.6 ±	2.44 ± 0.01	0.013	-17.3	
Th(IV)-	11.0 ±	2.45 ± 0.02	0.009	-17.3	
Th(IV)-AHA	10.1	2.43	0.013	1.0	/1/
Th(IV)-	9.4	2.44	0.012	1.0	/1/
Th ⁴⁺ (aq)	10.8 ±	2.45 ± 0.01	0.007	4.0	/3/

Within the experimental error, the obtained results agree with those determined by Denecke et al. /1/. Coordination number and bond length of Th(IV)-AHA are comparable with those reported for Th⁴⁺(aq) /3/. That means that the interaction of Th(IV) with humic acid carboxyl groups induces no shortening of the Th-O bond lengths. Thus, a differentiation between coordinated water molecules and carboxylate groups of the HA is not possible. To identify the predominant binding mode of carboxylate groups onto Th(IV), the Th-O bond length is compared to those of Th(IV) model compounds. Monodentate coordinated carboxylate groups in different Th(IV) malonates /4/ show Th-O bond distances between 2.337 Å and 2.469 Å. The obtained bond length of 2.44 Å for Th(IV)-AHA lies in this range, indicating a predominantly monodentate coordination of humic acid carboxylate groups. The comparison of the Th(IV) data with those for the interaction of Np(IV) with AHA and Bio-Rex70 /2/ shows, that both tetravalent actinides are coordinated by about 11 oxygen. However, the Np-O bond distance is shorter (R=2.36±0.01 Å) than the Th-O bond length. The bond length difference (0.08 Å) is close to the difference of the effective ionic radii of Th⁴⁺ and Np⁴⁺ in aqueous solution (0.06±0.02 Å) /5/.

Acknowledgment: This work was supported by BMWi (no. 02E9299).

References:

- /1/ Denecke, M.A. et al., J. Synchr. Rad. 6, 394 (1999).
- /2/ Schmeide, K. et al., this report.
- /3/ Moll, H. et al., Inorgan. Chem. 38, 1795 (1999).
- /4/ Zhang, Y.-J. et al., Polyhedron 19, 1757 (2000).
- /5/ Neck, V. et al., Radiochim. Acta 89, 1 (2001).

 ROBL-CRG	Experiment title: Application of EXAFS to technetium speciation in pyrometallurgy reprocessing of spent nuclear fuel and in sulfur-rich environmental samples. Part 1. Technetium in chloride system.	Experiment number: 20_01_23 EU-R06
Beamline: BM 20	Date of experiment: from: 21/06/2000 to: 23/06/2000	Date of report: 19/03/2001
Shifts: 9	Local contact(s): T. Reich	Received at ROBL: 30/03/2001
Names and affiliations of applicants (* indicates experimentalists): Simonoff M.*, CNRS-UMR 5084, Le Haut Vigneau, B.P. 120, F33175 Gradignan Cedex, France Guerman K.*, CNRS-UMR 5084, Le Haut Vigneau, B.P. 120, F33175 Gradignan Cedex, France Reich T.*, FZR, Institute for Radiochemistry, Dresden, Germany Hennig C.*, FZR, Institute for Radiochemistry, Dresden, Germany Deves G.*, CNRS-UMR 5084, Le Haut Vigneau, B.P. 120, F33175 Gradignan Cedex, France Vesvres M.H.*, CNRS-UMR 5084, Le Haut Vigneau, B.P. 120, F33175 Gradignan Cedex, France		

Report:

EXAFS is one of most promising methods to enable us with speciation of radioactive nuclides. It is important to use it for Tc speciation in pyrometallurgy which is now considered the alternative approach to reprocessing of nuclear fuel. The associated study of long-lived fission products forms the basis for its non-hazardous treatment in radioactive wastes. During pyrometallurgical reprocessing, technetium can remain in the molten salt or enter either the sedimented phase contaminating Pu enriched phase, either electrodeposited U phase. Our preliminary results show that under some conditions Tc can also form several oxydes, oxychlorides and chlorides of different but rather high volatility, turning on an important polluting risk for gas-off treatment. As the data on EXAF spectra of technetium is now very fragmentary and do not present the whole of the species possible in the pyrometallurgy conditions, it is of high importance to carry synthetic work to supply a large set of technetium compounds in the closed containers which will meet the ESRF/ROBL security and quality demands, radioactivity level, special requirements on sample size, thickness, sample homogeneity. The chemical part of the work is planned to be carried out in Laboratory of radioanalytical and bioenvironmental chemistry, UMR5084, Gradignan. It includes the construction of pyrometallurgical reactors for the treatment of radioactive technetium samples in molten salts permitting to separate the truly dissolved, as well as sediments and sublimates.

The first part of the program deals with the pyrochemical behavior of technetium under reducing conditions. It comprises a set of samples with 13 reference technetium compounds (2 chlorides, 2 bromides, 2 pertechnetates, 2 sulfides, 5 Tc alloys) and


some samples of simulated pyrometallurgically reprocessed nuclear fuel including technetium hexachlorides in fused salts, and Tc precipitated fraction from sulfur-rich environmental fresh water lake sediments with the only Tc as a radionuclide. These samples were studied by means of EXAFS spectroscopy at the Radiochemistry Hutch of ROBL providing with beamsizes of 3 x 20 mm², integrated flux at sample 6 x 10¹¹ /s, 200mA, 20 keV, spectral range 5-35 keV, 2/3 filling mode, beam line control carried out with VME, SUN workstation. A glove box was used for radioactive sample positioning.

During this series of shifts, we analysed 7 reference technetium compounds and 2 samples of simulated pyrometallurgically reprocessed nuclear fuel.

We are now involved in the treatment of spectra to obtain quantitative results.

Preliminary results have been presented by posters:

- K. GUERMAN, T. REICH, C. SERGEANT, R. ORTEGA, V. TASAROV, M. SIMONOFF
Technetium metal and pyrometallurgically formed sediments study and speciation by Tc-NMR and EXAFS/XANES
OECD/NEA Workshop on pyrochemical separations, march 14-15, 2000, Villeneuve les Avignon, France
- M. SIMONOFF, K.E. GUERMAN, T. REICH, C. HENNIG, R. ORTEGA, C. SERGEANT, G. DEVES, M.H. VESVRES
Technetium speciation in radioactive wastes generated in pyrochemical reprocessing
2nd Euroconference and NEA workshop on speciation, techniques, and facilities for radioactive materials at Synchrotron light sources, september 10-12, 2000, Grenoble, France
- K.E. GUERMAN, T. REICH, C. SERGEANT, R. ORTEGA, V.P. TARASOV, M. SIMONOFF, G. SIMONOFF
Etude et speciation par RMN et EXAFS du Technétium métallique et de sels formés par voie pyrométallurgique
7^e Rencontres Nationales de Radiochimie, september 27-29, 2000, Saint Rémy les Chevreuse, France

 ROBL-CRG	Experiment title: Polarized EXAFS measurements at uranyl sorbed montmorillonite	Experiment number: 20_01_024
	Beamline: BM 20	Date of experiment: from: 03/09/00 to: 04/09/00 from: 22/09/00 to: 25/09/00
Shifts: 18	Local contact(s): C. Hennig	<i>Received at ROBL:</i> 26/03/01
Names and affiliations of applicants (* indicates experimentalists): C. Hennig ^{1*} , T. Reich ^{1*} , H. Funke ^{1*} , A. Roßberg ^{1*} , R. Dähn ² , A. Scheidegger ² ¹ Forschungszentrum Rossendorf e.V., Institute of Radiochemistry, D-01314 Dresden ² Paul Scherrer Institut, Waste Management Laboratory, CH – 5232 Villigen		

Report:

EXAFS sorption studies of uranium with montmorillonite and related natural clays in the pH ranging from 3 to 5 have shown that uranyl complexes almost preserve the equatorial shell arrangement comparable to the structure observed in aqueous solution [1,2]. It is shown that uranyl adsorption occurs via ion-exchange as outer-sphere complexation. This result of intact uranyl aquo-ion structure is indicated by a lack of higher shells in the Fourier transform of the uranium L_{III}-edge EXAFS spectra. At near-neutral pH, two additional equatorial shells are observed indicating an inner-sphere complexation with the surface [3,4].

The used montmorillonite STx-1, (Si₄Al_{1.67})(Fe²⁺,Mg)_{0.33}O₁₀(OH)₂(Na_{0.33},H₂O), was purchased from Source Clay Minerals Repository of the Clay Minerals Society. Na⁺-STx-1 was converted by ion exchange in the Ca²⁺ form. The samples were prepared by mixing 2g/L STx-1 with uranyl nitrate solution and NaClO₄ buffer (Tab. 1). This clay suspension was in contact for 24 h. In order to avoid carbonate species the preparation was taken in a glove box. Aliquots of the supernatant solution were analyzed by ICP-MS in order to determine the amount of U(VI) sorbed onto the montmorillonite. The pH of each dispersion was measured prior to filtration.

	NaClO ₄ [mol]	[U] _{init} [10 ⁻⁶ mol]	pH _{final}	[U]/[solid] [μmol/g]	uptake [%]
A	0.1	5.0	5.06	14.53	5.9
B	0.1	2.5	5.11	14.53	11.8
C	0.1	1.0	5.25	12.45	25.2
D	0.0033	2.5	5.20	23.87	19.3

Tab. 1: Experimental conditions of sample preparation and amount of U(VI) sorbed onto montmorillonite

Polarization dependent EXAFS investigations were performed to study the orientation of the linear uranyl moiety and the equatorial oxygen atoms regarding to the basal plane {001} of montmorillonite. For that purpose highly oriented self-supporting films were prepared according a procedure described in [5]. The pole

density maximum of layer silicates is typical the basal plane {001}. Quantitative texture measurements shows that this procedure lead to an orientation distribution between ~20° and ~35° full width of half maximum [5,6].

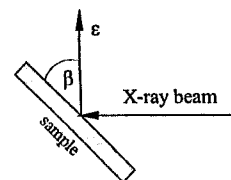


Fig. 1: Geometry of polarization dependent EXAFS experiments. The angle β is defined as tilt angle between the sample surface and the polarization vector ϵ . As angles β are used 10°, 35°, 55° and 80°.

The uranium L_{III}-edge EXAFS spectra measured at angles indicated by β are shown in Fig. 2. The EXAFS amplitudes show a very weak, but nevertheless systematic shift. From low to high β values their shift direction is marked by the arrows in Fig. 2. This is connected mainly with an reducing in the amplitude of the axial oxygen atoms.

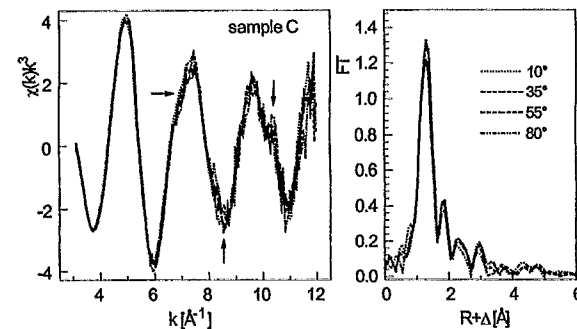



Fig. 2: U L_{III}-edge EXAFS (left side) and their Fourier transform (right side) of sample C.

References

- [1] Christolm-Brause, C.: Geochim. Cosmochim. Acta 58 (1994) 3625
- [2] Dent, A.J.: J. Colloid Interface Sci. 159 (1992) 45
- [3] Sylwester, E.R.: Geochim. Cosmochim. Acta 64 (2000) 2431
- [4] Thompson, H.A. et al.: in adsorption of metals by geomedia (ed. Jenne, E.A.) 16 (1998) 349
- [5] Manceau, A. et al.: Synchrotron X-ray methods in clay science, Clay Mineral Society (1999) 68
- [6] Schlegel, M.L. et al.: J. Colloid Interface Sci. 215 (1999) 140

 ROBL-CRG	Experiment title: Water coordination in U(VI) fluoride and oxalate complexes as studied by EXAFS and <i>ab initio</i> calculations	Experiment number: 21_01_26 EU-R04
	Beamline: BM 20	Date of experiment: from: 1.10.2000 to: 2.10.2000
Shifts: 6	Local contact(s): Tobias Reich, Christoph Hennig	<i>Received at ROBL:</i> 22.3.2001
Names and affiliations of applicants (* indicates experimentalists): Ingmar Grenthe* Zoltan Szabo* Department of Chemistry, Royal Institute of Technology (KTH) S-10044 Stockholm, Sweden		

Report:

Two different problems have been addressed.

The first concerns the structure of U(VI) fluoride complexes in aqueous solution. This part of the study has been completed and a manuscript has been submitted to *Inorganic Chemistry*.

Title and authors are as follows: **Solvent Effects on Uranium(VI) Fluoride and Hydroxide Complexes Studied by EXAFS and Quantum Chemistry.**

Valérie Vallet^{*a}, Ulf Wahlgren^a, Bernd Schimmelpfennig^b, Henry Moll^c, Zoltán Szabó^d and Ingmar Grenthe^{*d}

^aInstitute of Physics, Stockholm University, P.O. Box 6730-11385 Stockholm, Sweden

^bTheoretical Chemistry, Department of Chemistry, Teknikringen 30, Royal Institute of Technology (KTH) S-10044 Stockholm, Sweden


^cInstitute of Radiochemistry, Forschungszentrum Rossendorf e.V., P.O. Box 510119, D-01314 Dresden, Germany.

^dInorganic Chemistry, Department of Chemistry, Royal Institute of Technology (KTH), S-100 44 Stockholm, Sweden

The structures of the complexes $\text{UO}_2\text{F}_n(\text{H}_2\text{O})_{5-n}^{2-n}$, $n = 3-5$ have been studied by EXAFS. All have pentagonal bipyramid geometry with U – F of and U – H_2O distances equal to 2.26 and 2.48 Å, respectively. On the other hand the complex $\text{UO}_2(\text{OH})_4^{2-}$ has a square bipyramid geometry both in the solid state and in solution. The structures of hydroxide and fluoride complexes have also been investigated with wave function based and Density Functional Theory (DFT) methods in order to explore the possible reasons for the observed structural differences. These studies include models that describe the solvent by using a discrete second coordination

sphere, a model with a spherical, or shape adapted cavity in a conductor like polarizable continuum medium (CPCM), or a combination of the two. Solvent effects were shown to give the main contribution to the observed structure variations between the uranium(VI) tetra-hydroxide and the tetra-fluoride complexes. Without a solvent model both $\text{UO}_2(\text{OH})_4(\text{H}_2\text{O})^{2-}$ and $\text{UO}_2\text{F}_4(\text{H}_2\text{O})^{2-}$ have the same square bipyramid geometry, with the water molecule located at a distance of more than 4 Å from uranium and with a charge distribution that is very near identical in the two complexes. Of the models tested, only the CPCM ones are able to describe the experimentally observed square and pentagonal bipyramid geometry in the tetra-hydroxide and tetra-fluoride complexes. The geometry and the relative energy of different isomers of $\text{UO}_2\text{F}_3(\text{H}_2\text{O})_2^-$ are very similar, indicating that both isomers are present in comparable amounts in solution. All calculated bond distances are in good agreement with the experimental observations, provided that a proper model of the solvent is used.

In the second project we have studied the coordination geometry of binary and ternary oxalate complexes of U(VI) with the composition $\text{UO}_2(\text{oxalate})_2(\text{H}_2\text{O})^{2-}$; $\text{UO}_2(\text{oxalate})_3^{4-}$ and $\text{UO}_2(\text{oxalate})_2\text{F}^{3-}$. A first analysis of the EXFS data has been made and the bond distances have been compared with those obtained by using quantum chemical methods of the type described above. The agreement between the bond distances obtained by the two methods is in general within 0.05 Å, indicating that the more detailed structures provided by the quantum chemical methods may be a good representation of the structures of the species in solution. The structure information is an important part of our attempts to deduce the intimate reaction mechanism for water, oxalate and fluoride substitution/exchange in these complexes. This study is well under way and we expect to have two manuscripts ready within one month.

	Experiment title: First XAFS Measurements of Plutonium Complexed by Humic Substances	Experiment number: 20_01_027
	Beamline: BM 20	Date of experiment: from: 27/09/2000 to: 28/09/2000
Shifts: 6	Local contact(s): Tobias Reich	<i>Received at ROBL:</i> 22.03.2001
Names and affiliations of applicants (* indicates experimentalists): K. Schmeide*, S. Pompe*, T. Reich*, C. Hennig*, H. Funke*, A. Roßberg*, T.Ye. Zayarnaya ^{a)} , G. Geipel, K.H. Heise, G. Bernhard Forschungszentrum Rossendorf e.V., Institute of Radiochemistry, P.O.Box 510 119, D-01314 Dresden, Germany a) Institute of Metal Physics, Russ. Academy of Sci., Ekaterinburg, Russia		

Report:

The near-neighbor surrounding of Pu(III,IV) sorbed onto humic substances and Bio-Rex70 was studied at pH 2 by XAFS spectroscopy. The results are compared with literature data of Pu(III) and Pu(IV) hydrates.

Experimental: A Pu(III) stock solution (^{242}Pu), prepared by electrochemical reduction of a Pu(VI) solution, was used to prepare Pu(III) samples from synthetic humic acid type M42, Kranichsee fulvic acid (KFA), and Bio-Rex70 (from Bio-Rad) at pH 2 under inert gas conditions. The Pu loading of the resulting wet pastes of M42, KFA and Bio-Rex70 was 61, 71 and 6 mg Pu per g sorbent, respectively. Pu L_{III}-edge XAFS spectra were collected in fluorescence mode at the Rossendorf Beamline at the ESRF in Grenoble.

Results: The trivalent oxidation state of Pu in the stock solution as well as in the supernatants obtained during preparation of the Pu sorbates was verified by UV-vis absorption spectroscopy using the absorption band at 600 nm. Pu(IV) could not be detected (at 470 nm) in the solutions stored under inert gas conditions, even 4 months after sample preparation. That means, an oxidation of Pu(III) by humic substances or Bio-Rex70 can be excluded. However, according to the XANES spectra of the Pu sorbates the samples contain predominantly Pu(IV) with small amounts of Pu(III). That means, the trivalent oxidation state of Pu was not stable within the time of our experiment. The most likely reason is that during the sample transport to the beamline oxygen diffused through the PE bags and the Capton tape used for sealing the Teflon sample holders for pastes.

The EXAFS oscillations and the Fourier transforms of M42 and KFA, shown in Fig. 1, are similar to each other but different from those of Bio-Rex70. The structural parameters are given in Tab. 1.

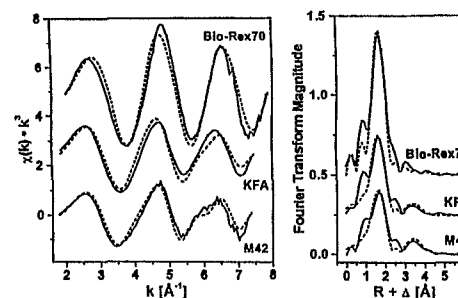


Fig. 1: Raw Pu L_{III}-edge k^3 -weighted EXAFS spectra of Pu samples and corresponding Fourier transforms (without phase corrections). Solid lines: experiment, dashed lines: fit.

Tab. 1: Structural parameters of Pu samples

Sample	Shell	N	R [Å]	σ^2 [Å ²]
Pu-M42	Pu-O	7.8±1.7	2.38±0.03	0.0250
	Pu-Pu	1.9±1.9	3.78±0.04	0.0086
Pu-KFA	Pu-O	8.3±1.8	2.38±0.03	0.0228
	Pu-Pu	1.5±2.4	3.77±0.05	0.0112
Pu-Bio-Rex70	Pu-O	6.8±1.2	2.34±0.01	0.0098
Pu(III):nH ₂ O /1/	Pu-O	7.6±0.6	2.48±0.01	0.0102
Pu(IV):nH ₂ O /2/	Pu-O	8	2.39	0.0118

The 95 % confidence limits are given for N and R as estimated by EXAFSPAK.

Within the experimental error, the coordination number of the Pu-O shell of all samples is comparable with those of Pu(III) and Pu(IV) hydrates. The bond length of the Pu-Bio-Rex70 sorbate, which contains the highest amount of Pu(IV), is about 0.05 Å shorter than that of Pu(IV) hydrate. A similar shortening (0.04 Å) was found for Np(IV) samples due to complexation by humic substances and Bio-Rex70 /3/.


According to the XANES results, the Pu sorbates of M42 and KFA contain a slightly higher amount of Pu(III) compared to the Pu-Bio-Rex70 sorbate. This results in a slightly larger bond length ($R_{\text{Pu-O}}=2.38$ Å) which is due to the larger ionic radius of Pu^{3+} (1.12 ± 0.02 Å) compared to Pu^{4+} (1.01 ± 0.02 Å) /4/. The broader distribution of R of the humates due to the two oxidation states is evident in the larger Debye-Waller factor.

The Fourier transforms of the M42 and KFA samples (cf. Fig. 1) show an additional broad peak at about 3.4 Å. Fitting a Pu-Pu shell, 1 to 2 Pu atoms were found at a bond distance of 3.78 Å. This indicates the formation of polynuclear Pu species which is characteristic for Pu(IV). This effect was not observed for Pu-Bio-Rex70, probably due to the lower Pu loading of Bio-Rex70 compared to the humic substances.

The results have shown that in case of humate and Bio-Rex70 sorbates of such redox sensitive actinide ions as Pu much attention has to be paid to the selection of sample containers to minimize diffusion of oxygen. Another possibility is to prepare the samples on-site directly before the XAFS measurements.

Acknowledgment: This work was supported by the BMWi (no. 02 E 9299).

References: /1/ Reich, T., et al., Report FZR-285, 72 (2000); /2/ Ankudinov, A.L., et al., Phys. Rev. B 57, 7518 (1998); /3/ Schmeide, K., et al., Proceedings of Internat. Conf. Actinide-XAS-2000, Grenoble, France, in press; /4/ Neck, V., Kim, J.I., Radiochim. Acta 88, 815 (2000).

	Experiment title: Catecholate complexes of NpO_2^{2+} and NpO_2^{2+} in aqueous solution	Experiment number: 20_01_28 (a) EU-R01
	Beamline: BM 20	Date of experiment: from: 8/11/00 to: 10/11/00
Shifts: 6	Local contact(s): C. Hennig	<i>Received at ROBL:</i> 31.01.2001
Names and affiliations of applicants (* indicates experimentalists): Professor Francis R Livens, Department of Chemistry, Manchester University, Manchester, M13 9PL, UK, Dr Iain May, Department of Chemistry, Manchester University, Manchester, M13 9PL, UK, Dr David Collison, Department of Chemistry, Manchester University, Manchester, M13 9PL, UK.		

Report:

This beamtime allocation was used to analyse samples from two separate sub-projects: 1) Catecholate complexes of NpO_2^{2+} and NpO_2^{2+} in aqueous solution and 2) Reactions of NpO_2^{2+} with the surface of mackinawite (tetragonal FeS) (see separate Report Form).


In sub-project 1), a Np(V) stock solution was used as received, and a portion was oxidised by treatment with HClO_4 to Np(VI). These were reacted with aqueous solutions of catechol (1,2-dihydroxybenzene) and tiron (3,5-disulfonatecatecholate) to form the 1:2 complexes. These were characterised by UV-visible near ir spectroscopy in Manchester, then shipped to ESRF for XAS analysis. During shipment to ESRF, the Np(VI) samples were reduced to Np(V), presumably accompanied by partial oxidation of the ligands. Nevertheless, all the samples were analysed using Daresbury Laboratory programs Excalib, Exback and Excurv98, using curved wave theory and

including full cluster multiple scattering calculations. The fitting parameters are summarised in Table 1.

Table 1. EXAFS fitting parameters for NpO_2^{2+} /catecholate, NpO_2^{2+} /tironate, NpO_2^{2+} /catecholate and NpO_2^{2+} /tironate. C.N.- coordination number; r- interatomic distance; R- overall goodness of fit; $2\sigma^2$ - Debye-Waller factor; uncertainty in CN ± 1 .

Sample	C.N.	Atom	r (Å)	$2\sigma^2$ (Å ²)
NpO_2^{2+} /catecholate R = 56.64	2	O	1.80 ± 0.02	0.001
	5	O	2.47 ± 0.02	0.004
	1	Np	4.44 ± 0.04	0.001
NpO_2^{2+} /tironate R = 35.8	2	O	1.83 ± 0.02	0.001
	4	O	2.50 ± 0.02	0.006
NpO_2^{2+} /catecholate R = 54.2	2	O	1.83 ± 0.02	0.002
	4	O	2.48 ± 0.02	0.007
NpO_2^{2+} /tironate R = 48.2	2	O	1.85 ± 0.02	0.003
	2	O	2.31 ± 0.02	0.002
	2	O	2.52 ± 0.02	0.005

These results show that the Np(V) catecholate forms a dimeric complex in solution. This complex is unlike that formed by U(V) in that the axial O atoms remain coordinated to the Np centre whereas the U complex contains mono-oxo U centres. However, the Np(VI) catecholate complex, which had reduced to Np(V), is monomeric, perhaps reflecting the presence of oxidised ligand. Both tironate complexes are monomeric, probably reflecting the presence of the bulky sulfonate substituents in the 3- and 5- positions, which subsequent modelling studies have suggested prevents dimerisation.

 ROBL-CRG	Experiment title: Reactions of NpO_2^{2+} with the surface of mackinawite (tetragonal FeS)	Experiment number: 20_01_28 (b) EU-R01
	Beamline: BM 20	Date of experiment: from: 8/11/00 to: 10/11/00
Shifts: 6	Local contact(s): C. Hennig	<i>Received at ROBL:</i> 31.01.2001
Names and affiliations of applicants (* indicates experimentalists): Professor Francis R Livens, Department of Chemistry, Manchester University, Manchester, M13 9PL, UK, Professor Richard A D Patrick, Department of Earth Sciences, Manchester University, Manchester, M13 9PL, UK, Professor David J Vaughan, Department of Earth Sciences, Manchester University, Manchester, M13 9PL, UK		

Report:

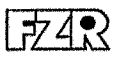
In sub-project 2) , we found that uptake of Np(V) on to the surface of FeS was much less efficient than that of U (15-20% removal from solution as opposed to >90%). Moreover, the mechanisms of reaction are different. UO_2^{2+} initially forms surface complexes on oxidised regions of the surface and, when these are saturated, a surface mediated redox reaction occurs, with partial reduction of U and growth of a mixed oxidation state oxide phase. At no stage is there any evidence of coordination of the U centre by surface S atoms.[†] By contrast, Np is quantitatively reduced to oxidation state (IV), as shown by the shift in the absorption edge position, and is coordinated by both S and O atoms (Table 2). These results demonstrate coordination of the reduced Np centre by surface S atoms and filling of the coordination sphere by solvent molecules or hydroxide ions. The presence of both Np and Fe

atoms in the outer coordination shells indicates the formation of a discrete Np phase on the surface.

Table 2. Fitting parameters for NpO_2^{2+} on mackinawite. C.N.- coordination number; r- interatomic distance; R- overall goodness of fit; $2\sigma^2$ - Debye-Waller factor; uncertainty in CN \pm 1.

Np(ppm)	Shell	No, type	r (Å)	$2\sigma^2$ (Å ²)
1000	1	3 O	2.16	0.005
	2	3 S	2.34	0.009
	3	2 Fe	3.83	0.013
	4	1 Np	4.02	0.009
4000	1	3 O	2.21	0.006
	2	3 S	2.38	0.011
	3	2 Fe	3.96	0.016
	4	1 Np	4.06	0.012
20000	1	3 O	2.20	0.012
	2	3 S	2.36	0.022
	3	2 Fe	3.84	0.012
	4	1 Np	4.01	0.015

1. L N Moyes, R H Parkman, J M Charnock, D J Vaughan, F R Livens, C R Hughes & A Braithwaite 2000. Uranium uptake from aqueous solution by interaction with goethite, lepidocrocite, muscovite and mackinawite: an X-ray absorption spectroscopy study. Environ. Sci. Technol., 34, 1062-1068.

 ROBL-CRG	Experiment title: EXAFS study of Np(VII) solutions	Experiment number: 20_01_029
	Beamline: BM 20	Date of experiment: on: 29/09/2000
Shifts: 3	Local contact(s): Dr. Reich, Tobias	<i>Received at ROBL:</i> 27/03/2001
Names and affiliations of applicants (* indicates experimentalists): Henry Moll*, Tobias Reich*, Christoph Hennig*, Harald Funke*, Susanne Pompe*, Katja Schmeide*, Andre Rosberg*, T.Ye. Zayarnaya* ^{a)} and Thomas Fanghänel		
Institute of Radiochemistry, Forschungszentrum Rossendorf e.V., P.O. Box 510119, D-01314 Dresden, Germany		
a) Institute of Metal Physics, Russ. Academy Sci., Ekaterinburg, Russia		

Report:

Experimental. For synthesis of Np(VII), we followed in general the description given by Clark et al. [1]. Finally, ozone was bubbled through a mixture of $\text{NpO}_2(\text{OH})_2$ and 2.5 M NaOH. The solid dissolved to dark green Np(VII). The characteristic absorption maxima at 412 nm and 618 nm, and the molar absorption coefficients published in [2] were used to determine the Np(VII) concentration, 0.015 M, of the solution measured at ROBL. The absorption spectra of the solution measured before and after the XAS measurement showed no difference. The alkaline Np(VII) solution was hermetically sealed under O_3 atmosphere in a polyethylene cuvette of 3 mm diameter. The EXAFS transmission spectra were recorded at room temperature using a water-cooled Si(111) double-crystal monochromator of fixed-exit type ($E = 5\text{--}35$ keV) at the Rossendorf Beamline (ROBL) at ESRF, Grenoble. The energy scale was calibrated using the first inflection point of the absorption spectrum of a Y foil (17038 eV). The scattering phases and amplitudes were calculated for a cluster of $\text{NpO}_4(\text{OH})_2$ using FEFF7. The atomic coordinates were taken from $\text{Co}(\text{NH}_3)_6\text{NpO}_4(\text{OH})_2 \cdot 2\text{H}_2\text{O}$ reported in [3].

Results and Discussion. The XANES spectrum of Np(VII) in alkaline solution is significantly different compared to those of Np(IV), Np(V), and Np(VI) [4]. The Np(VII) species shows different symmetry properties indicating that no actinyl unit is present as in Np(V) and Np(VI). Soderholm et al. [5] reported a similar XANES spectrum of their Np(VII) sample. Four oxygen atoms at 1.89 Å are coordinated in the first shell around Np (Tab. 1 and Fig. 1). The Debye-Waller factor of 0.0020 \AA^2 is typical for actinyl compounds indicating a short and strong bond. The distance of these oxygens is significantly longer compared to Np(V), 1.82 Å, and Np(VI), 1.75 Å [4]. The amplitude of this shell is larger compared to "normal" actinyl compounds [4].

Table 1. EXAFS structural parameters measured for dark-green Np(VII) in 2.5 M NaOH. In parenthesis XRD values are given that were taken from reference [3].

Sample	Shell	N	$\sigma^2 (\text{\AA}^2)$	R (Å)	$\Delta E_0 (\text{eV})$
0.015M Np(VII) in 2.5M NaOH	Np=O	3.6 ± 0.3 (4.0)	0.0020	1.89 ₄ (1.88 ₆)	-5.0
	Np-O	3.3 ± 1.3 (2.0)	0.0133	2.32 ₆ (2.32 ₃)	

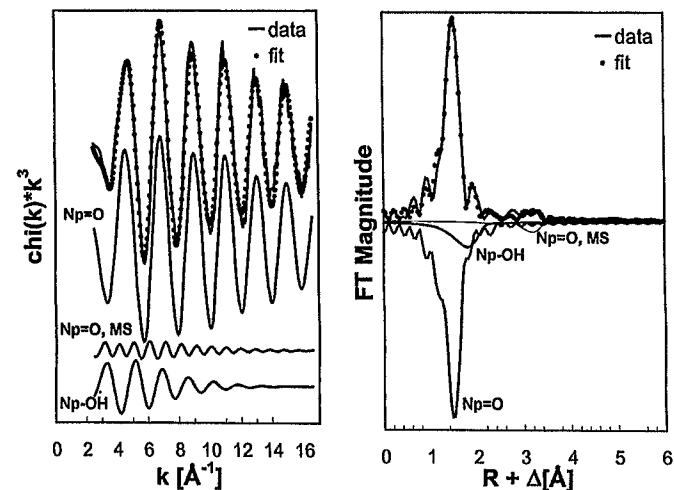



Fig. 1. Np L_{III} -edge k^3 -weighted EXAFS data including the best fit and corresponding FT measured for 0.015 M Np(VII) in 2.5 M NaOH.

An average coordination number of 3 and a distance of 2.33 Å were determined for the second shell. The error of N is large because of the low amplitude and the strong interference with the "yl" oxygens. The atomic surrounding of Np(VII) in solution measured by EXAFS is in excellent agreement with the XRD results (see Tab. 1) of $\text{Co}(\text{NH}_3)_6\text{NpO}_4(\text{OH})_2 \cdot 2\text{H}_2\text{O}$ [3]. To summarize, the XAS experiments and additional information from XRD lead to the conclusion that the structure of Np(VII) in alkaline solution is most likely $\text{NpO}_4(\text{OH})_2^{3-}$. We will compare our experimental findings with new quantum chemical calculations.

References

- [1] Clark, D. L., et al., *J. Am. Chem. Soc.* **119**, 5259 (1997).
- [2] Spitsyn, V.I., et al., *J. Inorg. Nucl. Chem.* **31**, 2733 (1969).
- [3] Grigorev, M.S., et al., *Radiokhimija* **28**, 690 (1986).
- [4] Reich, T., et al., *Radiochim. Acta* **88**, 633 (2000).
- [5] Soderholm, L., et al., in press (2000).

	Experiment title: EXAFS investigation on uranium uptake by plants	Experiment number: 20_01_030
	Beamline: BM 20	Date of experiment: from: 01/12/00 to: 02/12/00
Shifts: 5	Local contact(s): C. Hennig, T. Reich, A. Rossberg	<i>Received at ROBL:</i> 10/04/01
Names and affiliations of applicants (* indicates experimentalists): A. Rossberg* ¹ , T. Reich* ¹ , C. Hennig* ¹ , H. Funke* ² , H. Moll* ² , S. Amayri* ² , A. Günther ² , G. Bernhard ²		
¹ ESRF – ROBL / CRG, Avenue des Martyrs, B.P. 220, 38043 Grenoble Cedex, France ² Forschungszentrum Rossendorf e.V., Institut für Radiochemie, P.O. Box 510119, 01314 Dresden, Germany		

Report:

Experimental: To obtain first results on the change of uranium speciation during the soil-to-plant transfer, we have investigated the uranium uptake by lupins. The uranium speciation were investigated in dependence on the growth-conditions and the pieces of the plants. The three different growth-conditions were a) soil culture without uranium (injection of $2.5 \cdot 10^{-2}$ M $UO_2(NO_3)_2$ in roots or shoot axis), b) soil culture (1 g U(VI) in 1 kg soil) and c) hydroponics ($2.5 \cdot 10^{-2}$ M $UO_2(NO_3)_2$). After harvesting for case a, b and c, the lupins were washed, separated into roots, shoot axis and leaves, and cut in small pieces. The U L_{III} -edge EXAFS spectra of the dried samples were recorded in fluorescent mode using a 4-pixel germanium detector.

Results and discussion: The raw L_{III} -edge k^3 -weighted EXAFS spectra of the samples 1-8 and their corresponding Fourier transforms are shown in Fig. 1 and the fit results with the experimental conditions in Tab. 1. According the results in Tab. 1 the average radial $U-O_{ax}$ distance between U(VI) and the axial oxygen atoms is 1.79 Å. The data are mainly influenced from the changes in the radial $U-O_{eq}$ distances between U(VI) and the equatorial oxygen atoms and the coordination number of the equatorial oxygen atoms (Tab. 1).

If one consider that two different $U-O_{eq}$ distances determine the data then a simple cluster analysis can show the dependencies between the uranium speciation in different pieces of plants and the growth-conditions. If the $U-O_{eq}$ distances of 2.29 ± 0.02 Å and $U-O_{eq}$ distances equal or greater than 2.36 ± 0.02 Å are characteristic for bonding type A and B then the experimental conditions can arranged like Tab. 2.

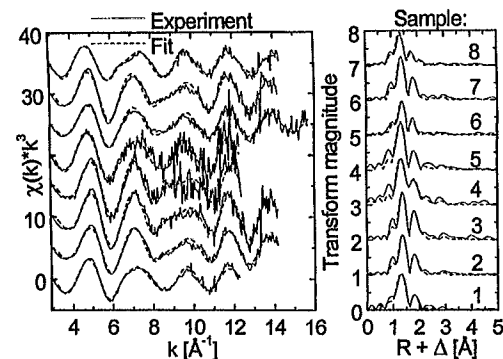


Fig.1: Raw L_{III} -edge k^3 -weighted EXAFS spectra of the plant samples (left) and their corresponding Fourier transforms (right)

Tab. 1: EXAFS structural parameters of the plant samples with different preparation conditions.

Sample	preparation	U-O _{axial}		U-O _{equatorial}		
		R	$\sigma^2 \cdot 10^{-3}$	N	R	$\sigma^2 \cdot 10^{-3}$
1	i, root	1.783(2)	2.7(1)	4.4(5)	2.359(7)	12(1)
2	i, shoot axis	1.793(2)	1.6(1)	2.8(2)	2.295(4)	4.5(5)
3	s, root	1.794(2)	0.8(2)	3.5(3)	2.289(4)	3.5(6)
4	s, shoot axis	1.783(5)	1.2(3)	4.0(6)	2.268(8)	4(1)
5	h, root	1.786(7)	0.8(4)	6(2)	2.36(2)	15(5)
6	h, shoot axis	1.787(2)	1.9(1)	2.8(4)	2.310(7)	7(1)
7	h, leaf	1.788(2)	1.2(1)	3.9(4)	2.297(6)	6.1(8)
8	h, i, root	1.779(2)	2.4(1)	3.6(5)	2.412(8)	11(2)

i – injection, s – soil culture, h – hydroponics, N – coordination number, R – radial distance in Å with an uncertainty of ± 0.02 Å, σ^2 – Debye-Waller factor in Å², the standard deviations are given in parenthesis.


Tab. 2: The bonding types A ($R_{U-O_{eq}} = 2.29 \pm 0.02$ Å) and B ($R_{U-O_{eq}} \geq 2.36 \pm 0.02$ Å) in dependence from the experimental conditions for the samples 1-7.

growth-conditions	root	shoot axis	leaf
hydroponics ($2.5 \cdot 10^{-2}$ M $UO_2(NO_3)_2$)	B	A	A
soil culture (1 g U(VI) in 1 kg soil)	A	A	-
injection ($2.5 \cdot 10^{-2}$ M $UO_2(NO_3)_2$)	B	A	-

From Tab. 2 one can obtain that the bonding type A is characteristic for the shoot axis and is independent from the growth-conditions. The root and the shoot axis show bonding type A if the plants were grown as soil culture. For the root the bonding type change dependent on the growth-conditions. Bonding type B is also characteristic for sample 8 (hydroponics and additional injection of U(VI)). In case of the bonding type A the average coordination number of 3-4 equatorial oxygen atoms and the short average bond distance of 2.29 Å corresponds to the expected structural parameters observed for uranyl phosphates [1].

References

[1] Hennig, C., et al., Radiochimica acta, accepted (2000)

 ROBL-CRG	Experiment title: X-ray absorption spectroscopy investigation on uranyl complexes with alpha-substituted carboxylic acids	Experiment number: 20_01_31
	Beamline: BM 20	Date of experiment: on: 04/12/2000
Shifts: 3	Local contact(s): Dr. Reich, Tobias	Received at ROBL: 27/03/2001
Names and affiliations of applicants (* indicates experimentalists): Henry Moll, Tobias Reich, Christoph Hennig*, Harald Funke*, Samer Amayri*, M. Walter*, and Thomas Fanghänel Institute of Radiochemistry, Forschungszentrum Rossendorf e.V., P.O. Box 510119, D-01314 Dresden, Germany		

Report:

We are reporting the first preliminary results within this project. Alpha-substituted carboxylic acids are present in nature as degradation products and their interactions with metal-ions are therefore important. They are often assumed to form chelates using the alpha-OH group and one carboxylate oxygen. But there is no experimental proof and little information on the structure of the species formed. Szabó and Grenthe found that the alpha-OH proton can dissociate when the alpha-OH-group is coordinated [1]. The experiments in this proposal will provide experimental information about the structure of uranyl complexes with α -substituted carboxylic acids: (a) alpha-OH group: glycolic acid and alpha-hydroxyisobutyric acid, and (b) alpha-NH₂-group: alpha-aminoisobutyric acid. The soluble species will be analysed by XAS to get experimental proof if at low pH a bidentate coordination of the carboxylic group dominates and at which pH a chelating coordination to uranyl due to the deprotonation of the alpha-OH-group of the ligand will take place.

Experimental. Aliquots of the U(VI) stock solution were taken to get the final concentrations between 0.005 and 0.05 M. Appropriate amounts of glycolic acid and alpha-hydroxyisobutyric acid were dissolved to obtain the ligand concentrations. The pH values of the test solutions were adjusted using NaOH/TMA-OH and/or HClO₄. The EXAFS data were recorded in transmission or fluorescence mode at the Rossendorf Beamline (ROBL) at the ESRF in Grenoble. For energy calibration of the sample spectra, the spectrum from a Y foil was recorded simultaneously. The ionization energy of the U L_{III} electron, E₀, was arbitrarily defined as 17 185 eV. The data were treated using the EXAFSPAK software developed by George and Pickering (1995) at SSRL [2]. Theoretical backscattering phase and amplitude

functions were calculated using the FEFF6 [3] program. The MS path O-U-O (4 legged path) of the linear UO₂²⁺ unit was included in the model fitting.


First Results. In this first attempt we were investigating the structure of soluble uranyl species with the two alpha-hydroxycarboxylic acids under acidic (pH=2) and alkaline conditions (pH>10). The distance of the equatorial oxygens are an indication for the coordination mode of the ligand to the linear uranyl unit. Denecke et al. found that in the case of bidentate ligation the resulting U-O_{eq} bond distance should be 2.48 Å [4]. The average distances for monodentate and bridging ligation are 2.39 and 2.36 Å, respectively. In the test solution at pH=2, the 1:1 complexes, UO₂(HOCH₂COO)⁺ and UO₂(HOC₃H₆COO)⁺, are dominating the uranyl speciation. In both systems, the measured average distance for the equatorial oxygens were 2.39 Å. This is significantly shorter compared to 2.44 Å determined in the acetate system [5]. In contrast to the bidentate coordinated acetate, the alpha-hydroxycarboxylic acids under investigation are most likely bound in a monodentate ligation to the linear uranyl unit.

Under alkaline conditions the alpha-OH group should be deprotonated and the complexes, UO₂(OCH₂COO)₂²⁻ and UO₂(OC₃H₆COO)₂²⁻, might be the major uranyl species [1]. A decreased U-O_{eq} bond distance, 2.36 Å, with increasing pH were detected for the glycolate system. This is a strong indication for a chelating coordination to uranyl due to the deprotonation of the alpha-OH-group. The EXAFS spectrum depicted a narrow peak at 3.85 Å. This feature could be fitted as a U-U interaction. One explanation would be the formation of a polynuclear species, e.g. [(UO₂)₂(OCH₂COO)₄]⁴⁻, at pH values above 10. An average U-O_{eq} bond distance of 2.28 Å was detected in the alpha-hydroxyisobutyrate system at pH > 10. This distance is, however, too short for a chelating coordination of the ligand. Whereas the value of 2.28 Å is similar to U-O_{eq} (2.26 Å) found for UO₂(OH)₄²⁻ [6]. We assume that under the given circumstances the mononuclear uranyl hydroxo species are dominating the U(VI) speciation instead of UO₂(OC₃H₆COO)₂²⁻.

In further experiments, we will measure more samples between pH 2 and 8. This approach might help to explore at which pH a chelating coordination to uranyl due to the deprotonation of the alpha-OH-group of the ligand will take place. Furthermore we will investigate the influence of the NH₂-group compared to that of the OH-group in alpha-hydroxyisobutyric acid by means of EXAFS.

References

- [1] Szabó, Z., et al., *Inorg.Chem.* **39**, 5036 (2000).
- [2] George, G.N., Pickering, I.J., 1995. EXAFSPAK, A suite of computer programs for analysis of X-ray absorption spectra. Stanford Synchrotron Radiation Laboratory, Stanford, USA.
- [3] Rehr, J.J., et al., *Phys. Rev. Lett.* **69**, 3397 (1992).
- [4] Denecke, M.A., et al., *Radiochim. Acta* **79**, 151 (1997).
- [5] Reich, T., et al., *Surface Investigation* **13**, 557 (1998).
- [6] Moll, H., et al., *Radiochim. Acta* **88**, 411 (2000).

	Experiment title: Annealing temperature dependence of atomic structure in submicrocrystalline Cu	Experiment number: 20_01_IH2
	Beamline: BM 20	Date of experiment: from: 10.11.1999 to: 11.11.1999
Shifts: 5	Local contact(s): Tobias Reich	<i>Received at ROBL:</i> 17.2.2001
Names and affiliations of applicants (* indicates experimentalists): Tobias Reich* Forschungszentrum Rossendorf, Dresden, Germany Harald Funke* Forschungszentrum Rossendorf, Dresden, Germany Yuri Babanov*, Institute of Metal Physics, Ekaterinburg, Russia		

Report:

Ultradispersive materials with the grain size less than 100 nm have unusual properties differed from coarse grained samples of polycrystalline analogues. Investigated object (submicrocrystalline Cu (smc-Cu)) was previously studied in our group [1]. We find that saving lattice parameter and strong decreasing of coordination number in can be explain both boundary-particles effect (small size of submicrocrystalline blocks) and high numbers of lattice vacancies. Present work was devoted to the series of smc-Cu samples.

The samples smc-Cu were prepared by a method of severe plastic deformation under quasigidrostatic pressure with shear up to a true logarithmic degree $\dot{\epsilon} = 5$. The average size of a grain in Cu samples is 100 nm [2]. Then the samples were annealed at the different temperatures: 150°C, 175°C and 225°C. Also 'as prepared' smc-Cu and polycrystalline Cu (poly-Cu) were added to the collection.

Absorption X-ray experiments was performed in ESRF (BM20, ROBL line) in transmission mode. The new method of sample inhomogeneity estimation and correction was applied. Due to this method additional spectrum without sample (ground spectra) was collected. The next process of extracting normalized oscillating part from absorption spectra and solution inverse ill-posed problem with the help of regularization method was written earlier [1].

After processing sample annealed at the temperature 150°C was removed from the joint analyses. This sample has nearest interatomic distance different from other samples due to W included in the time of pressure. All other samples has nearest interatomic distance equal to pure polycrystalline Cu. This fact is in a good agreement with our previous work. The first coordination numbers are given in the table. Also in the table we can see values of normalised resistivity for corresponding samples. Two conclusions should be done:


- 1) Annealing leads to vacancy relaxation, as well as annealing temperature higher coordination numbers increases up to poly-Cu one.
- 2) There is the clearly pronounced correlation between coordination numbers and resistivity. We assumed that in the case of smc-materials growth of resistivity could be explain by electron reflections from the grain boundaries and vacancies. When annealing temperature increases smc-particles become larger, vacancies disappears and resistivity returns to the normal polycrystalline value.

Coordination numbers and conductivity for smc- and poly-Cu samples

sample	'as prepared'	annealed, 125° C	annealed, 225° C	poly-Cu
Coord. number	10,9	11,3	11,35	12,1
Norm.resistivity	1,00	0,75	0,55	0.45

1 Yu.A.Babanov, L.A. Blaginina, A.V.Ryazhkin, R.R.Mulyukov, A.F.Sidorenko, N.V.Fadyushina, Nuclear instruments & Methods in Physics Research A 448 (2000) 372

2 R.Z.Valiev, A.V.Korznikov, R.R.Mulyukov, Mater.Sci. and Eng. A168 (1993) 141

 ROBL-CRG	Experiment title: Analysis of correlation in the distribution of disorientations in deformed copper and aluminium single crystals	Experiment number: 20_02_023
	Beamline: BM 20	Date of experiment: from: 22.09.1999 to 24.09.2000
Shifts: 6	Local contact(s): Dr. Norbert Schell	Received at ROBL: 16.05.2000
Names and affiliations of applicants (* indicates experimentalists): Martin Haberjahn *, Institute of Physical Metallurgy, Freiberg University Mykhailo Motylenko *, Institute of Physical Metallurgy, Freiberg University		

Report: Plastic deformation of metallic materials on multislip conditions leads frequently to the formation of dislocation patterns accompanied by considerable disorientations between adjacent cell walls or subboundaries. The determination of the substructure requires a breakdown of the total dislocation content into the density of excess dislocations causing the disorientations and the density of redundant dislocations (dislocations which are not carriers of disorientations). In a simple model, the redundant dislocation density affects the radial intensity distribution whereby the excess dislocation density mainly affects the azimuthal intensity distribution. Cu single crystals cold-rolled at room temperature with $[111] \parallel \text{RD}$ and $(112) \parallel \text{ND}$ up to thickness reductions $\eta=95\%$ were used to measure the radial and azimuthal intensity distribution at the installation of ROBL, BM 20, Materials Research Hutch, at the ESRF, Grenoble. Measurements were performed on the 6 circle diffractometer with monochromatic X-rays of $E=8.048$ eV. The radial and azimuthal intensity of the (111) reflex was registered by scanning $\theta-2\theta$ and ω , as well the ω -scans were measured with different beamsizes on the sample by changing the slitwidth. The true slitwidths were checked before by measuring the beamsize on the sample. From the broadening of the radial intensity distribution the redundant dislocation density and the cut off radius of the deformed samples can be estimated using the theory of Wilkens [1] and Krivoglaz et al [2]. The results obtained from the linear branch in the *Krivoglaz-Wilkens*-plot [3] are shown in figure 1. The azimuthal intensity distribution (rocking curve) of the deformed samples was checked for its dependence on the size of the irradiated volume, given by the beamsize on the sample. In the dislocation cell model containing disorientation between adjacent cells by Krivoglaz et al [4] which connects the broadening of the azimuthal intensity distribution to a mean excess dislocation density, a dependance of the width of the

rocking curve to the number of cells is predicted. The results printed in figure 2 showing only a small dependance in the lower deformation states but a much stronger dependance at higher deformations.

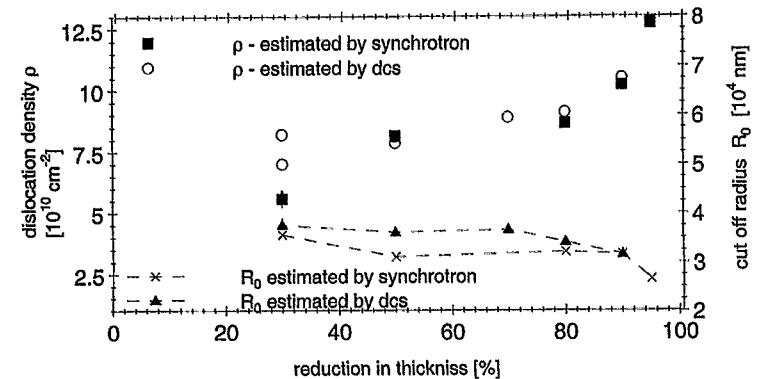


Fig. 1: Dislocation density ρ and cutoff radius R_0 of the measured samples compared to results obtained from a double crystal diffractometer (dcs) at the Institute of Physical Metallurgy, TU Freiberg

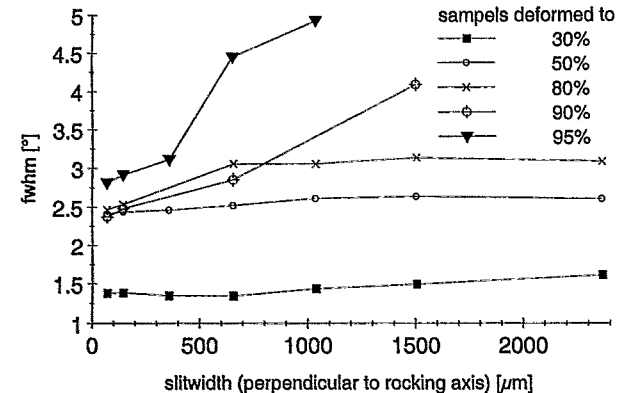
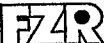


Fig. 2: Full width at half maximum (fwhm) of the azimuthal intensity distribution (rocking curves) as a function of the beamsize for different deformation states

- [1] Wilkens, M. (1970a). In: Fundamental Aspects of Dislocation Theory (Ed. J. A. Simmons et al.) N. B. S. Spec. Publ. 317, Vol. 2, Washington, 1195
- [2] Krivoglaz, M.A. (1996). X-ray and Neutron Diffraction in Non-Ideal Crystals. Springer Verlag, Berlin - Heidelberg 1996
- [3] Klimanek, P. (1989). Problems in diffraction analysis of real polycrystals. In: X-ray and Neutron Structure Analysis in Materials Science (Ed. J. Hasek). Plenum Press, New York, 125
- [4] Krivoglaz, M., Ryaboshapka, K. & Barabash, R. (1970). Fiz. Metallov Metalloved. 30, 1134

 ROBL-CRG	Experiment title: High- Precision Determination of Atomic Positions In 6H- And 4H-SiC Crystals and Investigation of Germanium Nanostructures on Silicon Carbide	Experiment number: 20_02_024
	Beamline: BM 20	Date of experiment: from: 9/24/99 to: 9/28/99
Shifts: 12	Local contact(s): Dr. Norbert Schell	Received at ROBL: 02.12.99
Names and affiliations of applicants (* indicates experimentalists): Andreas Bauer* Dr. Günter Hess* Dr. Jürgen Kräußlich* Prof. Dr. Konrad Goetz Friedrich Schiller University of Jena Institute of Optics and Quantumelectronics, Department of X-ray Physics Max-Wien-Platz 1 D-07743 Jena / Germany		

Report:

In this period at the beamline BM 20 at the ESRF we carried out the following investigations:

- (i): Completion of the measurements for the structure refinement of the silicon carbide (SiC) polytypes 6H and 4H (Ref.[1]).
- (ii): Silicon and germanium clusters on silicon carbide substrates.

(i): To complete previous measurements at the BM20 [1] the following measurements were done. An absolute calibration of the integrated intensities of the “quasiforbidden” reflections rocking curves required measurements on a nearly perfect silicon crystal. Selected SiC-reflections, e.g. the 00.2-reflection of the 6H polytype (Fig. 1) with phase invariants ϕ_3 close to 0° and 180° , respectively, were investigated. Such combinations of reflections allow a very precise determination of the phase invariant to obtain an unambiguous structure refinement model. We also measured the forbidden 6H-SiC 00.9 reflection (same angular position as the “quasiforbidden” 00.6-reflection of the polytype 4H) to ascertain the polytype-purity of the crystal. An azimuthal scan of the 00.9 reflection shows no asymmetry of the “Umweg”-reflection. More over an ω -scan displays no peak.

[1] Forschungszentrum Rossendorf, Project-Group ESRF-Beamline (ROBL-CGR), Report January 1998 – June 1999, p 68.

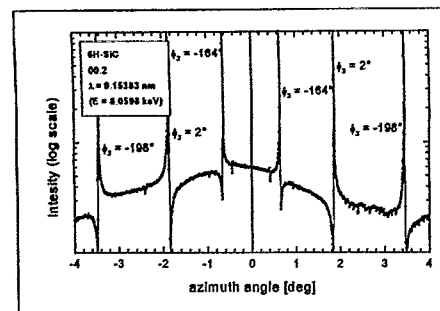


Fig. 1: Azimuth scan of the “quasi-forbidden” 6H-SiC 00.2 reflection. The phase invariant is given by $\phi_3 = \phi_L + \phi_{H-L} - \phi_H$, were H characterizes the weak “quasiforbidden” reflection, L and $H-L$ the two remaining strong “Umweg”-reflections.

(ii): Different SiC-surfaces were coated with thin layers of Si resp. Ge and subsequently annealed to 900 °C respective 600 °C. Such a procedure produces, according to AFM, Si- or respectively Ge-clusters whose number, size distribution and shape depends on the process parameters. Three of those samples were investigated on the ROBL-beamline at the ESRF. The $\theta/2\theta$ - scans show for all samples 111- and 220-reflections of Si respectively Ge (Fig. 2). This reveals unambiguously that the clusters grow preferentially in two different orientations ($\langle 111 \rangle$, $\langle 110 \rangle$). Interestingly, for the Ge-samples those reflections are shifted towards the angular position of the respective Si-reflection. Such a peak shift could be explained by a lattice distortion due to the lattice mismatch or by the change in the lattice constant due to the formation of a Si/Ge solid solution. The lateral orientation of the (111)- and (110)-clusters was investigated by comparison of the ϕ -scans of an appropriate cluster-reflection (220-reflection for (111)-clusters and 111-reflection for (110)-clusters) with an appropriate substrate-reflection (Fig. 3). This comparison showed that the (111)-clusters as well as the (110)-clusters grow coherently with respect to the substrate.

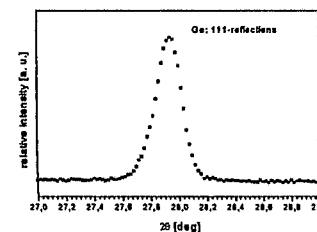


Fig. 2: $\theta/2\theta$ scan of Ge-clusters on 6H-SiC: 111-reflections of Ge

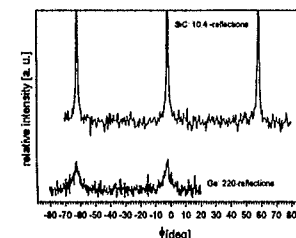



Fig. 3: Comparison of ϕ -scans of the Ge(111)-clusters (220-reflection, $\chi = 35.27^\circ$) with the the SiC substrate (10.4-reflection, $\chi = 54.79^\circ$)

 ROBL-CRG	Experiment title: Structure of thin Ta-based films	Experiment number: 20_02_025
	Beamline: BM 20	Date of experiment: from: 07.11.99 to: 08.11.99
Shifts: 5	Local contact(s): Dr. N. Schell	<i>Received at ROBL:</i> 13.03.2000
Names and affiliations of applicants (* indicates experimentalists): *N.Mattern IFW Dresden M. Hecker IFW Dresden		

Report:

The aim of the experiment was to characterise the microstructure of ultra-thin Ta-N films by reflectometry and diffraction ($\lambda=1.3817 \text{ \AA}$). Thin films were obtained by reactive sputtering onto silicon wafer. Thickness and sputtering parameters were varied. Fig. 1 shows as an example the measured reflectometry curves. Density, thickness and roughness parameters were extracted. All curves exhibit beside the ripples coming from the Ta(N) film additional oscillation. Fit of the sample set-up to the data as shown in Fig. 2 give evidence of a 2 nm Ta(N,O) film on the top of the Ta(N) film. The mass density of the Ta(N) films is identical for all samples ($15.2 \pm 0.5 \text{ gcm}^{-3}$ within a error limit of 3 %. This value is in a good agreement with

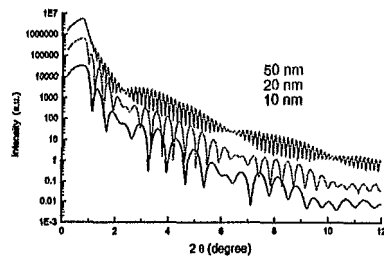


Fig.1: Reflectometry curves of Ta-N films

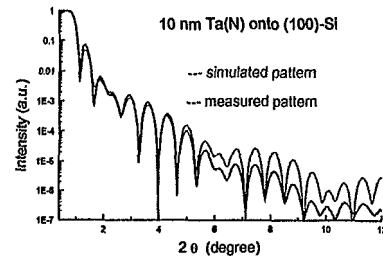


Fig.2: Comparison of reflectometry curves

interstitial solution of nitrogen in bcc Ta ($a=3.42 \text{ \AA}$). The density of the interlayer is estimated to be about $(8.3 \pm 0.5) \text{ gcm}^{-3}$. The layer sequence could be confirmed by TEM analysis [1]. The roughness of the Ta(N) films onto Si is very low. A r.m.s. value of about $1.0 - 1.5 \text{ \AA}$ is obtained independent of thickness and variation of sputtering parameters. On the other hand the deposition onto oxidized silicon leads to higher r.m.s. value ($\text{r.m.s.} = 2 \text{ \AA}$) due to the transportation of the roughness of the SiO_2 layer.

First diffraction measurement on a 10 nm Ta(N) film has been done at constant grazing incident angles with collimator. Fig. 3 shows the obtained curve ($\alpha=2^\circ$) at a short wave length ($\lambda=0.7105 \text{ \AA}$). Only diffuse maxima are visible indicating an amorphous structure. It is not possible to extract the interference function due to the high background caused by Ta-fluorescence. This test measurement promises that using a secondary monochromator this could be done. Fig. 4 shows diffraction measurements below the Ta-L edge ($\lambda=1.3817 \text{ \AA}$) varying the incident angle below and above the critical angle. Diffuse maxima of the Ta(N) film overlap with contribution of Si. The comparison with calculated pattern of bcc Ta(N) 3 nm in size shows that the film is amorphous or consists of very small bcc Ta(N) crystals.

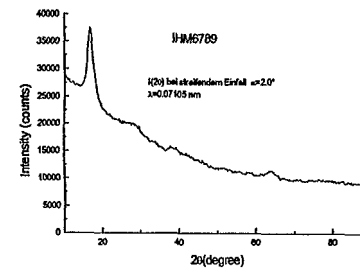


Fig.3: XRD ($\alpha=2.0^\circ$) of 10nm Ta(N) film

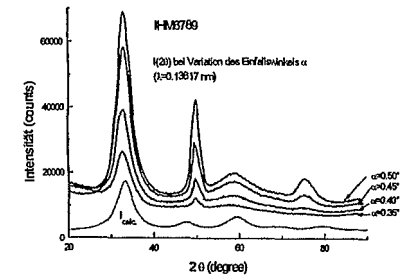



Fig.4: XRD of 10 nm Ta(N) film

[1] N. Mattern, D. Fischer, C. Wenzel, N. Schell, H. J. Engelmann, E. Zschech : "Structure characterization of Ta-N barrier layers", Proc. International Interconnect Technology Conference 05.-07.06. 2000, San Francisco

 ROBL-CRG	Experiment title: Influence of O₂ integration in a NiFe/Cu multilayer sequence on the structural properties of the layers and interfaces	Experiment number: 20_02_026
	Beamline: BM 20	Date of experiment: from: 5 / XI / 99 to: 7 / XI / 99
Shifts: 6	Local contact(s): Dr. N. Schell	<i>Received at ROBL:</i> 14.03.2000
Names and affiliations of applicants (* indicates experimentalists): * Dr. M. Hecker, IFW Dresden, Helmholtzstr. 20, 01069 Dresden Dr. C.M. Schneider, IFW Dresden, Helmholtzstr. 20, 01069 Dresden Dr. N. Mattern, IFW Dresden, Helmholtzstr. 20, 01069 Dresden		

Report:

Structural properties of metallic multilayers showing giant magnetoresistance (GMR) have been investigated by methods of X-ray reflectometry. A series of Co/Cu and NiFe/Cu multilayers with individual layer thickness of about 2nm corresponding to the second coupling maximum of the GMR have been annealed at different temperatures up to 400°C in vacuum. After annealing GMR measurements and X-ray scattering experiments were performed. The results of the experiments have been compared with those of samples annealed in air where structural changes are overlapped by the influence of oxide at the surface. Thus, the goal was to extract the changes of the interface structure due to thermal treatment from those due to surface oxidation. Although multilayers of these types have been investigated extensively in the past, the structural reasons for changes of the GMR, e.g. after heat treatment, are not completely clarified (e.g. [1-3]).

The electrical measurements of the samples show an continuous increase of the GMR from 24% in the as deposited state up to 30% after annealing at 400°C for the Co/Cu system, whereas for NiFe/Cu initial values of about 10% and a breakdown of the GMR between the annealing at 220°C and 300°C were found.


To improve the contrast for the scattering experiments between the used material combinations, the X-ray wavelength was adjusted to the Cu absorption edge. The specular scans indicate a stable layer sequence showing Kiessig fringes and Bragg peaks in the whole temperature range investigated. The interface r.m.s. roughness of initially 0.5nm was found to be nearly constant up to 400°C for Co/Cu and to increase slightly up to 0.6nm at 300°C, followed by a rising up to a formal value of 1.1nm at 400°C for NiFe/Cu. It should be considered that the latter value cannot be interpreted as the roughness of sharp interfaces but corresponds to the onset of interdiffusion in the NiFe/Cu system as proved by AES.

From the measurements of the diffuse scattering a nearly constant correlation of the roughness between the layer interfaces can be deduced for both multilayer systems, decreasing for NiFe/Cu beyond 300°C. Thus, the scattering measurements indicate that the GMR breakdown is accompanied a relatively small roughness increase. Additional diffraction experiments in the wide-angle region yield growing grains, increasing tensile stresses and modifications of the initially sharp {111}-texture. The experiments suggest that the key mechanism responsible for the GMR changes could be the onset of grain-boundary diffusion at elevated temperatures.

[1] D.E. Joyce, C.A. Faunce, P.J. Grundy, B.D. Fulthorpe, T.P.A. Hase, I. Pape, B.K. Tanner, *Phys. Rev.* **1998**, B58, 5594.

[2] C.C. Tang, E.J. Mac Lean, N.D. Telling, *J. Magn. Magn. Mat.* **1999**, 198-199, 653.

[3] K. Rätzke, M.J. Hall, D.B. Jardine, W.C. Shih, R.E. Somekh, A.L. Greer, *J. Magn. Magn. Mat.* **1999**, 198-199, 653.

 ROBL-CRG	Experiment title: Scanning XRD Investigations of the gradient of martensite content in fatigued steel X6CrNiTi18.10	Experiment number: 20_02_027
	Beamline: BM 20	Date of experiment: from: 03-Nov-99 to: 05-Nov-99
Shifts: 6	Local contact(s): Dr. N. Schell	Received at ROBL: 10.02.2000
Names and affiliations of applicants (* indicates experimentalists): Mirco Grosse*, Markus Niffenegger*, Paul Scherrer Institut Villigen, Switzerland		

Report:

Cyclic strains lead to material degradation known as fatigue damage and finally to failure of engineering components. However, in some meta-stable austenitic steels such cyclic loads are accompanied by strain-induced martensitic transformation. In order to investigate under which conditions the formation of martensite occurs, the martensite content in dependence on the radial (y-) and axial (x-) location was estimated by X-ray diffraction (XRD) at a length cut of a „hour glass“ sample (ASTM E606, Fig. 1). Due to this sample shape, different strain amplitudes were realised at different axial positions of one sample.

In order to use the structure data from literature, the wavelength of the Mo-K α radiation ($\lambda = 0.07107$ nm) was applied. A mapping of the axial and radial martensite distribution were gained by scanning the sample through the fixed beam.

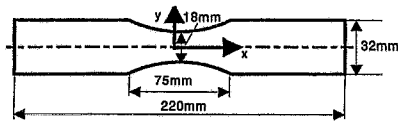


Fig. 1: Geometry of the hour glass sample

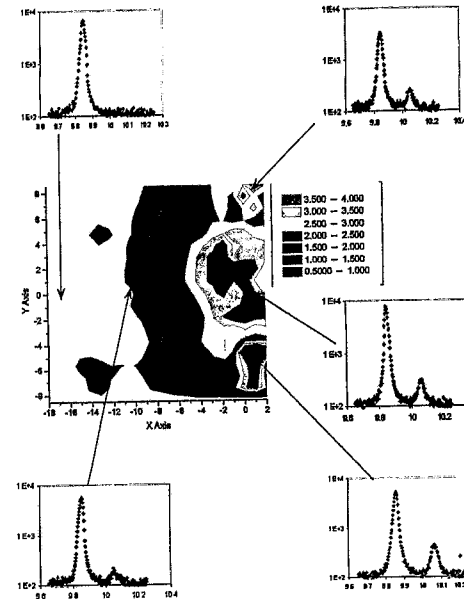


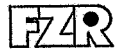
Fig. 2: Axial (x) and radial (y) mapping of martensite content depending on the sample location connected with typical diffraction patterns.

Due to the applied wave length and the beam cross section of 0.2 mm * 0.5 mm, a gauge volume of about 1 mm (axial) * 0.5 mm (radial) * 0.005 mm (in depth) was achieved.

For the estimation of the martensite content, the intensity of the {111} austenite and the {110} martensite peak were compared. Due to the very small beam size, the very small beam divergence and

relative large grain size of the austenite (diameter about 20 - 30 μ m), the statistic condition for a polycrystal (number of grains seen by the beam $N_G \rightarrow \infty$, in reality $N_G > 1000$) is not completely fulfilled. As a consequence, the intensity values of the {111} austenite reflexion of different locations are in a large scattering band. The grain size of the martensite is small enough and their number high enough to fulfil this condition. Because the mentioned percentage of the martensite is very small the mean value of the austenite {111} intensity can be used for phase analysis. Using this mean value, the relative error is in order of magnitude of the martensite content (< 6 %).

Fig. 2 shows the axial and radial mapping of the martensite content. Some typical scattering pattern are included. At x-locations below -16 mm, corresponding to a strain amplitude of 2.25 mm/m, no martensite was found. At $x = -10$ mm martensite can be found at the whole sample diameter. This location correlates with a strain amplitude of 2.65 mm/m. At the smallest sample cross section the martensite is concentrated near the surface. Additionally, a broad area with a relative high martensite content was found in the middle of the sample ($x = 0$, $y = 0$). At the crack location ($x = 1$ mm, $y = -8 .. -4$ mm) the martensite content reaches maximum values.

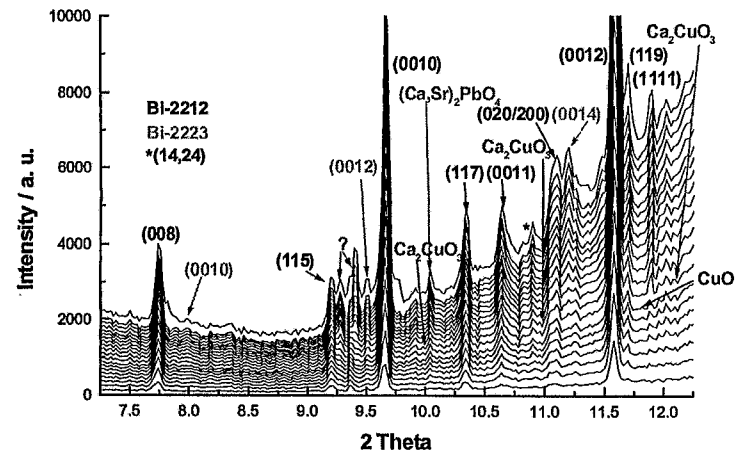
 ROBL-CRG	Experiment title: Diffraction of Synchrotron Radiation at Bi-2223/Ag Superconductors at High Temperature	Experiment number: 20_02_28
	Beamline: BM 20	Date of experiment: from: 24-Nov-99 to:30-Nov-99
Shifts: 18	Local contact(s): Schell, Norbert	<i>Received at ROBL:</i> 02. 05. 2000
Names and affiliations of applicants (* indicates experimentalists): Fahr, Torsten (*), Haessler, Wolfgang (*), Kobernik, Gert (*) Institute of Solid State and Materials Research Dresden, P. O. Box 27 00 16, D-01171 Dresden, Germany		

Report:

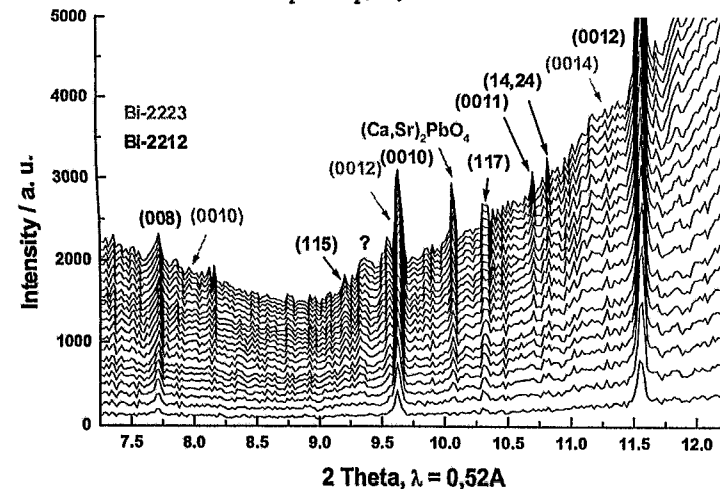
Diffraction measurements on Bi-2223/Ag superconducting tapes have been performed under reaction conditions. A reactor chamber PAAR HTK 900 has been employed with the specimens mounted on a sample holder (Ni-based alloy). This setup allowed for heating the samples in controlled atmosphere with the measurements performed in Bragg-Brentano geometry (reflection with transmission of the Ag surrounding the ceramics). The specimens investigated had two different chemical compositions of the starting precursor material (tape A and B). The state of the processing of the tapes was prior to the thermal treatment to characterise the changes in the crystalline phase assemblage during the first annealing cycle. The figure shows in situ measured diffraction patterns in reaction gas atmosphere. It is shown that the intensity of the reflections is rather low. The patterns could only be recorded after the upper silver layer has slightly been grinded off from the specimens. This might be due to the fact that the diffracted intensity was too low for the long penetration pathway through the silver at diffraction angles in the range $6 \leq 2\theta \leq 16^\circ$. Nevertheless, in both samples qualitatively the same reaction could be detected. At the first, the Bi-2212 phase shows a strong crystal growth and formation of a c-axis fibre texture, evident by strong (00l) reflections with respect to (hkl) reflections and a decrease of FWHM (00l). In both cases only a very slow formation


of Bi-2223 could be found. Instead, the precursor phases Ca_2CuO_3 and CuO form $(\text{Ca,Sr})_2\text{PbO}_4$ and $(\text{Sr,Ca})_{14}\text{Cu}_{24}\text{O}_x$ ((14,24)-phase).

Diffraction patterns of multifilamentary Bi-2223 / Ag conductors detected at 825 °C in N_2 / 8% O_2 ; Tape A



Diffraction patterns of multifilamentary Bi-2223 / Ag conductors detected at 825 °C in N_2 / 8% O_2 ; Tape B



 ROBL-CRG	Experiment title: Study of structural properties of sputter-deposited and selfassembled multilayer waveguides	Experiment number: 20_02_029
	Beamline: BM 20	Date of experiment: from: 21.-24.01.00 and 05.-06.07.00,
Shifts: 10 + 6	Local contact(s): N. Schell	Received at ROBL: 10.4.2001
Names and affiliations of applicants (* indicates experimentalists): Franz Pfeiffer*, Ulrike Mennicke*, Tim Salditt* Experimentalphysik, Universitaet des Saarlandes, Im Stadtwald 38, Postfach 15 11 50, 66041 Saarbruecken, Germany Email: salditt@mx.uni-saarland.de Fax: 49 681 302 2819; Phone: 49 681 302 2216		

Report:

We report a x-ray diffraction experiment of multilamellar membranes incorporated into a resonant beam coupler or x-ray waveguide structure. In the device, the lipid bilayers are confined to one side by the silicon substrate and to the other side by an evaporated thin metal cap layer. By shining a highly brilliant x-ray beam onto the system, we could excite resonantly enhanced, precisely defined and clearly distinguishable standing wave field distributions (modes). The in-plane structure of the acyl chain ordering was then be studied by grazing incidence diffraction under simultaneously excited modes. A significant gain in signal-to-noise ratio as well as an additional spacial resolution can be obtained in such a setup. The technique can be generalized to various kinds of organic thin film samples, ranging from synthetic polymers to two-dimensional protein crystals, and can be used to study macromolecular and supramolecular structure, and in future possibly also dynamics. In the present experiment we have validating earlier measurements by our group carried out at the D4 bending magnet of HASYLAB, and, in addition, have shown for the first time, that the incorporated lipid membranes can undergo a phase transition from the liquid crystalline gel phase to the so-called liquid L_{α} -phase. The brilliance of an ESRF bending magnet is ideally suited to map out the short range structural correlations in the plane of the membrane (acyl chains), even at small scattering volumes corresponding to about 10 bilayers. The experiment was carried out at an x-ray energy of 13 keV. The grazing incidence diffraction scans performed under simultaneous excitation of the waveguide modes demanding high angular precision could easily be implemented on the Huber 6-circle diffractometer. A resonant enhanced standing electromagnetic field is generated between two parallel surfaces with an comparably large critical angle α_c separated by a medium that is suitable thick and x-ray transparent (low density organic films) [1-5]. Fig. 1 shows the reflectivity of a hybrid organic-inorganic waveguide consisting of a stack of about ten phospholipid bilayers prepared by a new spin-coating method on silicon substrate and cap-

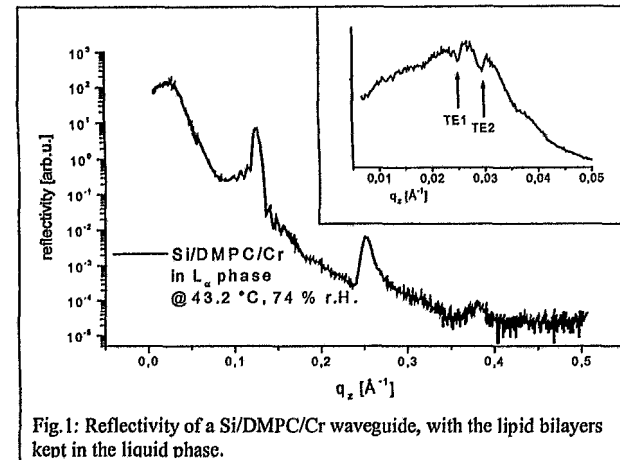
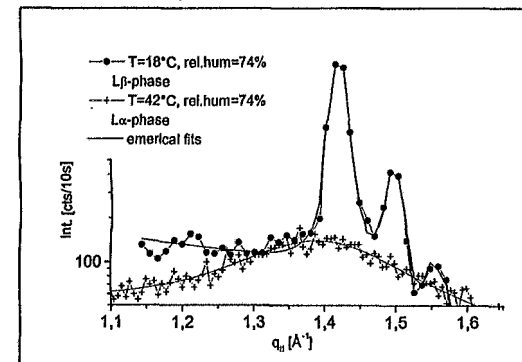


Fig. 1: Reflectivity of a Si/DMPC/Cr waveguide, with the lipid bilayers kept in the liquid phase.


ped by an evaporated Cr cap. Note that the lipid bilayers are in the liquid phase. Several different standing electromagnetic field-distributions (modes) are resonantly excited by shining a parallel beam onto the waveguide under grazing incidence at a set of discrete angles α_i slightly bigger than the critical angle of the spacer layer, as evidenced by the corresponding cups in the reflectivity profile (inset).

To gain an understanding of the mode excitation, we have calculated the internal (and external) standing electromagnetic field as a function of the structural and geometric parameters (layer-thickness, composition and density, interface roughness, angles of incidence, x-ray energy) by a transfer matrix algorithm similar to the one used in the case of optical waveguides. Equivalently, one can use the well known Parratt-formalism for such calculations. The measured reflectivity profiles along the GID scans with the peaks reflecting the acyl chain packing are currently analyzed. At this point we can safely claim that interesting projects on organic-inorganic waveguide hybrids will be possible in future. The setup may present an opportunity to study thin organic films in resonantly enhanced films with unprecedented signal to noise ratios.



References:

- [1] Y.P. Feng, S.K. Sinha, H.W. Deckmann, et al., Phys.Rev.Lett 71, 537 (1993); Y.P. Feng, S.K. Sinha, E.E. Fullerton, et al., Appl.Phys.Lett. 67 3657 (1995).
- [2] S. Lagomarsino, W. Jark, S. Di Fonzo, et al., J. Appl.Phys. 79, 4471 (1996); S. Lagomarsino, A. Cedola, P. Cloetens, et al., Appl.Phys.Lett. 71, 2557 (1997).
- [4] F. Pfeiffer, T. Salditt, P. Hoghoj, C. David, New design schemes for x-ray waveguides based on multiple guiding layers and two-dimensional structuring techniques SPIE, in press.
- [5] F. Pfeiffer, T. Salditt, P. Hoghoj, I. Anderson, N. Schell, X-ray waveguides with multiple guiding layers, Physical Review B 62, 16939-16943 (2000).

 ROBL-CRG	Experiment title: Investigation of the lateral ordering in InGaAsP/InP substrate	Experiment number: 20_02_030
	Beamline: BM 20	Date of experiment: from: 28.01.2000 to: 01.02.2000
Shifts: 12	Local contact(s): Dr. Norbert Schell Phone: 00 33 47688 2367 e-mail: schell@esrf.fr	Received at ROBL: 01.02.2001
Names and affiliations of applicants (* indicates experimentalists): Jerzy Sass*, Krystyna Mazur*, Institute of Electronic Materials Technology Wólczyńska 133, 01-919 Warsaw, Poland Phone: (4822) 835 30 41 -144; e-mail: sass_j@sp.itme.edu.pl; mazur_k@sp.itme.edu.pl Frank Eichhorn*, Institute of Ion Beam Physics and Materials Research, FZR, POB 510 119, D 1314 Dresden, Germany		

Report:

A series of $\text{In}_{0.86}\text{Ga}_{0.14}\text{As}$ epitaxial layers with different thicknesses grown on the InP (001) substrates were investigated. The theoretical critical thickness of this heteroepitaxial system is $h_c = 40 \text{ \AA}$. The investigations of the structural properties were performed in the thickness range above and below the critical thickness h_c . Nominal thicknesses of the epitaxial layers were: $h_1 = 12 \text{ \AA}$, $h_2 = 16 \text{ \AA}$, $h_3 = 28 \text{ \AA}$, $h_4 = 40 \text{ \AA}$, $h_5 = 60 \text{ \AA}$, and $h_6 = 120 \text{ \AA}$. The measurements were carried out for 004 symmetrical reflection using the ROBL high resolution diffractometer with the radiation wavelength $\lambda = 1.196 \text{ \AA}$. The minimum detectable layer thickness turned out to be 28 \AA . The best results obtained for the thickest epitaxial layer $h_6 = 120 \text{ \AA}$ and are presented in Figs.1 and 2. The appearance of high order sideband reflections indicates the very good crystalline structure of the investigated epitaxial layer. From the angular sideband positions the layer thickness has been calculated to be $h_6 = 152 \text{ \AA}$.

The omega scan performed for the layer 004 reflection (Fig. 2) shows that the relaxation mechanism is due rather to the formation of misfit dislocations than to a ripple structure. The kinematical scattering component (the upper part of the figure) and the diffuse component with two lobes are clearly visible. The presented distribution of the diffusion scattering intensity

indicates that the condition $\rho h < 1$ is fulfilled, where ρ is linear dislocations density.

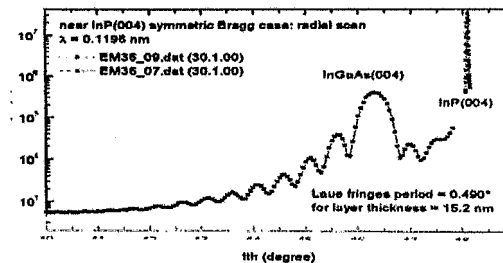


Fig.1. $\theta/2\theta$ scan for the epitaxial layer of the nominal thickness $h_6 = 120 \text{ \AA}$; 004 reflexion.

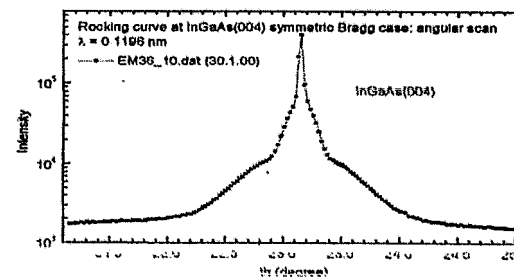



Fig.2. Omega scan for the epitaxial layer of nominal layer thickness $h_6 = 120 \text{ \AA}$; 004 reflexion.

Further, the studies at a stepped surface formed on the 5° cutoff (in the 110 direction) 001 GaAs samples were performed. The investigation were performed by means of high angle diffractometry and reflectometry (specular and non specular case). All these methods did not reveal any effects due to the lateral structure. Only the non specular method showed the typical intensity oscillations for the unetched 5° cutoff 001 GaAs sample. The omega measurements were performed at different 2θ position close to the critical angle. The best results we obtained for counter position $2\theta = 1.0^\circ$. The lateral correlation length as determined from the angular distance between neighbouring intensity maxima amounts to 97.5 nm .

	Experiment title: Structural changes during annealing processes of PII Implanted Ti64 alloys	Experiment number: 20_02_031(a)
	Beamline: BM 20	Date of experiment: (long term) from: 26.01.2000 to: 07.03.2001
Shifts: 12	Local contact(s): N. Schell	<i>Received at ROBL:</i> 15. 4. 2001
Names and affiliations of applicants (* indicates experimentalists): **F. Berberich, **W. Matz, **N. Schell, *E. Richter *Forschungszentrum Rossendorf, Institute of Ion Beam Physics and Materials Research, P.O. Box 510119, D-01314 Dresden, Germany #ROBL – CRG at ESRF		

Report:

The surface hardness of the titanium alloy Ti-6Al-4V, widely used as construction material, may be improved by nitrogen implantation [1]. Plasma immersion ion implantation (PIII) produces a nitrogen profile directly below the surface. In-situ X-ray diffraction experiments were performed using a high-temperature diffraction chamber. At the wavelength of 0.154 nm grazing incidence technique was applied. By varying the angle of incidence from 0.5° to 4° depth dependent structural information is obtained from 0.1 to 1 μm assuming an average density of 4.43 g/cm³ for Ti-6Al-4V.

In order to characterise the structural changes of different PIII samples during annealing, which should cause the increased hardness, in-situ XRD experiments were performed. Ti-6Al-4V samples implanted with a fluence of 1.7×10^{17} N⁺/cm² were used. The scanning time for each diffraction pattern was 30 min. So the duration of the in-situ experiment corresponds to the typical annealing time used for such alloys. The spectra measured at incidence angles of 1° are most sensitive to the surface layer and show the formation of the TiN phase much clearer than those ones received at higher incidence angles. Figure 1 depicts the spectra at the incidence angle of 1° for RT (before and after annealing) and at the various annealing temperatures.

At 500°C the pattern consists of the Bragg peaks of both Ti phases ($\alpha + \beta$) and TiN formed by implantation. The TiN peaks are very broad, indicating a small crystallite size of about 10 nm calculated with the Scherrer formula. The lattice constant of TiN

was determined to $a = 0.4217$ nm. This value is -0.7% different from the value for the stoichiometric phase [2] which may indicate a nitrogen deficit. With increasing temperatures the intensity of the TiN peaks decreases. In Figure 1 this can most clearly be observed for the (200)TiN peak at 2θ of 42.6°. At 750°C, however, a new peak appears at slightly lower Bragg angle than the TiN peak observed so far. It remains in the pattern after the annealing process when cooling the sample to RT. At isothermal time dependent experiments it was found, that this peak does not arise from a peak shift, but it is growing only after the disappearance of the original TiN peak. The two other peaks of low intensity, marked with '▼', which belong to the pattern are also observed. After annealing the lattice parameter of the phase TiN* is slightly different from the initial one and amounts $a = 0.428$ nm.

The start of Ti₂N formation is observed at temperatures between 600 and 650°C. At the final temperature of 750°C, as well as at the RT measurement after the annealing process, the Ti₂N peaks are clearly detected. These peaks are much sharper than the former TiN peaks, indicating crystallites of Ti₂N with average sizes of 35-40 nm.

The data were correlated with hardness, ERDA, and SEM results [3].

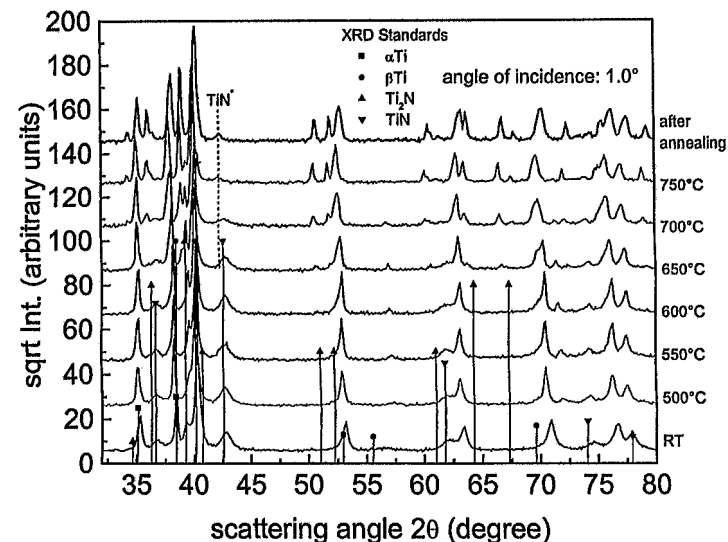



Figure 1: XRD spectra recorded at the angle of incidence of 1° during in-situ annealing of nitrogen implanted TiAlV alloy using PIII

- [1] F. Berberich, W. Matz, E. Richter, N. Schell, U. Kreißig and W. Möller, Surface and Coatings Technology, 128-129 (2000), 450-454
- [2] Powder diffraction file PDF-2, No. 38-1420; ICDD, Newton Square, PA 19073-3273, USA
- [3] F. Berberich, W. Matz, U. Kreißig, E. Richter, N. Schell, and W. Möller, Appl. Surf. Sci. (2001) in press (Proc. AOFA 11)

	Experiment title: Determination of activation energies of the phase dissolution of TiN and Ti₂N of N implanted Ti6Al4V	Experiment number: 20_02_031(b)
	Beamline: BM 20	Date of experiment: (long term) from: 26.01.2000 to: 07.03.2001
Shifts: 24	Local contact(s): N. Schell	Received at ROBL: 10. 4. 2001
Names and affiliations of applicants (* indicates experimentalists): **F. Berberich, **W. Matz, #N. Schell, *E. Richter *Forschungszentrum Rossendorf, Institute of Ion Beam Physics and Materials Research, P.O. Box 510119, D-01314 Dresden, Germany #ROBL – CRG at ESRF		

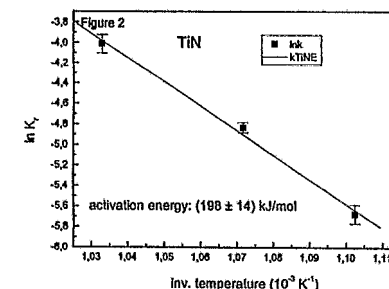
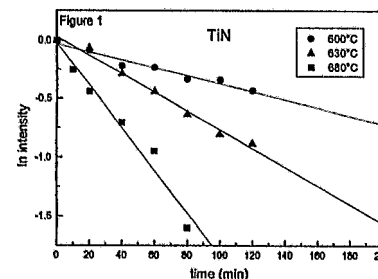
Report:

In former annealing experiments at the ROBL with nitrogen implanted Ti-6Al-4V a phase transformation from TiN to Ti₂N was found. This experiment was performed to find the activation energies for the dissolution of TiN and Ti₂N crystallites. The experiments were performed using the ROBL high temperature chamber. Ion beam and plasma ion immersion implanted samples were investigated. For the ion beam implanted samples different implantation energies were studied. The dynamic dissolution process of the TiN phase was studied recording the (200) Bragg peak during isothermal experiments at three different temperatures. The appropriate temperatures were estimated from the previously performed temperature scans. At the wavelength of 0.154 nm grazing incidence technique was applied. Some experiments were done at different incidence angles to compare the dynamical process in different depths but no significant changes were recorded.

All measured peaks were fitted with Gaussian curves. Without texture, the integrated intensity of the Bragg peak should be proportional to the amount of crystallites. With the data taken at three temperatures it is possible to

calculate three different reaction velocities. From estimated velocities at different temperatures follows the activation energy by an Arrhenius plot. The decrease of intensity of the TiN (200) Bragg reflection with time is depicted in figure 1. To normalisation of the intensities was performed relative to the room temperature peaks. Figure 2 shows the corresponding Arrhenius plot.

For a comparison with the literature data one has to take into consideration that the activation energy is a temperature dependent value, i.e. for TiN we found an activation energy of 198 ± 14 kJ/mol for the temperature range 600°C-800°C. The literature value [1] is given by 210 kJ/mol for a temperature range of 1300°C to 1670°C. As the activation energy becomes higher for higher temperatures the value obtained by the XRD measurement corresponds well.




Time dependent decomposition of TiN in Ti-6Al-4V alloy. Ion beam implanted sample at 80 keV with a fluence of 6×10^{17} N⁺/cm²

Figure 1: integrated intensity of the TiN 200 Bragg peak, measured with an angle of incidence of 1°.

Figure 2: corresponding Arrhenius plot to derive the activation energy

[1] F.W. Wood, O.G. Paasche, Thin solid films, 40 (1977) 133-137

	Experiment title: Depth resolved XRD analysis of nitrogen implanted Ti-6Al-4V alloys	Experiment number: 20_02_031(c)
	Beamline: BM 20	Date of experiment: (long term) from: 26.01.200 to: 07.03.2001
Shifts: 10	Local contact(s): N. Schell	<i>Received at ROBL:</i> 15.4.2001
Names and affiliations of applicants (* indicates experimentalists): ** F. Berberich, * W. Matz * Forschungszentrum Rossendorf, Institute of Ion Beam Physics and Materials Research, P.O. Box 510119, D-01314 Dresden, Germany # ROBL - CRG at ESRF		

Report:

With the x-ray diffraction analysis adapted for grazing incidence diffraction (GID) geometry it is possible to investigate depth distribution of crystalline phases. It is based on the changes the average penetration depth of the x-ray beam under variation of the incident angle (α_i). However, it is not easy to detect from such experiments the real depth distribution of a crystal structures. The scattering volume is not well defined because of the exponential attenuation of the x-ray intensity in the sample. The scattering is accumulative, so the signal from the surface will be present at all greater α_i . A difference method is not applicable because of different absorption coefficients. To find the real phase distribution the theory of the standing wave field was used. The scattered intensity is given by:

$$I(\alpha_i) = I_0 \int_{-\infty}^0 \int |E_r(r, k)|^2 g(z) dz$$

Were I_0 is the normal intensity, E_r is the electrical field calculated from the standing wave field [1] and $g(z)$ is the distribution function of the scatterers. Thus by fitting $I(\alpha_i)$ with a model function $g(z)$ to the measured values of a certain sample the depth distribution can be derived.

The aim of the experiment was to show the different phase distribution of TiN and Ti₂N in the nitrogen implanted Ti-6Al-4V alloys. The used samples were implanted with ion beam implantation technique at different energies (from 20 keV to 180 keV) and different fluences ($1 - 6 \times 10^{17} \text{ N}^+/\text{cm}^2$). So, it was possible to compare in the GID implantation depth profiles of 100 up to 200 nm. Further samples were implanted by plasma ion immersion

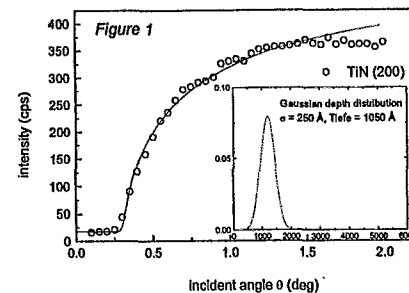


Figure 1: measured and simulated depth distribution of TiN (200) reflex of an ion beam implanted Ti-6Al-4V sample. Implanted fluence: $6 \times 10^{17} \text{ N}^+/\text{cm}^2$ with an implantation energy of 80 keV

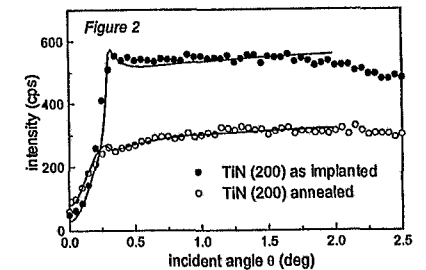
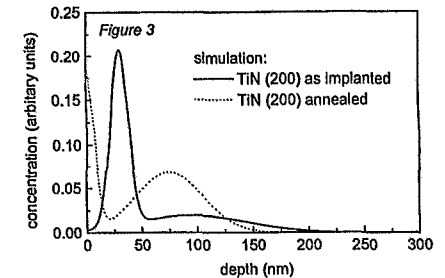


Figure 2 measured and **Figure 3** simulated depth distribution of TiN (200) reflex of a PII implanted Ti-6Al-4V sample. Implanted fluence: $2 \times 10^{17} \text{ N}^+/\text{cm}^2$ with an implantation energy of 40 (20) keV.




(PII) with a fluence of $2.0 \times 10^{17} \text{ N}^+/\text{cm}^2$. With this technique nitrogen is deposited only very near to the surface.

All samples were studied in the as-implanted and in the annealed state. For all samples the depth profile of characteristic Bragg reflections were recorded by varying the incident angle from 0° to 2° at a wave length of $\lambda = 0.154 \text{ nm}$.

The result for an ion beam implanted sample in the as-implanted state is given in Figure 1. The simulation shows the maximum of the Gaussian depth profile at a depth of 135 nm. Former investigations with the elastic recoil detection analysis [2] have indicated that the maximum of the nitrogen concentration lies at a depth of 146 nm with also a Gaussian depth profile.

Figure 2 depicts the result for a PII implanted sample in the as-implanted state and after annealing at 680°C for 2 h. Both curves show in principle the same behaviour: the occurrence of a resonance peak near the critical angle of Ti-6Al-4V of $\alpha_{\text{crit}} = 0.3^\circ$. For this example it is only possible to get a well adapted curve if two Gaussian distributions are used as it is shown in Figure 3. One at the surface, the second one in the deeper region of about 80 nm. The ratio of the two normalized concentrations give a hint to a starting diffusion process and beyond to the phase formation in deeper regions.

- [1] D. Windt, Computers in Physics, IMD--Software for modeling the optical properties of multilayer films: 12 (4) (1998), 360
 [2] F. Berberich, W. Matz, E. Richter, N. Schell, U. Kreißig and W. Möller, Surface and Coatings Technology, 128-129 (2000), 450-454

	Experiment title: Analysis of the defect structure in severely deformed micro-, submicro- and nano-crystalline nickel after thermal treatment.	Experiment number: 20_02_032
	Beamline: BM 20	Date of experiment: from: 04-Mar-00 to: 08-Mar-00
Shifts: 12	Local contact(s): Dr. Norbert Schell	<i>Received at ROBL:</i> 2 June 2000
Names and affiliations of applicants (* indicates experimentalists): Ellen Thiele*, Robert Klemm* Institute of Physical Metallurgy, Technical University Dresden D-01062 Dresden Germany		

Report:

Introduction. Due to their small grain size combined with high internal stresses metals treated by severe plastic deformation show unusual mechanical properties, e.g. a sufficient ductility at a comparatively high yield stress. For the application of these materials the knowledge of the thermal stability of the structure is necessary. Therefore the purpose of the present experiment was to characterise the structure both in compact submicrocrystalline (sc) nickel samples (mean grain size $d \approx 300\text{nm}$) produced by equal channel angular pressing [1] and in nanocrystalline (nc) nickel powder ($d \approx 70\text{nm}$) obtained by ball milling [2] and to study the structure changes in different annealing stages.

Experimental. Using a wavelength $\lambda = 0.154\text{nm}$ BRAGG-diffraction profiles of seven different $\{hkl\}$ -types from $\{111\}$ - up to $\{331\}$ -type were measured with diffraction vectors g perpendicular to the sample surface. Taking into account the strong profile broadening caused by small coherently scattering regions and by lattice defects in principle it was possible to measure diffraction profiles with negligible instrumental broadening and background. For the evaluation of the measuring data quantitative parameters of the profiles as for example the half width FWHM and the integral breadth IB as well as the profile fourier coefficients were determined.

Results and discussion. The mean size D of coherently scattering regions and the root mean square stress $\langle \sigma^2 \rangle^{1/2}$ were calculated from a modified WILLIAMSON-HALL-plot of the FWHM-values taking into account the $\{hkl\}$ -dependent elastic module. To get information concerning the mean dislocation density ρ the KRIVOGLAZ-WILKENS-plot of the fourier coefficients was employed. The dependencies of D and $\langle \sigma^2 \rangle^{1/2}$ from the temperature T after isochronal annealing for 30 min are shown in Fig. 1 for the sc nickel, and in Fig. 2 for the nc nickel.

In the high-purity sc nickel samples $\langle \sigma^2 \rangle^{1/2}$ is reduced by about 40% at 175°C while D remains constant. In the narrow temperature range $175^\circ\text{C} < T < 225^\circ\text{C}$ the rms stress decreases to zero whereas the size D increases sharply. From SEM investigations it is known that after annealing at 225°C the mean grain size is about 500nm .

In contrast, there is a higher thermal stability of the nc nickel. Though the nc nickel of lower purity due to the milling process shows a remarkably higher rms stress and a smaller D -value than the sc nickel before annealing, the recovery of lattice defects and the increase of D take place in stages over the whole temperature range from 75°C up to 900°C . The increase of D sets in at $T > 350^\circ\text{C}$ after a diminishing of $\langle \sigma^2 \rangle^{1/2}$ to a half. The growth of D is coupled with a gradually vanishing of $\langle \sigma^2 \rangle^{1/2}$.

Analysing the behaviour of the different $\{hkl\}$ -reflection types on the one hand there is a significant influence of the elastic anisotropy on the profile broadening. On the other hand the different reflection types are sensitive to different lattice defects. So especially for the sc samples the $\{311\}$ -profiles already change at lower annealing temperatures, and $\{111\}$ -profiles at higher temperatures than the other reflection types.

From the KRIVOGLAZ-WILKENS-analysis [3] of the fourier coefficients of $\{311\}$ - and $\{111\}$ -profiles one has to conclude that not only the size of coherently scattering regions D and a mean dislocation density can be responsible for the profile broadening. According to the profile width reduction observed at comparatively low temperatures where dislocations cannot recover this is a hint for the existence of lattice strains which can relax at temperatures where point defects become mobile.

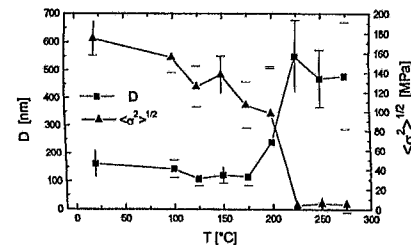


Fig. 1 submicrocrystalline nickel

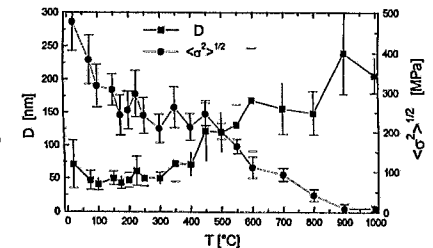
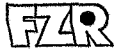


Fig. 2 nanocrystalline nickel

Mean size D of coherently scattering regions and rms stress $\langle \sigma^2 \rangle^{1/2}$ after annealing of the sc and nc nickel samples for 30 min at the temperature T . The error bars indicate mainly the data scattering in the Williamson-Hall plot due to the different annealing behaviour and grain growth observed on the different $\{hkl\}$ lattice planes.

References


- [1] R.Z. Valiev, Mat. Sci. Eng. **A234-236** (1997) 59-66.
- [2] J. Eckert, J.C. Holzer, C.E. Krill, W. L. Johnson, J Mater. Res. **7** (1992) 7, 1751-1761.
- [3] D. Breuer, P. Klimanek, U. Mühle, U. Martin, Z. Metallkd. **88** (1997) 680-686.

 ROBL-CRG	Experiment title: X-Ray Investigation of Silicon / Germanium Nanostructures on Silicon Carbide	Experiment number: 20_02_33
	Beamline: BM 20	Date of experiment: from: 4/14/2000 to: 4/18/2000
Shifts: 12	Local contact(s): Dr. Norbert Schell	<i>Received at ROBL:</i> 2. 9. 2000
Names and affiliations of applicants (* indicates experimentalists): Andreas Bauer* Dr. Günter Heß* Dr. Jürgen Kräußlich* Prof. Dr. Konrad Goetz Friedrich Schiller University of Jena Institute of Optics and Quantumelectronics, Department of X-ray Physics Max-Wien-Platz 1 D-07743 Jena / Germany		

Report:

In the following we present results about Si/Ge-nanocrystal samples, selectively grown under the following conditions. Si was evaporated by means of an electron beam and deposited on 6H-SiC(0001) at a substrate temperatures of 600°C (sample A: Si, growth rate 5 ML/min). Ge was deposited on a carbon-rich 6H-SiC(0001) surface from effusion cells at a substrate temperature of 470°C, but with different growth rates (sample C: Ge, 0.8 ML/min, sample D: Ge, 4 ML/min). Additionally, one sample was grown on a Si-rich 6H-SiC(0001) surface by depositing Ge at 300°C and subsequent annealing at 800°C for 2 minutes (sample B: Ge, annealed). The x-ray diffractograms ($\theta/2\theta$ -scans) of sample A (Si-nanocrystals: average width is 200 nm, average height is 45 nm) showed the occurrence of 111- and 220-reflections at the respective bulk positions. This observation reveals unambiguously that the Si-nanocrystals grow preferentially in two different orientations $\langle 111 \rangle$ and $\langle 110 \rangle$ with respect to the surface normal. Considering the multiplicities and the structure factor,

the peak areas can be used to calculate the ratio between $\langle 111 \rangle$ - and $\langle 110 \rangle$ -nanocrystals. Such a calculation results 70% $\langle 111 \rangle$ - and 30% $\langle 110 \rangle$ -nanocrystals for sample A. A similar behavior has been found for Ge-nanocrystals grown with growth rates above 3 ML/min (sample D: 84% $\langle 111 \rangle$ - and 16% $\langle 110 \rangle$ -nanocrystals). However, by using Ge growth rate below 1 ML/min, the diffractograms showed that we were able to grow (111)-nanocrystals selectively (sample C). Interestingly, for Ge-nanocrystals grown on Si-rich SiC-surfaces (sample B), we observe that the Ge-reflections are shifted towards the angular position of the corresponding Si-reflection. Using Vegards law, it is possible to calculate the average composition of the nanocrystals from the peak shift (60% Si for sample B). The lateral orientation of the (111)-nanocrystals was investigated using skew reflections (surface normal inclined with respect to the scattering plane). ϕ -scans of skew 220-reflection of the (111)-nanocrystals around the surface normal reveal that the projection of the nanocrystal a -axis onto the surface plane is parallel to the $[10\bar{1}0]$ -direction of the substrate. This observation shows clearly that the $\langle 111 \rangle$ -nanocrystals grow coherently with respect to the substrate. Note, that the skew $10\bar{1}4$ -reflection of 6H-SiC(0001) was used as a reference to determine the position of the a -axis of the substrate. It should be mentioned here that a similar behavior was found for the $\langle 110 \rangle$ -nanocrystals. Furthermore, the six-fold symmetry of the ϕ -scans shows clearly the existence of rotation twins. Since the FWHM of the ϕ -scan reflects the degree of coherence between nanocrystals and substrate, our data reveal that the correlation between the Si-nanocrystals and SiC (FWHM = 0.8°) is much better than the correlation between Ge-nanocrystals (sample C: FWHM = 10°) and SiC. Moreover, the Ge-nanocrystals grown at "high flux" conditions (sample D: growth rate 4 ML/min, FWHM > 20°) grow almost incoherent to the substrate. Obviously, the Ge-nanocrystals avoid the stress and strain due to the larger lattice mismatch compared with Si by a poor alignment to the substrate. The ϕ -scan of sample B (Si/Ge alloy, FWHM = 5°) shows that the alignment might be improved by increasing the amount of Si within the Ge-nanocrystal.

 ROBL-CRG	Experiment title: Determination of phase formation processes in nanoscale Co-Ti layers using synchrotron radiation in conjunction with a high temperature chamber.	Experiment number: 20_02_034
	Beamline: BM 20	Date of experiment: from: 21.4.00 to: 23.4.00
Shifts: 6	Local contact(s): Florian Berberich, FZR	<i>Received at ROBL:</i> 15. 03. 2001
Names and affiliations of applicants (* indicates experimentalists): Jochen Rinderknecht*, AMD Saxony Manufacturing GmbH, Dresden Florian Berberich*, Forschungszentrum Rossendorf Dr. Ehrenfried Zschech, AMD Saxony Manufacturing GmbH, Dresden Dr. Wolfgang Matz, Forschungszentrum Rossendorf		

Report:

The goal of the experiment was to study the phase formation processes within the system Cobalt – Titanium – Silicon in the temperature range between 300°C and 775°C. All measurements were performed at the ROBL Beamline using a Huber six circle goniometer and a modified vacatable high temperature diffraction chamber HDC 2.4 using a grazing incidence X-ray diffraction geometry (GIXRD) with $\alpha_i = 0,5^\circ$. A wavelength of 1,648Å was used to avoid fluorescence radiation of Cobalt. All intensities were corrected for decreasing primary intensity over time.

Samples: 9 x 9 mm², cut at 45° to (100) Si orientation to avoid substrate diffraction peaks. Initial layer stack of the samples was epitaxially (004) grown Si on single crystal Si / 10 nm Co / 10 nm Ti. The Titanium layer is supposed to act as an Oxygen gettering layer to prevent Cobalt from oxidation.

Two different sets of measurements were performed:

- heating up – measuring – further heating up
- heating up – measuring – cooling down

Results:

Despite the fact that the theoretical phase formation process for bulk material predicts the formation of Co₂Si, no traces of Co₂Si could be identified. At 300°C, first hints of diffraction peaks of CoSi could be seen in coexistence with a very broad Co peak which vanishes at 325°C. Between 325°C and 525°C, only CoSi is present. At 575°C, CoSi is still present and first CoSi₂ peaks become clearly visible which rise in intensity very rapidly up to 625°C while CoSi vanishes completely. Neither Titanium oxide nor a ternary Co-Ti-Si phase could be identified (Figure 1).

Summary:

The phase formation process in these nanoscale layers was studied systematically and furthermore the starting temperatures of phase formation could be determined (Co → CoSi → CoSi₂). Within the very small temperature interval between 575° and 625°C, CoSi and CoSi₂ coexist. Neither Co₂Si nor a ternary Co-Ti-Si or other phases in the system Co-Si-Ti-(O) phase could be found.

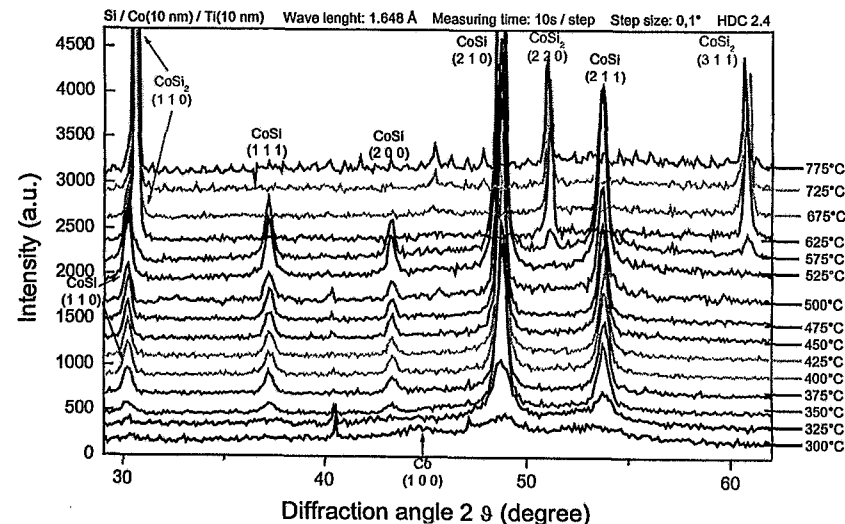



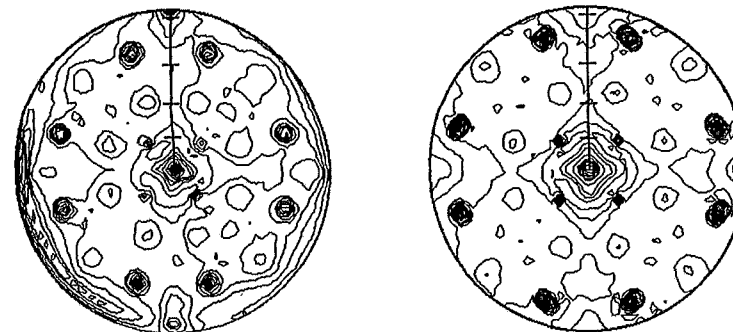
Figure 1: Diffraction data. Heating up – measuring – heating up again. T: 300-775°C

 ROBL-CRG	Experiment title: Study of preferential orientation of SiC particles formed by carbon implantation into silicon	Experiment number: 20_02_035
	Beamline: BM 20	Date of experiment: 31.5.-3.6.2000 and 6.-10.9.2000
Shifts: 21	Local contact(s): Dr. N. Schell	<i>Received at ROBL:</i> 02.04.2001
Names and affiliations of applicants (* indicates experimentalists): F. Eichhorn*, W. Matz, N. Schell* (a), R. Kögler, P.Reichel*, F. Berberich* Forschungszentrum Rossendorf Institute of Ion Beam Physics and Materials Research P.O.B. 510119, 01314 Dresden, Germany (a) present address: ROBL-CRG at ESRF Grenoble		

Report:

Due to its superior physical properties SiC is a useful semiconductor material for various devices requiring a wide bandgap. Thus, improvements in the epitaxial growth processes or synthesis of SiC by implantation of C into Si are of great interest. For technical application the SiC crystallites should be crystallographically aligned with the Si host lattice. Then one can combine the advantages of SiC with the well established Si technology in microelectronics.

Following earlier studies [1] of the strain and SiC particle formation in Si (experiment 20_02_001) now the orientation relationship between SiC crystallites and their Si matrix is investigated by texture studies. Below pole figures of SiC(311) are shown formed by implantation of $4 \times 10^{17} \text{ cm}^{-2}$ C ions into Si(001) at 500 °C (left-hand side) and 800 °C (right-hand side), respectively. The intense spots arise from the SiC{311} reflections, whereas the weak spots are formed by the extended tails of {331} reflections of the perfect Si matrix. The projection plane is (001). The polar angle scale is given in steps of 20°. and the iso-intensity lines in a logarithmic scale.




The SiC crystallites exhibit an orientation correlation with the single crystalline Si matrix. Three types of orientation are found by the present synchrotron x-ray diffraction studies, depending on the choice of implantation and/or annealing temperature:

- (i) Random orientation like in a powder material: Only a small fraction of the crystallites shows this behavior.
- (ii) Fibre texture with the axis parallel to the surface normal: For implantation at lower temperature (500 °C) this orientation type is more pronounced than for higher temperature. The growth of SiC at low temperature is determined predominantly by the concentration profile, which results in fibre texture.
- (iii) High alignment of SiC to the Si matrix with orientation relations $\text{SiC}\langle 001 \rangle \parallel \text{Si}\langle 001 \rangle$ and $\text{SiC}\langle 110 \rangle \parallel \text{Si}\langle 110 \rangle$ due to a coherent growth of SiC in the Si matrix: For implantation at higher temperature the SiC growth is determined predominantly by the surrounding Si matrix lattice because the C can diffuse in the matrix during the implantation process. The coherence between the crystal lattices of SiC and Si was proven by TEM analysis.

An additional important result is that an elevated temperature (800 °C) during implantation is more effective in forming an aligned crystallite distribution than a post-implantation treatment even at higher temperatures (1200 °C).

[1] F. Eichhorn et al., J. Appl. Phys. 86, 4184 (1999).

 ROBL-CRG	Experiment title: Microstructure of ultrathin diffusion barriers	Experiment number: 20_02_36
	Beamline: BM 20	Date of experiment: from: 7.6.2000 to: 13.06.2000
Shifts: 18	Local contact(s): Dr. Norbert Schell	<i>Received at ROBL:</i> 30. 10. 2000
Names and affiliations of applicants (* indicates experimentalists): * Dr. N. Mattern, IFW Dresden, Helmholtzstr. 20, 01069 Dresden, Germany. * Dr. M. Hecker, IFW Dresden, Helmholtzstr. 20, 01069 Dresden, Germany. * D. Fischer, TU Dresden, Institut f. Halbleiter- u. Mikrosystemtechnik, 01062 Dresden, Germany. Dr. C. Wenzel, TU Dresden, Institut f. Halbleiter- u. Mikrosystemtechnik, 01062 Dresden, Germany.		

Report:

Structural properties of Ta-based ultrathin films are of interest for the development of effective diffusion barriers required for Cu-based interconnections used in microelectronics. Both layer and lattice properties of 10nm Ta-N films with different N content covered with Cu were investigated by X-ray reflectometry and wide-angle diffraction. The structural information obtained was correlated to deposition conditions and thermal treatment varying within the investigated sample series. To diminish the intensity loss due to the relatively long path of the radiation through the capping Cu at small incident angles, the X-ray wavelength was adjusted just below the Cu absorption edge. Additional measurements up to large amounts of the scattering vector q were performed at 21 keV.

Reflectometry investigation of the as-deposited state reveals sharp interfaces of the diffusion barrier with a r.m.s. roughness of $\sigma = 0.1$ nm for the pure Ta layer and the Ta-25at%N layer and a slightly larger value of $\sigma = 0.3$ nm for the Ta-50at%N layer,

whereas a 50nm Cu film above the barrier has a relatively rough surface ($\sigma=1.2$ nm) in all three cases. The diffraction patterns show broad peaks of the tetragonal β -Ta in the case of the pure Ta barrier, a bcc-like Ta(N) phase with small crystallites (mean size $D \approx 2$ nm) and additional amorphous content and a fcc-like TaN phase with small crystallites (3nm) and also amorphous content. No influence of the substrate (Si or SiO₂) on the layer structure was found. Apart from the smaller crystallite size and the amorphous content, the structure of the layers corresponds to that of thicker (100nm) films [1].

After annealing of the samples, the barrier stability and their structural changes were investigated. For the pure Ta layer, both barrier and capping Cu film broke down after annealing at 550°C, accompanied by the formation of TaSi₂ and Cu silicides (Fig. 1). With increasing N content in the barrier, also their stability increases (cf. [2]).

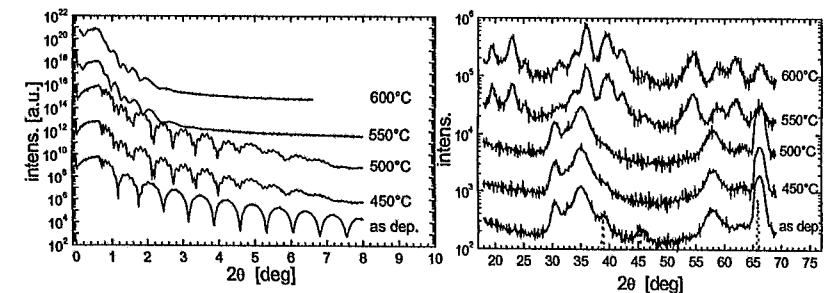



Fig. 1: Reflectometry curves (left) and wide-angle diffraction patterns (right) of the 10nm Ta / 50nm Cu layer stack annealed at different temperatures. The curves are shifted vertically for clarity. Dotted lines (right) denote positions of the Cu peaks.

[1] M. Stavrev, D. Fischer, C. Wenzel, K. Drescher, N. Mattern, Thin Solid Films 307, 79 (1997).

[2] N. Mattern, M. Hecker, D. Fischer, C. Wenzel, N. Schell, W. Matz, H. Engelmann, E. Zschech, Microelectronics Reliability 40 (2000) 1765-1770.

	Experiment title: Investigation of the lateral ordering and chemical composition in lattice matched A_3B_5 quaternary and ternary superlattices	Experiment number: 20_02_037 (a)
	Beamline: BM 20	Date of experiment: from: 03 06 2000 to: 05 06 2000
Shifts: 6	Local contact(s): Dr Norbert Schell Phone: 0033476882367 e-mail: schell@esrf.fr	Received at ROBL: 01.02.2001
Names and affiliations of applicants (* indicates experimentalists): Krystyna Mazur* , Jaroslaw Gaca* , Marek Wojcik* , Institute of Electronic Materials Technology, 01- 919 Warsaw, ul Wolczynska 133, Poland (+48 22) 835 30 41 ext.144		

Report:

The aim of the experiment was to investigate the structural properties of the InGaAsP/InP multilayered heterostructure grown on laterally inhomogeneous (001) InP substrate. The lateral inhomogeneity of the epilayer structure modifies the density distribution of reciprocal space nodes. In order to investigate the structure of reciprocal lattice nodes, a mapping of the region of reciprocal space around a chosen reflection of the substrate crystal is required. Such a map contains information concerning the crystal structure both in the growth direction and in the direction parallel to the interface. Reciprocal space mapping of 20 period quaternary $In_{0.595}Ga_{0.405}As_{0.35}P_{0.65}$ /InP superlattice grown on (001) InP substrate in vicinity of 004 InP was performed. The synchrotron radiation with $\lambda=1.196 \text{ \AA}$ was used. Data for the map were collected as a series of succeeding $\theta/2\theta$ asymmetrical scans for different initial values of θ angles. To establish the appropriate angular range for the map $\theta/2\theta$ and ω scans were performed. On the basis of diffraction profiles the angular ranges were chosen to be $-2\text{deg} < 2\theta < +2\text{deg}$, $-0.1 \text{ deg} < \omega < +0.1 \text{ deg}$. The modulation wavelength of 389.22 \AA , number of 004 atomic planes in one modulation period of 272, and the mean interplanar spacing parallel to the growth direction = 1.4523 \AA have been estimated. Similar measurement procedure was adopted for ternary $In_{0.524}Ga_{0.476}As/InP$ superlattice. On the basis of obtained profiles the angular ranges were

chosen to be $-4\text{deg} < 2\theta < +4\text{deg}$, $-0.15 \text{ deg} < \omega < +0.15 \text{ deg}$. The following results were obtained: the modulation wavelength = 322.67 \AA , number of 004 atomic planes in one modulation period = 220, and the mean interplanar spacing parallel to the growth direction = 1.4667 \AA . Two additional layers with different chemical composition were found in one modulation period. These layers are composed of 10 atomic planes, and their chemical composition is InGaP and InAs. We were not able to perform similar measurement for ion implanted ternary superlattice because of the synchrotron break-down.

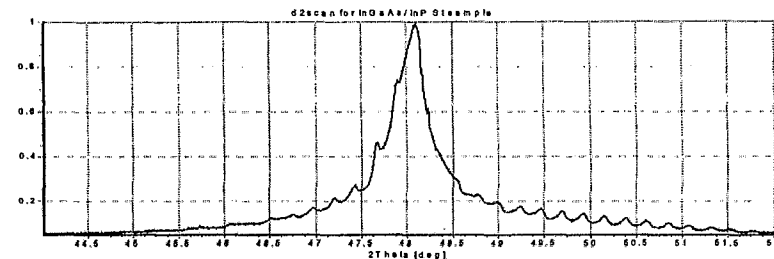


Fig. 1) The $\theta/2\theta$ scan measured for the angular range: $-4\text{deg} < 2\theta < +4\text{deg}$, step = 0.001deg , time per point 1 sec.

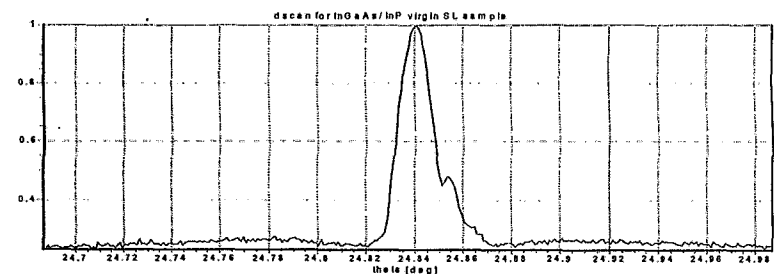
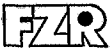


Fig. 2) The ω scan measured for the angular range $-0.15 \text{ deg} < \omega < +0.15 \text{ deg}$ and $2\theta = \text{constans} = 48.152 \text{ deg}$.

 ROBL-CRG	Experiment title: Investigation of the lateral ordering and chemical composition in lattice matched A_3B_5 quaternary and ternary superlattices	Experiment number: 20_02_037 (b) EU-M01
	Beamline: BM 20	Date of experiment: from: 24 11 2000 to: 25 11 2000
Shifts: 6	Local contact(s): Dr Norbert Schell Phone: 0033476882367 e-mail: schell@esrf.fr	<i>Received at ROBL:</i> 01.02.2001
Names and affiliations of applicants (* indicates experimentalists): Jerzy Sass* Marek Wojcik* Institute of Electronic Materials Technology, 01- 919 Warsaw, ul. Wolczynska 133, Poland (+48 22) 835 30 41 (144)		

Report:

The aim of the experiment was to continue investigations of the structural properties of the InGaAsP/InP layers, heterostructures and superlattices grown on (001) InP substrate crystals. To this end both the $\theta/2\theta$ and ω scans have been performed to obtain information on the crystal structure as well in the growth direction in the direction parallel to the interface.

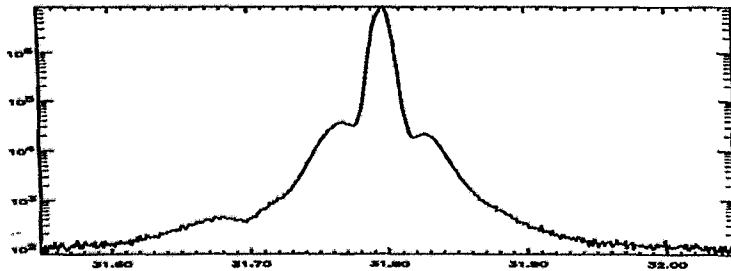


Fig. 1) The ω scan for the sample with layer thickness $t=3000\text{\AA}$

$\text{In}_{0.47}\text{Ga}_{0.53}\text{As}$ epitaxial single layers grown on (001) InP substrate with thickness: 2000Å, 3000Å and 4000Å were investigated. Intensity profiles of the diffuse scattered radiation for ω scans were measured to determine the density of misfit dislocations (Figs 1). For these three samples the lattice misfit $\Delta a/a$ (relaxed state) was calculated to be: $4.33 \cdot 10^{-3}$, $4.79 \cdot 10^{-3}$ and $4.33 \cdot 10^{-3}$, respectively. The In concentration for samples with thickness 2000 Å and 4000 Å amounts to $x = 46,9\%$, and $x = 46,27\%$ for the sample with the thickness of 3000 Å.

Two heterostructures containing 10nm $\text{In}_{0.14}\text{Ga}_{0.86}\text{As}$ active buried layer grown on 001 GaAs substrate, deposited at different growth rate (2 ML/sec and 0.5 ML/sec), were also investigated. In order to determine the shape of the interface regions, the $\theta/2\theta$ profiles were registered (Fig 2).

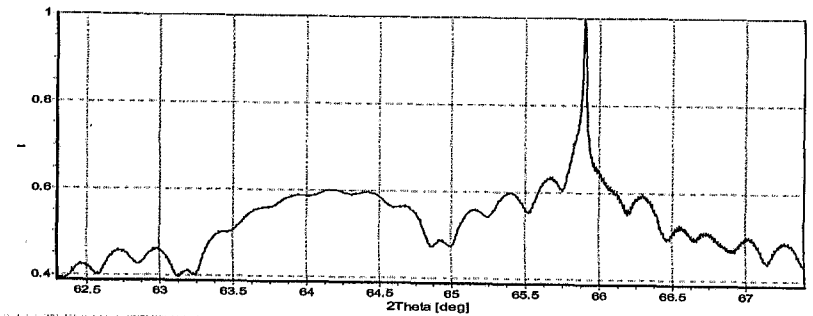



Fig. 2) The $\theta/2\theta$ scan for the heterostructure with 2ML/sec growth rate.

Two 20 periods InGaAsP/InP superlattice crystals with small (1000 ppm) and large (-10000 ppm) lattice misfits produced by 2 MeV As-ion implantation with doses 4×10^{13} and $6 \times 10^{13} \text{ cm}^{-2}$ were investigated. The $\theta/2\theta$ profiles were measured to determine the chemical composition and interplanar spacing profiles. Map of a region of the reciprocal space in the vicinity to the 004 InP substrate reflection was registered that showed high lateral homogeneity investigated samples.

	Experiment title: Thin film growth studies by <i>in situ</i> x-ray diffraction	Experiment number: 20_02_038 EU-M02
	Beamline: BM 20	Date of experiment: from: 26.10.2000 to: 31.10.2000
Shifts: 15	Local contact(s): Dr. Norbert Schell	Received at ROBL: 01. 03. 2001
Names and affiliations of applicants (* indicates experimentalists): *J. Bøttiger, University of Aarhus, Denmark *K. Rasmussen, University of Aarhus, Denmark *N. Schell, A. Bauer, ROBL-CRG, Germany *W. Matz, FZR, Germany		

Report:

During growth, the microstructural development – especially the change in texture with film thickness – of TIN films, which were deposited by use of magnetrons, was studied. The films were grown in a vacuum chamber that was equipped with two magnetrons and mounted on the goniometer located in MRH of ROBL. Kapton windows enabled *in situ* x-ray diffraction and reflection to be carried out to follow the microstructure as a function of film thickness. With the deposition parameters that were chosen, we observed a crossover – grains with a (002) plane parallel with the film surface dominated at small thickness, while, at larger thickness, (111) grains dominated. Recrystallization was identified as a mechanism that controlled this texture development. The driving force for change of orientation of the individual grains arised from minimalisation of the sum of the surface energy and the strain energy of the individual grains.

EXPERIMENTAL: The growth chamber (together with the detailed scattering geometry and the quality of the data, like intensity, resolution, background, which can be obtained with the set-up) is described in detail in Ref. 1. The magnetrons, commercially available from AJA International, are placed at a distance of 100 mm from the substrates and tilted 30 degrees away from the substrate normal. To avoid cross contamination of the two targets, each with a diameter of 1 inch, chimneys are mounted on the magnetrons. Air-pressure-controlled shutters are placed in front of the chimneys. The base pressure was about 2×10^{-5} Pa. The reactive sputter gas was a mixture of Ar (99.9996%) and N₂ (99.99990%) with the ratio 4:1, with a total gas pressure of 0.3 Pa. Only one magnetron was used at the time. It was run at a dc power of 80 W. The deposition rate was about 1.4 Å/s. The substrates were silicon wafers with a 1000 Å amorphous oxide layer on top. A resistive heater was mounted below the substrate so the temperature could be varied from room temperature up to 700 °C. The temperature was measured by use of a thermocouple. A negative bias voltage could be applied to the substrate.

The deposition chamber was mounted on the six-circle goniometer in MRH. The incident x-rays were monochromatized to 12.651 keV ($\lambda = 0.980$ Å). To study the growth of TIN films *in situ*, three different scattering geometries were used:

1. Vertical Bragg-Brentano large-angle scattering (XRD). Such measurements reveal the texture. In addition, from the exact positions of the Bragg peaks, information on the out-of-plane lattice strain is obtained, and from the widths and shape of the peaks, out-of-plane grain sizes and microstrain (lattice defects) are obtained.
2. Grazing incidence and grazing exit in-plane large-angle scattering (GIXS). With an incident angle of 0.2° , the calculated penetration depth of the x-rays was about 100 Å, assuming a mass density of TIN of 5.43 g/cm^3 . Crystallographic planes perpendicular to the surface are identified and, from the positions and widths of the Bragg peaks, in-plane lattice parameters (strain), grain sizes and microstrain are calculated.
3. Low-angle specular reflectivity. The film thickness and information on surface roughness is obtained.

The deposited films were also checked by x-ray diffraction carried out *ex situ* with a Philips powder diffractometer using standard Bragg-Brentano geometry and $\text{CuK}\alpha$ radiation which was filtered with a monochromator in front of the detector. The film composition was obtained by Rutherford backscattering spectrometry with 2.0 MeV He⁺ and a scattering angle of 161° . Electron diffraction patterns and micrographs were obtained by use of a Philips CM20 transmission electron microscope.

We studied the growth of five different TIN films deposited with different deposition parameters: two were grown at a substrate temperature of 250 °C and a bias voltage of -30 V, two with a bias voltage of -30 V and substrate temperatures of 350 °C and 450 °C, respectively. The fifth film was grown with bias voltage -60 V at temperature 350 °C. With regular intervals during growth, the deposition was interrupted, and the film was characterised by XRD, GIXS and low-angle specular reflectivity.

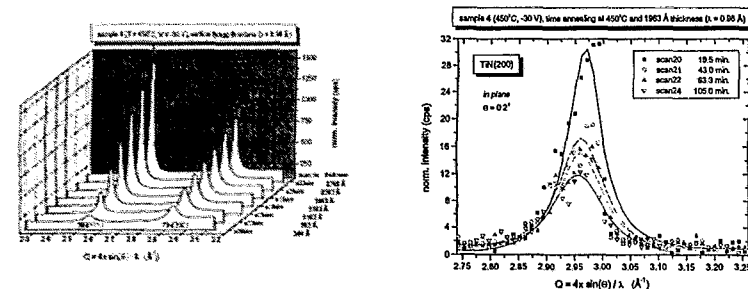



Fig. 1 (left: crossover in vertical BB geometry) and Fig. 2 (right: recrystallization of TIN(002) in GIXS with incidence angle 0.2°) are examples of the obtained data.

SUMMARY: Recrystallization was unambiguously identified as the dominant mechanism that controlled the development of the texture. The data were consistent with the driving force for the change of orientation of the grains that was suggested by Pelleg *et al.*². The grain size increase with film thickness during growth was not due to normal grain growth but was probably controlled by the kinetics.

- [1] W. Matz, N. Schell, W. Neumann, J. Bøttiger, and J. Chevallier, *submitted to Rev. Sci. Instrum.*
 [2] J. Pelleg, L.Z. Zevin, S. Lungo, and N. Croitoru, *Thin Solid Films* 197, 117 (1991).

 ROBL-CRG	Experiment title: Investigation of grain structure and lattice defects in fatigued and annealed submicro- and nanocrystalline nickel	Experiment number: 20_02_39
	Beamline: BM 20	Date of experiment: from: 16/09/00 to: 19/09/00
Shifts: 9	Local contact(s): Dr. Norbert Schell	Received at ROBL: 24. 4. 2001
Names and affiliations of applicants (* indicates experimentalists): Ellen Thiele*, Robert Klemm* Institute of Physical Metallurgy, Technical University Dresden D-01062 Dresden, Germany		

Report:

Recently, extensive theoretical and experimental studies of nanostructured metals were done due to their peculiar physical properties. The aim of the present experiment was to study grain structure and lattice defects in Ni samples showing a grain size below $1\mu\text{m}$, produced by different synthesis routes as severe plastic deformation (spd Ni), ball milling (bm Ni) and pulsed electrodeposition (ped Ni). Furthermore, the stability of these structures towards thermal treatment and cyclic plastic deformation was investigated.

Using a wavelength $\lambda=0.15365\text{nm}$ BRAGG-diffraction profiles with a negligible instrumental broadening were measured at room temperature for seven different $\{hkl\}$ -reflections from $\{111\}$ - up to $\{331\}$ -type in the initial stage of the samples, after annealing for 30min at different temperatures T (spd and bm Ni) and after fatigue at different plastic deformation amplitudes ε_{pa} (spd Ni). To evaluate the size of coherently scattering regions D

which is equated usually with the grain size and, to estimate the distribution of internal strains and stresses, quantitative parameters of the X-ray diffraction profiles as the half width $FWHM$ and the integral breadth IB as well as the profile fourier coefficients were determined.

It could be shown that in analogy to the procedure in [1] a modified WILLIAMSON-HALL-plot is suitable to calculate the grain size D_{WH} and the root mean square stress $\langle\sigma^2\rangle^{1/2}$ from the $FWHM$ -values taking into account the $\{hkl\}$ -dependent elastic moduli E . This analysis was done for the kinds of samples (cf. Fig. 1 and Table 1).

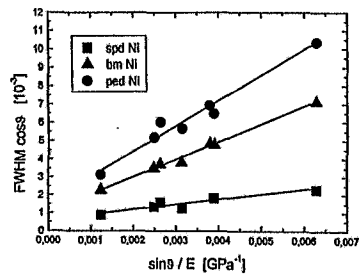


Fig. 1 Modified WILLIAMSON-HALL-plot for the spd, bm and ped Ni samples in their initial stage.

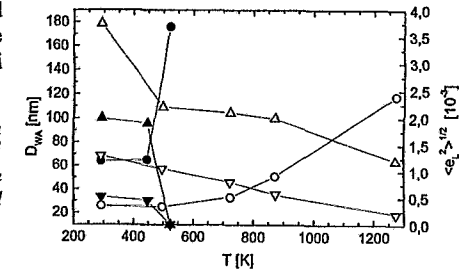
Sample	N2_3 (spd)	P1 (bm)	E1B (ped)
D_{WH} [nm]	120 \pm 32	72 \pm 9	46 \pm 12
$\langle\sigma^2\rangle^{1/2}$ [MPa]	136 \pm 23	481 \pm 19	683 \pm 55

Table 1 Grain size D_{WH} and rms stress $\langle\sigma^2\rangle^{1/2}$ in the initial stage of the samples investigated.

Apparently, the grain size is maximum for the spd Ni samples whereas the rms stress is minimum. The ped Ni sample shows the smallest grain size connected with the highest rms stress. These results are in agreement with the expectations considering the preparation procedure of the specimens.

Now, the WARREN-AVERBACH-algorithm [2] was applied to the profile fourier coefficients in order to estimate the grain size D_{WA} and the rms strains $\langle e_L^2 \rangle^{1/2}$ for different fourier lengths L which can be attributed to the range of the internal strains. For $L=5\text{nm}$ and $L=D$ in Fig. 2 the dependence of D_{WA} and of $\langle e_L^2 \rangle^{1/2}$ on the annealing temperature T is shown for the bm and spd Ni samples.

Fig. 2: Grain size D_{WA} (circles), rms strain $\langle e_{5nm}^2 \rangle^{1/2}$ (up triangles) and $\langle e_D^2 \rangle^{1/2}$ (down triangles) in dependence on the annealing temperature T for the spd Ni (full symbols) and the bm Ni (open symbols).



In a narrow temperature interval the two rms strains are reduced to zero and the grain size is increased sharply for the spd Ni. In contrast, for the bm Ni at first the short-range strains are reduced followed by a stepwise increase of D_{WA} and a diminishing of long-range strains at comparatively high temperatures. The enhanced thermal stability of the bm Ni should be due to the ball milling induced higher content of impurities compared with that in the spd Ni.

The Fig. 3 illustrates for the spd Ni the stability of the structure towards cyclic plastic deformation by the dependences of D_{WH} and $\langle\sigma^2\rangle^{1/2}$ on the deformation amplitude ε_{pa} .

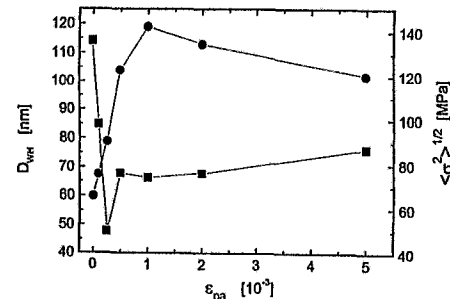



Fig. 3 Grain size D_{WH} (circles) and rms stress $\langle\sigma^2\rangle^{1/2}$ (squares) in dependence on the deformation amplitude ε_{pa} .

After fatigue at room temperature D_{WH} slightly increases with ε_{pa} whereas a decrease of $\langle\sigma^2\rangle^{1/2}$ was observed. As suggested by TEM investigations this is could be caused by moving dislocations sweeping the grain interior free from dislocations, dissolving low angle grain boundaries and forming a dislocation wall structure in coarsened grains, especially at higher deformation amplitudes.

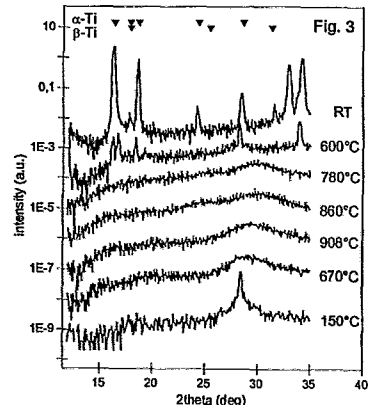
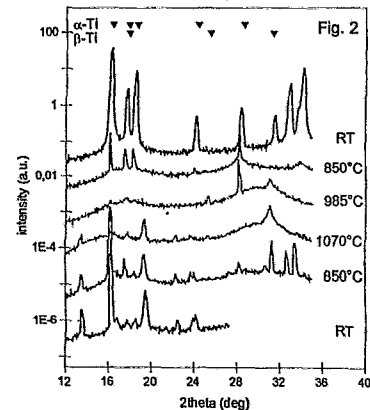
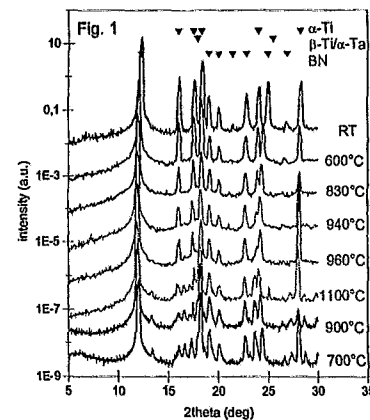
[1] K. Reimann, R. Würschum, J. Appl. Phys., 81 (1997) 11, 7186.

[2] B. E. Warren, X-Ray Diffraction. Dover Publications Inc., New York, 1990.


 ROBL-CRG	Experiment title: Time-resolved pursuit of martensitic phase transformation in Ti	Experiment number: 20-02-40
	Beamline: BM 20	Date of experiment: from: 17-nov-00 to: 21-nov-00
Shifts: 12	Local contact(s): Florian Berberich / Dr. Norbert Schell	Received at ROBL: 19. 4. 2001
Names and affiliations of applicants (* indicates experimentalists): Dr. Nora Darowski* Prof. Dr. Gero Vogl* Hahn-Meitner-Institute, Glienicke Strasse 100, D-14109 Berlin, Germany		

Report:

Martensitic phase transformations are of great interest since shape memory transitions with high technical applicability have to be assigned to this type of transformations. The aim of the experiment was to study the dynamics and the orientation memory effect of the transformation between the hexagonal low-temperature (LT) phase and the cubic high-temperature (HT) phase of titanium as a function of time by means of monochromatic x-ray diffraction. By varying the temperature in an interval of 800°C to 1000°C ($T_{\alpha \leftrightarrow \beta} = 882^\circ\text{C}$) the decay of the LT-Bragg reflections and simultaneous growth of those of the HT phase should be observed. The titanium α to β transition was chosen because theory explicitly refers to this material as a model case for bcc-hcp transition. Usually experiments at elevated temperatures are demanding due to the high temperature differences between heater, sample and sample holder leading to systematic deviations of the measured values from the exact sample temperature. Due to geometric restrictions we used powder diffraction to calibrate the temperature scale. Figure 1 shows the curves of a BN/ α -Ti pill mounted in the standard ROBL HTC as a function of the temperature of the sample holder. The peak positions of the α phase correspond to the PDF values but no significant intensity decrease, i.e. clear transition temperature is observable. In order to eliminate the influence of the boron nitride the experiment was repeated with a α -Ti



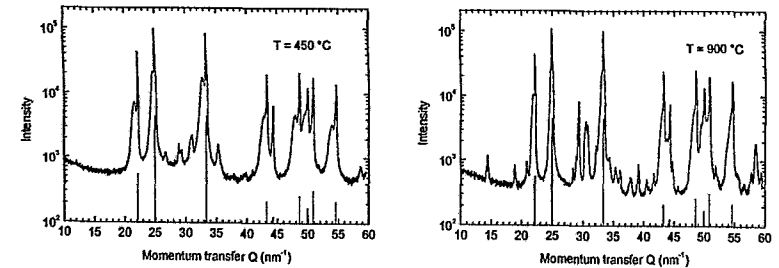
polycrystal of high purity. The results are shown in figure 2. Here a decrease of the LT phase peak intensities is evident. But even far above $T_{\alpha \leftrightarrow \beta}$ only weak indication of the cubic phase can be found by the broad diffuse scattering and a small instable peak at $\theta_B \approx 25^\circ$. An explanation for the different intensity distribution before and after the heating could be a strongly developed texture of the polycrystalline material. A 2D CCD image of the sample confirms this assumption. In order to exclude the disturbance by the Ta-environment heater of the commercial chamber (a metal precipitate was found on the sample) a HTC from the university of Vienna was utilized, which had been calibrated pyrometric via the power consumption. The curves recorded at a comparable sample (figure 3) display only diffuse scattering intensity above the transition temperature. The experiment was planned as a feasibility test. It will be of considerable value for our further studies because we have learned that a successful investigation of the dynamic of phase transformations needs a more sophisticated experimental environment and sample preparation than the utilized one. Accordingly a small HTC has been designed with a Be-hemisphere which will allow for experiments under UHV without geometrical restrictions. The vacuum conditions reached in this experiment ($\approx 10^{-6}$ mbar) are a possible reason for the incomplete transformation since titanium especially at elevated temperatures is known as a getter material.

	Experiment title: Crystalline phases in tungsten carbide material after the implantation of light B ions	Experiment number: 20_02_IH2
	Beamline: BM 20	Date of experiment: From: April, 12 to: April 14, 2000
Shifts: 6	Local contact(s): Dr. N. Schell	Received at ROBL: 2.04.2001
Names and affiliations of applicants (* indicates experimentalists): F. Eichhorn *, I. Mrotchek, N. Schell * (a) Forschungszentrum Rossendorf Institute of Ion Beam Physics and Materials Research P.O.B. 510119, 01314 Dresden, Germany (a) present address: ROBL-CRG at ESRF Grenoble		

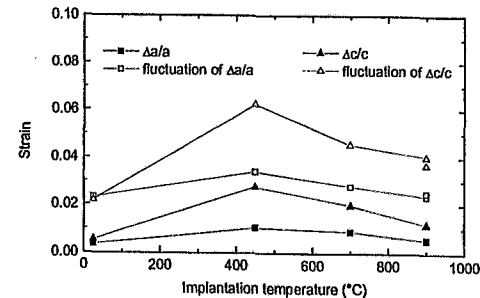
Report:

Tungsten carbide (WC) is a well-known material for high speed machining tools, especially a WC-Co combination is very suitable for machining Ti and its alloys [1]. In the hard material WC sintered with Co, mechanical properties like hardness and wear resistance can be improved by boron implantation. Comparing the results for B implantation of $5 \times 10^{17} \text{ cm}^{-2}$ with an energy of 40 keV at temperatures from RT, 450 °C, 700 °C to 900 °C, the highest values for hardness and wear resistance are found for implantation at 450 °C, and the lowest values for 900 °C.

In order to reveal the structural features connected with these properties the material was studied by X-ray diffraction. The synchrotron radiation allows firstly to choose the wavelength beyond the Co edge to suppress the unwanted Co fluorescence, secondly to control the penetration depth in the grazing incidence technique and to ensure the separation of neighbouring diffraction lines of various crystalline phases due to its very low divergence, and thirdly to give a sufficient signal also from minor phases due to its high intensity.



The Figures above show the diffraction pattern for the material implanted at 450 °C and 900 °C, respectively. The WC peaks are marked; each of them show shoulders at the low momentum transfer region caused by the strained phase WC* formed at the implanted surface of the material. It was found that the optimum mechanical values are correlated with the highest lattice strain of the hexagonal WC in the material implanted at 450 °C.

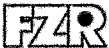


The Figure on the left give the strain results of the WC* phase. The hexagonal unit cell is anisotropically strained; the strain amounts to higher values parallel to the hexagonal axis than perpendicular to it. It should be noted that the strain

fluctuation is higher by a factor of 2 than the strain value itself.

Obviously, at 900 °C the maximum content of newly grown crystalline phases CoWB and Co₃W (indicated by the diffraction lines in the momentum transfer range $Q = 35 \dots 45 \text{ nm}^{-1}$) reduces the entireness of the material. It can be stated that the enhanced hardness and wear resistance due to boron implantation is caused by strain instead of dispersed particles of other phases.

[1] M. Fitzsimmons, V. K. Sarin, Surface and Coatings Technology **137**, 158 (2001).

 ROBL-CRG	Experiment title: Crystallisation of TaSi thin layers	Experiment number: 20_02_IH3
	Beamline: BM 20	Date of experiment: from: 07.07.2000 to: 09.07.2000
Shifts: 7	Local contact(s): F. Berberich	<i>Received at ROBL:</i> 25.4.2001
Names and affiliations of applicants (* indicates experimentalists): W. Matz*, M. Peikert*, E. Wieser Forschungszentrum Rossendorf, Institute of Ion Beam Physics and Materials Research, P.O.B. 510119, 01314 Dresden, Germany		

Report:

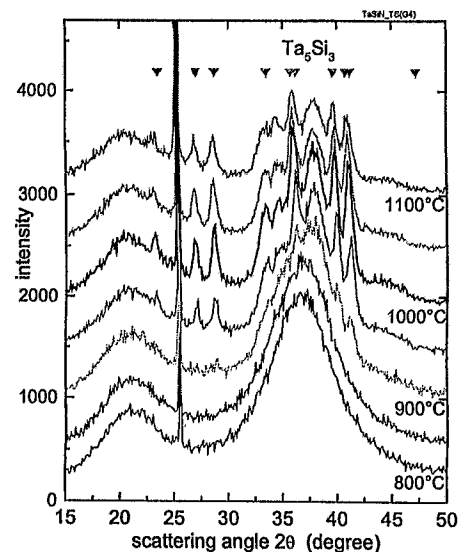
Tantalum or TaSi layers are promising materials for diffusion barriers in microelectronics circuits with copper conduction paths. It is known, that layers of 100 nm thickness show columnar crystals and that in such cases diffusion along grain boundaries plays a great role. Therefore, the suppression of crystallisation of Ta-containing layers is a way to improve the diffusion barrier. This crystallisation suppression should be guaranteed up to temperatures of 700°C in order to allow for the thermal processes during circuit production.

One way to destroy crystalline order is the ion irradiation of the layer, preferably with ions forming badly crystallising Ta compounds (e.g. N, O, B). For 100 nm TaSi layers the crystallisation of TaSi₂ was observed after annealing at 650°C for 1 h. After irradiation of the same film with 3x10¹⁷ N/cm² no crystallisation was observed up to 800°C [1].

In the actual study 50 nm TaSi layers on Si/SiO₂ substrate were compared with respect to thermal stability of the non-crystalline state for an as-deposited sample and another which was subjected to 1.5x10¹⁷ N/cm². For temperatures from 600 to 1100°C the diffraction was recorded in the high

temperature chamber. A wavelength of 0.154 nm and an grazing incidence angle of 1° was used.


The initial diffraction pattern of both materials appears amorphous. With increasing temperature some Bragg-reflection of crystalline phases occur. For the as-deposited TaSi-layer at 900°C the first indications of crystalline Ta₂O₅ occur. Increasing the temperature up to 1100°C leads to a narrowing of the oxide peaks which is due to grain growth. The amorphous scattering contribution remains in the pattern up to 1000°C, which indicates the oxidation from the surface (vacuum in the chamber: 5x10⁻⁶ mbar). No other phases and no indication of the involvement of Si is detected.



The nitrogen-implanted TaSi layer remains amorphous up to 850°C (see figure on the left). Above this temperature the crystallisation starts and the compound is identified as Ta₅Si₃. The peak positions are indicated by triangle in the figure. Up to 1000°C there is a significant amorphous scattering contribution indicating a step by step crystallisation of the layer. The silicide peaks narrow up to 1050°C and then broaden again. The latter effect is regarded as the beginning dissolution of the crystallites. The effect of nitrogen implantation in TaSi is not primarily the stabilisation of

the amorphous state of the TaSi layer as expected from implantation into pure Ta [1]. The onset of crystallisation is only 50 K higher than for pure Ta. The mixing of Ta and Si obviously makes the formation of a tantalum silicide possible, since in the unimplanted sample no such compound occurs.

[1] E. Wieser, J. Schreiber, C. Wenzel, J. Bartha, B. Bendjus, V. Melov, M. Peikert, W. Matz et al., Proc. Adv. Metallization Conf. 99, MRS, Warrendale, PA (2000) p. 257

	Experiment title: X-ray reflectivity of Fe/Cr multilayers grown by MBE on Al₂O₃	Experiment number: 20_02_IH4
	Beamline: BM 20	Date of experiment: from: 14. 07. to: 18. 07. 2000
Shifts: 12	Local contact(s): N. Schell	<i>Received at ROBL:</i> 12. 05. 2000
Names and affiliations of applicants (* indicates experimentalists): Dr. E. Kravtsov, Prof. Y. Babanov Russ. Acad. of Science, Institute of Metal Physics, Ekaterinburg, Russia * Dr. F. Prokert, FZ-Rossendorf, FWIS * Dr. N. Schell, CRG ROBL at ESRF, Grenoble and FZ- Rossendorf		

Report:

GMR and magnetic behaviour of Fe/Cr multilayers (MLs) depends strongly not only on the layer thickness relations but also on the Fe/Cr interface structure [1- 2]. The aim of the experiment was to use the advantages of the anomalous X-ray scattering for the study of roughness and their morphology of the Fe and Cr layers because the compositional properties of the transition region play important parts in forming ML properties. Therefore specular and off-specular diffuse scans were taken at the energy near the absorption K-edge of Fe ($E=7.111$ keV) as well as of Cr ($E=5.989$ keV).

Out of a MBE grown series with varied Fe-layer thickness and Cr buffer layer of 7 nm, a ML (sample UU-9-8) of the composition $Al_2O_3/Cr(7nm)/16x[^{57}Fe(1.3nm)/Cr(7nm)]$ was selected for this experiment.

Experimental: For the two selected energies the measurements were done in the reflectometry ROBL standard set-up (incident beam divergence $\approx 0.006^\circ$, angular detector acceptance 0.03°). Different ω scans (rocking scans with detector fixed at $2\theta_f$) and a $(\theta+\Delta\theta)$ - 2θ offset scan were done besides the 0 - 2θ specular scans.

Evaluation and Results

From the simulations (RefSim Code of Bruker/AXS) of the specular scans measured at the energy of the Fe K-edge and the Cr K-edge, respectively, we got the values of layer thickness, rms-roughness and density. The simulation parameters are compiled in Table 1. The quality of the fit could be improved by assuming that the Cr top layer is covered by an oxidised overlayer having a reduced electron density and a high roughness. The simulations show that the Fe layer roughness in the stack is just of the extension of layer thickness.

If we use Sinha's fractal model of a self-affine interface structure, incorporated in the REFS simulation software package (Bede Scientific), the simulations of the diffuse (transverse and offset) scans give the lateral roughness correlation length ξ the roughness exponent h (Hurst parameter),

Fe/Cr multilayer layer type	RefSIM simulations of the measurements at Fe-edge			RefSIM simulations of the measurements at Fe-edge		
	thickness t (nm)	rms σ (nm)	density (g/cm^3)	thickness (nm)	rms σ (nm)	density (g/cm^3)
Cr ₂ O ₃	3.26	1.28	4.17	3.13	0.46	4.00
Cr	8.53	0.09	6.49	8.34	0.04	6.98
Fe	0.93	0.17	6.28	1.03	0.07	7.05
Sublayers: 2 Periods: 15						
Cr	8.49	0.44	7.20	8.52	0.25	7.20
Fe	1.07	1.05	7.86	1.05	1.00	7.52
Cr	4.53	0.55	7.20	4.53	0.55	6.20
Al ₂ O ₃		[0]	[3.97]		[0]	[3.97]

Table 1 Compilation of results received by fitting and simulations of specular scans of the Fe/Cr multilayer UU-9-8 using RefSim Code. The values given in [] brackets are not refined.

and the part of the roughness which is vertically correlated C_v in the multilayer. Table 2 contains the obtained parameters

Fe K-edge						
	$2\theta_f$ (deg)	rms σ_{Fe} (nm)	rms σ_{Cr} (nm)	h	corr. length ξ (nm)	C_v (%)
Bragg peak 3 rd order	3.24	1.00	0.75	0.35	15	100
Kiess.minimum	2.66	1.00	0.4	0.35	20	0
Cr K-edge						
Bragg peak 3 rd order	2.60	1.0	0.7	0.3	25	>50
Kiess.maximum	2.12	1.0	0.7	0.4	17	50-80%
Kiess. minimum	2.39	1.0	0.7	0.3	25	0

Table 2 Compilation of results received from fitting and simulations of specular and non-specular scans of UU-9-8 using REFS code

In the Cr/Fe MLs the rms-roughness of Cr ($\sigma_{Cr} \approx 0.7$ nm) is smaller than the rms-roughness of Fe ($\sigma_{Fe} \approx 1.0$ nm). They have an interface structure with a short lateral roughness correlation length $\xi \approx 20 \pm 5$ nm. With $h \approx 0.35 \pm 0.05$ the h parameter indicate that the 'jaggedness' is relatively high. From this the fractal dimension $D=3-h$ of the interface is estimated at about 2.65. In the transverse diffuse scans from the resonance scattering, which is observed if the detector is fixed at Bragg maxima, it is obvious that the Fe-Cr interface roughness is nearly fully correlated. It means that the most of the measured rms roughness comes from the vertically correlated one. However, the longitudinal diffuse scan shows that the total-layer thickness fringes are nearly disappeared at $\Delta\omega = 0.1^\circ$. This means that the roughness correlation through the multilayer - from the substrate to the top layer - is not so high. This is supported from the diffuse transverse scan with detector position fixed at $2\theta_f$ fixed at a Kiessig maximum. With detector position $2\theta_f$ fixed at a Kiessig minimum, the diffuse scattering is mainly received from the surface. In this case no correlated roughness is found.

References

- [1] R. Schad et al., Phys. Rev. B59, 1242 (1999)
- [2] B. Heinrich and J.F. Cohran, Adv. Phys. 42, 52 (1993)



Experiment title: Structural investigation on molten eutectic Cu-Ge using anomalous X-ray scattering		Experiment number: HS-1183
Beamline: BM 20	Date of experiment: from: 1-Feb-2000 to: 8-Feb-2000	Date of report: 15-Dec-2000
Shifts: 18	Local contact(s): N. Schell	<i>Received at ESRF:</i>
Names and affiliations of applicants (* indicates experimentalists): W. Hoyer, Th. Halm*, J. Nomssi Nzali*, H. Giegengack* TU Chemnitz, Institut für Physik -123402-, D-09107 Chemnitz, Germany		

Report:

The aim of the experiment was to get different weighted total scattering functions for the molten eutectic alloy $\text{Cu}_{64}\text{Ge}_{36}$ (which subsequently allow the determination of partial structural functions) using anomalous scattering. Wavelengths of 1.391 Å and 1.440 Å as well as 1.122 Å and 1.148 Å were used, which correspond to energies close to these of the Cu-K and Ge-K absorption edge, respectively. During the experiment the sample was held in graphite crucibles placed in a commercial high-temperature chamber which was filled with helium after evacuation. The scattering intensity from the free sample surface was measured in reflexion geometry at temperatures of 650, 800 and 1000°C at every wavelength mentioned above. A PIN-diode was used as detector which allowed to separate the elastic scattering from the fluorescence (the latter became dominant especially at the shorter wavelengths).

Fig. 1 shows the Faber-Ziman structure factors $S(Q)$ for a temperature of 650°C which were finally calculated from the measured intensities by

$$S(Q) = \frac{I_A^{\text{coh}}(Q) - c_1 c_2 (f_1 - f_2)^2}{(c_1 f_1 + c_2 f_2)^2}$$

- c_i, f_i - concentration and scattering factor of atomic species i
 I_A^{coh} - coherent scattering intensity per atom

In their general shape they are in reasonable agreement with structure factors resulting from conventional X-ray scattering experiments.

It must be stated, however, that the structure factors corresponding to slightly different energies near the absorption edge under consideration and even these due to different absorption edges do not show a distinct difference. Consequently, the calculation of partial structure functions became difficult and did not lead to satisfactory curves.

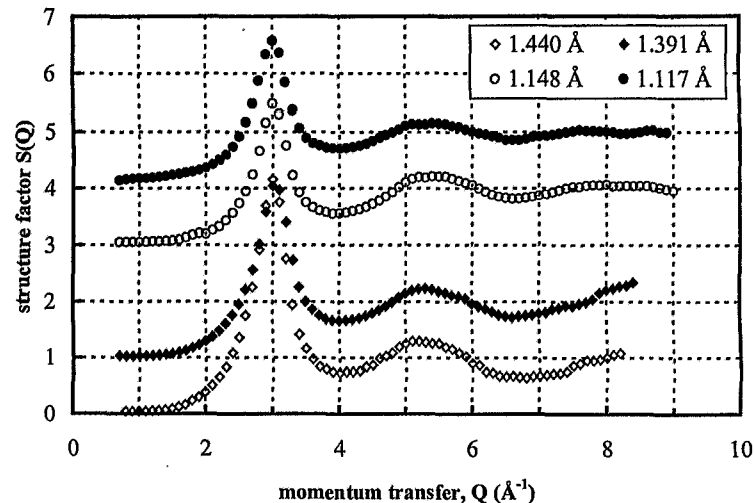


Figure 1 Structure factor of molten $\text{Cu}_{64}\text{Ge}_{36}$ at a temperature of 650°C for different wavelengths



	Experiment title: Structure investigation of the liquid Ag-Bi alloy using anomalous X-ray scattering in reflection geometry	Experiment number: HS-1184
Beamline: BM 20	Date of experiment: from: 3-May-2000 to: 9-May-2000	Date of report: 30-Jan-2001
Shifts: 18	Local contact(s): N. Schell	<i>Received at ESRF:</i>
Names and affiliations of applicants (* indicates experimentalists): W. Hoyer, Th. Halm*, J. Nomssi Nzali*, H. Giegegack* TU Chemnitz, Institut für Physik –123402-, D-09107 Chemnitz, Germany		

Report:

The aim of the experiment was to get different weighted total scattering functions of molten Ag-Bi alloys (containing 10, 30, 40 and 60 at.% Ag) using anomalous scattering, which

subsequently allow the determination of partial structural functions. The scattering power of every constituent of the alloy was varied by the use of two different incident energies slightly below an absorption edge of the considered constituent. The energies chosen were 25.28 keV and 25.48 keV (due to Ag K-edge) and 13.18 keV and 13.28 keV (due to Bi L_{III}-edge).

The samples were held in graphite crucibles placed in a commercial high-temperature chamber (Bühler HDK2.4) which was filled with helium after evacuation. The scattering intensity from the free sample surface was measured in reflexion geometry at temperatures of 20 K above the liquidus line at every energy mentioned above. To separate the elastic scattering a monochromator crystal (graphite or Germanium) was inserted in the scattered beam.

It turns out that there was a parasitic scattering which became more spurious when measuring at the two high energies and which could not be suppressed. This leads subsequently to difficulties in the normalization procedure to obtain the Faber-Ziman

structure factors $S(Q)$, which were finally calculated from the measured intensities by

$$S(Q) = \frac{I_A^{coh}(Q) - c_1 c_2 (f_1 - f_2)^2}{(c_1 f_1 + c_2 f_2)^2}$$

c_i, f_i - concentration and scattering factor of atomic species i

I_A^{coh} - coherent scattering intensity per atom

As seen in fig.1 not all $S(Q)$ do oscillate reliably around a horizontal line over the whole Q -range in the case of the two highest energies. Furthermore, the differences between the $S(Q)$ measured at different energies for the same alloy are only weak. This makes the calculation of partial structure functions difficult, which does not result in satisfactory curves.

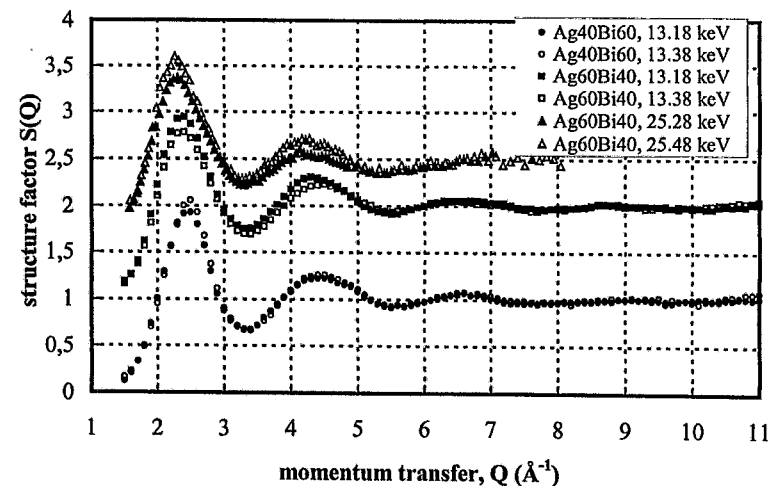


Figure 1 Structure factors of molten $Ag_{60}Bi_{40}$ and $Ag_{40}Bi_{60}$ at different energies



Experiment title: EXAFS studies of [^{99m} Tc] technetium carbonyl complexes		Experiment number: LS - 1395
Beamline: BM 20	Date of experiment: from: 06/09/99 to: 09/09/99 20/11/99 23/11/99	Date of report: March 2001
Shifts: 27	Local contact(s): T. Reich, C. Hennig	Received at ESRF: 30.3.2001
Names and affiliations of applicants (* indicates experimentalists): S. Seifert* ¹ , J.-U. Kuenstler* ¹ , T. Reich* ² , H. Funke* ² , C. Hennig* ² , A. Rossberg* ² , B. Johannsen ¹ ¹ Institute of Bioinorganic and Radiopharmaceutical Chemistry ² Institute of Radiochemistry Research Center Rossendorf P.O. Box 510119, 01314 Dresden, Germany		

Report:

Nowadays, most of all radiopharmaceuticals used in routine nuclear medicine imaging procedures are ^{99m}Tc labelled compounds, and intensive research is going on to design new ^{99m}Tc radiopharmaceuticals. Complexes with N-donor or S-donor chelating ligands coordinated to the Tc(I) or Re(I) tricarbonyl moiety with high stability in aqueous solution may serve for the design of radiopharmaceuticals. Coordination of peptides with the [Tc(CO)₃]⁺ moiety is of great interest for the design of ^{99m}Tc labelled peptides [1, 2].

The aim of this work was to investigate the stability of model Tc(I) thioether tricarbonyl complexes in aqueous solution, their reactivity against histidine and to estimate structural parameters of the dissolved compounds. The reaction of the precursor [Tc(CO)₃Cl₃]²⁻ with histidine, glycine and simple model peptides was studied. The possibility of detecting other than the ligating atoms of the amino acids and peptides was to be checked by Tc K-edge EXAFS analysis.

Due to the extremely small concentration of the radionuclide present in the radiopharmaceutical preparation (10⁻⁶ – 10⁻⁸ M), XAS studies as well as most of chemical investigations employ the long-lived isotope ⁹⁹Tc. We prepared the complexes [Tc(CO)₃CIL¹], Tc1, [Tc(CO)₃(H₂O)L¹]⁺, Tc1a, [Tc(CO)₃L²], Tc2, and as reference [Tc(CO)₃His], Tc3, both at ⁹⁹Tc and ^{99m}Tc levels using 3,6-dithiooctane, L¹, and 1-carboxy-3,6-dithiaheptane, L², as prototypical bidentate thioethers without and with an additional donor atom in the chelating unit. ⁹⁹Tc solutions of Tc1 and Tc1a were prepared by dissolving solid Tc1 in water/methanol and adding of Cl⁻ or Ag⁺, respectively. With an excess of chloride the equilibrium between Tc1 and Tc1a is on the side of the Tc1 complex. If chlorine is removed from the equilibrium by precipitation as AgCl, Tc1a is the solution species. For studying a possible substitution of the thioether ligands in the complexes Tc1

and Tc2 by histidine, an excess of the challenge ligand was given to the complex solutions; the resulting complexes were named Tc1b and Tc2b. The samples TcGlyHis, TcHisGly, TcGlyGlyGly, TcHisGlyGly, TcGlyGlyHis, TcGlyHisLys, TcGly and TcGlyGly were prepared by dissolving the precursor complex (NEt₄)₂[Tc(CO)₃Cl₃] in water/methanol (1/1) and adding Gly-His, His-Gly, Gly-Gly-Gly, His-Gly-Gly, Gly-Gly-His, Gly-His-Lys (in an approximately 1.2-fold excess) and Gly, Gly-Gly (approximately 2-fold excess).

We applied Tc K-edge EXAFS measurements (Tc K-edge at 21044 eV), chromatography (UV and γ-ray detection), electrophoresis and mass spectroscopy to investigate the behaviour of the complexes. EXAFS analyses (transmission mode, room temperature, Tc concentration ~ 0.01 to 0.02 M) were carried out at the Rossendorf beamline (ROBL). To obtain a satisfactory evaluation of the EXAFS spectra and the Fourier transforms, single-scattering paths including the C, O, N/O, and S/Cl coordination shells and multiple-scattering paths to model the oxygen atom of the carbon monoxide ligand were taken into account.

We found that the complex Tc1 is reversibly transformed into the complex Tc1a in aqueous solution. Tc K-edge EXAFS measurements confirmed the composition of the compounds. The estimated atomic distances are 1.92 Å (Tc-C), 2.49 Å (Tc-S or Tc-Cl), 2.19 Å (Tc-O_{aq}) and 3.06 Å (Tc-O_{CO}). EXAFS analysis of Tc1a shows the same structural parameters for the C, S/Cl and CO coordination shells as Tc1 except that the coordination number for the S/Cl coordination shell is lowered by approximately one. In addition, the detection of 1.2 ± 0.3 oxygen atoms at 2.19 Å proves the substitution of chlorine by water.

We found that the complexes Tc1 and Tc2 react with histidine to the products Tc1b and Tc2b in aqueous solution which are identically with the reference Tc3. The estimated atomic distances in Tc1 (see above) and Tc2 (1.92 Å (Tc-C), 2.21 Å (Tc-O), 2.50 Å (Tc-S) and 3.07 Å (Tc-O_{CO})) are almost the same as those found by single crystal X-ray diffraction analyses of similar Re carbonyl complexes containing dithioether ligands [2]. The estimated coordination numbers agree with the expected values. The results of the EXAFS measurements of Tc1b and Tc2b are almost identical to the results of EXAFS analysis of reference Tc3 (atomic distances: 1.91 Å (Tc-C), 2.20 Å (Tc-N and Tc-O) and 3.06 Å (Tc-O_{CO})). This fact proves the substitution of bidentate dithioether and tridentate carboxylato dithioether ligands by histidine, which coordinates in a tridentate manner. The obtained atomic distances are in agreement with those found for the Re congener by single crystal X-ray diffraction analysis [3]. Detection of any other than the ligating atoms of the thioether ligands or histidine was not possible mainly because of overlapping with the very strong backscattering off the three oxygen atoms of carbon monoxide, which is enhanced by a strong multiple-scattering effect.

The products of the reaction of the precursor [Tc(CO)₃Cl₃]²⁻ with histidine, glycine and small peptides containing these amino acids were studied in solution. Tc K-edge EXAFS measurements confirmed the exchange of chloride, the mononuclear structure and typical structural parameters expected for such type of complexes (atomic distances: 1.91 Å (Tc-C), 2.20 Å (Tc-N and Tc-O) and 3.06 Å (Tc-O_{CO})). For all complexes, the same local structure was observed. Detection of any other than the ligating atoms of the amino acids or peptides was not possible.

References:

- [1] R. Alberto et al., *Coordination Chem. Rev.* 190-192 (1999) 901.
- [2] H.-J. Pietzsch et al., *Bioconj. Chem.* 11 414 (2000) 414.
- [3] R. Schibli et al., *Bioconj. Chem.* 11 (2000) 345.



Experiment title: Uranium sorption onto LaPO ₄ and La(PO ₃) ₃ surfaces : EXAFS studies		Experiment number: ME - 44 (a)
Beamline: BM 20	Date of experiment: from: 27 avr 00 to: 02 mai 00	Date of report: 15 Jan. 01
Shifts: 15	Local contact(s): Ch. Hennig	<i>Received at ESRF:</i> 24.1.2001
Names and affiliations of applicants (* indicates experimentalists): *DROT Romuald, IPN, Université Paris-Sud Orsay, 91406 Orsay cedex, France *SIMONI Eric, IPN, Université Paris-Sud Orsay, 91406 Orsay cedex, France *ORDONEZ REGIL Eduardo, IPN, 91406 Orsay cedex, France		

Report:

The sorbed samples have been prepared using the classical batch procedure at room temperature by mixing a weighed amount of powdered phosphate with an uranyl solution. After 24 hours stirring, the solution is removed and the solid is washed with distilled water at equilibrium pH value, and dried at room temperature. The concentration of uranyl ions on the surface has been determined directly on the solid by PIXE experiment. The sorbed samples have been first studied by spectrofluorimetry and XPS in order to identify the number of complexes on the surface.

The U L_{III} edge has been recorded using the 4-elements detectors. The backscattering phases and amplitudes have been extracted from *ab-initio* calculated EXAFS spectrum (FEFF7.02 code) of the reference compound UO₂(H₂PO₄)₂ · 3H₂O.

We have checked different conditions in order to detect any change concerning the structure of the sorbed species versus pH, nature of the background salt or uranyl concentration in solution. We have obtained the following results:

LaPO ₄ / La(PO ₃) ₃ [UO ₂ ²⁺] = 10 ⁻² M ; [NaClO ₄] = 0.5 M ; pH = 3.0	Axial Oxygens	Equatorial Oxygens	Equatorial Oxygens
N	2.15 / 2.2	2.4 / 3.0	1.8 / 1.8
σ (Å)	0.068 / 0.066	0.045 / 0.044	0.060 / 0.058
R (Å)	1.77 / 1.77	2.31 / 2.33	2.47 / 2.50
ΔE (eV)	2.89 / 7.02	8.2 / 8.2	13.0 / 13.0

The value at 1.77 Å for the axial oxygen atoms is a classical value and is very closed to the one that we have previously obtained for uranyl sorption on zirconium and thorium phosphate compounds (1.76 Å).

There are two different distances U- equatorial oxygens for both solids. As the second contribution of the Fourier transform, for uranyl ions in a non-complexing solution, is due to 5 oxygens at 2.41 Å, we assume that the two oxygens at 2.47 Å belong to hydroxyl groups or water hydration molecules. Therefore, for U/LaPO₄ in sodium perchlorate medium (Fig. 1), we have a bidentate surface complex as we observe 2 oxygen atoms at 2.31 Å. These oxygens belong probably to the surface PO₄ groups.

For the samples prepared in potassium nitrate solution, the spectrofluorimetry and XPS studies indicate that there are two different kind of surface complexes which are the free uranyl ions and the nitrate complex. The corresponding Fourier transform is the same as the one in perchlorate medium, which is not surprising because it is not possible to distinguish the backscattering of the oxygens belonging to water molecules and to nitrate ions. Therefore, the obtained distances are averaged.

In both media, the distance U-P, corresponding to the third shell, have been determined. One phosphorus atom is at 2.74 Å which corresponds to an angle around 90 ° between the bonds U-O (2.31 Å) and P-O (1.50 Å). Therefore, if the two oxygen atoms (U-O 2.31 Å) belong to the same PO₄ surface group, the angle between the two bonds P-O should be around 114 °, which is a reasonable value for the tetrahedron PO₄.

In the case of the U/La(PO₃)₃ system, we observe 3 oxygens at 2.33 Å and two others at 2.50 Å. It seems that the surface complex could be rather a tridentate complex with the oxygen atoms of the surface PO₃ groups. Like U/LaPO₄, there is one phosphorus atom at 2.74 Å in both media which can have the same interpretation as the U/LaPO₄ system.

These results indicate clearly that the sorbed species form an inner-sphere complex for both solids, in both NaClO₄ and KNO₃ media (monodentate or tridentate). These informations will be very useful for the determination of the corresponding sorption constants by simulation of the retention data.

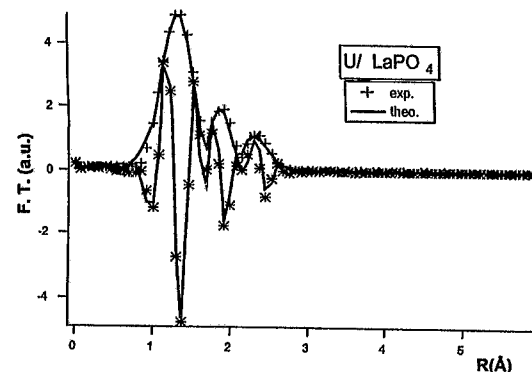


Fig. 1 : Fourier transform (not phase corrected) of the first third shells



Experiment title: Uranium sorption onto ZrSiO ₄ surfaces : EXAFS studies		Experiment number: ME - 44 (b)
Beamline: BM 20	Date of experiment: from: 27 Apr. 00 to: 02 May 00	Date of report: 15 Jan. 01
Shifts: 15	Local contact(s): Ch. Hennig	<i>Received at ESRF:</i> 24.1.2001
Names and affiliations of applicants (* indicates experimentalists):		
* LOMENECH Claire, IPN, 91406 Orsay cedex, France		
* SIMONI Eric, IPN, Université Paris-Sud Orsay, 91406 Orsay cedex, France		
* DROT Romuald, IPN, Université Paris-Sud Orsay, 91406 Orsay cedex, France		

Report:

The sorbed samples have been prepared using the classical batch procedure at room temperature by mixing a weighed amount of powdered solid with an uranyl solution. The concentration of uranyl ions on the surface has been determined directly on the solid by PIXE experiment and the sorbed samples have been first studied by spectrofluorimetry and XPS in order to identify the number of complexes located on the surface.

The U L_{III} edge has been recorded using the 4-elements detectors. The backscattering phases and amplitudes have been extracted from *ab-initio* calculated EXAFS spectrum (FEFF7.02 code) of the reference compounds UO₂(TBP) and uranyl silicate compound (UO₂)₂ SiO₄ · 2H₂O. We have prepared different sorbed samples in order to detect any change concerning the structure of the sorbed species versus pH or nature of the background salt. The same study has been performed on the U/ZrO₂ system as comparison. The results are the following:

The obtained results, for both *in situ* and dried samples, are rather similar and clearly show that there is no effect of the drying step on the structure of the sorbed species.

For the UO₂²⁺ (10⁻² M) / NaClO₄ / ZrSiO₄ system prepared at pH=3.0, it seems that the uranyl ions are sorbed on the surface as a tridentate complex (three oxygens at 2.36 Å). Moreover, the XPS results on UO₂²⁺ / ZrSiO₄ and UO₂²⁺ / ZrO₂ systems have shown that the uranyl ions are bound to the oxygen atoms of the surface silicate groups. The two oxygens at 2.54 Å could be attributed to the OH groups or to water molecules. The third peak of the Fourier transform is attributed to one silicium atom contribution at 2.76 Å. For this sample, it appears another intense peak which comes from the backscattering of one zirconium atom located at 3.50 Å (Fig. 1). It is interesting to note, using FEFF calculations, that these results could correspond to an

uranyl ion located on the (100) face of the zircon crystal which is one of the natural crystallographic faces of this solid.

Nevertheless, the zirconium contribution is not present for the sample prepared at pH equal 5.4 ([U]=2 · 10⁻⁴ M) and the contribution at 2.76 Å is shifted to 2.72 Å (Fig. 1). Moreover, the uranyl emission spectrum of the sample prepared at pH = 3.0 is quite different than the one prepared at pH = 5.4, which means that the sorbed species are not the same for these two pH values. This difference is not yet well-understood. One hypothesis could take into account the uranyl speciation in solution and thus, the species obtained at pH=5.4 could be one amorphous precipitate (UO₂)(OH)₂. Therefore, the pic at 2.72 Å could be due to the OH contribution.

For the UO₂²⁺ (10⁻² M) / KNO₃ / ZrSiO₄ sample prepared at pH equal 3.0, the spectrophotometry experiments have shown that there is only one sorbed species on the surface which should be the same as the one in NaClO₄ medium, the free aquo uranyl ion. Moreover, the Fourier transforms are identical in both media (3 oxygens at 2.37 Å, 2 oxygens at 2.54 Å and one silicium at 2.77 Å).

[NaClO ₄] = 0.5 M ; pH = 3.0 / 5.0	Axial Oxygens	Equatorial Oxygens	Equatorial Oxygens
N	2.3/2.2	3.0/2.7	2.0/1.8
σ	0.041/0.020	0.064/0.075	0.0078/0.086
R (Å)	1.81/1.81	2.36/2.35	2.54/2.54
ΔE (eV)	-2.4/-5.4	11.9/13.3	11.9/13.3

Up to now, the analysis of the UO₂²⁺ (10⁻³ M) / NaClO₄ / ZrO₂ (pH=3.5) and UO₂²⁺ (10⁻² M) / KNO₃ / ZrO₂ (pH = 3.0) systems gives the following results : 3 oxygens at 2.37 Å, 2 oxygens at 2.54 Å and one zirconium at 3.52 Å. This part of the study is still under progress.

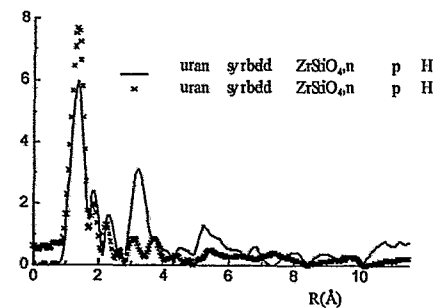


Fig. 1 : Fourier transform (not phase corrected) of the experimental EXAFS spectra



Experiment title: Local Structure of Th Complexes on Montmorillonite Clay Mineral Determined by Extended X-ray Absorption Fine Structure (EXAFS) Spectroscopy	Experiment number: ME-49	
Beamline: BM 20	Date of experiment: from: 14.6.2000 to: 19.6.2000	Date of report: 11.01.2001
Shifts: 18	Local contact(s): C. Hennig	<i>Received at ESRF:</i> 20.03.2001
Names and affiliations of applicants (* indicates experimentalists): R. Dähn*, Paul Scherrer Institut, CH-5232 Villigen PSI A. Scheidegger*, Paul Scherrer Institut, CH-5232 Villigen PSI P. Spieler*, Paul Scherrer Institut, CH-5232 Villigen PSI		

Report:

The research at the Waste Management Laboratory, PSI, concentrates on the understanding of safety relevant mechanisms and processes that govern the release of radionuclides from waste matrices, and their transport through engineered barrier systems and the surrounding geosphere. For this reason, detailed sorption studies of radionuclides in clay and cement systems are conducted. The studies are combined with extended X-ray absorption fine structure (EXAFS) spectroscopy measurements in order to understand the sorption mechanisms on an atomic level.

In this manuscript, a case study of Th(IV) uptake on montmorillonite is presented. EXAFS samples were prepared by incubating a montmorillonite suspension with Th for 7 days at pH = 5 ($Th_{initial}$: 4.3×10^{-5} - 4×10^{-4} M). The resulting Th loadings on the clay varied between 14 and 166 $\mu\text{mol/g}$. L_{III} -Th EXAFS spectra of Th treated montmorillonite were measured at the Rossendorfer Beamline at the European Synchrotron Radiation Facility. Data analysis revealed the presence of two O shells at 2.27 Å and 2.45 Å in all samples. The spectra at low Th uptake suggest the presence of Si/Al and Th backscattering atoms at distances of 3.85 Å and 3.77 Å

respectively. The presence of a Th-Si/Al backscattering pair suggests that Th is bound to Si tetrahedra in a double corner-sharing manner. At higher Th uptake, however, the spectrum shows a strong similarity with the spectrum of amorphous $Th(OH)_4$ and suggests that Th is predominately present as a newly formed $Th(OH)_4$ -like phase.

Dähn, R., Scheidegger, A. M., Manceau A., Baeyens, B., and Bradbury, M. H., 2001. "Local Structure of Th Complexes on Montmorillonite Clay Mineral Determined by Extended X-ray Absorption Fine Structure (EXAFS) Spectroscopy." Speciation, Techniques and Facilities for Radioactive Materials at Synchrotron Light Sources, NEA Publication, in press



	Experiment title: Elucidation of structural environment of Th(IV) in clay minerals using EXAFS	Experiment number: ME-50
Beamline: BM 20	Date of experiment: from: 7.4.2000 to: 10.4.2000	Date of report: 18.8.2000
Shifts: 12	Local contact(s): C. Hennig	<i>Received at ESRF:</i> 20.3.2001
Names and affiliations of applicants (* indicates experimentalists): R. Dähn*, Paul Scherrer Institut, CH-5232 Villigen PSI A. Scheidegger*, Paul Scherrer Institut, CH-5232 Villigen PSI P. Spieler*, Paul Scherrer Institut, CH-5232 Villigen PSI M. Glaus, Paul Scherrer Institut, CH-5232 Villigen PSI		

Report:

Aims of the experiment and scientific background

The aim of this experiment is to develop and test models, and to acquire selected data in support of the performance assessments of Swiss nuclear waste repositories. The flow of ground water through a repository can potentially result in the release of radionuclides from waste matrices. The released radionuclides can then be transported through engineered barrier systems and the surrounding geosphere. The release of radionuclides can be considerably retarded due to interactions with solid phases. Thus, a detailed molecular level understanding of sorption mechanisms of radionuclides in clay systems is of great importance for safety assessment.

On clay minerals several uptake mechanisms of divalent metal ions such as Ni(II), Co(II), and Zn(II) have been proposed: Sorption on edge sites, sorption on interlayer sites, and the formation of lamellar nucleation phases such as neoformed layer silicates and mixed layered double hydroxides [1-4].

The aim of this study is to use EXAFS to determine sorption mechanisms of Th on montmorillonite. Montmorillonite is an important smectitic mineral responsible for the retention of metals in the geosphere. Furthermore, the clay is used as a backfill material in the Swiss concept for a high level radioactive waste repository and thus, metal sorption on montmorillonite has been investigated in our laboratory in great details [5].

Experiments + Results

Samples were prepared in a glove box by reacting Th and montmorillonite at pH 3.0 and at high ionic strength 0.1 M NaClO₄ to block cation exchange processes. The initial Th concentrations for the samples were 2.7·10⁻⁶ - 4·10⁻⁴ M Th. After a reaction time of 7 days the samples were centrifuged and the wet pastes were transferred into

a sealed Plexiglas sample holder. Th-L_{III}-edge fluorescence were recorded for samples containing 1-157 μmol/g Th sorbed onto the montmorillonite. k³-weighted EXAFS spectra for Th sorbed on montmorillonite are shown in Fig. 1. With increasing Th loading the intensity of k³χ(k) increases and the wave frequency between ~6 and ~10 Å⁻¹ shifts to higher values. The corresponding experimental Radial Structure Functions (RSF's) are shown in Fig.2. The figure reveals that the amplitude of the first peak (Th-O contribution) is decreasing with decreasing Th loading and that the peak is split into two oxygen shells. The second RSF peak (Th-Si contribution) increases with decreasing loading and its position is shifted to higher distances. To date, the data analysis is finalised using theoretical approaches.

References

- [1] Schlegel, M., A. Manceau, D. Chateigner, and L. Charlet, J. Colloid Interface Sci., 1999. 215: p. 140-158.
- [2] Scheidegger, A.M., G.M. Lamble, and D.L. Sparks, J. Colloid Interface Sci., 1997. 186: p. 118-128.
- [3] Scheinost, A.C. and D.L. Sparks, J. Colloid Interface Sci., 2000. 223: p. 1-12.
- [4] Dähn, R., A.M. Scheidegger, A. Manceau, M. Schlegel, B. Baeyens, and M.H. Bradbury, Journal of Synchrotron Radiation, 2001. 8: p. 533-535.
- [5] Baeyens, B. and M.H. Bradbury, J. Contam. Hydrol, 1997. 27: p. 199-222.

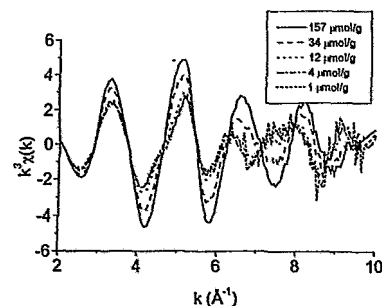


Figure 1: k³-weighted Th L_{III}-edge EXAFS spectra for different Th-concentrations sorbed onto montmorillonite

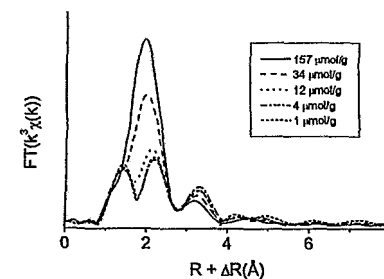


Figure 2: Concentration dependence of the Th L_{III}-edge RSFs of Th sorbed onto montmorillonite



	Experiment title: Uranyl and Th sorption onto illite and montmorillonite	Experiment number: ME-129
Beamline: BM 20	Date of experiment: from: 01.11.2000 to: 06.11.2000	Date of report: 22-02-01
Shifts: 18	Local contact(s): Tobias Reich	<i>Received at ESRF:</i> 20-03-01
Names and affiliations of applicants (* indicates experimentalists): I. Bonhoure*, R. Dähn*, Peter Spieler*, A. M. Scheidegger, E. Wieland, B. Baeyens. Waste Management Laboratory Paul Scherrer Institute, CH 5232 Villigen, Switzerland		

Report:

The Waste Management laboratory at PSI is involved in providing relevant data to assess the performance of future Swiss nuclear waste repositories. In particular, the saturation of the depository with ground water could provoke the release of radionuclides from its containment into the near field (engineered barriers) and the far field (geosphere). The detailed knowledge of the interaction of radionuclides with the natural mineral phases is hence of great importance to predict their mobility and long term fate. Among the different mineral phases, illite and montmorillonite are of great interest as they are major components of Opalinus clay (up to 50-80 %), a potential host-rock formation for a Swiss high-level nuclear waste repository.

We have used EXAFS to study the local environment of uranyl and Th(IV) sorbed onto illite and montmorillonite (pH= 6). As an example Fig. 1 and 2 show the EXAFS and the pseudo radial distribution function (PRDF) of samples containing 750, 2400 and 3800 ppm Uranium. Data analysis was performed on filtered back transformed data (0.9-3.4 Å) using Feff7 calculated phases and amplitudes. The origin of all features (A-D) in the PRDF's could unambiguously be determined using multiple-shell fitting (Fig. 2 and Tab. 1). A is due to axial uranyl oxygens (1.78 Å), B and C to equatorial oxygens (first shell at ~ 2.29 Å, second shell at ~ 2.47 Å) and D to multiple scattering of the fourth order along the uranyl entity. No further contribution at higher R could be observed.

Fig. 1 and Fig. 2 clearly reveal that the local structure around uranium varies with surface loading. Data analysis supports this finding and suggests that the number of closest equatorial oxygens increases from 2.8 to 4.3 as the Uranium content in the samples decreases from 3800 ppm to 750 ppm. The splitting of the equatorial oxygen distance suggests the formation of inner-sphere complexes and has been observed in

previous studies on uranyl uptake on mineral surfaces [1]. Further research is needed to identify the uranyl sorption sites and structurally explain the observed loading-dependant structural changes in the sorption system.

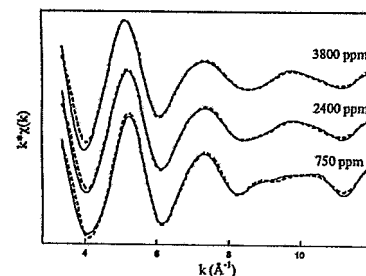


Figure 1: Experimental (—) and calculated (---) modulus of the U L_{III} PRDF for Uranyl sorbed onto illite with different loadings.

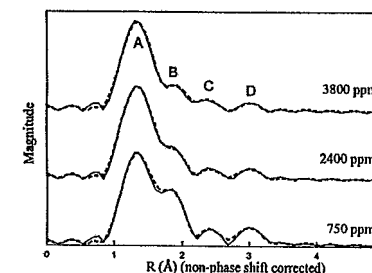


Figure 2: Experimental (—) and calculated (---) EXAFS oscillations at the U L_{III} edge for Uranyl sorbed onto illite with different loadings.

Table 1: Best fit parameters for the EXAFS oscillations at the U L_{III} edge (*rf means residual factor).

		N	R (Å)	σ (Å)	ΔE ₀ (eV)	*rf (%)
3800ppm	U-O _{ax}	2.0	1.78	0.025	-2.1	1.2
	U-O _{eq}	2.8	2.30	0.030	-2.1	
		2.5	2.47	0.038	-2.1	
	UO ₂ MS	-	3.57	0.091	-2.1	
2400 ppm	U-O _{ax}	2.0	1.78	0.025	-2.1	1.5
	U-O _{eq}	3.1	2.29	0.038	-2.1	
		2.2	2.46	0.046	-2.1	
	UO ₂ MS	-	3.57	0.070	-2.1	
750 ppm	U-O _{ax}	2.0	1.78	0.025	-2.1	1.8
	U-O _{eq}	4.3	2.29	0.039	-2.1	
		2.0	2.49	0.052	-2.1	
	UO ₂ MS	-	3.57	0.001	-2.1	

References

[1] Sylwester, E. R., Hudson, E. A. and Allen, P. G. 2000 *Geochim. Cosmochim. Acta* 64, 2431.



Experiment title: Influence of dopant atoms in cubic boron nitride (c-BN) thin films on lattice parameters and intrinsic stress investigated by X-ray diffraction

Experiment number: ME-130

Beamline: BM20	Date of experiment: from: 10-Sep-2000 to: 16-Sep-2000	Date of report: 08.02.2001
Shifts: 15	Local contact(s): N. Schell	<i>Received at ESRF:</i>

Names and affiliations of applicants (* indicates experimentalists):

F. Richter, Th. Peifer, V. Linß*
TU Chemnitz, Institut fuer Physik -123202-, D-09107 Chemnitz, Germany

W. Hoyer, H. Giegengack, Th. Halm*
TU Chemnitz, Institut fuer Physik -123402-, D-09107 Chemnitz, Germany

Report:

c-BN thin films can be deposited by quite a large number of different deposition methods. Using each of the methods results in highly stressed c-BN films. Modifications of deposition conditions which prevent high film stress do not yield the cubic BN phase either.

Owing to the large YOUNG'S modulus of c-BN, a stress of about 10 GPa corresponds to a strain of about one percent. On the other hand, incorporation of impurity atoms in c-BN may change the lattice constant by one or two percent even for low concentrations (few at.%). Hence, doping incorporation can influence the lattice constant to the same extent as the high stress does. Therefore, it should be possible to influence stress in c-BN by adding or leaving off appropriate dopant atoms during growth. The aim of this experiment was to investigate the influence of the incorporation of Al dopants on the lattice constant.

A preliminary study on such c-BN films revealed that the reflex of the (111) lattice planes is well pronounced, therefore, this reflex was chosen to be studied. To obtain a great variety of different orientations of these (111) planes relative to the sample surface, a monochromatic beam of 1.1 Å was used. The angle between the incident

beam and the sample surface was fixed at values of 0.25 ° ... 0.43 ° (slightly above the angle of external total reflection).

To access differently oriented planes, the detector was moved either around a horizontal axis (2θ) or a vertical axis (2ω) while the remaining axis was held constant.

The sin²Ψ method (where Ψ is the angle between the vector normal to the lattice plane and the vector normal to the sample surface) was applied to analyze the biaxial stress state.

Assuming a reliable value for the c-BN POISSON'S ratio from the literature, the spacing d₀(111) of the unstressed lattice planes was obtained. It was found that the unstressed lattice constant of c-BN grows linearly with the Al concentration, C_{Al}, and could be increased by up to at least 0,7 % (Fig. 1). For higher Al content, d₀(111) went into saturation and for C_{Al} > 1.3 at.% no cubic BN phase formation could be observed.

The biaxial strain and, hence, stress values of the films were found independent of the aluminium percentage. When the bulk material value of YOUNG'S modulus was used for stress determination, all films were within -(15.6±1.5) GPa.

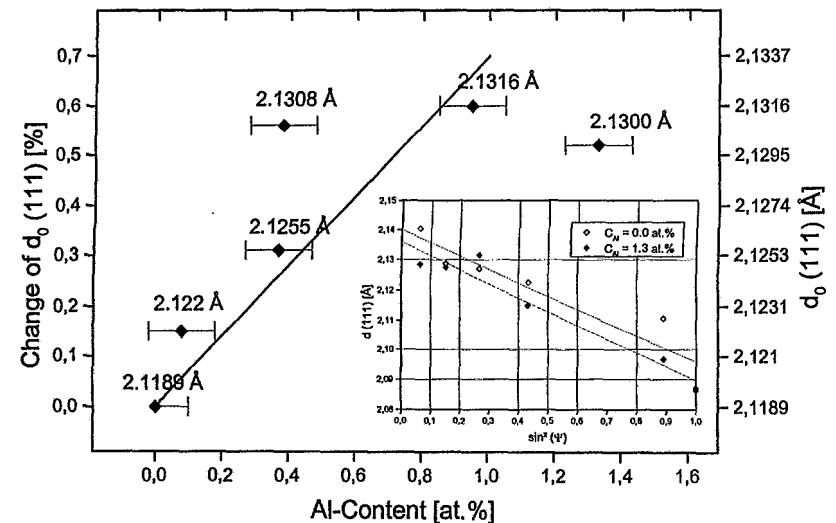


Figure 1 Unstressed lattice constant d₀ of the c-BN (111) planes in dependence on the Al-content. The inset shows the plot of d₍₁₁₁₎ against sin²Ψ for the sample with none and the highest Al content, respectively.



Experiment title: Application of EXAFS to technetium speciation in pyrometallurgy reprocessing of spent nuclear fuel and in sulfur-rich environmental samples. Part 1. Technetium in chloride system.		Experiment number: ME-131
Beamline: BM 20	Date of experiment: from: 11/11/2000 to: 14/11/2000	Date of report: 29/01/2001
Shifts: 24	Local contact(s): T. Reich, C. Hennig	<i>Received at ESRF:</i>
Names and affiliations of applicants (* indicates experimentalists): Simonoff M.*, CNRS-UMR 5084, Le Haut Vigneau, B.P. 120, F33175 Gradignan Cedex, France Guerman K.*, CNRS-UMR 5084, Le Haut Vigneau, B.P. 120, F33175 Gradignan Cedex, France Reich T.*, FZR, Institute for Radiochemistry, Dresden, Germany Hennig C.*, FZR, Institute for Radiochemistry, Dresden, Germany Sergeant C.*, CNRS-UMR 5084, Le Haut Vigneau, B.P. 120, F33175 Gradignan Cedex, France Ortega R.*, CNRS-UMR 5084, Le Haut Vigneau, B.P. 120, F33175 Gradignan Cedex, France Pravikoff M.*, CNRS-UMR 5084, Le Haut Vigneau, B.P. 120, F33175 Gradignan Cedex, France Deves G.*, CNRS-UMR 5084, Le Haut Vigneau, B.P. 120, F33175 Gradignan Cedex, France Vesvres M.H.*, CNRS-UMR 5084, Le Haut Vigneau, B.P. 120, F33175 Gradignan Cedex, France Kawai T.*, CNRS-UMR 5084, Le Haut Vigneau, B.P. 120, F33175 Gradignan Cedex, France		

Report:

EXAFS is one of most promising methods to enable us with speciation of radioactive nuclides. It is important to use it for Tc speciation in pyrometallurgy which is now considered the alternative approach to reprocessing of nuclear fuel. The associated study of long-lived fission products forms the basis for its non-hazardous treatment in radioactive wastes. During pyrometallurgical reprocessing, technetium can remain in the molten salt or enter either the sedimented phase contaminating Pu enriched phase, either electrodeposited U phase. Our preliminary results show that under some conditions Tc can also form several oxydes, oxychlorides and chlorides of different but rather high volatility, turning on an important polluting risk for gas-off treatment. As the data on EXAF spectra of technetium is now very fragmentary and do not present the whole of the species possible in the pyrometallurgy conditions, it is of high importance to carry synthetic work to supply a large set of technetium compounds in the closed containers which will meet the ESRF/ROBL security and quality demands, radioactivity level, special requirements on sample size, thickness, sample homogeneity. The chemical part of the work is planned to be carried out in Laboratory of radioanalytical and bioenvironmental chemistry, UMR5084, Gradignan. It includes the construction of pyrometallurgical reactors for the treatment of radioactive technetium samples in molten salts permitting to separate the truly dissolved, as well as sediments and sublimates.

The first part of the program deals with the pyrochemical behavior of technetium under reducing conditions. It comprises a set of samples with 13 reference technetium compounds (2 chlorides, 2 bromides, 2 pertechnetates, 2 sulfides, 5 Tc alloys) and some samples of simulated pyrometallurgically reprocessed nuclear fuel including technetium hexachlorides in fused salts, and Tc precipitated fraction from sulfur-rich environmental fresh water lake sediments with the only Tc as a radionuclide. These samples were studied by means of EXAFS spectroscopy at the Radiochemistry Hutch of ROBL providing with beamsizes of 3 x 20 mm², integrated flux at sample 6 x 10¹¹ /s, 200mA, 20 keV, spectral range 5-35 keV, 2/3 filling mode, beam line control carried out with VME, SUN workstation. SPEC Hot cells are used for radioactive sample positioning.

During this first series of shifts, we analysed 8 reference technetium compounds and the samples of simulated pyrometallurgically reprocessed nuclear fuel. In november, we have learned during three days with help of Tobias Reich and Christoph Hennig how to use the softwares Exafspak and Feef. We are now involved in the treatment of spectra to obtain quantitative results.

The difficulties encountered during this session concern too low Tc concentrations in samples and precipitation of some compounds in liquid phase.

We have some samples of this series to reanalyse and 5 samples to analyse for the first time.

Preliminary results have been presented by posters:

- K. GUERMAN, T. REICH, C. SERGEANT, R. ORTEGA, V. TASAROV, M. SIMONOFF

Technetium metal and pyrometallurgically formed sediments study and speciation by Tc-NMR and EXAFS/XANES

OECD/NEA Workshop on pyrochemical separations, march 14-15, 2000, Villeneuve les Avignon, France

- M. SIMONOFF, K.E. GUERMAN, T. REICH, C. HENNIG, R. ORTEGA, C. SERGEANT, G. DEVES, M.H. VESVRES

Technetium speciation in radioactive wastes generated in pyrochemical reprocessing

2nd Euroconference and NEA workshop on speciation, techniques, and facilities for radioactive materials at Synchrotron light sources, september 10-12, 2000, Grenoble, France

- K.E. GUERMAN, T. REICH, C. SERGEANT, R. ORTEGA, V.P. TARASOV, M. SIMONOFF, G. SIMONOFF

Etude et speciation par RMN et EXAFS du Technétium métallique et de sels formés par voie pyrométallurgique

7^e Rencontres Nationales de Radiochimie, september 27-29, 2000, Saint Rémy les Chevreuse, France



	Experiment title: Photoacoustic Detection of the XAS Signal	Experiment number: MI-346
Beamline: BM 20	Date of experiment: from: 18/11/1999 to: 19/11/1999	Date of report: 28.03.2001
Shifts: 6	Local contact(s): Dr. T. Reich	Received at ESRF: 30.03.2001
Names and affiliations of applicants (* indicates experimentalists): Dr. G. Geipel* Prof. G. Bernhard Forschungszentrum Rossendorf, Institute of Radiochemistry, P.O.Box 510 119 D-01314 Dresden		

Report:

XAS experiments are normally carried out by detecting transmitted X-rays. The signal is detected by gas ionization chamber detectors positioned before and after the sample. This method is limited in the concentration of the absorber because too low absorption generates a very small difference in the signals of the two ion chamber detectors.

In a photoacoustic measurement, the signal is generated by the production of transient heat after absorption of X-rays^{1,2)}. This signal is directly proportional to the concentration of the absorber. Therefore, a lower detection limit for the absorber is expected. The method can be compared to Laser-Induced Photoacoustic Spectroscopy (LIPAS). Comparing this method to conventional UV-Vis spectroscopy, we have an increase in the detection limit up to three orders of magnitude³⁾.

In a first run of 4 shifts we tested a normal photoacoustic design using ring piezo ceramics and piezo plates. The sample was mounted on the piezo using TESA-film. The electrical signal from the piezo was amplified by a spectroscopic amplifier to reduce the impedance and the noise of the signal and measured with an oscilloscope. The synchrotron beam was interrupted using a chopper system. A signal of this chopper was used for synchronisation of the measured signal with the frequency of the chopped beam. Unfortunately, we did not observe the prospected photoacoustic signal. This may have been caused by the following disadvantages:

- i) The contact between the sample and the piezo ceramic detector was not stable enough. In a next run we will avoid this problem by using special contact paste.
- ii) The concentration of the absorber in the sample was not adequate to the proposed signal.
- iii) The used chopper did not absorb enough of the synchrotron radiation, so that the sample was excited continuously. If this is the case, we have no interruption of the beam, which causes at least no detectable signal.

Using a frequency analyzing system, we tested the frequency of the photoacoustic signal. The measurements at the ESRF showed a very small difference signal between a run with and without an absorbing sample. The maximum of the difference in the frequency was at 30 Hz. At this frequency we can expect the photoacoustic signal. The next step is to determine the delay time between the chopped synchrotron beam and the photoacoustic signal. In laser-induced photoacoustic measurements, this delay time is about 30 μ s. This may be somewhat shorter in the synchrotron based photoacoustic measurement due to the shorter distance between the sample and the detector.

A chopped cw-laser will be used to measure the signal delay.

A second experimental run with synchrotron radiation at the ESRF is planned after test measurements of the photoacoustic signals with very low chopped laser energies.

¹⁾ T. Masujama, Photoacoustic X-Ray Absorption Spectroscopy, in P. Hess and J. Pelzl (Eds.), Photoacoustic and Photothermal Phenomena, Springer Series in Optical Sciences 58, Springer Verl. Berlin, Heidelberg 1988, p.19

²⁾ T. Masujama, X-Ray Photoacoustics for Characterization and Non-Destructive Evaluation, in J.C. Murphy et.al. (Eds.), Photoacoustic and Photothermal Phenomena II, Springer Series in Optical Sciences 62, Springer Verl. Berlin, Heidelberg 1990, p.222

³⁾ G. Geipel, G. Bernhard, V. Brendler, H. Nitsche, Complex Formation between UO_2^{2+} and CO_3^{2-} : Studied by Laser-Induced Photoacoustic Spectroscopy (LIPAS), Radiochimica Acta, 82, 59 (1998).